

FOR FURTHER TRAN

AD A 054841

Final Technical Report,

on the

REGIONALIZATION OF THE ARCTIC REGION, SIBERIA  
AND EURASIAN CONTINENTAL AREA

Sponsored by

Advanced Research Project Agency

ARPA Order No. 1827

Principal Investigator:

Professor Leon Knopoff  
(Telephone No. 213-825-1885)

Program Manager:

Mr. William Best  
(Telephone No. 202-694-5456)

Contract Number:

Air Force Contract  
F49620-76-C-0038

Effective Dates of Contract:

March 1, 1973 to  
September 30, 1977

Program Code:

4F10

Institute of Geophysics and Planetary Physics  
University of California, Los Angeles

October 1, 1977

DISTRIBUTION STATEMENT A

Approved for public release  
Distribution Unlimited

DDC  
RECEIVED  
JUN 8 1978  
B

# TABLE OF CONTENTS

Technical Report Summary . . . . . 1

## Technical Report

I.	Purposes of project . . . . .	8
II.	Review of scientific background . . . . .	8
	Regionalization . . . . .	8
	Theoretical seismograms . . . . .	13
III.	Objectives, methods, and results . . . . .	15
	Data collection . . . . .	15
	Regionalization . . . . .	22
	Inversion 1 . . . . .	31
	Inversion 2 . . . . .	37
	Inversion 2.1 . . . . .	38
	Inversion 2.2 . . . . .	39
	Inversion 3 . . . . .	40
	Inversion 3.1 . . . . .	41
	Inversion 4 . . . . .	44
	Inversion 5 . . . . .	44
	Arctic study . . . . .	46
	Theoretical seismograms . . . . .	49
IV.	Bibliography . . . . .	53

## Appendices

I.	Surface-wave dispersion computations: Rayleigh waves on a spherical gravitating earth.
II.	Generation of complete theoretical seismograms for SH III.
III.	Determination of seismometer instrumental parameters by general linear inversion.
IV.	Computation of complete theoretical seismograms for torsional waves.

ACCESSION 100	
NTB	NTB Section <input checked="" type="checkbox"/>
DOC	DOC Section <input type="checkbox"/>
UNANNOUNCED	<input type="checkbox"/>
JUSTIFICATION	<input type="checkbox"/>
DISTRIBUTION/AVAILABILITY CODES	
Dist.	AVAIL. and/or SPECIAL
A	

## TECHNICAL REPORT SUMMARY

One purpose of this investigation has been to regionalize the upper several hundred kilometers of the mantle under the Arctic region, Siberia and the Eurasian continental area using seismic surface waves. A second purpose has been to develop and test efficient computer techniques for the computation of accurate theoretical seismograms for hypothetical sources located within Eurasia and which make use of the results of the regionalization part of this study. These theoretical seismograms are complete in the sense that they contain both body and surface waves; they can be applied directly in a discrimination program by comparing the theoretical seismograms, computed for both earthquakes and underground explosions, with the actual recorded seismogram.

Regionalization. The program of regionalization involves the measurement of phase velocities for Rayleigh waves traversing the regions under investigation. The phase velocity curves were obtained with the single-station phase velocity method, which is described in the main text of this report. Briefly, the method involves selecting records of earthquakes from the library of the World Wide Standardized Seismographic Network (WWSSN) for events which: (1) occurred within, or on the perimeter of, the area of interest, (2) produced good long-period surface wave records at WWSSN stations for which the

epicenter-to-station lines lie within the regions being investigated, and (3) generated good, large recordings at a sufficient number of stations to ensure an accurate fault plane solution. When a suitable earthquake was found, an extensive data processing and data reduction system was applied to transform the data into phase velocity curves for each of the selected epicenter-to-station lines.

The complete set of phase velocity curves (for fundamental-mode Rayleigh waves recorded by the WWSSN instruments), which are then used for the regionalization of the Arctic region, Siberia, and the Eurasian continental area, consists of about 50 dispersion curves. Based on this data set, we have regionalized the area of interest by making use of an assumption that large parts of the region with similar geophysics or basement geology and age will have similar upper mantle structures. A similar assumption was made with success in the regionalization of the Pacific Ocean basin (Kausel, Leeds and Knopoff, 1974; Leeds, Knopoff and Kausel, 1974).

The inversion has proceeded by the use of both linearized and non-linear inversions procedures with the mantle properties in each of the geographic regions as unknowns. Our regionalization has made use of maps of basement geology of Eurasia coupled with a postulate of similarity of mantle cross-section for regions of similar basement age, made previously in small-scale regional studies (Knopoff, 1972).

From our regionalization studies on the Eurasian continent, we draw the following conclusions: First, the properties of the mantle of the sediment-covered Siberian and Russian platforms are highly consistent with those of the Baltic and Siberian shields and with ancient shields observed worldwide (Knopoff, 1972). Second, the Tibetan plateau has an extremely thick crust, perhaps as great as 75 km from surface to Moho. Furthermore, the upper mantle under the Tibetan plateau has high seismic velocities, indicating the absence of partial melting to relatively great depths. This can be accounted for by emplacement of the Indian shield under Tibet during the collision of the Asian and Indian plates. Third the Alpide folded belt of Iran and Turkey has a very well-developed low-velocity channel in the mantle, with good contrast to the lid above, implying the presence of a zone of partial melting at a depth of about 90 to 100 km. Fourth, the Mongolia -Sinkiang geophysical province has a well-developed low-velocity zone in the upper mantle and the more-or-less stable part of Eastern China also has a low velocity channel at typical depths.

The principal problem in the inversion has been the construction of the boundaries to the geophysical provinces, for which only incomplete information is found in the literature. A full resolution of this problem is still in the future, but the regionalization used to date, in which Eurasia is divided into 6 rather large regions, is statistically consistent with the data

and has about the correct number of degrees of freedom in the model parameterization.

Theoretical Seismograms. The second phase of our work has been the development and testing of techniques for the computation of realistic theoretical seismograms at the WWSSN and HGLP installations, for earthquake and explosive sources within the areas under investigation. For SH waves excited by both earthquakes and explosions, we can construct complete seismograms down to a period of 10 sec. (and occasionally to shorter periods). The difficulty of calculating diffraction effects due to the presence of lateral heterogeneity remains as an important unsolved problem; as long as the waves cross regional boundaries at conditions remote from grazing incidence, our theoretical seismograms are probably quite accurate. The extension, development and optimization of these algorithms and computer programs for Rayleigh, or P-SV waves on a spherical, gravitating earth has also been one of the main efforts under this contract. The efficient construction of accurate, theoretical SH seismograms for realistic models of the earth's structure using multimode methods is based on effective dispersion computations, attenuation calculations, structural transformations, and computations of eigenfunction characteristics, effects of sphericity, and point-source response; we have studied all these ingredients in detail.

Our work with theoretical seismograms has concerned the

multi-mode surface wave phases Lg, Sa and Sn; references to this work are appended. For discrimination studies, it is also desirable to have body-wave phases on the theoretical seismograms; this has been one major thrust of our most recent work; another has been the improvement in efficiency, control of accuracy and increased power and flexibility of the computational algorithms and computer programs. We have reported our ability to generate theoretical seismograms with body and surface waves, on the same record using up to twenty-one modes. Multimode theoretical seismograms containing body wave phases have been generated in the past (Satô, Usami and Landisman, 1968); however, these time series were limited to ultralong periods. The important point of our recent results is that, owing to the efficiency of our new algorithms, we have been successful in extending the period content of the theoretical seismograms through the range covered by the WWSSNLP instruments. Thus, we can generate the theoretical time series which, for the first time we believe, permits us to compare theoretical seismograms directly with the entire records obtained at the WWSSN and the HGLP installations down to a period of ten seconds. This requires that 90-100 modes be used in the multi-mode synthesis. The necessary frequency-domain information is obtained in a single, relatively inexpensive computer run; time series, for any source specification, are then obtained with a single run of a second program (Liao, Schwab and Mantovani 1977; preprint appended).

In the case of Rayleigh waves, sphericity and gravity introduce complications not encountered with Love waves. For Love waves, optimized flat-structure programs can be used since the sphericity of the real earth can be handled by exact transformation, and since gravity does not affect Love waves. At present, accurate Rayleigh-wave computations for a real earth require that sphericity and gravity be handled directly in the computational algorithms and programming; hence, our first task here was to improve the accuracy characteristics of direct Rayleigh-, or spheroidal-wave computations. The difficulty, expense, and time required for this analysis showed us why this information was not in the literature, even though the basic algorithm is available (Alterman, Jarosch and Pekeris, 1959). The results of our work (Schwab et al, 1977) are appended. They include: (1) an improved and simplified computational algorithm for the computation of the phase velocity of Rayleigh waves. (2) What we believe to be the first direct method for computing the group velocity, i.e., without appeal to variational methods; (3) numerical analyses and examples of numerical difficulties encountered in this type of computation; (4) detailed analysis of the efficiency of our optimized algorithm and programming. Even in this optimized form, these direct Rayleigh-wave computations for a spherical, gravitating earth, are about six times slower than the comparable Love-wave computations; whereas we know that computations for Rayleigh waves on a flat, non-gravitating structure are only twice as slow. Our conclusion,

from the Rayleigh wave work done here, is that new algorithms are required before the efficiency of the Rayleigh-wave computations (including sphericity and gravity) will approach a level justifying computation of the associated multimode, theoretical seismograms down to the desired period of ten seconds. We have developed a sufficiently improved algorithm (Schwab, 1977), but the necessary numerical verification and testing are only in their initial stages.

References to our own work on theoretical seismograms for Sa, Lg and Sn include: Knopoff, Schwab and Kausel (1973); Knopoff et al (1974); Nakanishi, Schwab and Kausel (1976); Kausel, Schwab and Mantovani (1977); Mantovani et al (1977). References to our work on theoretical seismograms which include both body and surface waves are: Nakanishi, Schwab and Kausel (1976); Kausel, Schwab and Mantovani (1977); Mantovani et al (1976); Mantovani (1977a,b); Liao, Schwab and Mantovani (1977).

## TECHNICAL REPORT

## I. Purposes

→ One purpose of this project was to determine the regional variations of the crust and upper mantle in the regions under investigation using the properties of surface wave dispersion in the Arctic region and the Eurasian continental area. The regions of high seismicity within and around the region, plus the dense set of WWSSN stations located around the perimeter of the region, gave assurance that we could acquire sufficient single-station phase velocity data for the application of regionalization procedures.

A second purpose was to develop computational techniques for calculating complete, accurate theoretical seismograms for both earthquake and explosion sources within the area under investigation, and which could be compared with those recorded at the WWSSN and HGLP stations at the edge of this region. ★

## II. Review of scientific background

Regionalization. The single-station surface wave method allows all stations to be located at the edge of the region under investigation; this technique is ideal for the study of Eurasia. Knopoff and Schwab (1968) extended the description of the single station method (Brune, Nafe and Oliver, 1960) to take into account the frequency dependence of the apparent initial phase of the source. The success of the single-station method depends on the calculation of the initial phase. For dislocation

sources in layered media, the initial phase can be determined by a method due to Ben Menahem and Harkrider (1964) and Harkrider (1964, 1970) who obtained the surface wave response to double couple sources. The far-field response to displacement-dislocation faulting is equivalent to that from a point-source, double-couple in an unfaulted medium (Burridge and Knopoff, 1964). Thus if the source focal mechanism is known from fault-plane, surface wave amplitudes, or other methods, the initial phase can be determined for small or moderate sized earthquakes. By means of transformation techniques (Biswas and Knopoff, 1970) or empirical correction methods (Bolt and Dorman, 1961), it is possible to provide corrections for sphericity.

The first inversions of surface wave dispersion data to give upper mantle structure were carried out by Dorman and Ewing (1962), Brune and Dorman (1964) and Knopoff, Mueller and Pilant (1966). These papers were concerned with obtaining a single structure which fit the experimental data. Knopoff (1961, 1962) pointed out that the inversion of noise-free data is not unique. Subsequent efforts were mainly concerned with finding the set of structural models which fit the data to within the experimental accuracy (Keilis-Borok and Yanovskaya, 1967; Press, 1968, 1969). The inversion of noisy data enlarges the span of non-unique, acceptable models over that for noise-free data.

Two methods of inversion are available. In the first of the

techniques, perturbation methods are applied in a linearized version of the problem. The problems of inconsistent or correlated data are accounted for by smoothing in the data-space, usually by a least-squares procedure. The problems of over-parameterization of the model space are taken care of by smoothing in the model space, by a procedure usually described as "deltaness". Further reductions of the number of model parameters can stabilize the inversions. Examples of linearized inversions are given by Backus and Gilbert (1968, 1970), Knopoff & Jackson (1972) Jackson (1972), and Wiggins (1972).

The full non-linear inverse problem in a multidimensional parameter space of high order has been attacked by Monte Carlo methods (Press, 1968, 1969). The inefficiency of Monte Carlo methods can be minimized at the sacrifice of reducing the dimensionality of the parameterization to a value less than about seven by exploring a neighborhood of acceptable solutions for other acceptable solutions. Such a program has been called Hedgehog and has been much used in this laboratory (e.g. Biswas and Knopoff, 1974 ; Knopoff and Schlue, 1972 ; etc.); copies of this program exist in Moscow, Bologna, Edmonton, Bari, Cambridge (UK), Paris, etc. Both linearized and Hedgehog methods have been used in our inversions.

The single-station, surface wave regionalization of an area is based on the assumption that the surface waves travel paths, and the assumption that the phase travel time from epicenter to station is the sum of the travel times through the homogeneous subdivisions of the laterally heterogeneous region (Knopoff, 1969). This permits the travel-time at each frequency to be expressed as a system of inhomogeneous equations; for each path, the total travel time is the inhomogeneous term, the distances through the subdivisions are the coefficients, and the slownesses in the subdivisions are the unknowns. We have pointed out (Leeds *et al.* 1974) that the solution of this system of equations can yield the experimental phase slownesses associated with each of the subdivisions only if we make the assumption that the errors in each region are uncorrelated. Since these errors are not uncorrelated, we must consider the model parameters as the primary unknowns in the inversion and derive the phase slownesses in the pure regions therefrom.

The first application of the use of single-station phase delay measurements in the pursuit of regionalization of a large inhomogeneous area was performed by Kausel, Leeds and Knopoff (1974), Leeds, Kausel and Knopoff (1974) and Leeds (1975). In the above work, phase delays along long paths across the Pacific area were found to vary systematically with distance from the East Pacific Rise. This persuaded us that the appropriate geographic regionalization was plausibly based on a basement

i.e. magnetic, age of sea-floor spreading. Our geographic provinces then took the form of broad magnetic age stripes. An inversion using this regionalization showed that although the number of criss-crossing paths was plentiful, the number of degrees of freedom in the data was remarkably small. Furthermore, we found that the data set did not permit one to obtain detailed information concerning the bottom of the low-velocity channel. We did find that the lithosphere increased in thickness monotonically with age: at the ridge crest, the lid of the channel has almost zero thickness, while in the oldest ocean this lid is about 100 km thick. The lid thicknesses are consistent with a geochemical model in which the lid-channel interface is at the solidus for wet peridotite.

Because they have not developed good long-period instruments, Soviet seismologists have not been able to focus attention on upper mantle studies. Also, their extensive program in deep seismic sounding has focused interest upon crustal studies. The Soviet surface wave work has been limited to short-period investigations -- usually less than 40 seconds -- and has been concerned mainly with determining crustal properties. References to Soviet surface-wave work include Arkhangel'skaya (1960), Savarensky and Ragimov (1958, 1959), Savarensky, Solov'eva and Shechkov (1959) and Savarensky and Sikharulidze (1959), Popov (1960), Shechkov (1961, 1964, 1970), Savarensky and Shechkov (1961), Shechkov and Solov'eva (1961), Savarensky and Peshkov, 1968; Sikharulidze and Makharadze, 1968; Savarensky et al. 1969.

Since appropriate Soviet-based seismic data are not available to us, our own work has thus far focused on the estimation of upper mantle properties in Eurasia through the use of the only reasonable tools available to us, namely phase delays of surface waves on long paths, criss-crossing the region of interest. This, plus a plausible model of regionalization -- based in part on the observations in Knopoff (1972) for continents --, permits an attack on the problem of regionalization of the upper mantle of Eurasia.

Theoretical seismograms. Relative to the discrimination problem, probably the most important feature in the calculation of theoretical seismograms which requires improvement over previously existing systems for such computations is the capability of extending both body- and surface-wave portions of the theoretical computer seismograms to short periods. In this context, by "short-period" we refer to the period range covered by the long-period instruments of the WWSSN installations. In our formulation, the successful accomplishment of this task is dependent upon improved techniques for obtaining multimode dispersion-attenuation information for reasonably realistic models of the earth, i.e. spherical, radially heterogeneous, anelastic models.

Optimization of this type has been one of the main interests in our laboratory for several years. The results of our early work, based on the Thomson (1950)-Haskell (1953) technique and on Knopoff's (1964) method for treating flat-layered structures,

are reported by Schwab (1970) and Schwab and Knopoff (1970; 1971; 1972; 1973). The results of our work on spherical-to-flat-structure transformation techniques, which permit the use of flat-structure programs in dispersion-attenuation computations with Love waves for spherical models of the earth, are given by Biswas and Knopoff (1970), Schwab and Knopoff (1971; 1972; 1973), and Kausel and Schwab (1973). In this last reference, we have also given an outline of the approach we have adopted to handle the synthesis of multimode seismograms once the dispersion, attenuation, source, and excitation functions have been specified. The entire theoretical seismogram for a dislocation source in a spherical earth can be expressed as a simple sum of normal mode contributions (Saito, 1967; Takeuchi and Saito, 1972). We first applied our scheme for generating theoretical seismograms to the interpretation of the seismic phase Lg (Knopoff, Schwab and Kausel, 1973; Knopoff et al. 1974). This phase is a multimode interference phenomenon which belongs to the surface wave portion of the seismogram. In this report we indicate that we have developed a system for synthesis where both body and surface waves appear on the same seismogram for realistic models for the earth, and where the period range spans that covered by the long-period instruments of the WWSSN. Earlier work of this type, which was performed with simplified models of the earth, is summarized by Alterman and Loewenthal (1972). Satô, Usami and Landisman (1968)

describe the computation of complete theoretical seismograms for realistic models of the earth. However, their results are limited to ultralong periods.

### III. Objectives, methods and results.

Data collection. Accurate surface wave phase delays across the area with single-station method require that we know the focal mechanism and the depth of focus in order to obtain the corrections due to the apparent initial phase. We have confined our attention to the measurement of the phase velocity dispersion of the fundamental mode. Frez and Schwab (1976) have computed the importance of the structural parameters on the determination of the initial phase.

Long period records from the 47 WWSSN stations which border the region of interest have been used in the study. The locations of these stations are shown in Figure 1. We have also obtained several seismograms (through World Data Center B) of Soviet records made in Central Asia on experimental long-period instruments. However, the precision of these latter recordings plus an uncertain calibration impulse response has not permitted us to use them.

An example of the intermediate magnitude seismicity of the area is given in Figure 2. Epicenters are plotted for earthquakes which occurred during the interval from February, 1963 to February, 1967 and having magnitudes between 5.9 and 6.6. In addition to the epicenters shown in Figure 2,

FIG. 1. Locations of WWSSN and HGLP stations.

FIG. 2. Seismicity of the Eurasian region. The regions of high seismicity along the eastern border of the Kamchatka peninsula and along the Aleutian arc also provide useful events for the study.

Fig. 1

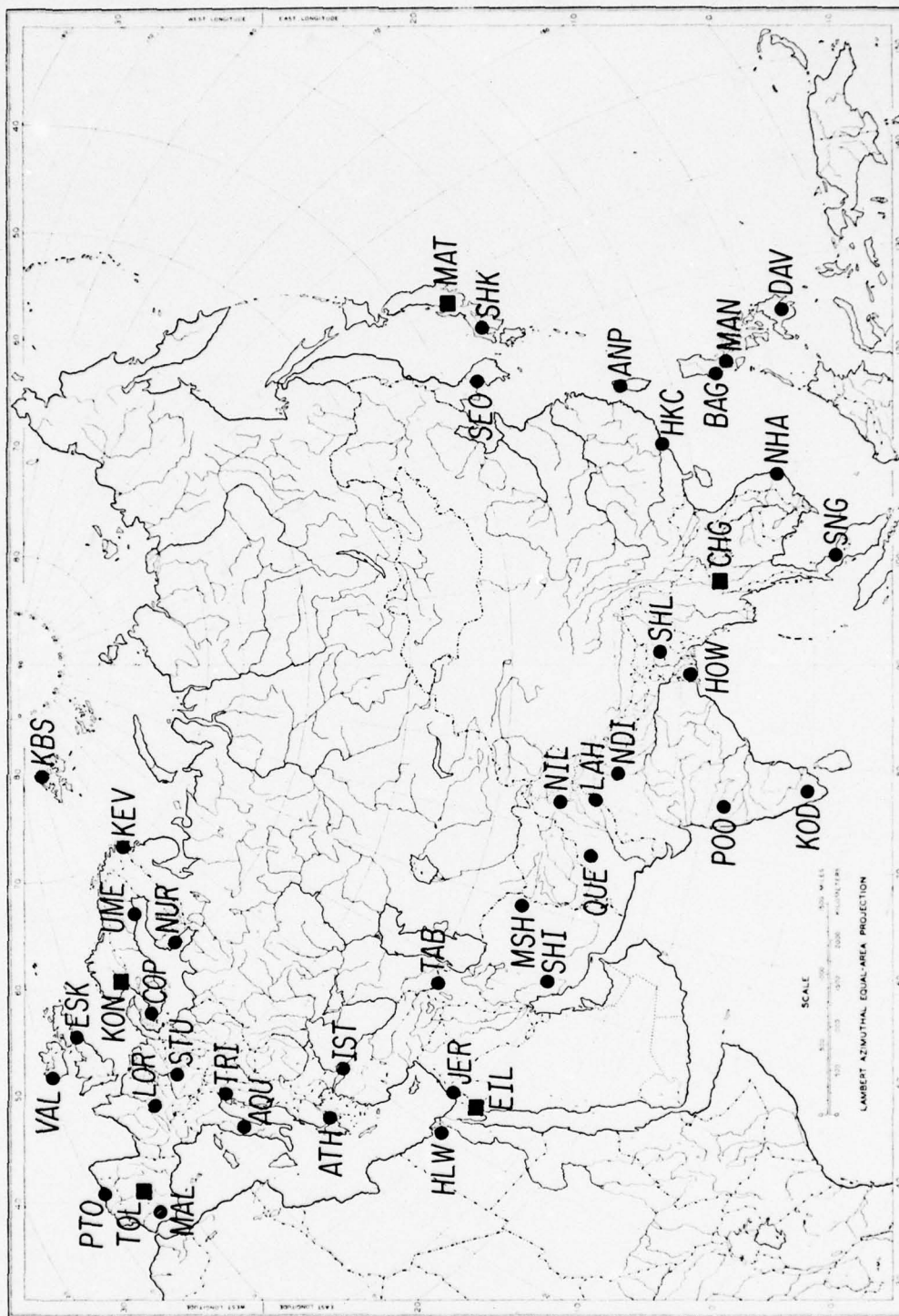
● COL

● GDH

● KTG ● CCG

● NOR

● AKU



● WWSSN STATIONS  
 ■ HIGH-GAIN, LONG-PERIOD STATIONS

Fig. 2



USEFUL EPICENTERS  
 $5.9 \leq \text{MAGNITUDE} \leq 6.6$   
FEB. 1963 - FEB. 1967

there are regions of high seismicity along the eastern border of the Kamchatka peninsula and along the Aleutian arc. The choice of this range of magnitudes is governed by two considerations. First, experience has shown that good long-period surface wave information requires events with magnitudes above a certain value; of course, a shock which is so large as to send the instrument off-scale is useless for our purposes. Second, the application of the single-stations method requires knowledge of the focal mechanism. We must therefore use events large enough to allow us to obtain an accurate fault plane solution for each event we select for processing.

Since the set of stations around the area to be studied is dense as are the regions of high, intermediate-magnitude seismicity located within and around the area, there has been no problem in obtaining sufficient data for the project. It is interesting to note that the area is almost completely encircled by either stations or epicenters or both. The limits of the area, which we have covered with a sufficiently dense set of paths from earthquakes to epicenters, are shown in Figure 3 by the solid lines. The shaded regions are those of high, large-magnitude seismicity.

Recordings from fifteen events were processed. The list of events is given in Table I, with their USCGS-NOAA specifications. The focal parameters and other data are listed in Table II. We have constructed fault plane solutions for 11

FIG. 3. Limits (solid lines) of the region covered with a dense set of epicenter-to-station paths. Solid regions are those of high seismicity.

Fig. 3

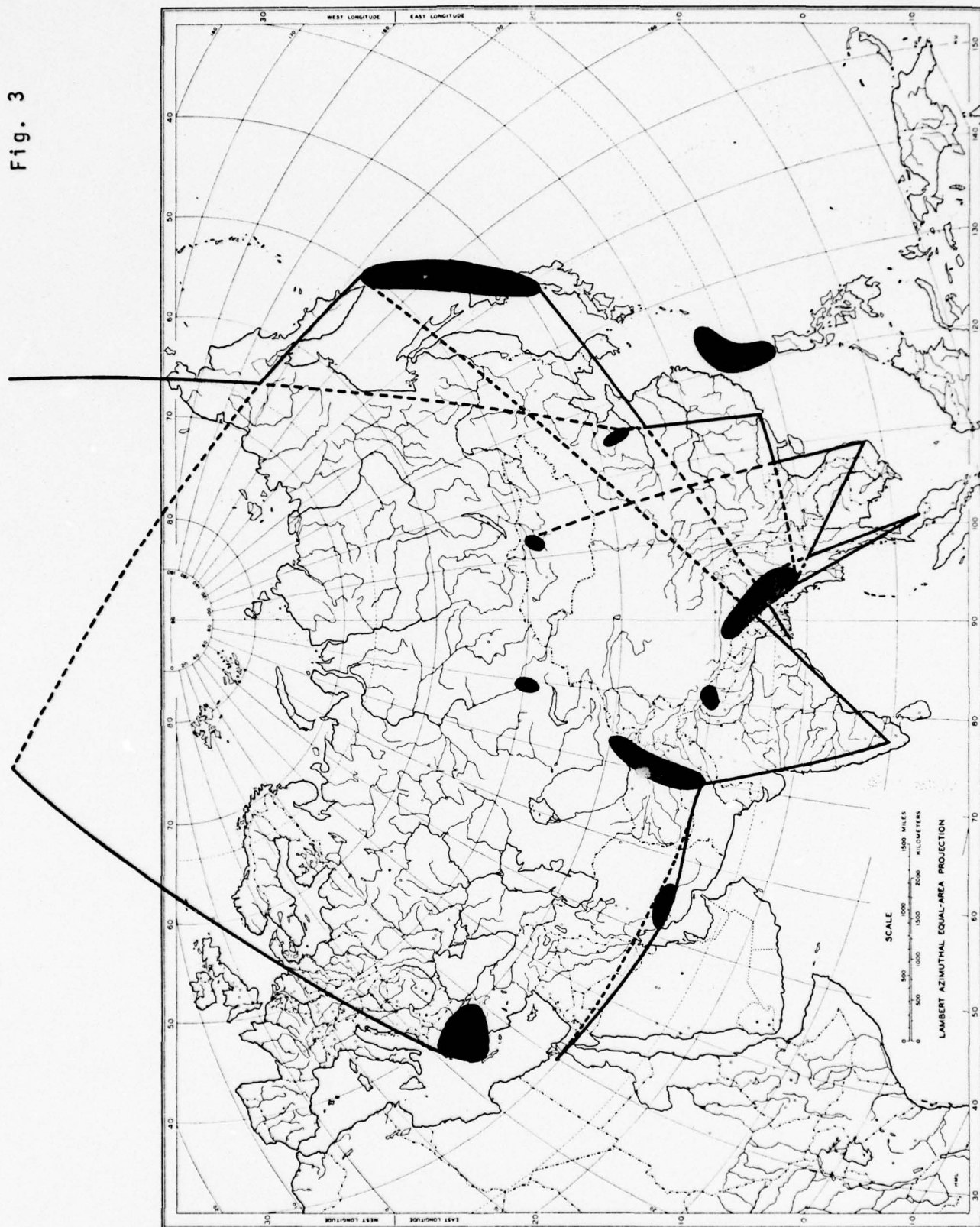


Table I

Events used in phase velocity determinations  
(USCGS specifications)

		Date	Time	Lat.	Long.	h (km)	M
1.	Red Sea	Mar. 31, 1969	07:15:54.4	27.7°N	34.0°E	33	6.0 to 6.8
2.	Hsingtai	Mar. 7, 1966	21:29:17.4	37.3°N	114.9°E	33	6.0
3.	Kamchatka	Dec. 26, 1964	14:30:29.1	51.8°N	156.8°E	136	5.7
4.	Lena River	Aug. 25, 1964	13:47:20.6	78.2°N	126.6°E	50	6.1
5.	Tashkent	Apr. 25, 1966	23:22:49.3	41.3°N	69.2°E	8	5. 3
6.	Lop Nor	Oct. 14, 1970	07:29:58.6	40.9°N	89.4°E	0	--
7.	Yunnan	Feb. 13, 1966	10:44:41.3	26.1°N	103.2°E	33	5.7
8.	Hindu Kush I	June 6, 1966	07:46:16.1	36.4°N	71.1°E	221	6.2
9.	Hindu Kush II	Dec. 28, 1974	12:11:43.7	35.1°N	72.9°E	22	6.0
10.	East. Aleut.	Feb. 6, 1965	01:40:33.2	53.2°N	161.9°W	33	6.4 to 6.7
11.	East. Aleut.	Feb. 6, 1965	16:50:23.6	53.3°N	161.8°W	33	6.1 to 6.6
12.	West. Aleut.	Feb. 5, 1965	09:32:09.3	52.3°N	174.3°E	41	5.9 to 6.5
13.	West. Aleut.	Feb. 6, 1965	04:02:53	52.1°N	175.7°E	35	5.9 to 6.2

Table II

## Focal Parameters for Events Studied

Event No.	$\phi$	$\delta$	$\lambda$	h(km)	Fault Plane Solutions	Paths
1.	133 <sup>o</sup>	66 <sup>o</sup>	242 <sup>o</sup>	15	Fig. 4	Fig. 14
2.	122 <sup>o</sup>	82 <sup>o</sup>	0 <sup>o</sup>	14.5	5	15
3.	210 <sup>o</sup>	90 <sup>o</sup>	90 <sup>o</sup>	136.	6	16
4.	165 <sup>o</sup>	58 <sup>o</sup> W	260 <sup>oa,b</sup>	11.5 <sup>a,b</sup>	7	17
5.	305 <sup>od</sup>	70 <sup>od</sup>	90 <sup>od</sup>	8.		22
6.	explosion			0.		22
7.	190 <sup>o</sup>	70 <sup>o</sup>	279 <sup>o</sup>	33.	8	18
8.	77 <sup>o</sup>	50 <sup>o</sup>	76 <sup>o</sup>	221.	9	18
9.	122 <sup>o</sup>	40 <sup>o</sup>	61 <sup>o</sup>	22.	10	18
10.-11.	(twin earthquakes)				11a,b	19
12.-13.	(twin earthquakes)				12	20

a. Depth obtained from Rayleigh wave spectra.

b. Rayleigh wave spectra for event 2 shown in Fig. 13

c. Sykes (1967) gives fault planes for this event as

$$\phi = 4^{\circ}, \quad \delta = 58^{\circ}\text{W}$$

$$\phi = 338^{\circ}, \quad \delta = 54^{\circ}\text{E}$$

of these cases (including two pairs of twin earthquakes). The list of figures of these fault plane solutions is given in Table II. In one case (No. 5) we have used the fault plane solution of Zakharova et al (1971). In one case (No. 6) we have assumed the source that of an explosion. In two cases (Nos. 1, 2) we have used Rayleigh wave spectra to help determine the focal parameters; in these cases, we were able to obtain the depth of focus more accurately than by conventional methods. In the case of No. 2 the spectra (Fig. 13) also helped refine the fault plane parameters and permit us to modify Sykes' (1967) values. The methods used to determine fault-plane parameters from surface wave spectra are given by Ben Menahem and Toksöz (1963).

FIG. 4. Fault plane solution for event 4 (Red Sea)  
occurring at 07:15:54.4 GMT, March 31, 1969.

FIG. 5. Fault plane solution for event 1 (Hsingtai)  
occurring at 21:29:17.4 GMT, March 7, 1966.

FIG. 6. Fault plane solution for event 3 (Kamchatka)  
occurring at 14:30:29.1 GMT, December 26, 1964.

FIG. 7. Fault-plane solution for event 2 (Lena River)  
occurring at 13:47:20.6 GMT, August 25, 1964.  
The solution given by Sykes (1967) is indicated  
by dotted lines.

FIG. 8. Fault plane solution for event 7 (Yunnan)  
occurring at 10:44:41.3 GMT, February 13, 1966.

FIG. 9. Fault plane solution for event 8 (Hindu Kush)  
occurring at 07:46:16.1 GMT, June 6, 1966.

FIG. 10. Fault plane solution for event 9 (Hindu Kush)  
occurring at 12:11:43.7 GMT, December 28, 1974.

FIG. 11a. Fault plane solutions for events 10 and 11  
11b. (Eastern Aleutians) occurring at 01:40:33.2  
(Fig. 11a) and 16:50:29 GMT (Fig. 11b), February 6,  
1965.

FIG. 12. Fault plane solution for events 12 and 13 (Western Aleutians) occurring at 09:32:09.3 GMT, February 5, 1965 and 04:02:53 GMT, February 6, 1965.

FIG. 13. Rayleigh-wave amplitude distributions for event 2 (Lena River) occurring at 13:47:20.6 GMT, August 25, 1964. The central set of radiation patterns are the results of theoretical computations based on the fault plane solution given in the text. The other four radiation patterns depict the experimental results.

Fig. 4

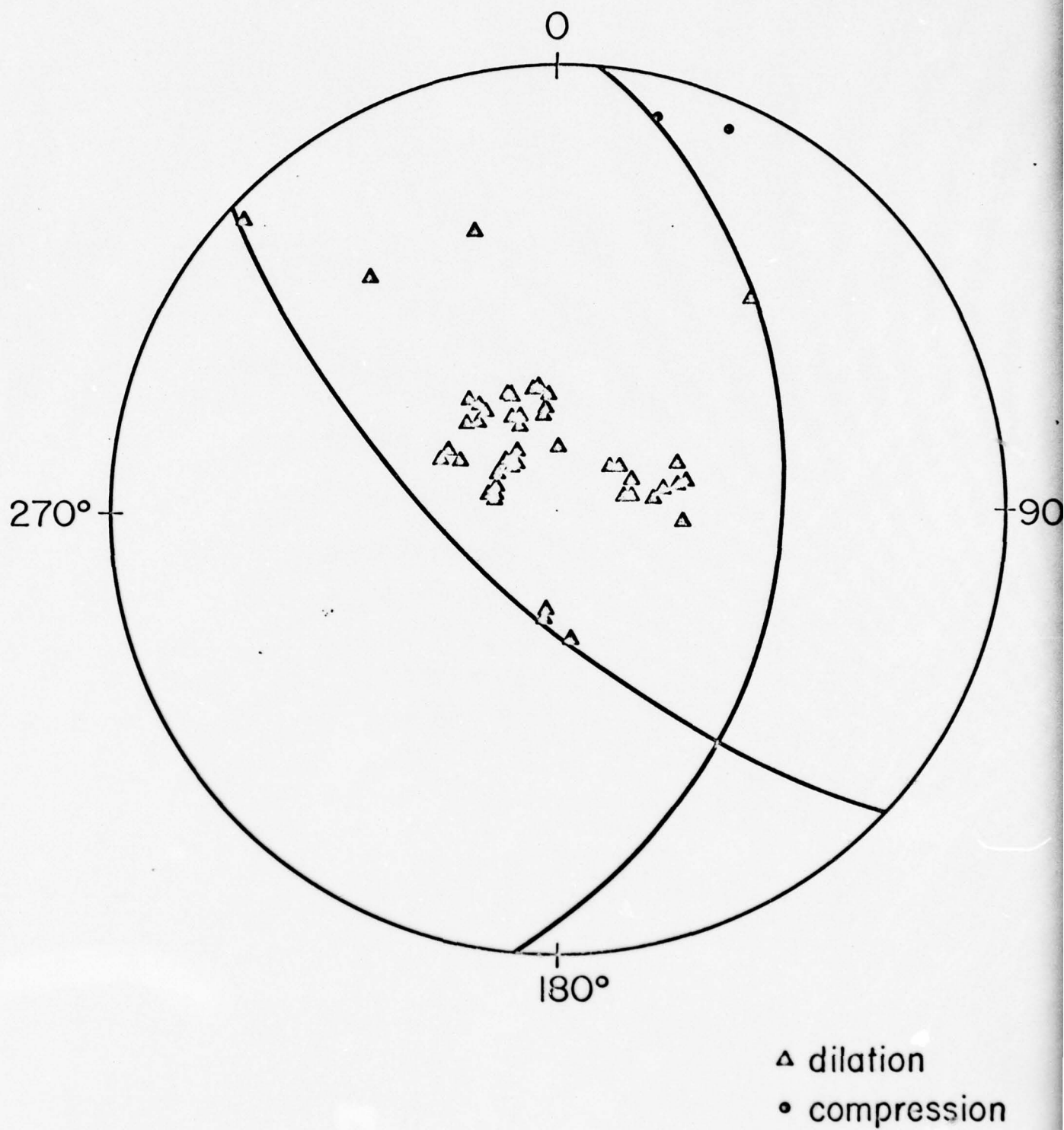


Fig. 5

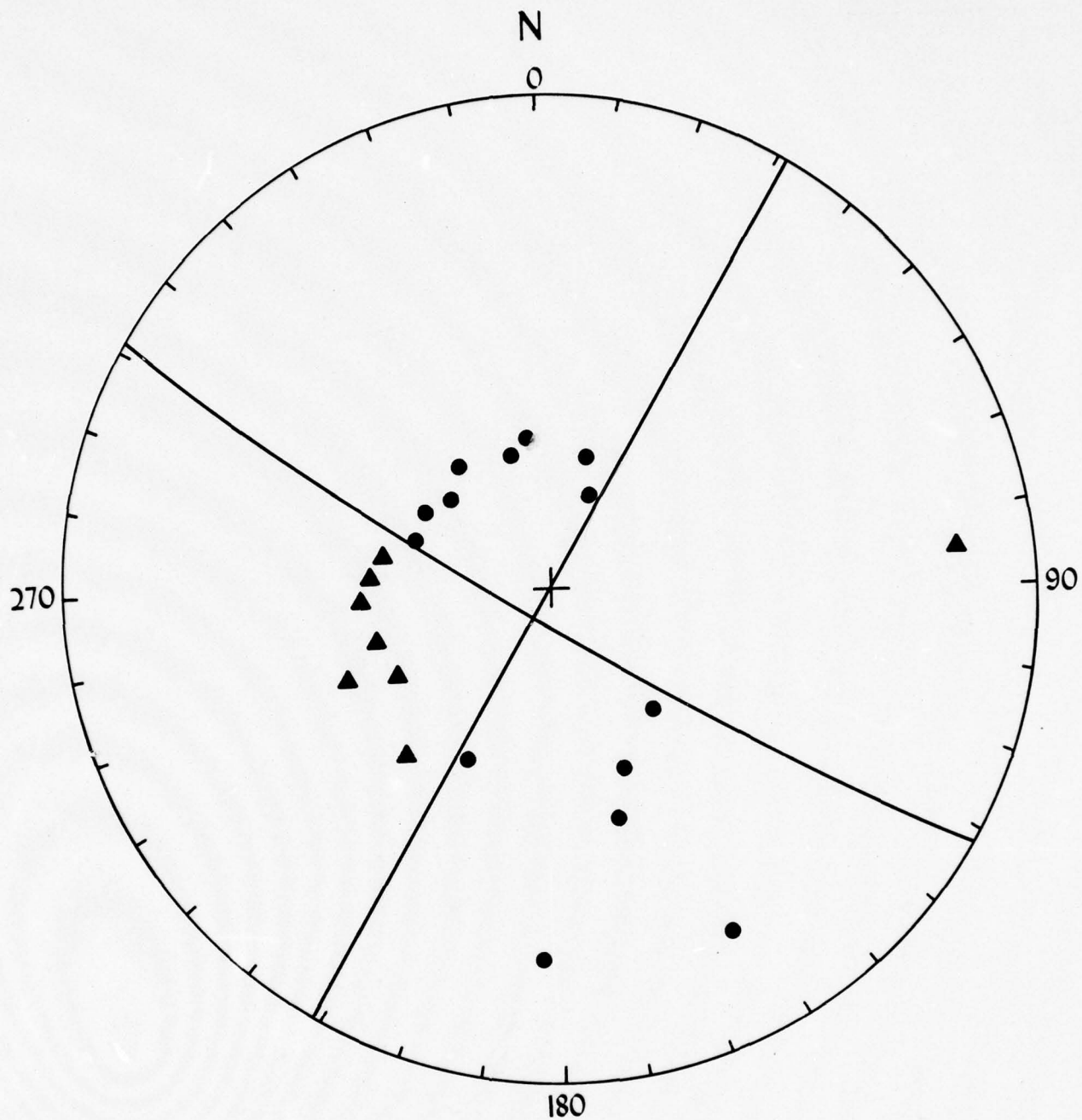
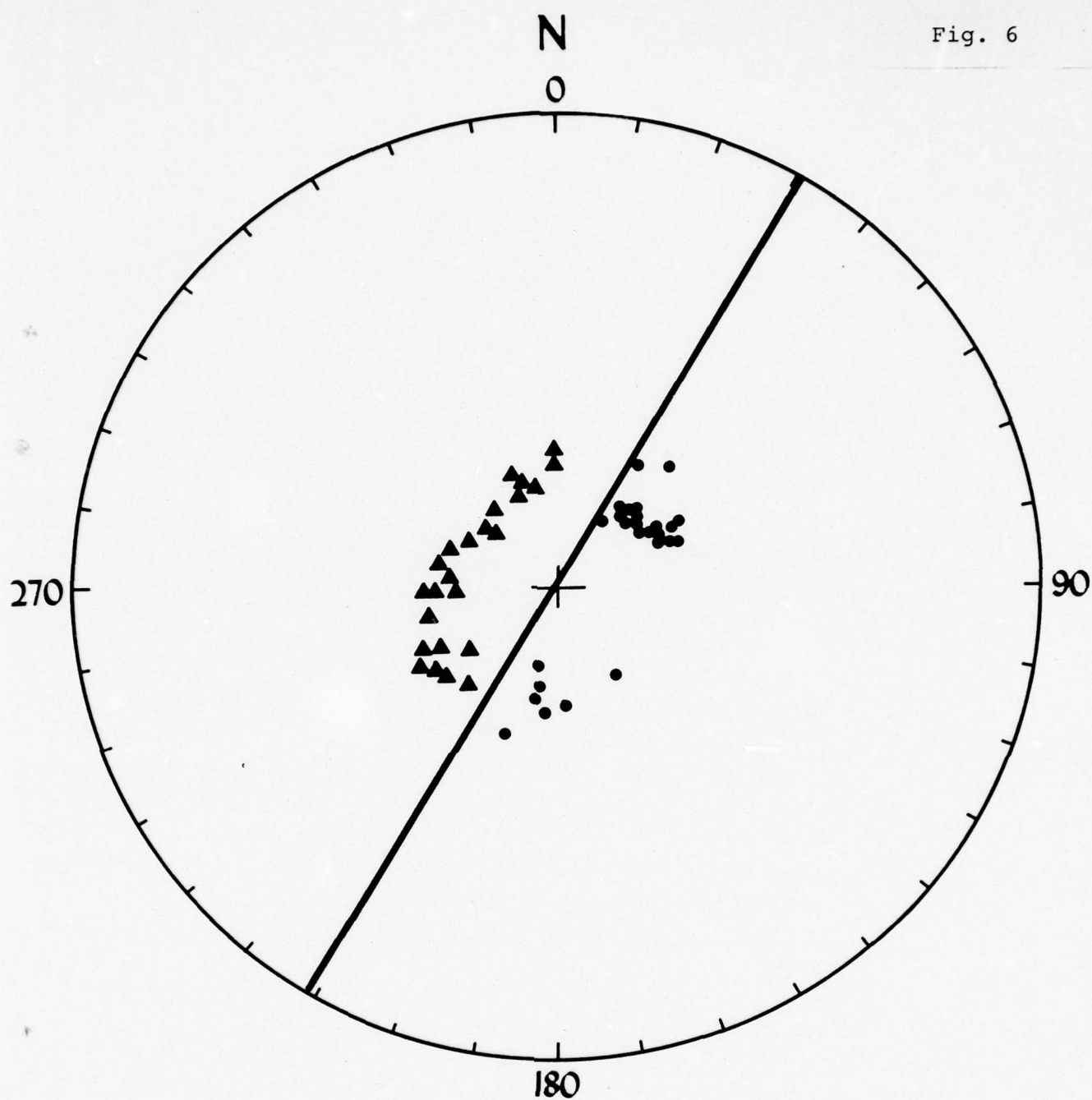


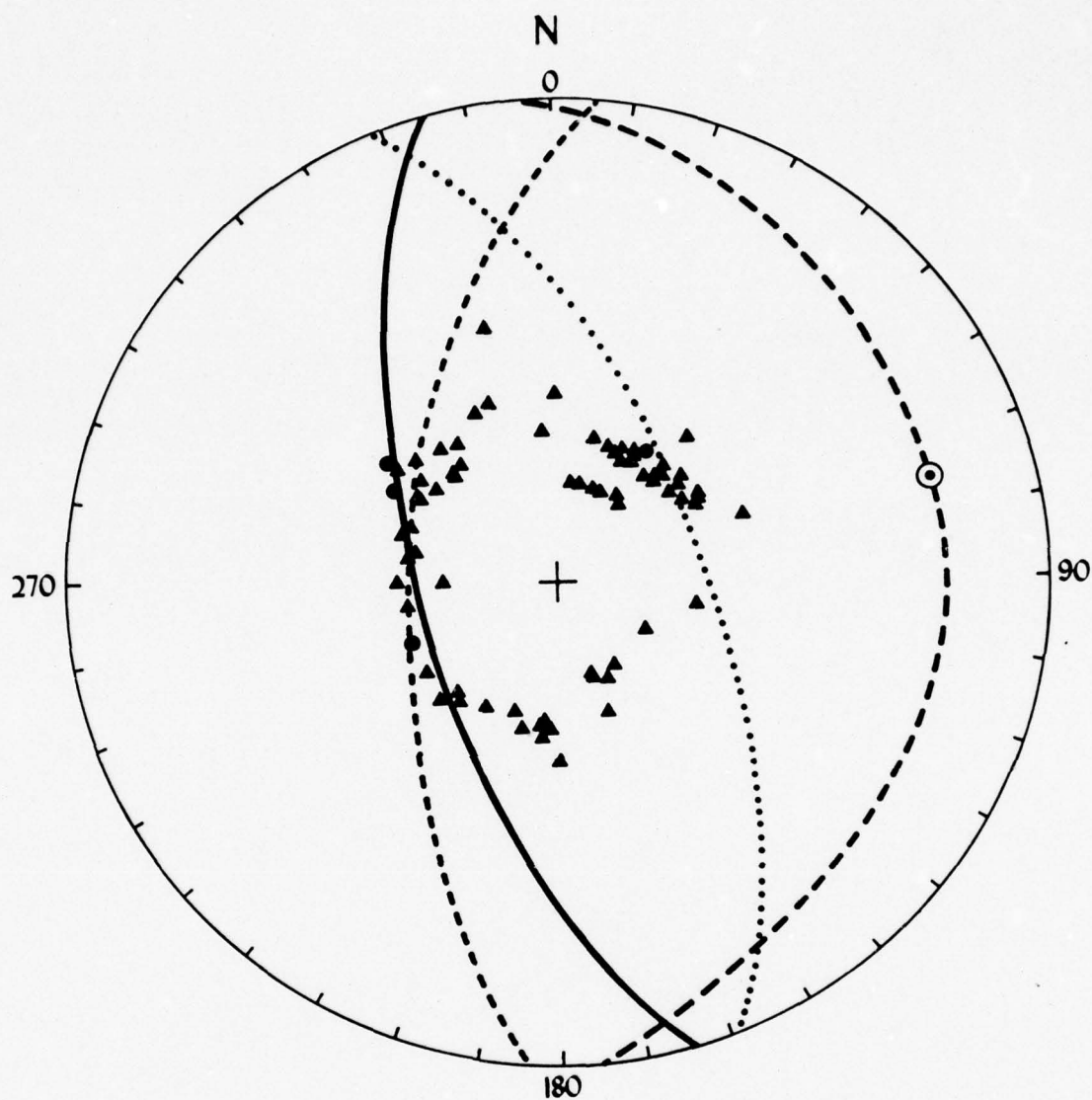
Fig. 6



**SOURCE DEPTH=136 KM**

- compression
- ▲ dilation

Fig. 7



SOURCE DEPTH=11.5 KM

- compression
- ▲ dilatation

Fig. 8

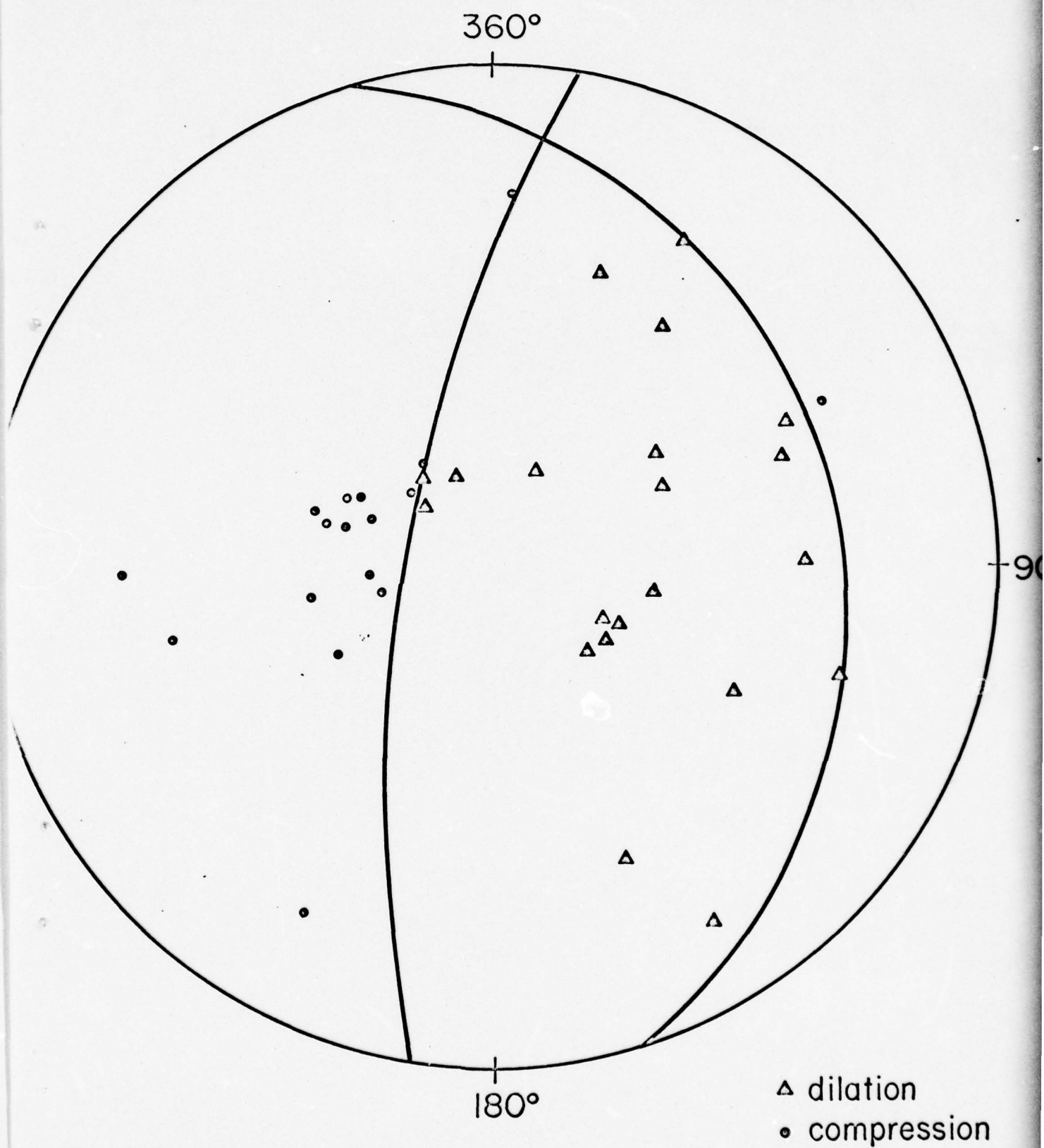


Fig. 9

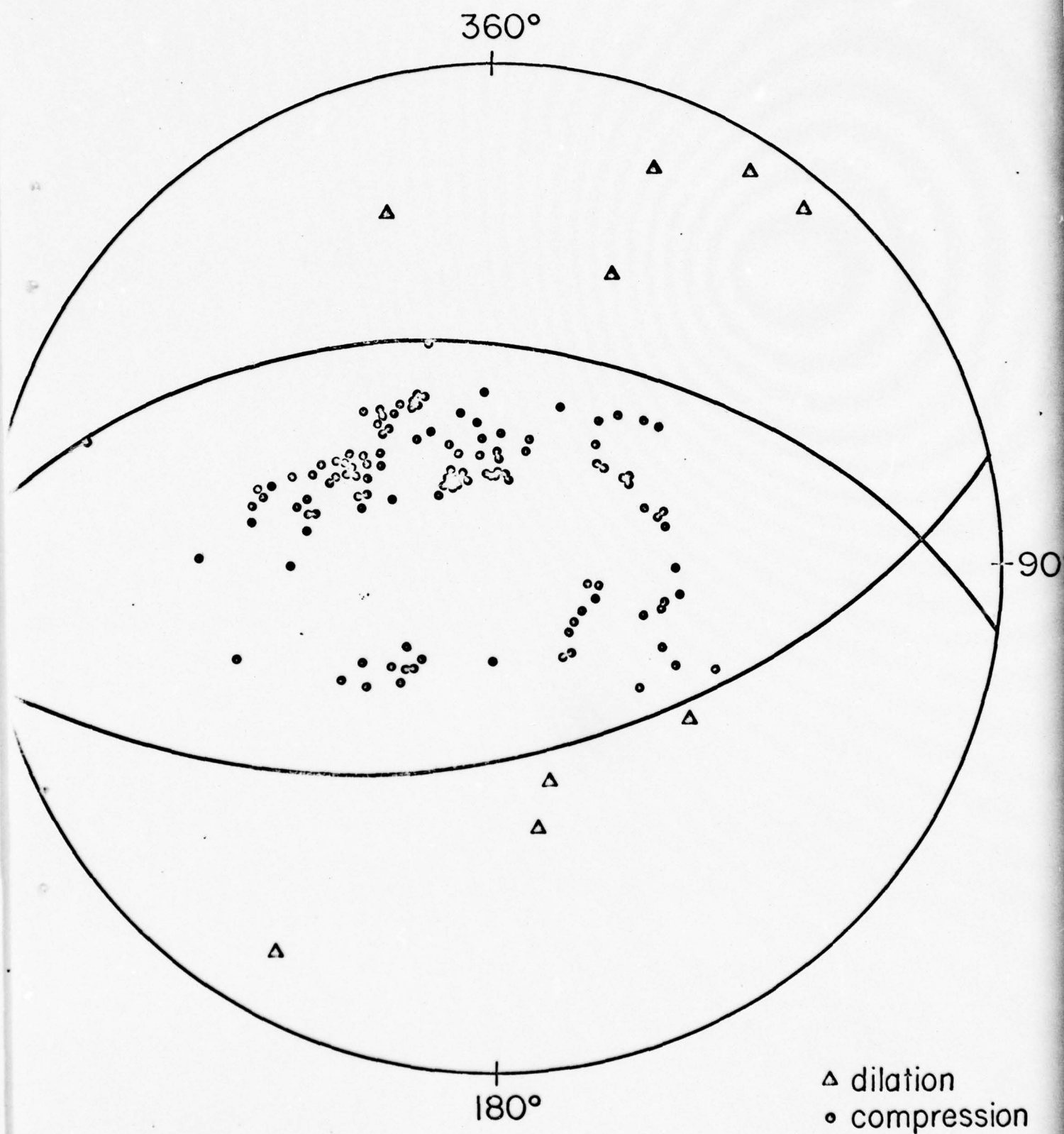


Fig. 10

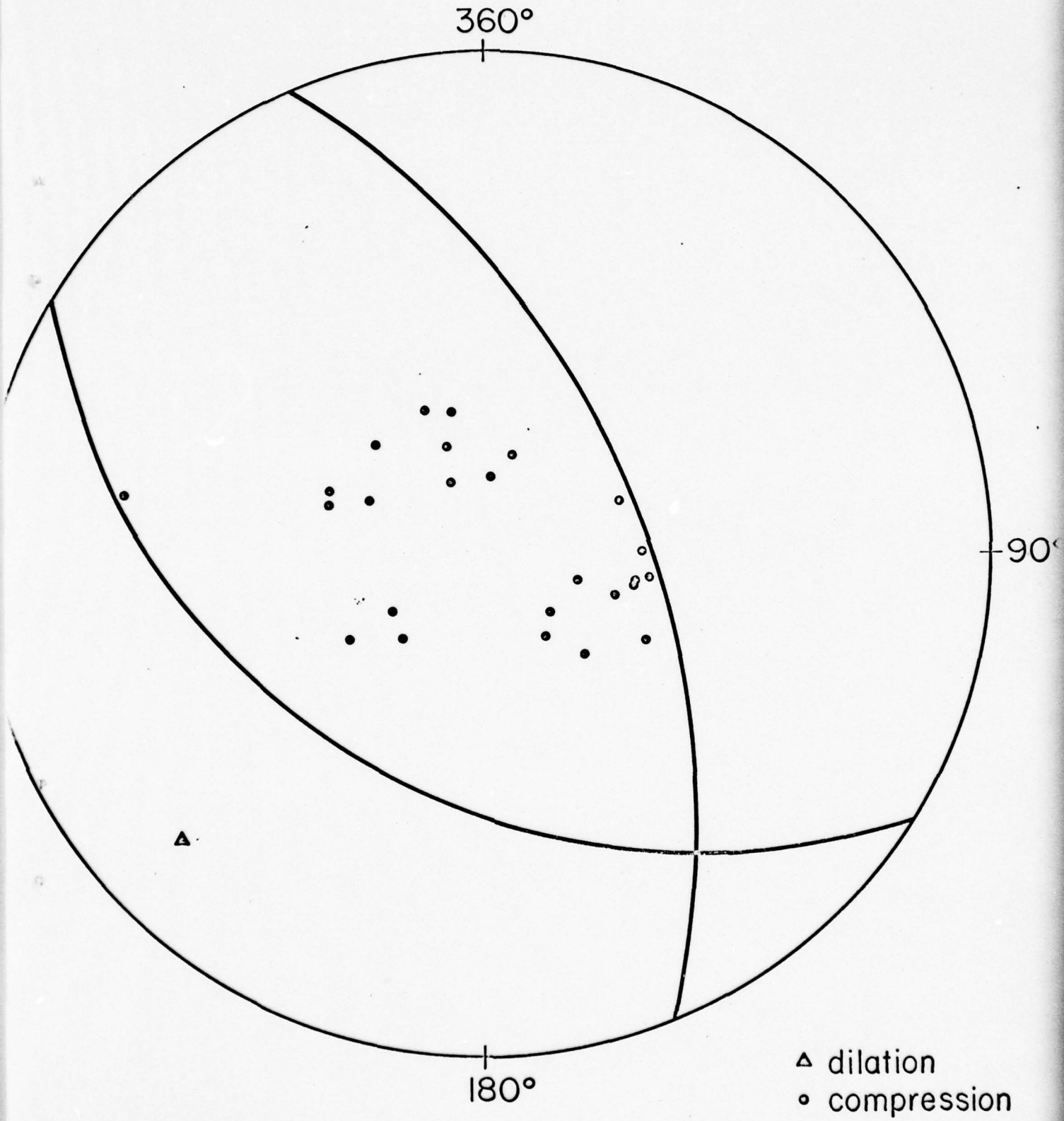
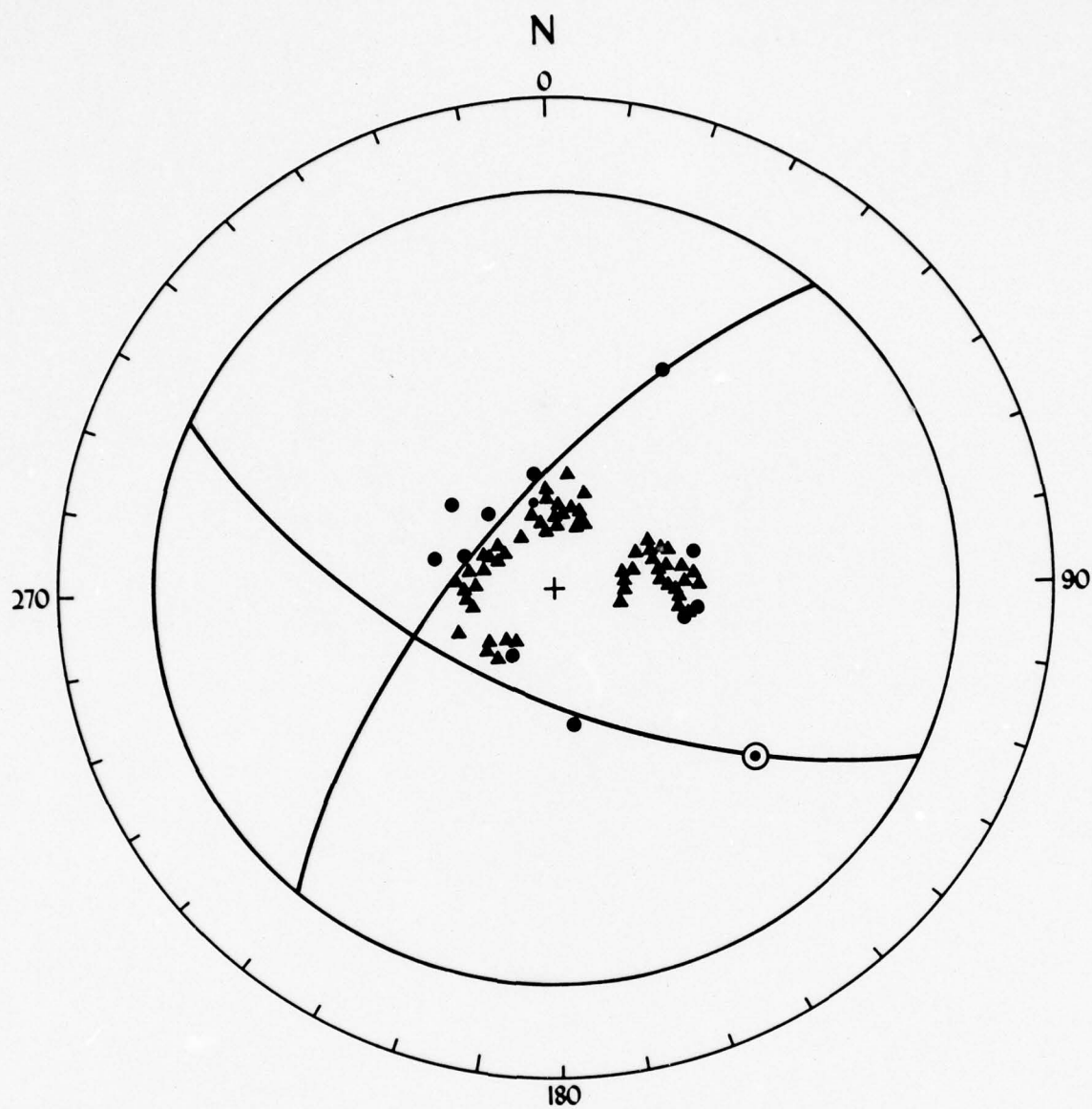
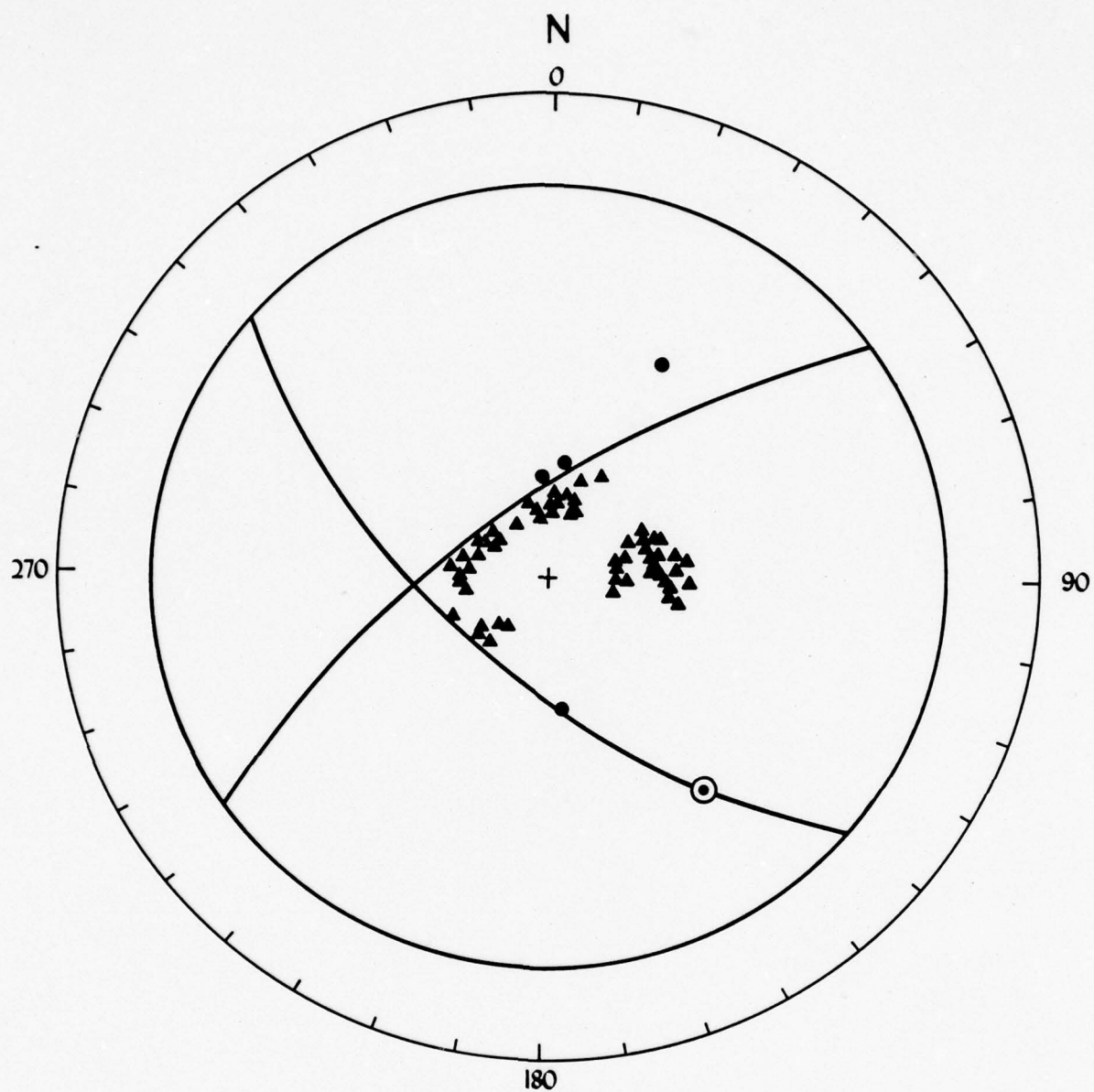


Fig. 11A



SOURCE DEPTH=33 KM

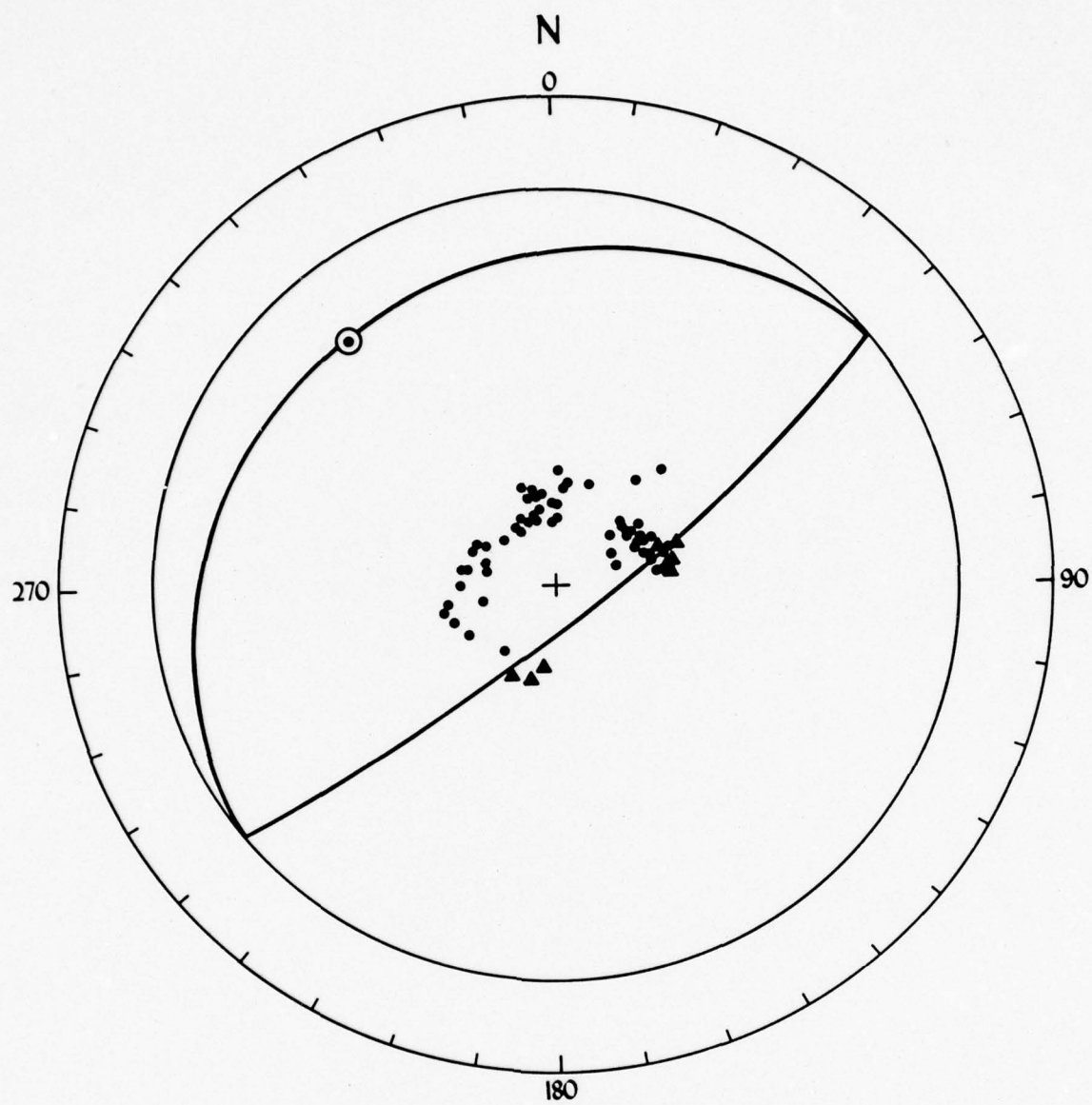
Fig. 11B



SOURCE DEPTH=33 KM

- compression
- ▲ dilatation

Fig. 12

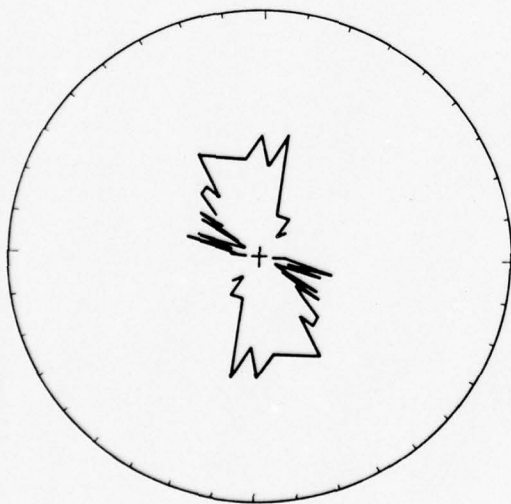


SOURCE DEPTH=41 KM

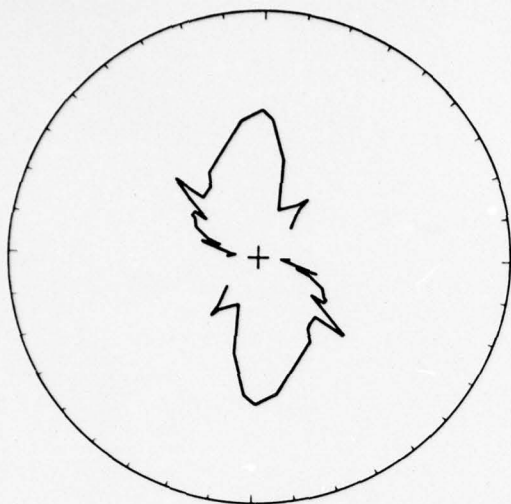
- compression
- ▲ dilatation

Fig. 13

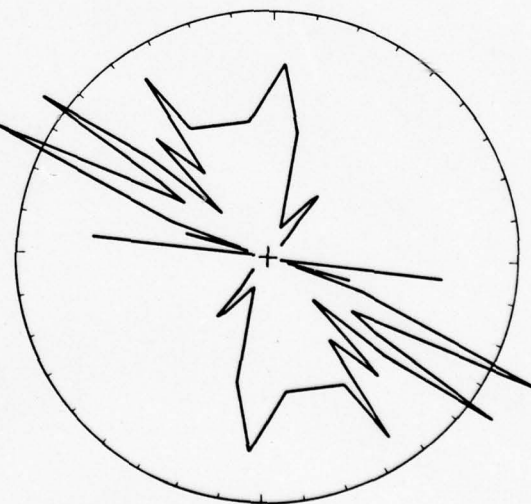
PERIOD = 208 SEC



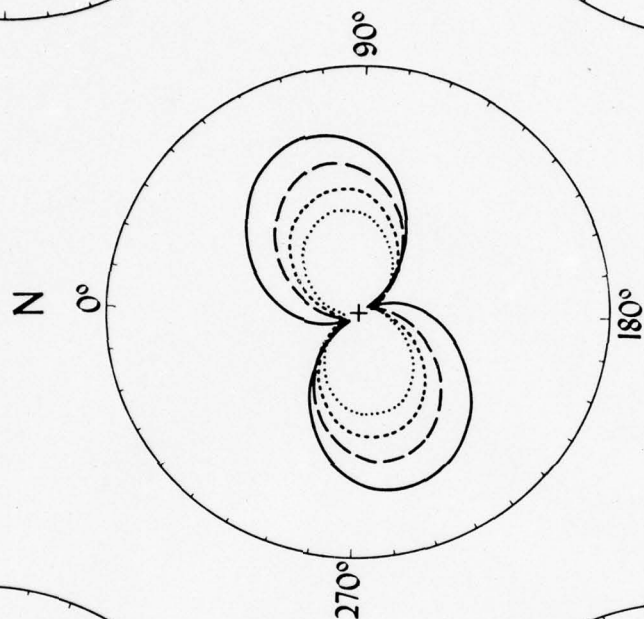
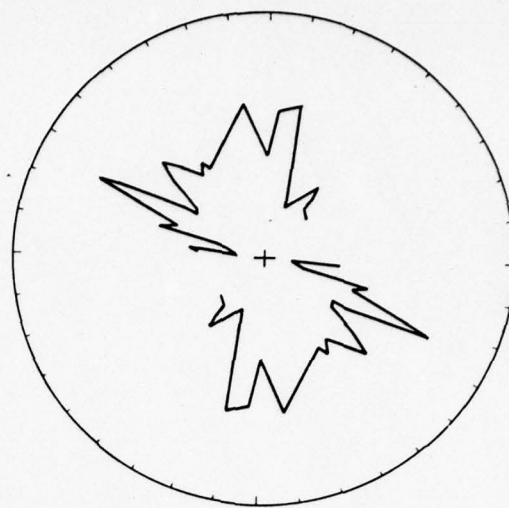
PERIOD = 100 SEC



PERIOD = 35 SEC



PERIOD = 50 SEC



SYMBOL	PERIOD (SEC)
—	35
- - -	50
· · ·	100
· · ·	200

Two points should be noted concerning the accuracy of the digitizations of the recorded events. First, most of the event records we have used are about as large as they could be without going off scale. This has necessitated a change in our data processing techniques which should be noted for the information of others involved in this type of work.

In the past, our standard procedure, when working with smaller-amplitude recordings, has been to digitize from copies of 35 mm microfilm records of the WWSSN seismograms made with a standard microfilm reader-printer (Itek 18.24 Reader-Printer). Tests which compare the phase velocity results obtained from full-size record copies provided by NOAA with the results obtained from our microfilm copies show that distortion in the copying process is of concern when working with large-amplitude recordings such as those employed in the present study. We encourage the use of full-size record copies of large events obtained directly from NOAA.

The second point concerns the fact that the direction of swing of the galvanometer may not be parallel to the axis of the recording drum. Although James and Linde (1971) term this phenomenon "a source of major error in digital analysis of WWSSN seismograms", our tests show the effect to be negligible on phase travel times computed using the single-station method for epicenter-station separations of a few thousand kilometers. In the case of

the poorest galvanometer alignment we encountered, about triple the normal ramp slope of  $0.3^{\circ}$ , we found only negligible differences between the phase velocity curve obtained with the correct digitization base line, and the curve obtained with the normal ramp as a base line.

The paths over which the phase delays have been measured from each of the seismic events are shown in Figs. 14-20 and are summarized in Table II. Sample phase velocity results are given in Figure 21, which illustrates the variation in dispersion for different propagation paths. We have obtained phase velocity data for most paths over a period range extending from about 30 or 38 sec. in most cases, to as long as 357 sec in a few rare cases. The instrumental response at these longest periods is unreliable; if the measured values of phase velocity and its first derivative were in significant disagreement with values from the free mode spectrum, then these long period values were rejected. For our present inversions, we have only used periods up to 250 sec. The specific period ranges, which we have used in the inversions are shown in Table 3.

The phase velocities from five earthquakes and one nuclear explosion for the 32 paths crossing Eurasia (Figure 22) sort themselves into two groups (Figures 23 and 24). The paths with higher phase velocities are generally those that cross the stable platforms and shields (such as paths from the Hsingtai earthquake to Scandinavian (KEV) and German (STU) stations; typical of the lower-velocity group is the phase velocity on the paths from the Red Sea earthquake to the southern Asiatic stations (SHL, MAN, etc.)).

FIG. 14. Epicenter-to-station paths processed for event 4 (Red Sea) occurring at 07:15:54.4 GMT, March 31, 1969.

FIG. 15. Epicenter-to-station paths processed for event 1 (Hsingtai) occurring at 21:29:74.4 GMT, March 7, 1966.

FIG. 16. Epicenter-to-station paths processed for event 3 (Kamchatka) occurring at 14:30:29.1 GMT, December 26, 1964.

FIG. 17. Epicenter- to-station paths processed for event 2 (Lena River) occurring at 13:47:20.6 GMT, August 25, 1964.

FIG. 18. Epicenter-to-station paths processed for event 7 (Yunnan) occurring at 10:44:41.3 GMT, February 13, 1966, and events 8 and 9 (Hindu Kush) occurring at 07:46:16.1 GMT, June 6, 1966 and 12:11:43.7 GMT, December 28, 1974.

FIG. 19. Epicenter-to-station paths processed for events 10 and 11 (Eastern Aleutians) occurring at 01:40:33.2 (dashed lines) and 16:50.29 GMT (solid lines), February 6, 1965.

FIG. 20. Epicenter-to-station paths processed for events 12 and 13 (Western Aleutians) occurring at 09:32:09.3 GMT, February 5, 1965 (dashed line) and at 04:02:53 GMT, February 6, 1965 (solid line).

FIG. 21. Sample phase velocity results for the paths from the Hsingtai earthquake (1966) to STU and from the Lena River earthquake (1964) to HOW. The paths are shown in Figures 15 and 16.

Fig. 14

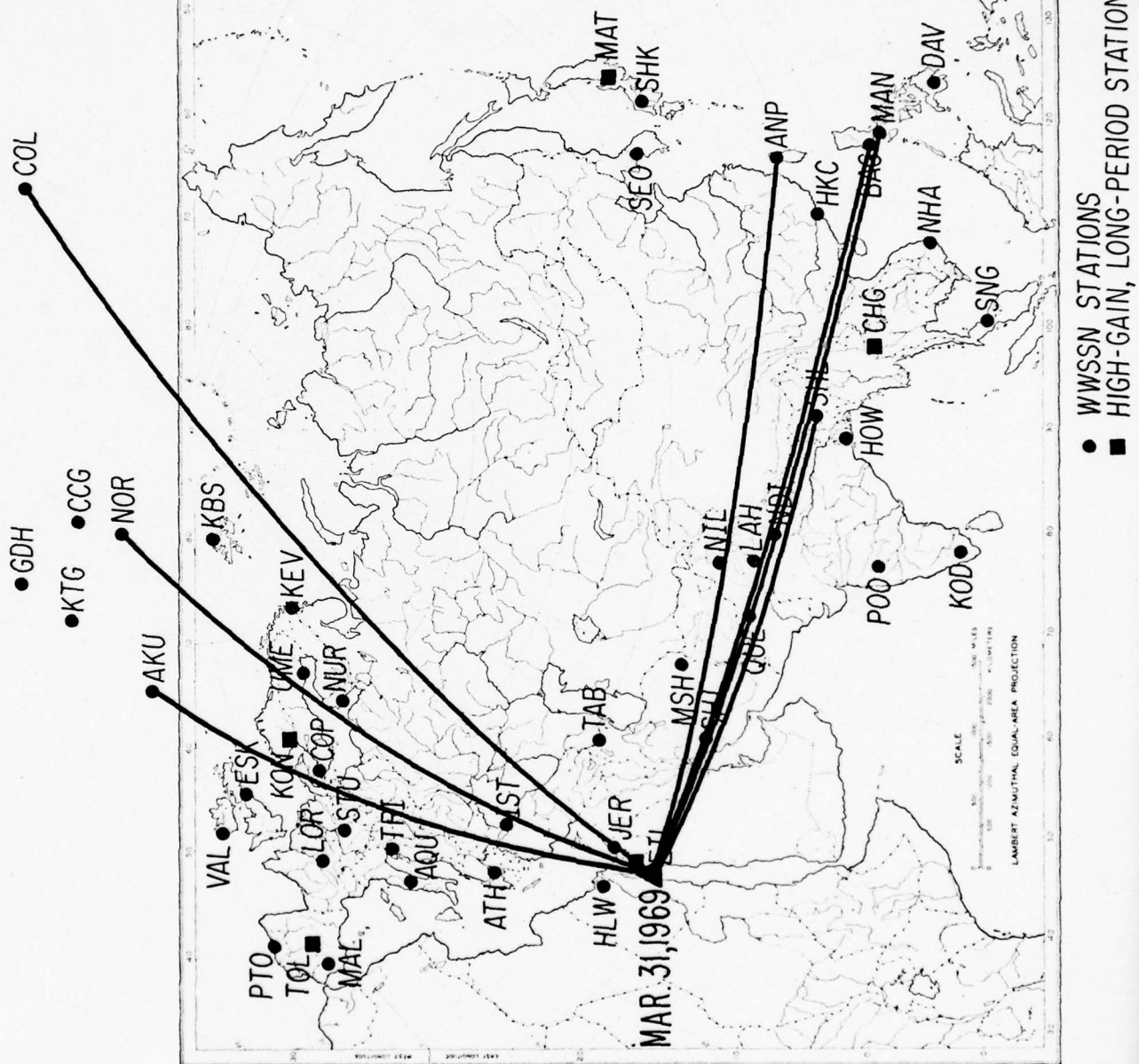


Fig. 15

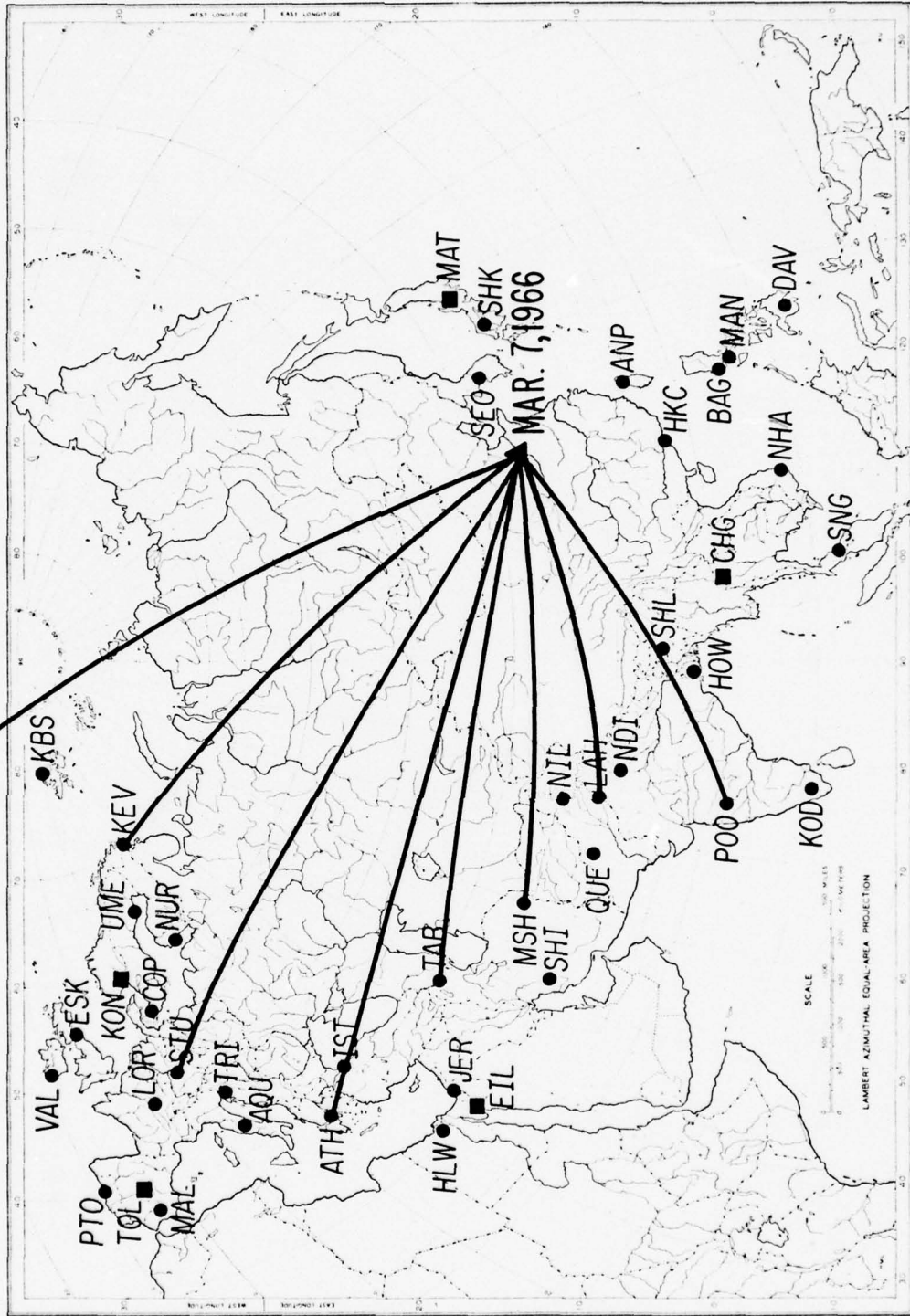
• COL

• GDH

• KTG • CCG

• NOR

• AKU



• WWSSN STATIONS  
 ■ HIGH-GAIN, LONG-PERIOD STATIONS

Fig. 16

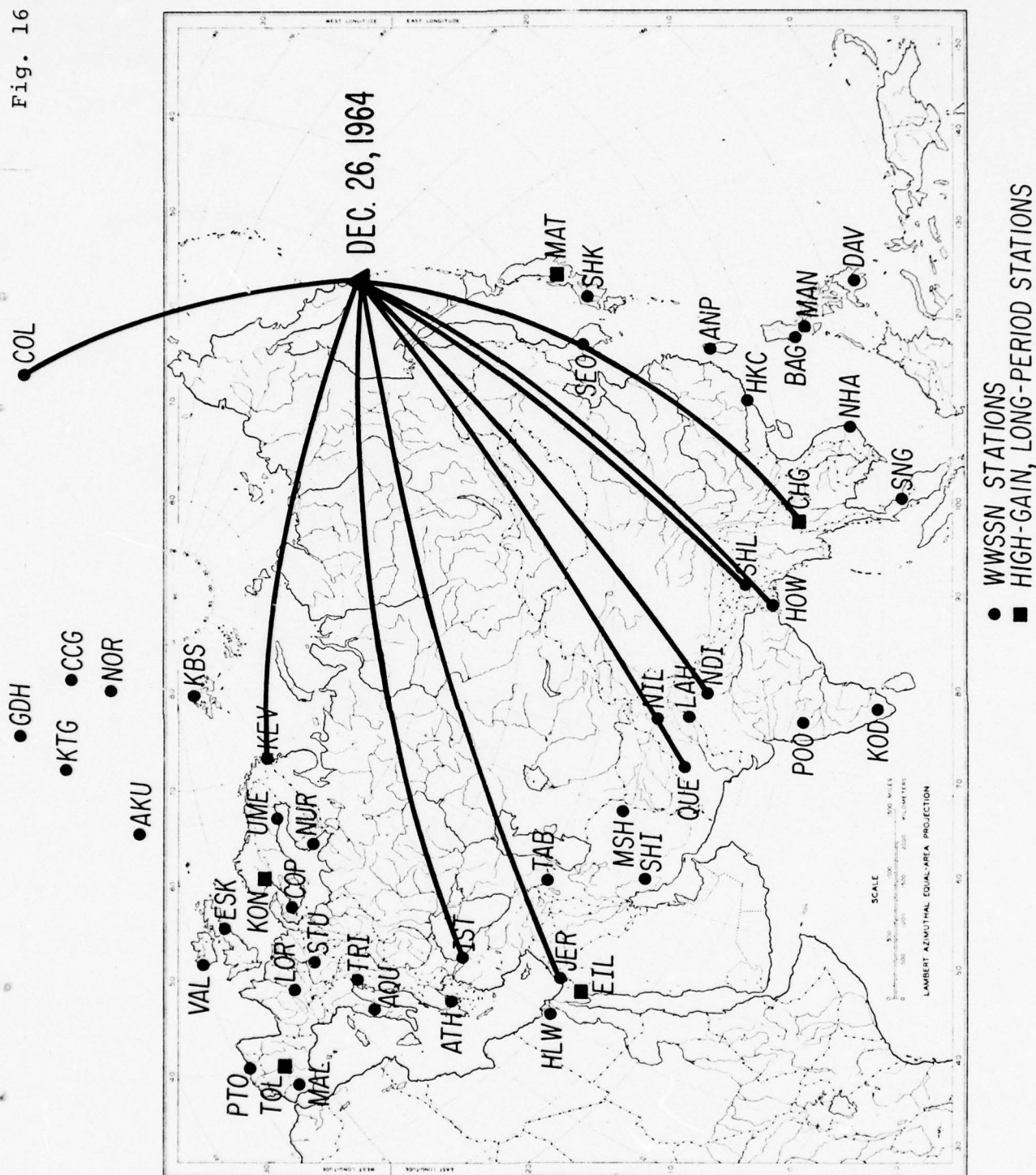


Fig. 17

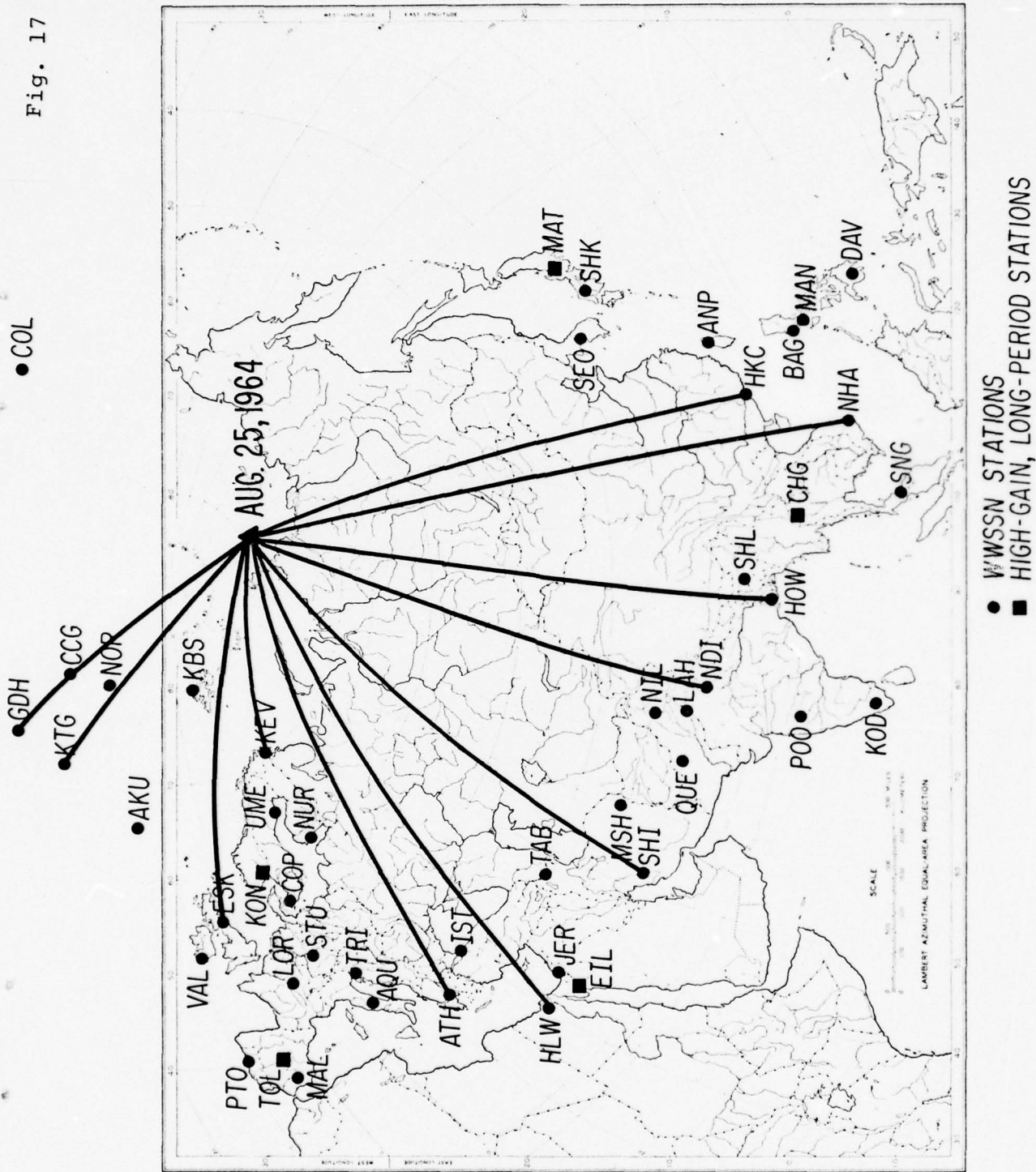


Fig. 18

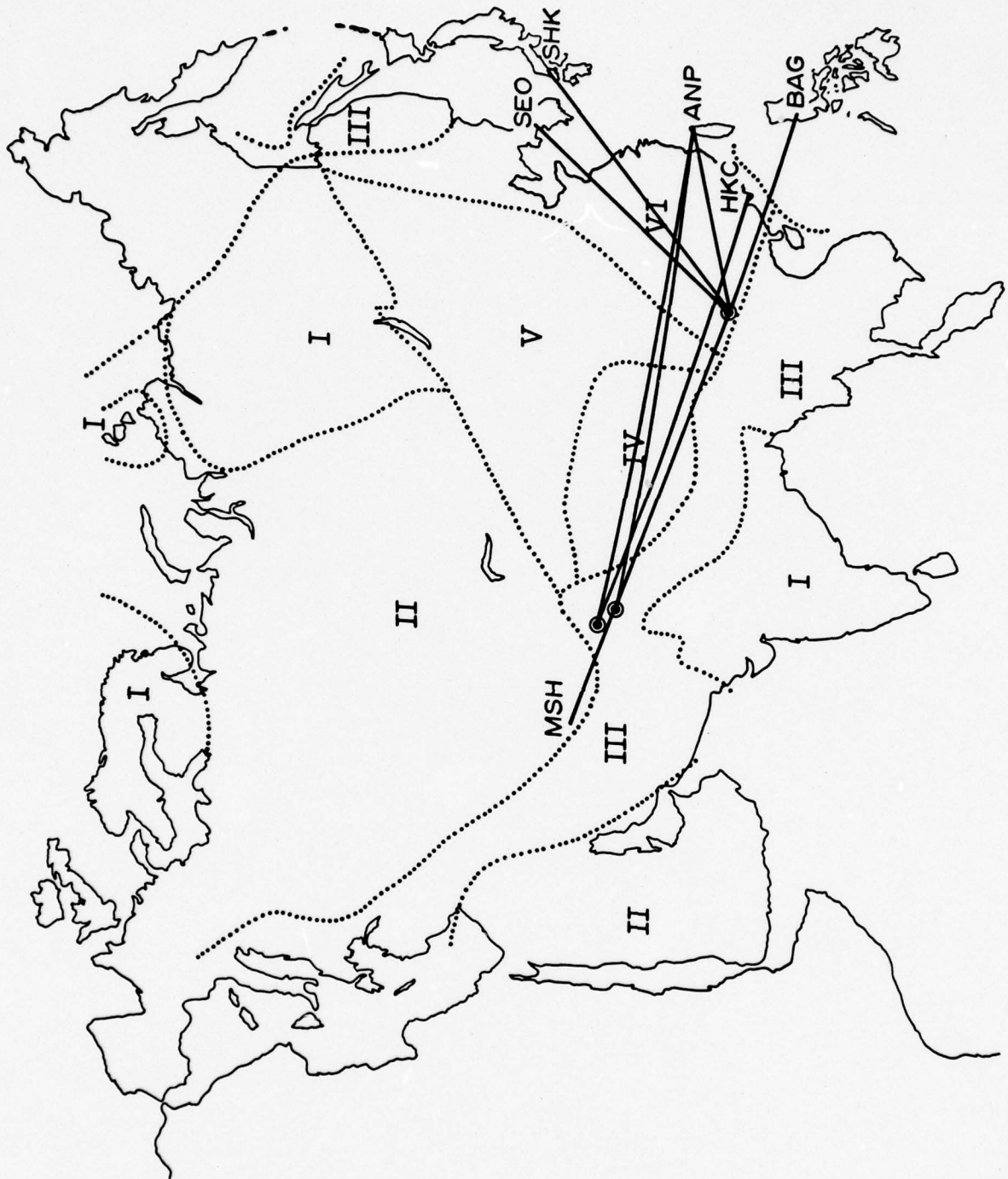


Fig. 19

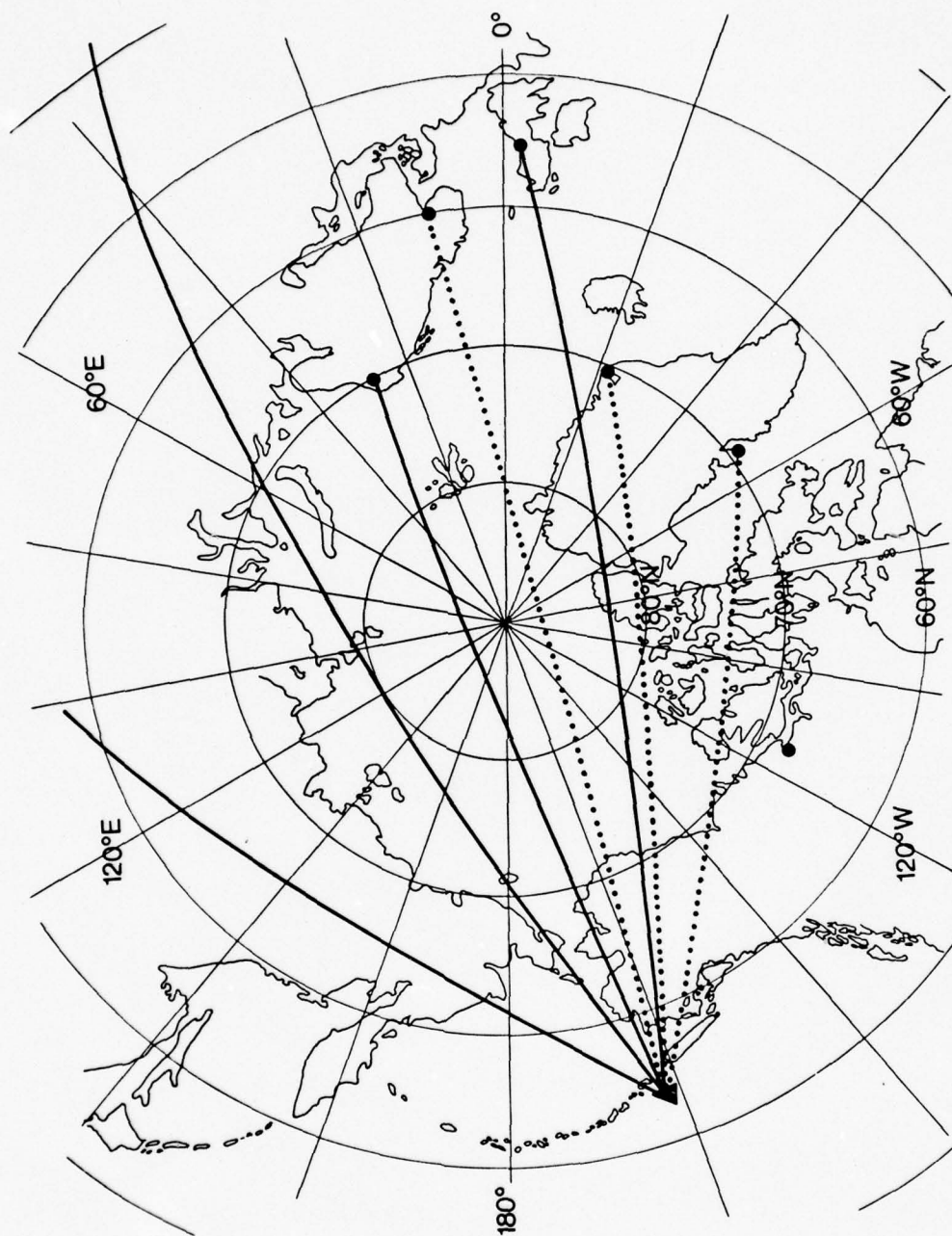


Fig. 20

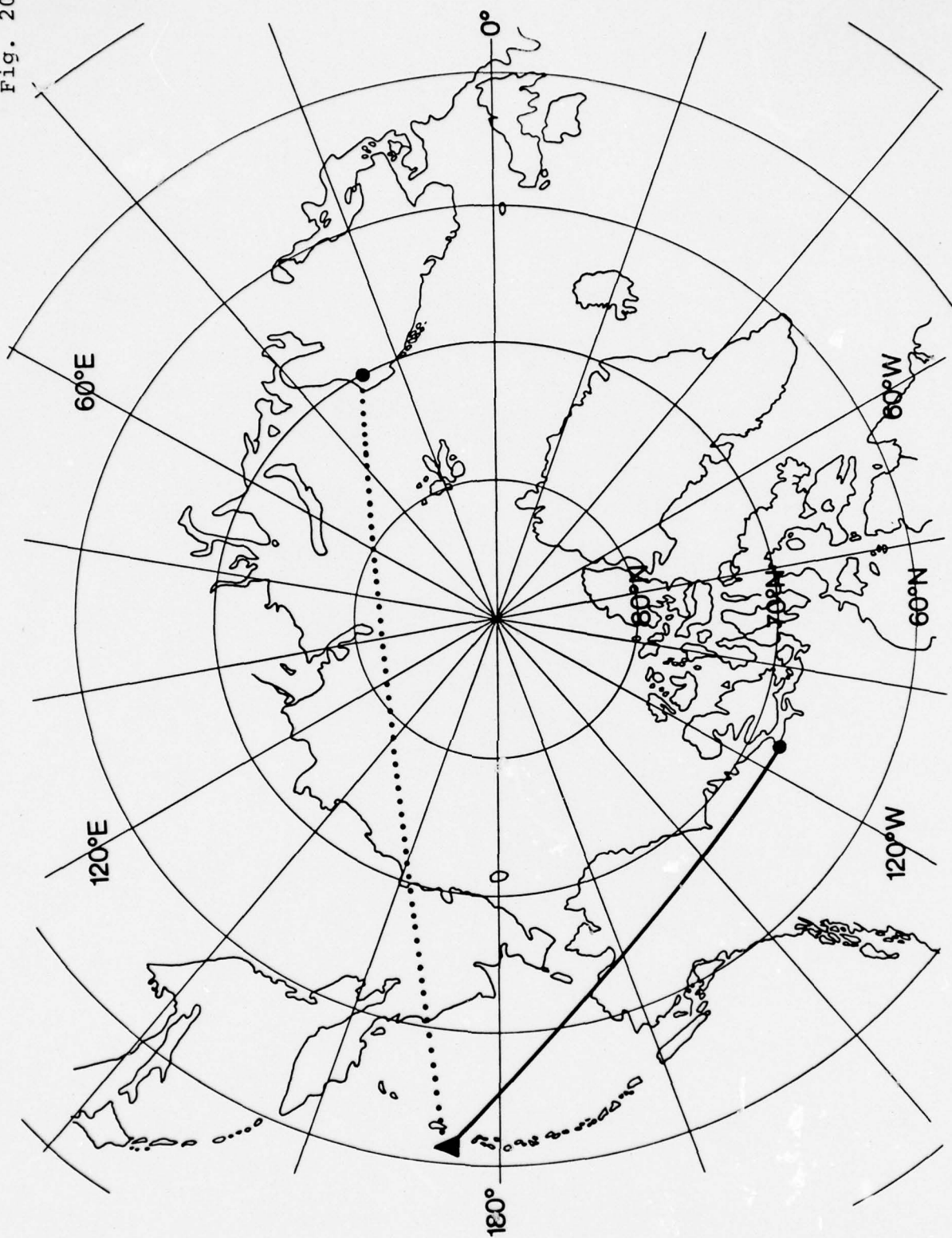


Fig. 21

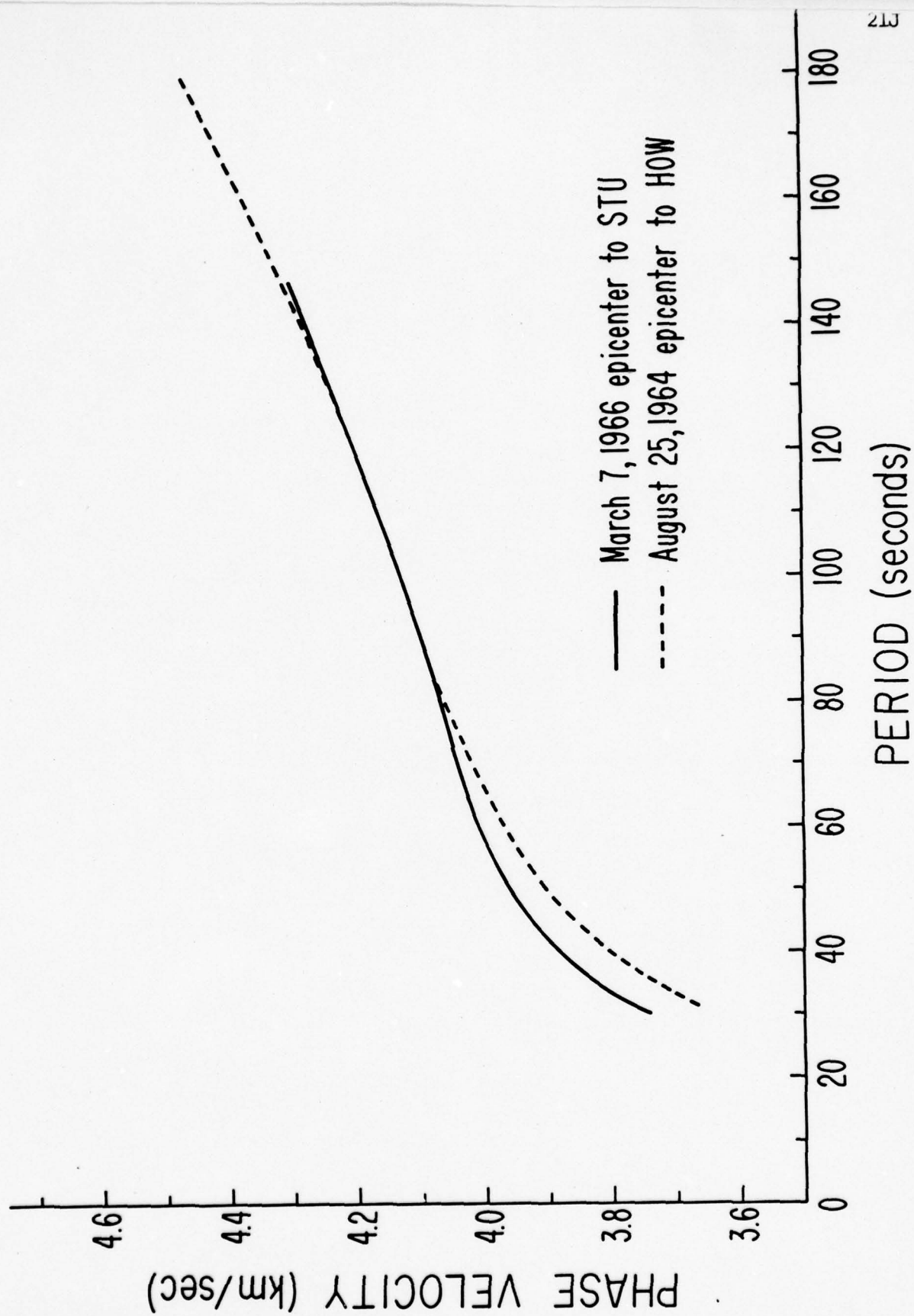


TABLE 3  
PERIOD RANGE (sec)

PATH	30	38	50	69	100	119	139	167	192	208	227	250
RED SEA-ANP		x						x				
-BAG	x											x
-MAN			x			x						
-SHL			x					x				
HSINGTAI-ATU		x						x				
-KEV		x			x							
-LAH	x			x								
-MSH		x		x								
-NDI	x		x									
-POO			x					x				
-STU	x							x				
-TAB	x					x						
KAMCHATKA-CHG			x									x
-HOW	x											x
-IST	x									x		
-JER		x						x				
-NDI	x											x
-QUE	x											x
-SHL	x											x
LENA RIVR-ATU		x			x							
-HKC		x				x						
-HLW		x						x				
-HOW		x										x
-KEV		x									x	
-NDI	x											x
-NHA		x										x
-SHI	x											x
TASHKENT -NDI	x	x										
-SHL	x		x									
LOP NOR -KBL	x			x								
-NDI	x			x								
-SHL	x			x								

TABLE 3

PERIOD RANGE (sec)

[illegible]

FIG. 22. Propagation paths across the Eurasian continent from five earthquakes and one nuclear explosion

FIG. 23. All Eurasian phase velocities can be sorted into two groups (shaded areas), except for phase velocities POO-2 and SHL-1, which fall between these two groups. Phase velocities for "standard" shield (FLO-GOL), younger stable regions (SHA-LUB) and rift zones (TUC-BOZ) are shown for comparison (Biswas and Knopoff, 1974). The global average phase velocities obtained from free-mode observations are also shown (F.M.) (Gilbert and Dziewonski, 1975).

FIG. 24. Propagation paths corresponding to the two phase velocity groups in Fig. 21. The solid line indicates a path with higher phase velocity; the dashed line indicates a path with lower phase velocity.

Fig. 22

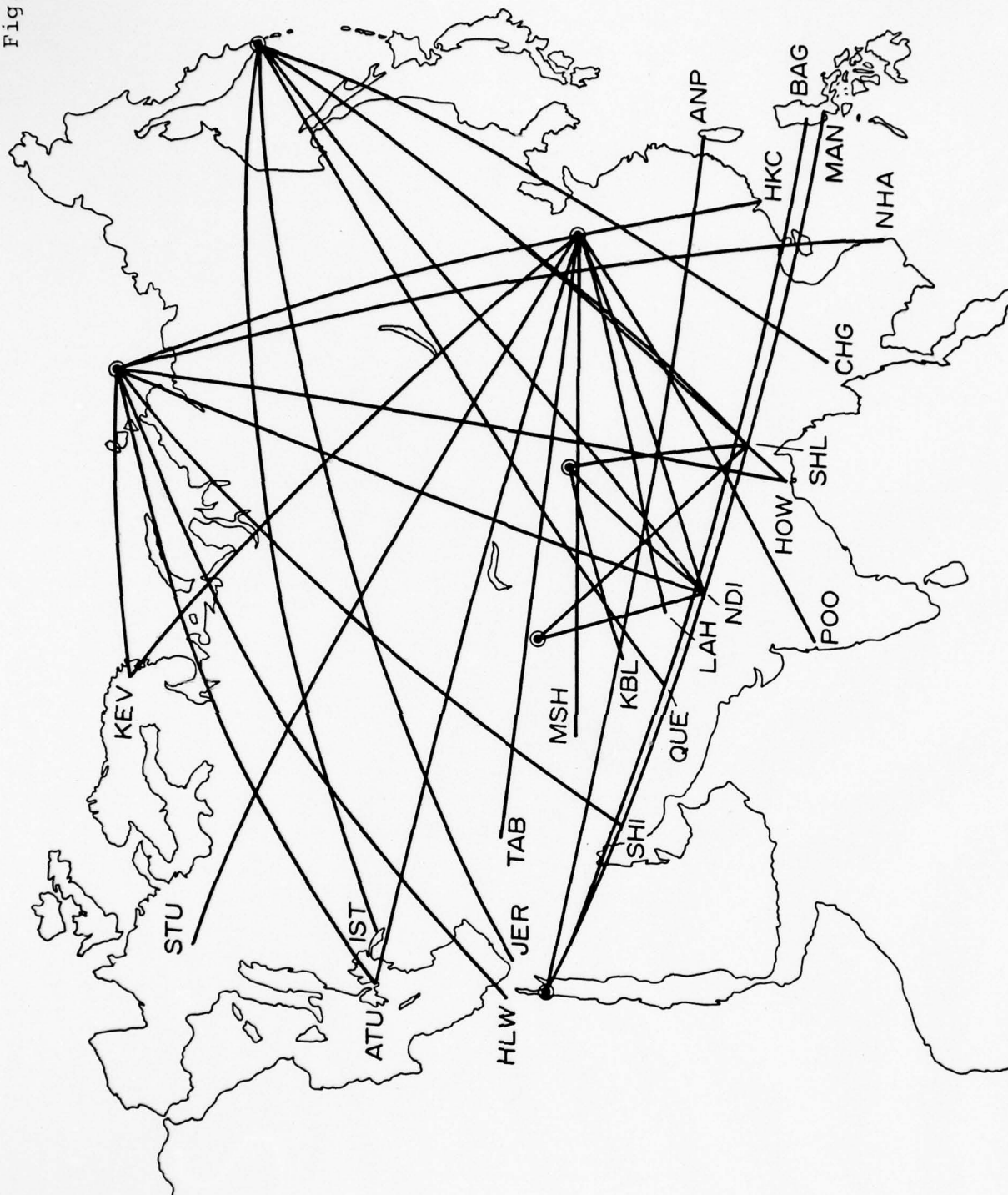


Fig. 23

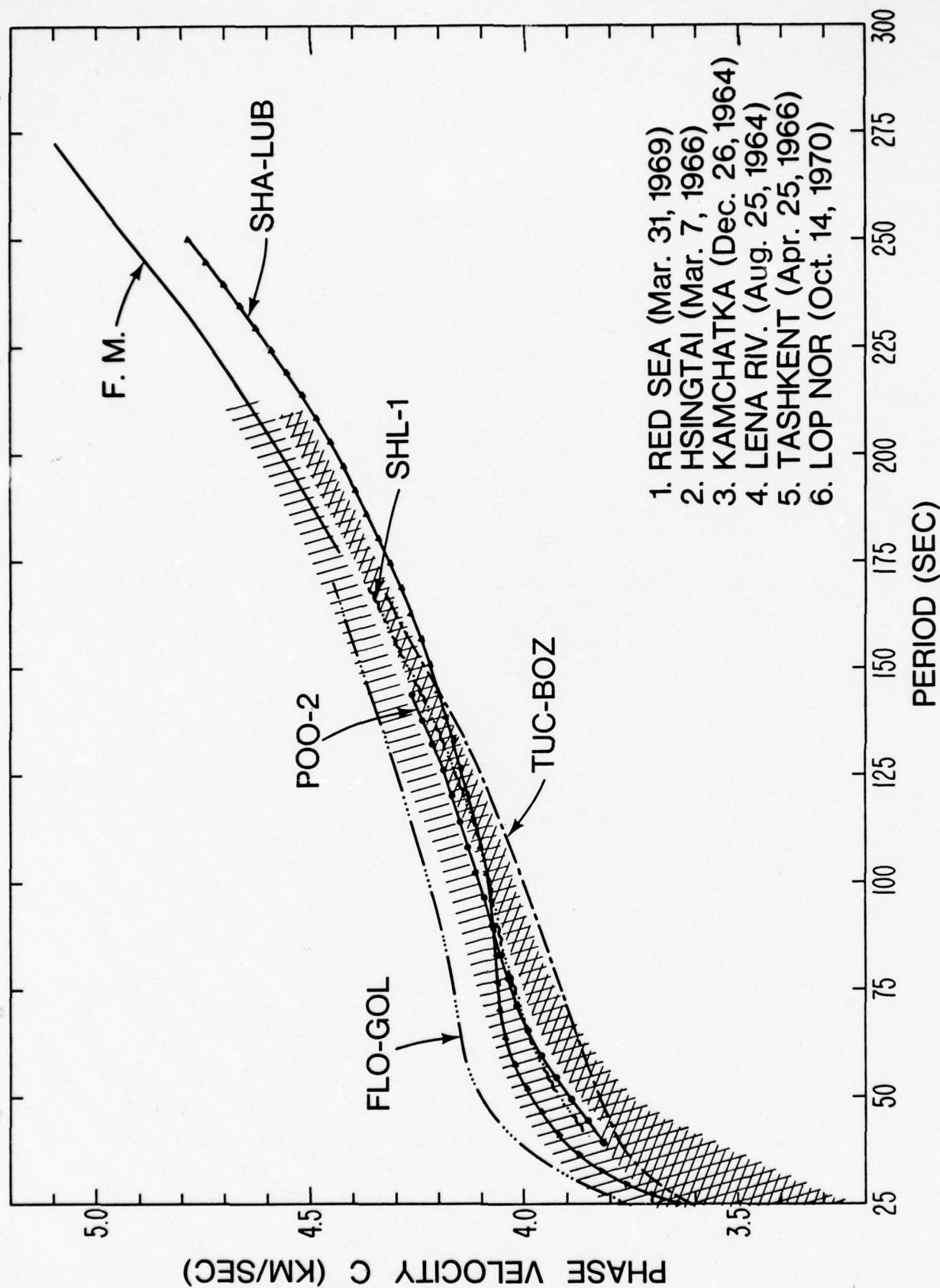
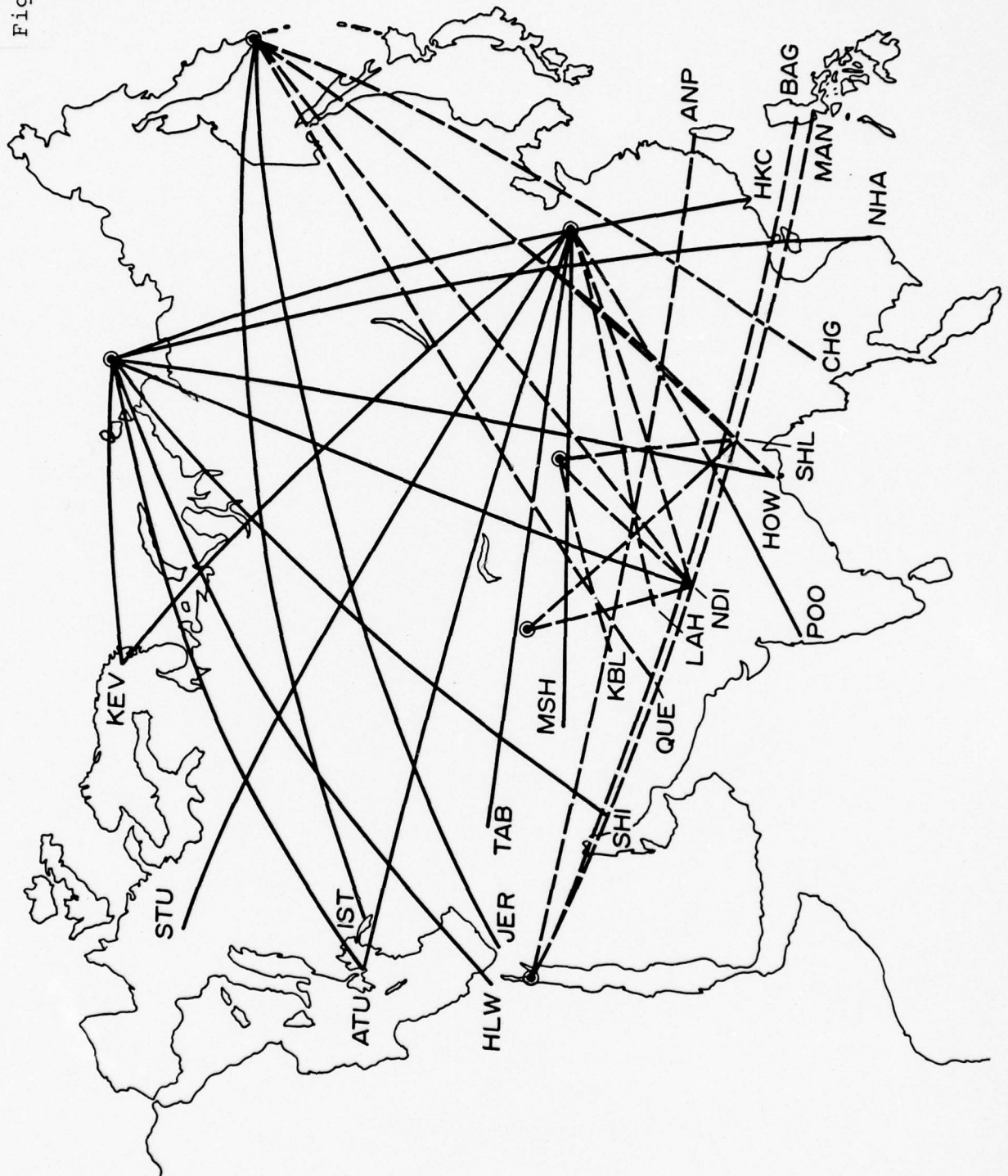


Fig. 24



Phase velocities for typical shield regions and young stable continental regions (Biswas and Knopoff, 1974) are shown for comparison. The incompatibility of most of the phase velocity observations for Eurasian paths with the "standard" curves for homogeneous regions testifies to the inhomogeneous nature of the Eurasian region.

### Regionalization

The first step in the structural analysis requires the division of the area into subregions; each of these is assumed to be laterally homogeneous. In our first attempt we have subdivided the Eurasian area into six broad regions (Fig. 25). These are:

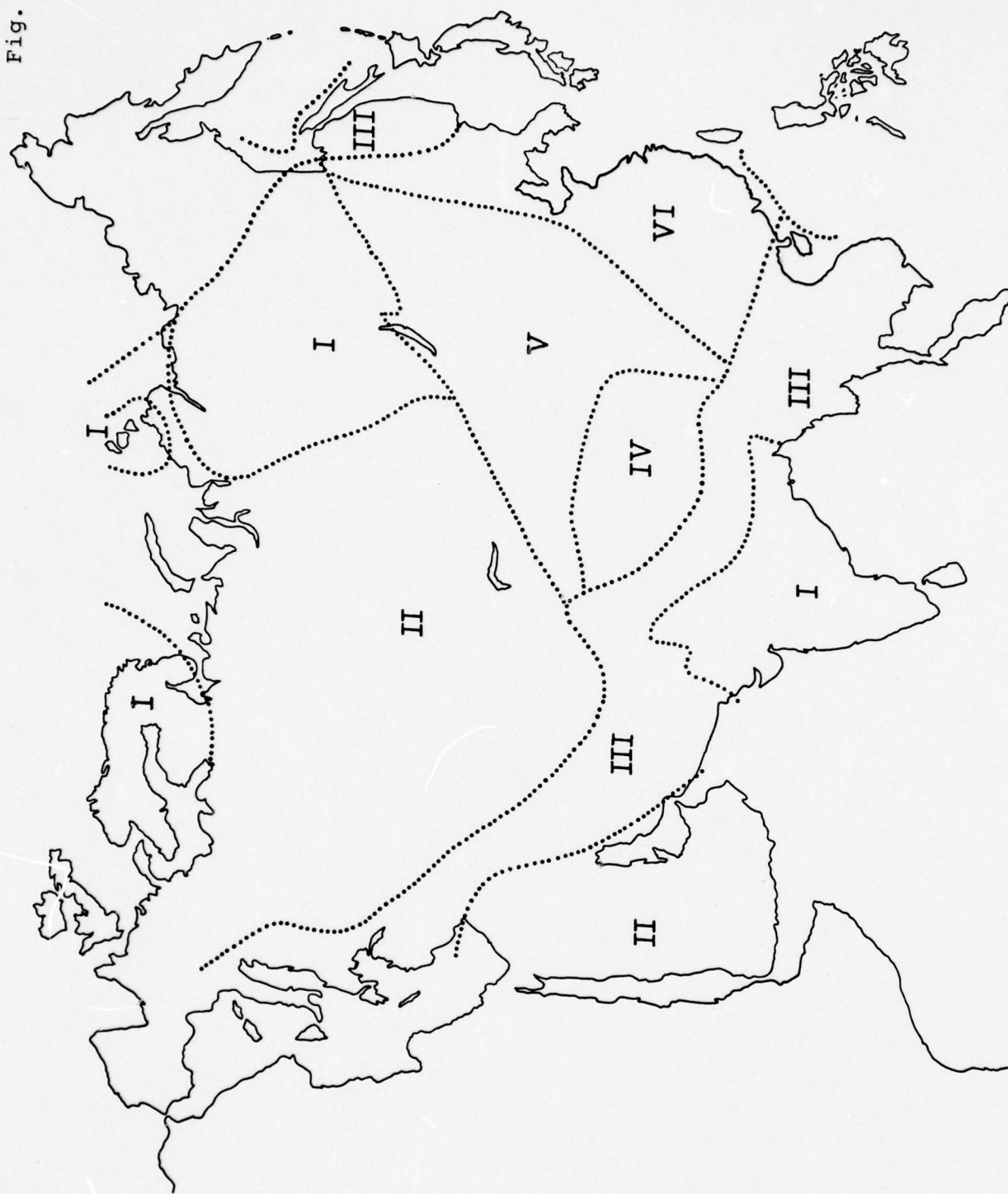
1. Ancient PreCambrian Shields
2. Stable Platforms
3. The Himalayan-Alpide Mountain Belt
4. The Tibetan Plateau
5. The Sinkiang-Mongolian Seismic Zone
6. The Chinese "Stable" Region

This choice of regionalization is largely governed by an attempt to define a small number of discrete geographically homogeneous provinces. In this choice we have been guided by tectonic maps of Eurasia (Khain and Muratov, 1969) as well as by seismicity and sparse heat flow information (Lubimova and Polyak, 1969). Our first impulse was to regionalize the stable parts of Eurasia according to the bimodal division of these regions into stable ancient shields and stable younger continents (Knopoff, 1972). However, information about basement ages

FIG. 25. Regionalization of the Eurasian continent  
based on the tectonic map of Khain and Muratov  
(1969).

Fig. 25

22B



of the Eurasian sediment-covered platforms is difficult to obtain, so we have taken the simple expedient of dividing the stable parts of the continent into the geologically identifiable shields and a second region which includes the rest of the seismically stable land mass; these form our regions 1 and 2. In selecting region 2 as a homogeneous region we impose no a priori condition that it be either of the north-central U.S. or the Gulf Coast (U.S.) types of sediment-covered stable regions: the first of these regions in the U.S. has been found to have an upper mantle with shield characteristics while the second has an upper mantle with a strong low velocity channel, and is the prototype younger stable region.

The next three regions are characterized by their high tectonic activity. We have chosen to identify the mountainous collision zone between the Asian and Indian plates as a single province; this is undoubtedly incorrect in detail, but is valid enough in view of our inability to provide detailed resolution of smaller regions by our use of long paths.

It should be noted that an increase in the density of path samples does not necessarily improve the resolution of structure of a small geographic area. Consider the limiting case of a region which is vanishingly small in area. An increase in the number of paths which transect this region does not improve our ability to estimate the cross-section under it, because the travel-time spent by the ray in this region is a vanishingly small part of the total delay. An increase in the number of paths

in a small area only increases the redundancy of the data. For this reason we had some hesitation regarding the possibility of determining the structure under a region as "small" as the Tibetan plateau. The Tibetan plateau is indeed small in comparison with the dimensions of the Eurasian continent, and herein lies one of the difficulties with the method of very long single-station transverses across the entire span of the continent. But the Tibetan plateau contains one of the important mysteries of modern Plate Tectonics, namely the reason for its great elevation and the nature of the architectural underpinning that holds it up, so we resolved to try to determine its structure, fully anticipating that the error bias in the determinations of structural parameters might be large; it became our region 4. To improve resolution here, we made use of shorter paths from two Hindu Kush and one Tashkent earthquakes plus a Lop Nor explosion all recorded at nearby stations to increase the fraction of the travel-times spent in the Tibetan region. It can be seen from the table of period ranges of the observations (Table 3) that the inability to obtain long-period information from the observations of the Tashkent earthquake and the Lop Nor nuclear explosion also limits our ability to resolve deeper structure under region 4. The complete sampling of all regions by the path-phase delays from the set of earthquakes and explosions is shown in Fig. 26.

The Sinkiang-Mongolia seismic zone is easily identified as one of the provinces in our regionalization. We have chosen to identify the relatively stable aseismic block of Southeast China as an additional province. The Hsingtai earthquakes of 1968 occurred on the boundary between these two regions. We have

identified Southeast China as a separate region without any a priori assumption that it has either a cross-section similar to those for the ancient shields or the younger stable continents. We prefer to allow the inversion to yield this determination. Should the inversion indicate that this region, or region 2 for that matter, is similar in cross-section to that for some other region, we may make the assumption that these regions are the same and use this information to perform a further simplified inversion. Although, within themselves, these regions encompass widely differing geologic structures and widely varying seismic activity, we have assumed that each of these regions is homogeneous in order to limit the number of parameters in the inversion.

Three small regions are treated specially. For the South China Sea, we have assumed the structure to be known, and to be that for typical marginal seas. The phase delays for this region are taken from two single-station phase velocity observations in marginal seas obtained by Leeds (1973) and from two phase velocity determinations by the two-station method across the Philippine Sea. Phase velocity corrections for the Sea of Okhotsk were obtained theoretically from a crustal structure given by Kosminskaya et al (1969) and derived from explosion work, in which the Okhotsk depression has a 25 km crustal thickness; we have used an oceanic mantle below this crust; These phase corrections have been applied to travel times for those paths that traverse these two regions.

Finally, a small fraction of the paths cross the Yakutsk-Magadan region of northeastern Siberia. The maps show this mountainous region to be tectonically different in a significant way from the shield immediately to the west of it. Since our samples of this region are all from the Kamchatka earthquake, and are all small in length, we have decided, without justification, to couple this region to our other mountainous province, region 3. We do not expect significant differences from a region 3 structure for this part of Eastern Eurasia to produce major changes in the inversions since the total fraction of path length in this region is small.

The total path length in each region summed over all event-paths is given in Table 4. Since the phase shifts have not been obtained over a uniform band of periods for all paths, in the last column of Table 4 we have also reported an estimate of the number of samples in each region by giving the product of sample path length by number of period estimates of phase shift. By either method of estimation, the very low fraction of sampling in regions 4 and 6 lead us to expect that large uncertainties in the structure will be obtained from the inversion for these regions.

We have inverted the data under the assumption that a simple ray theory for surface waves applies, that is, the phase shift for a surface wave passing through a given region is computed as though

TABLE 4

<u>Region</u>	<u>Path Length (km)</u>	<u>Percentage of Total Path Length</u>	<u>Weighted Percentage of Total Path Length</u>
1	20970	12.1	13.0
2	53150	30.6	30.4
3	38411	22.1	22.5
4	15292	8.8	6.9
5	37994	20.7	20.7
6	<u>9979</u>	<u>5.7</u>	<u>6.5</u>
TOTAL	173796	100.00	100.0

the region were laterally infinite in extent and uninfluenced by the presence of neighboring regions, no matter how close the great circle path approaches the regional boundaries. The assumption that diffraction effects are unimportant is evidently untenable but provides a basis for starting an inversion; we have tested this assumption in one of the inversions below.

The inversion proceeds using the method described by Leeds et al. (1974). We calculate the phase travel time for the  $n^{\text{th}}$  path and the  $p^{\text{th}}$  period as

$$t_{np} = \sum_{i=1}^6 \ell_{in} s_{ip}$$

where  $\ell_{in}$  is the path length of the  $n^{\text{th}}$  path in the  $i^{\text{th}}$  region ( $i=1, \dots, 6$ ) and  $s_{ip}$  is the (theoretical) phase slowness for the  $i^{\text{th}}$  region at the  $p^{\text{th}}$  period. The phase slownesses  $s_{ip}$  are functions of the model parameters in each region.

$$\sum_n \sum_p (t_{np_0} - t_{np})^2$$

where  $t_{np_0}$  is the observed travel-time for the  $n^{\text{th}}$  path at the  $p^{\text{th}}$  period. The minimization takes place with respect to the choice of model parameters.

We obtain larger and larger variances in the model parameters as the number of model parameters increases. We would like to be able to solve for the properties of the crust in each of the six regions. However, this a) requires much precise data at periods shorter than 30 sec., b) increases the number of model parameters significantly, and c) pushes our postulate of lateral homogeneity in each of the regions to an untenable extreme. We have therefore used model crusts for each of the regions which a) seem to be plausible when compared with results for similar parts of the earth where observations exist (such as locations typical of regions 1, 2 and 3), and b) agree with Soviet refraction results where available (Kosminskaya, et al, 1969; Sollogub, 1969). When large residuals were encountered at short periods, such as in the case of region 3 (Alpide-Himalayan belt) and region 4 (Tibetan plateau), we were obliged to introduce more low-velocity material into the crust. This was done by keeping crustal velocities fixed and increasing crustal thickness. In these two cases, this procedure leads to extraordinarily thick crusts. It should be realized that these model crustal thicknesses are consequences of the procedures used; if we had chosen to lower the crustal velocities, the thicknesses would have been less. We have used a crustal thickness of 70 km in the Tibetan Plateau (region 4) a value not inconsistent with other recent estimates (Chun and Yoshii, 1977). The crustal models we have used are listed in Table 5 and are assumed to be fixed in the inversions.

## Model parameters for inversion of phase velocity data

	Thickness	Depth	$\beta$ (km/sec)	$\alpha$ (km/sec)	$\rho$ (gm/cm <sup>3</sup> )
		0			
CRUST	(different crustal models for each region)				
		(fixed)			
LID	VAR		4.65	8.17	3.45
CHANNEL			VAR	7.80	3.45
SUBCHANNEL	VAR		4.80	8.80	3.65
		420(fixed)			
	94		5.128	9.609	3.806
		514			
	94		5.283	9.781	3.934
		608			
	63		5.419	9.902	4.051
		691			
	138		6.172	10.552	4.417
		809			
	139		6.266	11.238	4.505
		948			
	104		6.351	11.392	4.579
		1052			

TABLE 5 (cont'd)

## Crustal Models Used in Inversion

(thickness in km, velocities in km/sec, density in gm/cm<sup>3</sup>)

Region 1				Region 2				Region 3			
h	$\beta$	$\alpha$	$\rho$	h	$\beta$	$\alpha$	$\rho$	h	$\beta$	$\alpha$	$\rho$
2	2.63	4.56	2.41	2	2.63	4.56	2.41	2	2.55	4.41	2.41
7	3.57	6.18	2.75	7	3.57	6.18	2.75	35	3.50	6.06	2.75
13	3.75	6.50	2.85	13	3.75	6.50	2.85	26	3.67	6.35	2.85
26	3.93	6.81	3.08	26	3.93	6.81	3.08				

crustal thickness = 48

crustal thickness = 48

crustal thickness = 63

Region 4				Region 5				Region 6			
h	$\beta$	$\alpha$	$\rho$	h	$\beta$	$\alpha$	$\rho$	h	$\beta$	$\alpha$	$\rho$
6	2.51	4.35	2.41	2	2.56	4.41	2.41	3	2.63	4.56	2.50
26	3.41	5.91	2.70	20	3.64	6.28	2.85	19	3.35	5.80	2.75
24	3.63	6.29	2.85	27	3.81	6.58	3.08	17	3.75	6.50	2.95
14	3.81	6.60	3.08								

crustal thickness = 70

crustal thickness = 49

crustal thickness = 39

We have parameterized the mantle into a lid, channel and subchannel; each of these layers in a given region is taken to be homogeneous. The subchannel region terminates at a depth of 420 km. Below this depth, we place a standard lower mantle platform under all regions, indicated in Table 5. The unknowns in the inversions will be the shear velocities in each of the three upper mantle layers and the depths of the interfaces at top and bottom of the second ("channel") layer. The number of unknowns is thus 30, five in each of the six regions. This figure far exceeds the number of degrees of freedom in the data. Thus some reduction in the number of unknowns has to be made, by some assumptions which are geophysical in character.

#### Inversion 1

In a first attempt at inversion, we have fixed the lid S-wave velocity at 4.65 km/sec and the subchannel S-wave velocity at 4.8 km/sec in order to reduce the number of degrees of freedom. The value of 4.65 km/sec for the lid arises frequently in inversions for other parts of the world. For one case in which a 4.65 km/sec lid was not observed, namely for the Western United States (Biswas and Knopoff, 1974) in which the subcrustal material has S-wave velocity around 4.3 km/sec, we were able to assume that a model with a 4.65 km/sec lid with zero lid thickness was accepted by the inversion and that the 4.3 km/sec value represents channel material rising almost to the base of the crust. Should the lid velocity in some region be less than 4.65 km/sec in reality, then crustal thicknesses can be reduced. A similar comment can be made about the


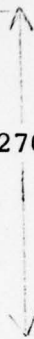
subchannel velocity: if the subchannel velocity should turn out to be less than 4.8 km/sec in some regions, channel thicknesses will be reduced.

This parameterization thus includes only two adjustable model parameters for each region. These are the lid thickness and the channel S-wave velocity. A thirteenth parameter is the subchannel thickness, which is presumed to be uniform across the entire continent and hence has the same value under each region. Since the crustal thickness and the depth to the 420 km interface are fixed, the parameterization of lid and subchannel thicknesses is equivalent to a parameterization of the depth below the surface of the top and bottom of the channel. This parameterization has 13 degrees of freedom.

After adjustment of the crust by the procedures described above (with interpretation of crustal parameters according to the remarks above), the parameterization and cross sections used in a linearized inversion procedure are given in Table 5. The superficial sedimentary layer that is introduced in the crusts of regions 3 and 4 is designed to reduce the residuals at the shortest periods.

The starting values of the thirteen parameters in this linearized inverse are (in the usual units):

Table 6

Region	$\beta_{CH}$	$h_{LID}$	$h_{SUB}$	Depth to top of channel	Depth to bottom of channel
1	4.51	110		155	
2	4.39	113		158	
3	4.30	54		119	
4	4.29	90		167	
5	4.08	92		137	
6	4.38	103		148	

The thirteen parameters in the rectangular box in Table 6 are those varied in the inversion. The standard errors of the travel-times in the inversion were taken to be the same as those used by Leeds et al. (1974), namely  $\sigma = \text{Max} (7, 0.1T)$  sec. These estimates were later found to be too large and required modification

In the inversion, an iteration process has been used in which the matrix of partial derivatives  $G$  was recalculated whenever we moved into a new portion of parameter space. This process was continued until we obtained convergence of the variable model parameters. The thirteen eigenvalues of the product matrix of partial derivatives  $G^T G$ , which were obtained in the final stage of the iteration process, are given in Table 7. Each eigenvalue corresponds to an eigenvector which, in every case (except nos. 5 and 6), points in a direction close to one of the thirteen parametric axes. Thus, each eigenvector can be said to be a discriminant for each of the thirteen degrees of

TABLE 7

Eigenvalue		Model parameter most closely resolved by eigenvector
1.	13.68	$\beta_{CH2}$
2.	8.43	$\beta_{CH5}$
3.	6.85	$\beta_{CH3}$
4.	3.56	$\beta_{CH1}$
5.	2.87	$\beta_{CH6}$ & $h_{SUB}$
6.	2.59	$\beta_{CH6}$ & $h_{SUB}$
7.	1.84	$\beta_{CH4}$
8.	1.61	$h_{LID5}$
9.	1.14	$h_{LID2}$
10.	1.04	$h_{LID3}$
11.	0.56	$h_{LID6}$
12.	0.36	$h_{LID1}$
13.	0.21	$h_{LID4}$

freedom in the model. The eigenvectors corresponding to the largest eigenvalues give reliable structural information concerning the model parameters closest to them, and the eigenvectors corresponding to the smallest eigenvalues give little information about their corresponding parameters.

From Table 7 it can be seen that, in general, the data yield the greatest information about the channel velocities and the least information about the lid thicknesses. In general, the data contain more information about regions 2, 3, and 5 than the the other three regions. This is clearly correlated with the higher percentages of total path length which sample regions 2, 3, and 5. (For complete details, see Table 4 and Fig. 26).

The variance of each model parameter decreases as successive models approach the fine one, which demonstrates the convergence of our inversion procedure. Fig. 27 gives our results for this inversion: the "best" model and the corresponding standard deviations of each model parameter. We see that the upper mantle structure for regions 1 and 2 are very similar although the lid in region 1 is somewhat thicker. The channel shear-wave velocity for region 1 is slightly less than that in region 2, but the uncertainty of the model parameter in region 1 is rather large and in any case, the velocity contrast to the lid in these regions is rather smaller than one would like to assert that a) a channel is indeed present and b) that a channel with velocities low enough to require partial melting is present. Thus, the existence of a low-velocity channel in region 1 is uncertain. The most striking result of this inversion is the very thin lid, and moderate shear wave velocity, in the channel for regions 3 and 5; as in the case of regions 1 and 2, regions 3 and 5 have strikingly similar upper mantles. These latter two regions are those which are tectonically active and have high seismicity. Region 4 is that in which the Eurasian and Indian continents are in collision. Although the upper mantle structure for this

region appears to be very similar to those of regions 1 and 2, the uncertainties in the model parameters are large. This is due 1) to the low percentage of total path length in this region, and 2) to the fact that most of the paths which sample this region have only short-period information. Region 6 has a thick lid and a pronounced low-velocity channel, but the standard deviations are rather large; additional assumptions may help to improve the resolution of the structural parameters in this region.

### Inversion 2

In a second attempt at inversion we have made the assumption that the chemical composition of the lids is everywhere the same across Eurasia (as before) and that, in this case, the chemical composition of the channels is similarly the same across Eurasia. We have allowed the lid velocity to be adjusted in this case; it was fixed in the preceding case. In this case the number of parameters in the fit is nine: the depth to the lid-channel interface in each of the six regions, the depth to the channel - subchannel interface, and the S-wave velocities in the lid and channel; the latter three parameters are constants across the entire region. The errors  $\sigma$  are assumed to be the same as before.

The results of this inversion are shown schematically in Fig. 28. The result for lid velocity was  $4.56 \pm .01$  km/sec and for channel velocity  $4.34 \pm .02$  km/sec. The results for lid thicknesses show striking similarity among regions 1, 2, 4 on the one hand and 3, 5, and 6 on the other.

FIG. 26. Propagation path in each subregion of the Eurasian continent. The percentage of total path length in each region is shown in Table 2.

FIG. 27. Final result for linearized inversion of 13 variable parameters in the model and their corresponding standard deviations.

FIG. 28. Schematic upper mantle cross-sections obtained in inversion 2.



$\beta$  (KM/SEC)

Fig. 27

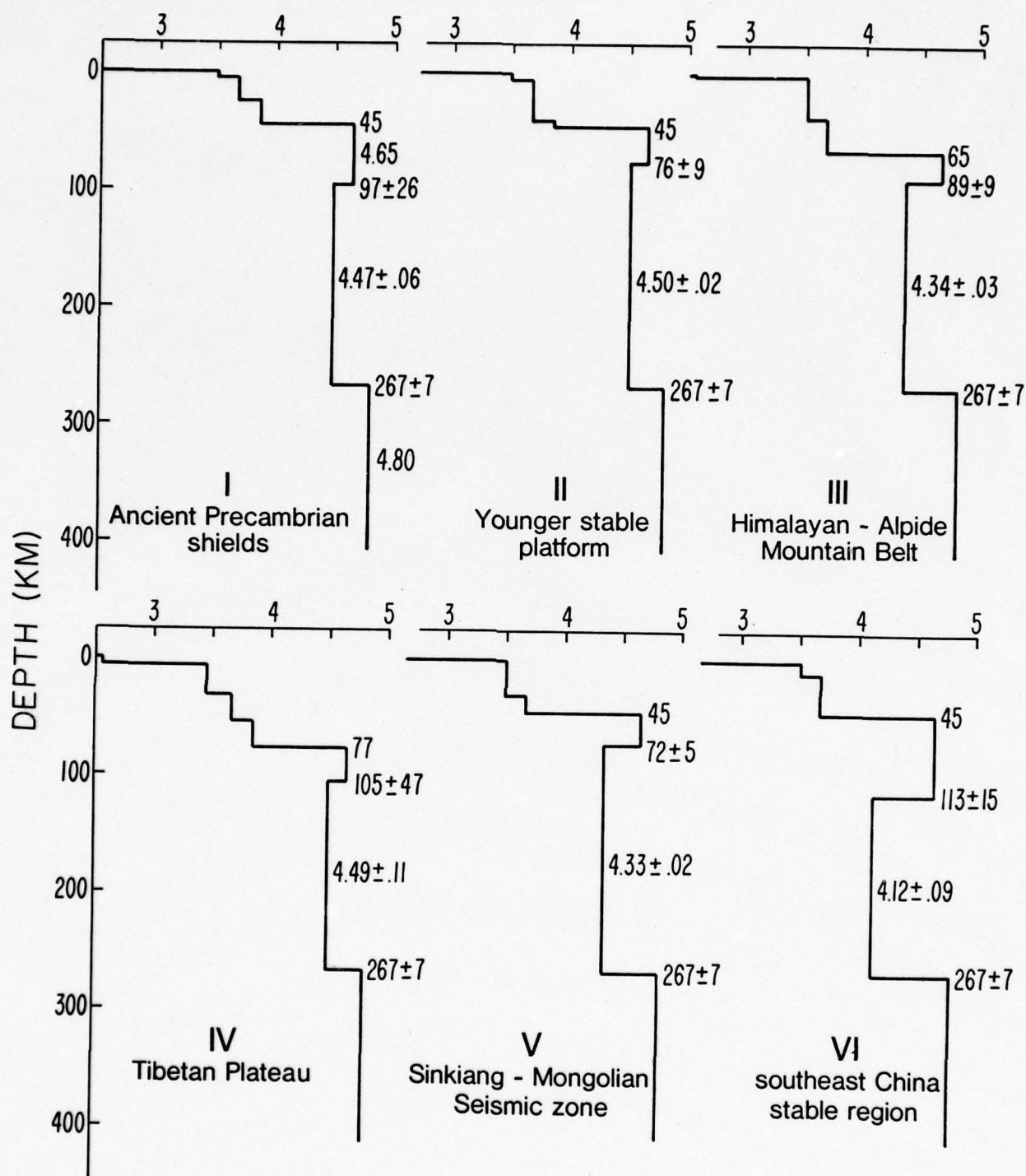
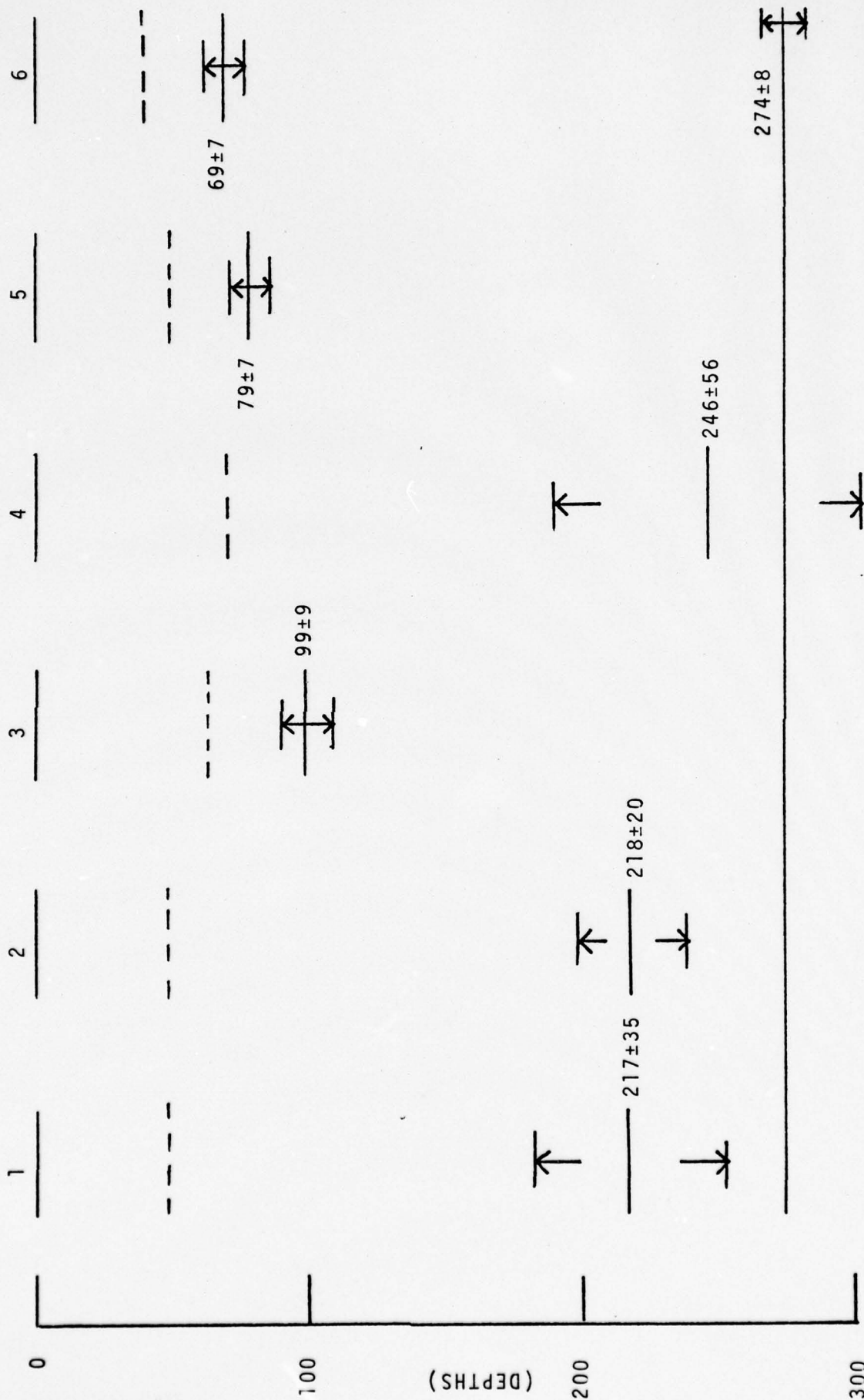


Fig. 28

REGIONS



Lid S-wave velocity =  $4.56 \pm 0.01$  km/sec  
 Channel S-wave velocity =  $4.34 \pm 0.02$  km/sec

This observation lends support to the interpretation of the first inversion, that the sediment-covered platforms of Russia and Siberia are largely sediment-covered shields. The result for Tibet we have obtained is that the upper mantle, to great depth, is largely shield-like in character. We interpret this to mean, if it should be substantiated, that the Indian Shield has been emplaced beneath the Tibetan crust during the collision of the plates and that the mantle beneath Tibet is presently at temperatures well below the melting point to great depth, i.e. the mantle under the Tibetan plateau is relatively cool compared with tectonically active collision zones such as region 3.

On the other hand regions 3, 5, and 6 all exhibit the development of a marked low-velocity channel at shallow depths in the mantle, which implies that a significant zone of partial melting, perhaps 200 km thick, is present. All these three regions are thus presumed to be tectonically active, despite the low seismicity of region 6 (the large recent earthquakes in China occurred in the northern part of region 6). The presence of a small channel at great depth is not considered to be significant: this may be an artifact of the inversion, due to improper choice of parameters at shallower depths. These deep channels are probably absent but we cannot be absolutely certain.

### Inversion 2.1

We have made a variation on inversion 2 by enlarging the extent of the Baltic shield in the preceding inversion, as shown

in Fig. 29 according to a hint in the tectonic map of Khain and Muratov (1969). As might have been expected, the results of the preceding inversion are not significantly changed in view of the result of inversion 2, namely that regions 1 & 2 are virtually identical in cross-section. Hence enlarging region 1 at the expense of region 2 cannot be expected to produce a significant change in the results.

A tabulation of the results of this inversion is as follows, and is listed only for purposes of comparison with the other inversions:

$$\beta_{\text{LID}} = 4.56 \pm 0.01 \text{ km/sec}$$

$$\beta_{\text{CH}} = 4.34 \pm 0.02 \text{ km/sec}$$

$$h_{\text{LID } 1'} = 206 \pm 25 \text{ km}$$

$$h_{\text{LID } 2'} = 229 \pm 29$$

$$h_{\text{LID } 3} = 99 \pm 9$$

$$h_{\text{LID } 4} = 246 \pm 56$$

$$h_{\text{LID } 5} = 79 \pm 7$$

$$h_{\text{LID } 6} = 69 \pm 7$$

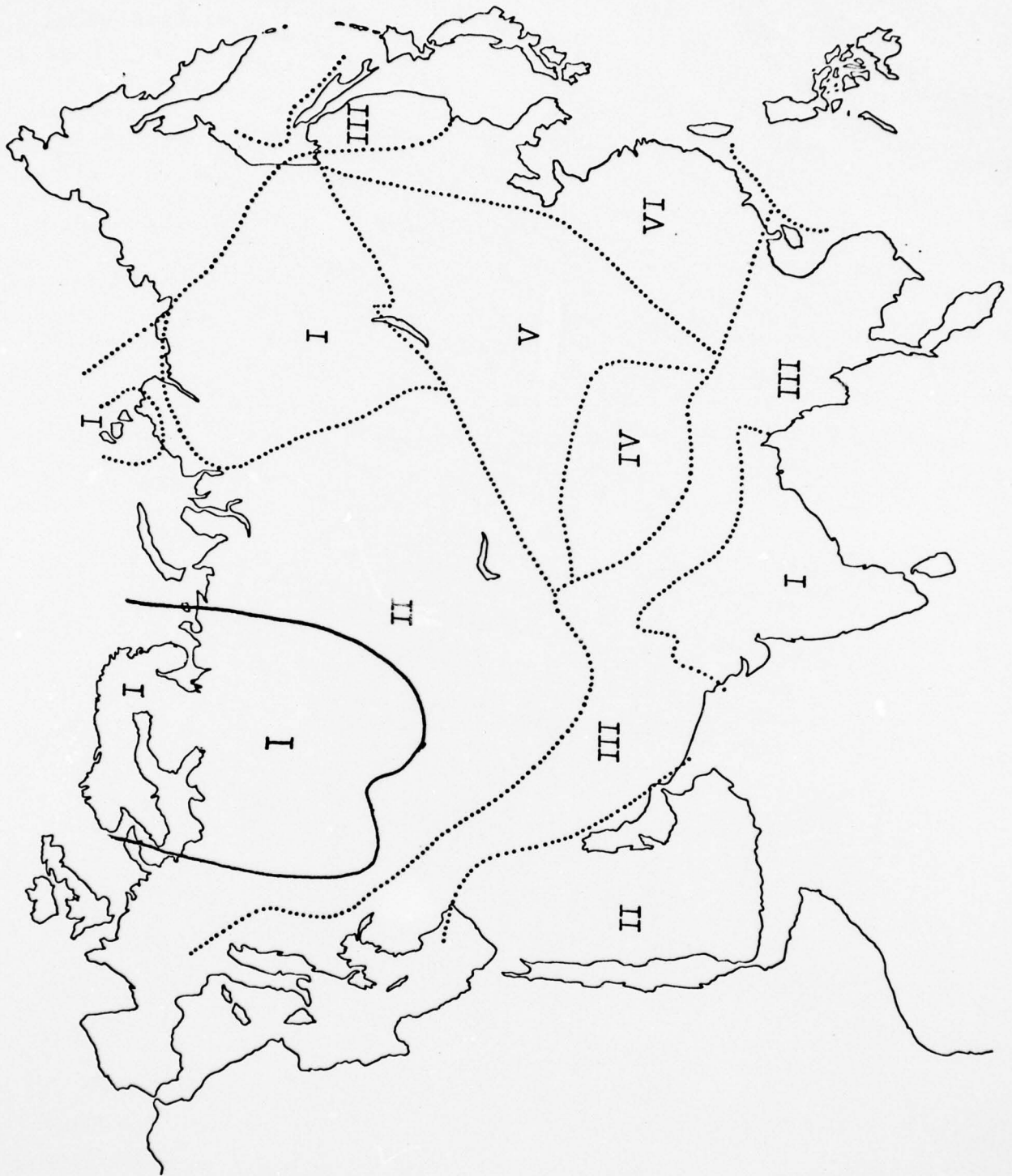
$$h_{\text{CH-SUB}} = 274 \pm 8$$

## Inversion 2.2

In each of the two preceding inversions we have obtained the result that the upper mantle of both regions 1 and 2 are remarkably similar. In both cases we have a deep continental root to essentially the same depths. We have therefore made

FIG. 29. Modification of regionalization of Fig. 25  
by enlargement of region 1 in Baltic shield  
area.

Fig. 29



the assumption that these two regions are indistinguishable in a new inversion 2.2. We call the coalescence of regions 1 and 2, a new region 1A (Fig. 30); there is now no separate region 2.

As might be expected the results of the inversions are not significantly changed from the earlier explorations. Indeed the results for inversion 2.2 are identical in all respects with that of inversion 2.1

$$\beta_{\text{LID}} = 4.56 \pm .01 \text{ km/sec}$$

$$\beta_{\text{CH}} = 4.34 \pm .02 \text{ km/sec}$$

$$h_{\text{CH-SUB}} = 274 \pm 8 \text{ km}$$

$$h_{\text{LID(IA)}} = 217 \pm 18 \text{ km}$$

$$h_{\text{LID(3)}} = 99 \pm 9$$

$$h_{\text{LID(4)}} = 246 \pm 55$$

$$h_{\text{LID(5)}} = 79 \pm 9$$

$$h_{\text{LID(6)}} = 69 \pm 7$$

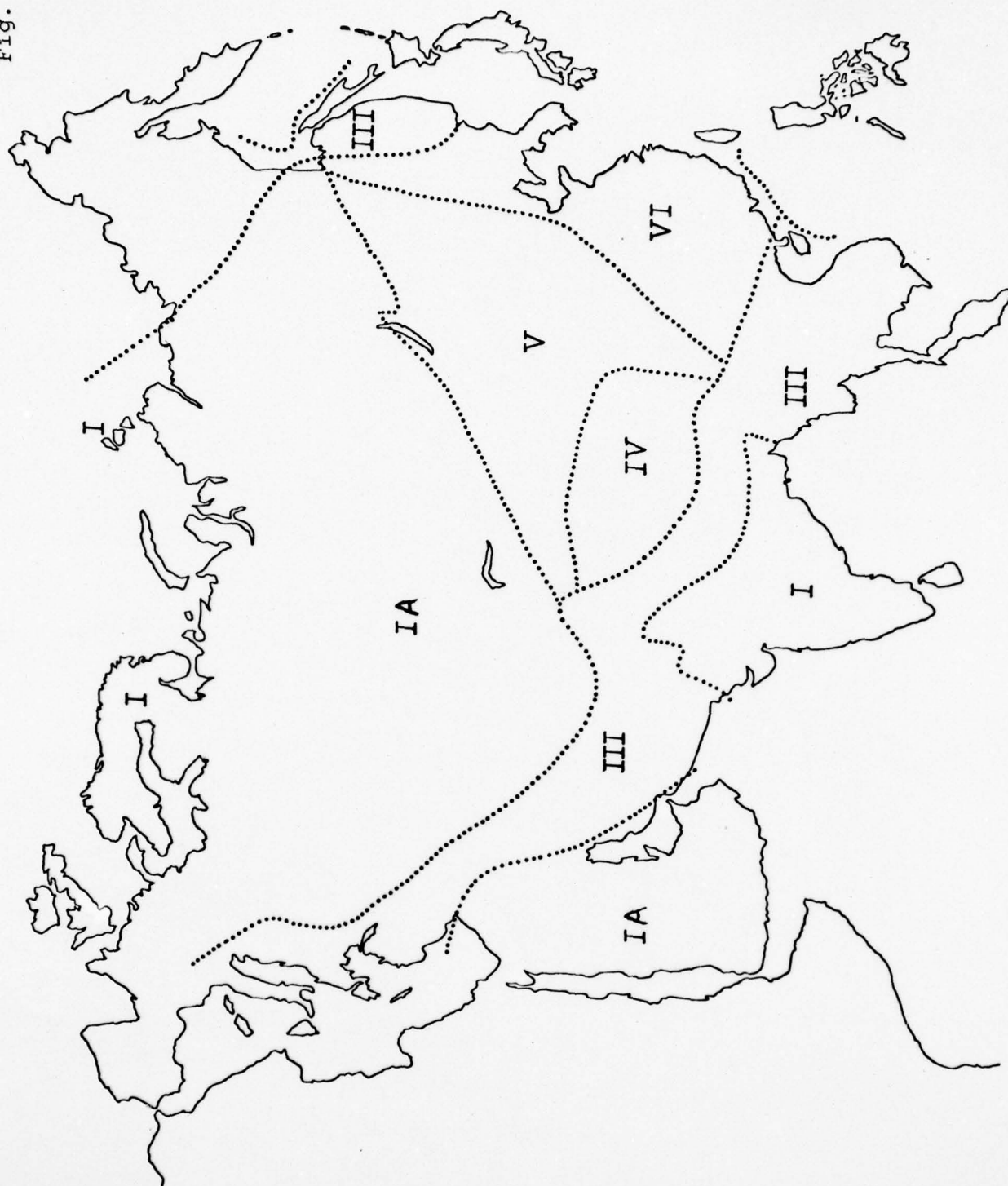
all depths  $h$  are measured from the surface.

### Inversion 3

A rather annoying aspect of the data concerns the fact that the phase travel-time residuals from any of the preceding models are not normally distributed. There is an unacceptably large number of residuals between  $2\sigma$  and  $4\sigma$ ; this result has been verified by a  $\chi^2$  test. We have deleted several of the data with large residuals and have proposed a new data set with a value of  $\chi^2$  which places the new data set within acceptable limits of a

FIG. 30. Modification of regionalization of Fig. 25  
by fusion of regions 1 and 2.

Fig. 30



a normal distribution with a new value of  $\sigma$  having 2/3 the former value:

$$\sigma = 2/3 \text{ Max } (7 \text{ sec}, 0.1T)$$

We have repeated inversion 2.2 with the revised data set and the new estimate of errors and have obtained the following results:

$\beta_{\text{LID}}$	=	4.57 $\pm$ .01 km/sec
$\beta_{\text{CH}}$	=	4.35 $\pm$ .01 km/sec
$h_{\text{CH-SUB}}$	=	276 $\pm$ 5 km
$h_{\text{LID(IA)}}$	=	204 $\pm$ 12
$h_{\text{LID(3)}}$	=	99 $\pm$ 7
$h_{\text{LID(4)}}$	=	256 $\pm$ 41
$h_{\text{LID(5)}}$	=	59 $\pm$ 4
$h_{\text{LID(6)}}$	=	55 $\pm$ 5

The shear velocities in the lid and channel are unchanged from the preceding inversion 2.2. But there have been some significant changes in the lid thickness of some of the regions. Regions 1A and 4 continue to have upper mantles consistent with ancient (cold) shield models. However, regions 5 and 6 now have very thin lids, implying high heat flow and the presence of strong tectonic processes.

### Inversion 3.1

To test the validity of the linearized inversion procedures especially in view of our observations that the final results are

strongly dependent on smoothing procedures in the model space, we have applied the power of our non-linear Hedgehog program whose results are independent of smoothing in the model space.

The data set is the reduced data set of Inversion 3 with a normal distribution of residuals relative to model 2.2. We have further fixed the channel-subchannel interface at the value given by inversion 3. The remaining seven parameters were explored in the space given by Table 6.

TABLE 6  
Parameters and Range of Search in Hedgehog Inversion  
for Inversion 3.1

	Starting Value	Step Size	Lower Limit	Upper Limit
P1	4.57	0.1	4.47	4.67
P2	4.35	0.1	4.25	4.45
P3	204	30	144	264
P4	99	30	69	189
P5	256	30	136	256
P6	59	30	59	179
P7	55	30	55	175

P1: Lid shear wave velocity in Km/Sec

P2: Channel shear wave velocity in Km/Sec

P3: Lid thickness of region 1A in Km

P4: Lid thickness of region 3 in Km

P5: Lid thickness of region 4 in Km

P6: Lid thickness of region 5 in Km

P7: Lid thickness of region 6 in Km

The results of the inversion gave the 67 acceptable solutions, acceptable within 1.4σ under the postulate that there is equal tradeoff between the effects of uncertainties in the model space and fit to the data (Table 7). The first, and most obvious result is that the lid velocity was accepted to be 4.57 km/sec; no other values are acceptable. The channel velocities accepted were only 4.25 and 4.35 km/sec. Although the lid thicknesses for the shields of region 1A could vary between 174 and 234 km and for the Tibetan plateau (region 4) between 226 and 256 km a) under some circumstances both lids could have the same thickness (models 14, 30, 31, etc.) and b) under no circumstances could the Tibetan plateau have a lid which was as thin as (say) 30 km, a result which would have implied a mantle appropriate to a tectonically active region, i.e., one with a well-developed high-contrast low velocity channel. Finally, although the linear inverse of inversion 3 implied a difference in lid thickness between region 3 on the one hand and regions 6 and 7 on the other, the non-linear model-independent inverse gave some solutions in which the lid thicknesses are such that the lid channel interface is roughly at a common depth below the surfaces of all three regions (e.g. solutions 35, 55, 23, 37, 46, 57). We conclude from these inversion results that cold shield properties extend to great depth under regions 1A and 4 while regions 3, 5, 6 may have similar properties (at least we cannot discount this result) with upper mantles characteristic of young active regions. What is remarkable is that region 6 is coupled together with the more obvious active regions.

## Successful solutions in Hedgehog inversion 3.1

	P1	P2	P3	P4	P5	P6	P7
1	4.57	4.35	204	99	256	59	55
2	4.57	4.35	174	99	256	59	55
3	4.57	4.35	234	99	256	59	55
4	4.57	4.35	204	69	256	59	55
5	4.57	4.35	204	129	256	59	55
6	4.57	4.35	204	99	226	59	55
7	4.57	4.35	204	99	256	89	55
8	4.57	4.35	204	99	256	59	85
9	4.57	4.35	174	69	256	59	55
10	4.57	4.35	174	129	256	59	55
11	4.57	4.35	234	69	256	59	55
12	4.57	4.35	234	129	256	59	55
13	4.57	4.35	174	99	226	59	55
14	4.57	4.35	234	99	226	59	55
15	4.57	4.35	174	99	256	89	55
16	4.57	4.35	234	99	256	89	55
17	4.57	4.35	174	99	256	59	85
18	4.57	4.35	234	99	256	59	85
19	4.57	4.35	204	69	226	59	55
20	4.57	4.35	204	129	226	59	55
21	4.57	4.35	204	69	256	89	55
22	4.57	4.35	204	129	256	89	55
23	4.57	4.35	204	69	256	59	85
24	4.57	4.35	204	129	256	59	85
25	4.57	4.35	204	99	226	89	55
26	4.57	4.35	204	99	226	59	85
27	4.57	4.35	204	99	256	89	85
28	4.57	4.35	174	69	226	59	55
29	4.57	4.35	174	129	226	59	55
30	4.57	4.35	234	69	226	59	55
31	4.57	4.35	234	129	226	59	55
32	4.57	4.35	174	69	256	89	55
33	4.57	4.35	174	129	256	89	55
34	4.57	4.35	234	69	256	89	55

	P1	P2	P3	P4	P5	P6	P7
35	4.57	4.35	174	69	256	59	85
36	4.57	4.35	174	129	256	59	85
37	4.57	4.35	234	69	256	59	85
38	4.57	4.35	234	129	256	59	85
39	4.57	4.35	174	99	226	89	55
40	4.57	4.35	234	99	226	89	55
41	4.57	4.35	174	99	226	59	85
42	4.57	4.35	234	99	226	59	85
43	4.57	4.35	174	99	256	89	85
44	4.57	4.35	204	69	226	89	55
45	4.57	4.35	204	129	226	89	55
46	4.57	4.35	204	69	226	59	85
47	4.57	4.35	204	129	226	59	85
48	4.57	4.35	204	69	256	89	85
49	4.57	4.35	204	99	226	89	85
50	4.57	4.25	234	129	256	89	55
51	4.57	4.25	204	129	256	89	85
52	4.57	4.35	174	69	226	89	55
53	4.57	4.35	174	129	226	89	55
54	4.57	4.35	234	69	226	89	55
55	4.57	4.35	174	69	226	59	85
56	4.57	4.35	174	129	226	59	85
57	4.57	4.35	234	69	226	59	85
58	4.57	4.35	234	129	226	59	85
59	4.57	4.35	174	69	256	89	85
60	4.57	4.35	234	69	256	89	85
61	4.57	4.35	174	99	226	89	85
62	4.57	4.35	234	99	226	89	85
63	4.57	4.35	204	69	226	89	85
64	4.57	4.25	234	129	256	89	85
65	4.57	4.35	174	69	226	89	85
66	4.57	4.35	234	69	226	89	85
67	4.57	4.25	234	129	226	89	85

#### Inversion 4

To test the importance of diffraction, we have deleted from the data set, phase travel times for those paths which lie close and parallel to a contrast between two dissimilar zones. The value of  $\sigma$  continues to be taken as in the result of Inversion 3. The linear inverse using the same regionalization and parameterization as inversion 3 for the results:

$$\begin{aligned}
 \beta_{\text{LID}} &= 4.58 \pm .01 \text{ km/sec} \\
 \beta_{\text{CH}} &= 4.36 \pm .02 \text{ km/sec} \\
 h_{\text{LID}(1A)} &= 181 \pm 13 \text{ km (below surface)} \\
 h_{\text{LID}(3)} &= 101 \pm 16 && " && " \\
 h_{\text{LID}(4)} &= 204 \pm 35 && " && " \\
 h_{\text{LID}(5)} &= 54 \pm 7 && " && " \\
 h_{\text{LID}(6)} &= 54 \pm 7 && " && " \\
 h_{\text{CH-SUB}} &= 268 \pm 6 && " && "
 \end{aligned}$$

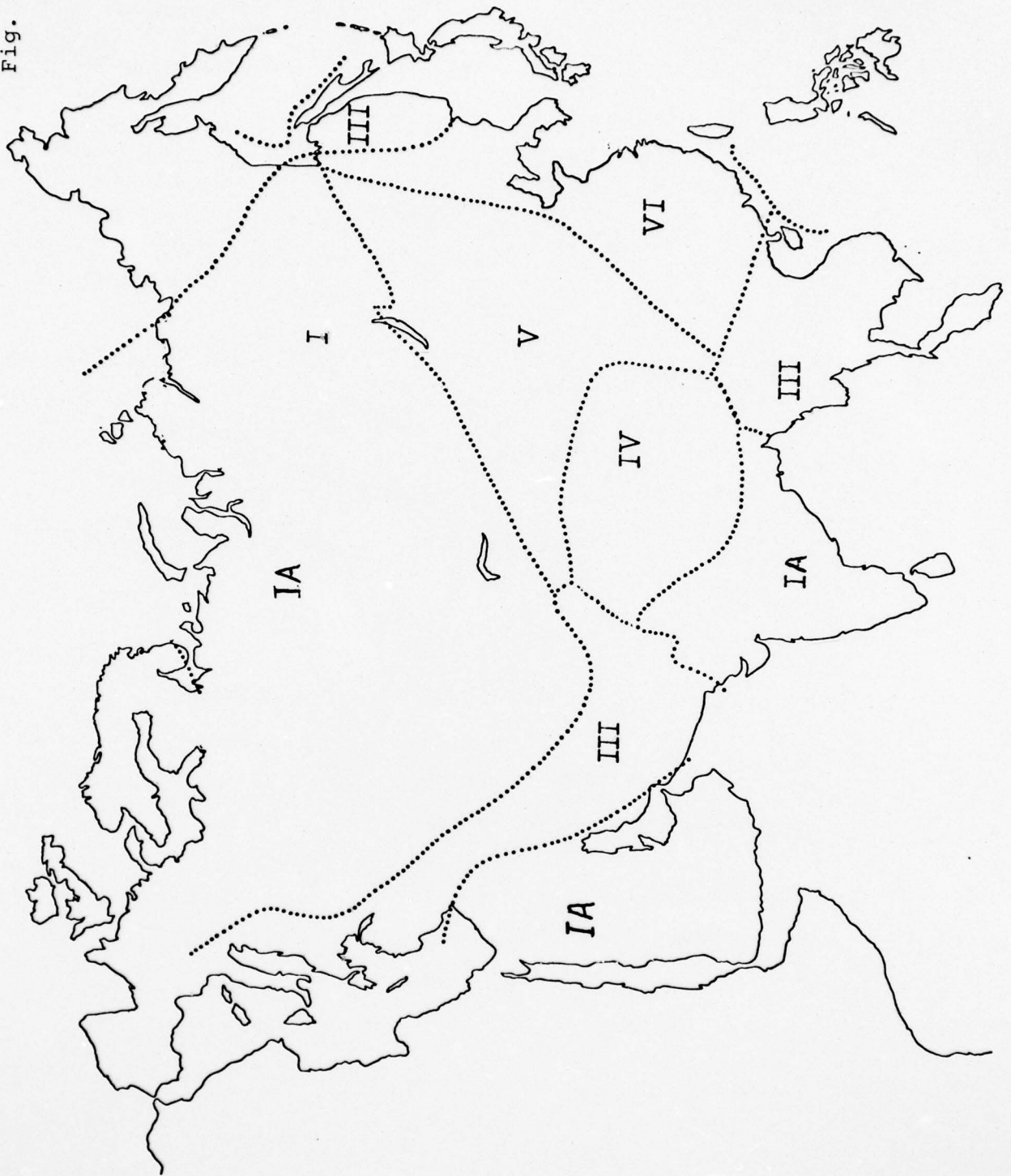
We detect no significant changes from the results of inversion 3.

#### Inversion 5

Finally, since the Tibetan structure appears to be associated with the collision of the Indian-Asian plates, we have incorporated the Himalayan part of region 3 into region 4, and re-analyzed the linear inversion with the data and errors as in inversion 3. A map of the new regionalization is shown in Figure 31.

FIG. 31. Modification of regionalization of Fig. 30  
by enlargement of region 4 in Himalayan region.

Fig. 31



The results of the inversion are

$$\begin{aligned}
 \beta_{\text{LID}} &= 4.58 \pm .01 \text{ km/sec} \\
 \beta_{\text{CH}} &= 4.34 \pm .01 \\
 h_{\text{LID}(1A)} &= 194 \pm 10 \text{ km} \\
 h_{\text{LID}(3)} &= 97 \pm 8 \\
 h_{\text{LID}(4)} &= 207 \pm 21 \\
 h_{\text{LID}(5)} &= 67 \pm 4 \\
 h_{\text{LID}(6)} &= 58 \pm 5 \\
 h_{\text{CH-SUB}} &= 273 \pm 5
 \end{aligned}$$

Again we observe no major change in the structure.

We conclude from all these tests that the stable sediment-covered regions of the USSR are probably stable preCambrian shields covered by sediments, that the Tibetan plateau is underlain by relatively cold shield mantle material with no major low-velocity zone at even moderate depths that might be expected of tectonically active zones or of young stable regions, that the mountainous collision zone between the Asian and Indian plates have a prominent low velocity zone at moderate depths, that the Sinkiang-Mongolian active seismic zone has a similar structure and that South Eastern China is also a region of tectonic activity as indicated by the similarity of its upper mantle structure to the other two seismically active regions.

Arctic Study. We have measured fundamental mode Rayleigh waves over a number of paths crossing the Arctic Ocean. We have used as sources four earthquakes whose focal parameters are:

4. Lena River	Aug. 25, 1964	13:47:20.6	78.2°N	126.6°E
10. Eastern Aleutians(1)	Feb. 6, 1965	01:40:33.2	53.2°N	161.9°W
11. Eastern Aleutians(2)	Feb. 6, 1965	16:50:23.6	53.3°N	161.8°W
13. Western Aleutians	Feb. 6, 1965	04:02:53	52.1°N	175.7°E

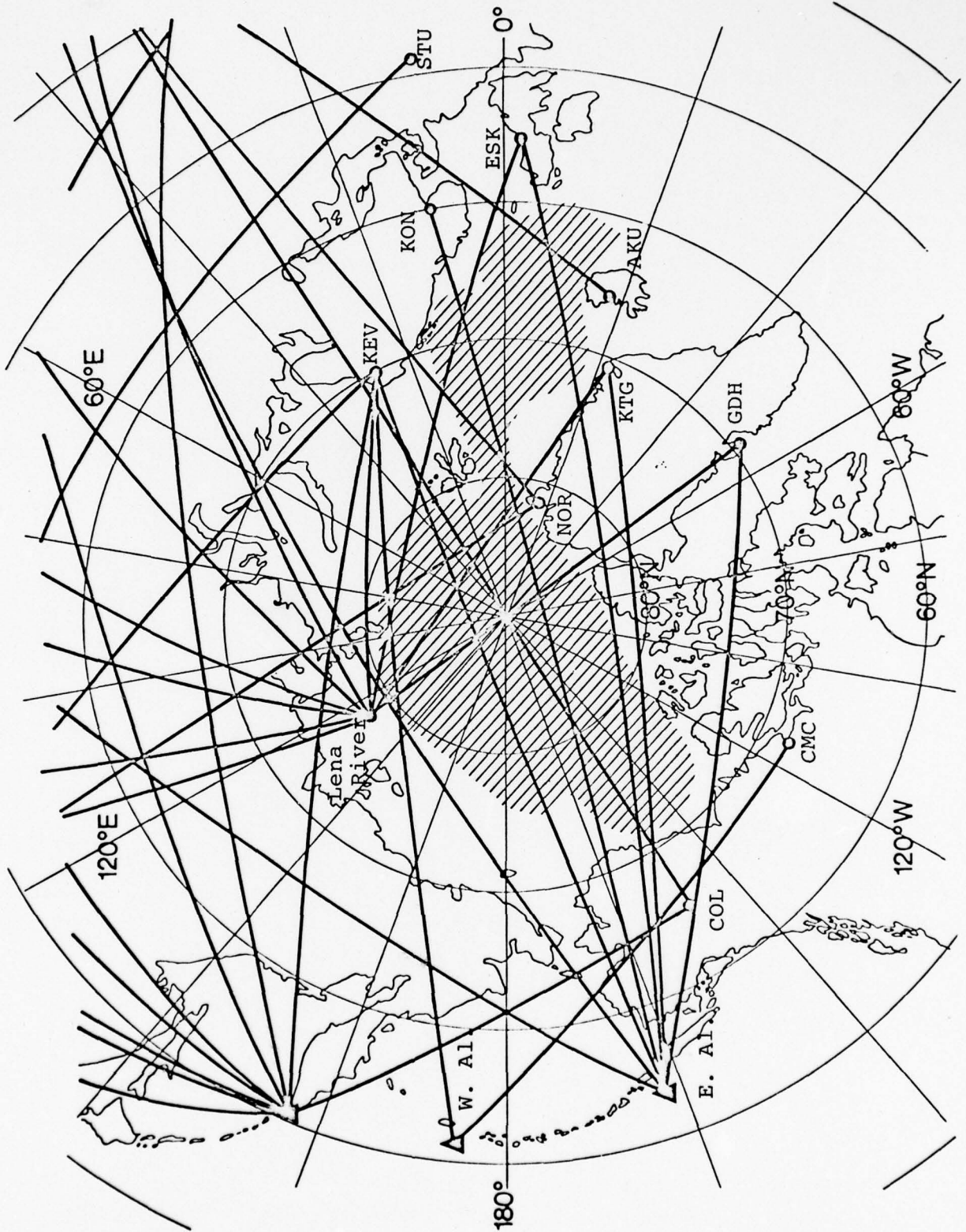
For each of these earthquakes we have obtained initial phases either from the fault plane solution or from the radiation pattern for Rayleigh waves (as in the case of the Lena River discussed above). We have obtained phase velocities by the single-station method for seven paths crossing the Arctic over the period range 50 to 208 sec. The paths are shown in Figure 32.

It can be seen that none of these are purely oceanic paths. The shaded area outlines our estimate of the boundary between the continental shelf and the deep ocean basins. The fraction of the geometrical path that each event has in the oceanic part is as follows:

<u>Event</u>	<u>Total path length</u>	<u>Oceanic length</u>	<u>Fraction oceanic</u>
1. Lena - ESK	4816 km	1904 km	.40
2. Lena - KTG	3386	1823	.54
3. East Aleut(1) - KON	7483	4603	.62
4. East Aleut(1) - KTG	5933	916	.15
5. East Aleut(2) - KEV	6347	2334	.37
6. East Aleut(2) - ESK	7818	2714	.35
7. West Aleut. - KEV	6263	844	.13

FIG. 32. Map of Arctic region showing all propagation paths used in dispersion and regionalization analysis.

Fig. 32



To reduce the available data to information regarding purely oceanic paths, we have decided to use the phase velocity data for the Lena River event recorded at KEV (see discussion above for Eurasia) as a typical continental value and to subtract these values, for the appropriate path length contribution, from the phase delays observed for the above 7 path-events. Unfortunately, the two events East Aleut.(1) - KTG and West Aleut.-KEV have such small parts of their total path that are oceanic that we are subtracting two numbers of comparable size and the result is quite unstable. The unreliability of the oceanic phase delay results for these two cases has obliged us to exclude them from our data set. Accordingly, we have investigated the inversions of the phase velocity results for the five remaining paths. The relevant data are given in Table 8:

TABLE 8  
(Pure) Oceanic Phase Velocities (km/sec)

<u>T(sec)</u>	<u>Lena-ESK</u>	<u>Lena-KTG</u>	<u>E.A1(1)-KON</u>	<u>E.A1(2)-KEV</u>	<u>E.A1(2)-ESK</u>
208	4.64	(4.83)	4.62	4.55	4.52
192	4.52	(4.61)	4.51	4.42	4.42
167	4.38	4.32	4.38	4.22	4.28
139	4.21	4.14	4.24	4.09	4.15
119	4.08	4.06	4.12	4.04	4.11
100	4.01	3.99	4.08	3.96	4.07
69	3.95	3.90	4.00	3.91	4.00
50	3.91	3.82	3.98	3.89	3.92

With so few data, we have not been able to regionalize the

the deep Arctic; the number of degrees of freedom in the data is too small. The best we can do is to consider the deep Arctic as a single province and investigate the consequences of inverting an "average" phase velocity for the region. The average phase velocity is obtained from the above table by weighting by the oceanic path length in each case. The result is (omitting the quantities in parentheses):

T(sec)	c(km/sec)
208	4.59
192	4.47
167	4.32
139	4.18
119	4.10
100	4.03
69	3.97
50	3.92

These results can be compared with those obtained for Pacific paths by Leeds (1973) from inversion of trans-Pacific phase velocity data by methods similar to those described above for trans-Eurasian paths. The pure-age phase velocities for the Pacific can be derived from the cross-sections resulting from the inversions; these are shown in Fig. 33 for Pacific ages 0-10 my, 20-40 my, 85-110 my. The Arctic data points are shown as circles. The Arctic cross-section averages out to about a 30 my Pacific structure. According to the model of Parker and Oldenburg (1973), the lid thickness as a function of the age is

$z(t) = 9.4t^{\frac{1}{2}}$  km, with  $t$  the age in my. Thus, assuming that the lid and channel S-wave velocities are of the same order as in the Pacific, the age at which the Arctic began to open is calculated to be about 70 my (before present), an unexpectedly small quantity.

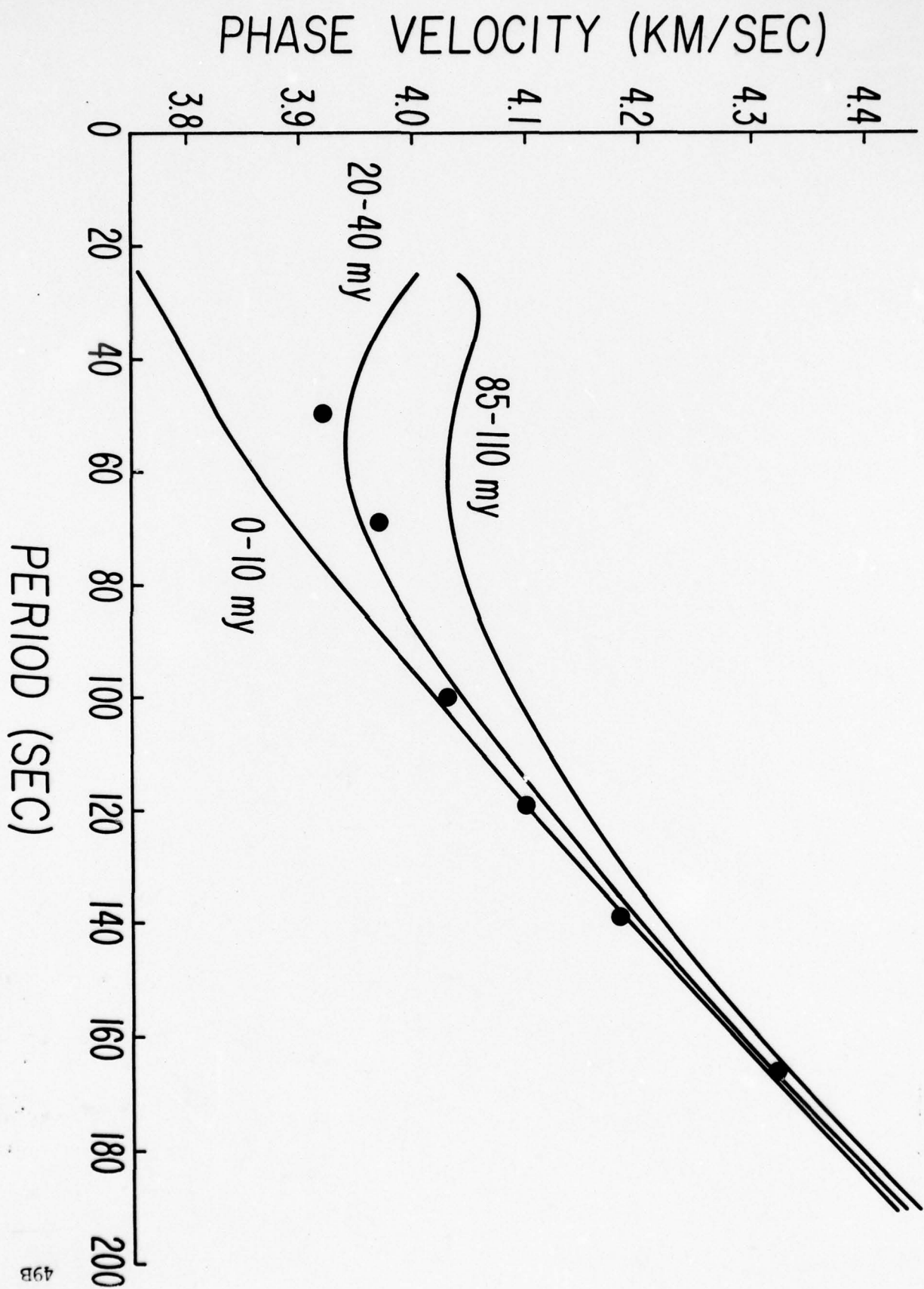
Theoretical seismograms. The main thrust of our work with time series synthesis has been directed toward improving the efficiency of existing computational techniques. This improvement is required to permit us to extend the information contained on the theoretical seismograms down through the period range covered by the long-period instruments of the WWSSN. Although up to the present time we have concentrated on laterally homogeneous structures, in all other respects our models of the earth have been highly realistic: approximately 200 layers are being used to model the radial heterogeneity of the crust-mantle system of a spherical earth, and the intrinsic attenuation is included.

A summary of the general methods we have applied in our computations is given by Kausel and Schwab (1973), and Knopoff et al (1974). An elaboration of, and certain justifications for these procedures have recently been given by Schwab and Kausel (1976). A recent contribution by Calcagnile et al (1976), also completed under this contract, is also pertinent here when only the surface-wave portion of the theoretical seismogram is desired.

The initial development of the algorithm and certain programming improvements, which were carried out under the present

FIG. 33. Results of phase velocity dispersion for Arctic region (circles). "Standard" phase velocity curves for Pacific age strips are shown for comparison (Leeds, 1973). Because the Pacific spreads at a different rate than the Arctic, this gives a different age for the Arctic (see text).

Fig. 33



contract, are contained in Nakanishi, Schwab and Kausel (1976), and Nakanishi, Schwab and Knopoff (1976). These manuscripts formed the necessary bridge between first generation and second generation dispersion programs. First generation techniques are based on full, detailed specification — a structure, a specific mode, and a specific period — from which a single phase velocity at a time is sought; second generation dispersion computations begin with only the structure and the mode specified, and they then compute all phase velocities down to whatever minimum period is desired. As the second generation software is developed, computations for the group velocity, phase attenuation, amplitude excitation function, and apparent initial phase are incorporated into the procedure (but not yet into a single, automatic routine combined with the phase velocity computations).

In a series of five later papers under this contract (Kausel, Schwab and Mantovani, 1977; Mantovani et al 1976, 1977; Mantovani, 1977 a,b) this second generation software was fully developed and applied to the generation of multimode theoretical seismograms containing as many as 21 modes; each of these was represented over the entire period range down to 1 second.

The final stage of our work on the generation of complete theoretical seismograms for torsional waves, was the development of a third generation program. This routine is fully automatic, and requires only the structural specification as input. The output, which is obtained in a single, relatively short computer run, contains all of the frequency-domain information required

to compute theoretical seismograms for arbitrary source specifications. As desired, all body-wave and surface-wave arrivals, for periods greater than ten seconds, are obtained from the 90-100 modes thus specified. Results from this work were recently prepared and a preprint is appended (Liao, Schwab and Mantovani, 1977). We are now in a position of being able to compare directly, the entire experimental, torsional-wave seismograms from the long-period WWSSN instruments with those computed from theoretically specified sources and structures.

Our work on the algorithm and the programming on the Rayleigh-, or spheroidal-wave theoretical seismograms, began with detailed analysis and improvements of the basic direct method for handling such calculations on a spherical, gravitating earth. In its original form, this method was initially developed in the series of papers by Hoskins (1920), Pekeris and Jarosch (1958), and Alterman, Jarosch and Pekeris (1959); some numerical details concerning such computations were given by Bolt and Dorman (1961), and later, by Takeuchi and Saito (1972). In the appended manuscript (Schwab et al, 1977) we describe: (1) the newly developed simplifications of the usual algorithm, which has made it possible — we believe for the first time — to develop a direct algorithm for group velocity computation, that is independent of the usual appeal to variational techniques; (2) the numerical problems that are associated with this type of computation, in quite detailed form, in relation to what has appeared previously in the literature;

(3) our optimization of the improved algorithm, and the efficiency of the optimization relative to various similar computations problems.

Relative to the efficiency determination, the most pertinent results affecting the work on this contract are: (1) that such computations — for Rayleigh-, or spheroidal waves on a spherical, gravitating earth — are about six times more expensive than the comparable torsional-wave computations, and (2) that spheroidal waves can be handled on a non-gravitating earth for only about twice the expense of torsional waves. From these results we conclude that the present optimization is still too expensive to use for the computation of theoretical seismograms for spheroidal waves (down to periods of only ten seconds), but that the optimization technique will be satisfactory for this purpose if a means can be devised to approximate the removal of gravity from the formulation. Such a technique has already been devised (Schwab, 1977), but the numerical tests have only just begun.

The final, practical purpose of our work under this contract — application of our results to the discrimination problem — will involve comparison of complete theoretical and experimental seismograms. It is therefore important that we have as accurate a means as possible of obtaining the instrumental constants from the impulse response of the experimental record. These constants then permit us to include, with a minimum of error, the effect of the instrumental response on the theoretical seismogram. Our improved scheme for inversion of the impulse response to obtain the instrument parameters, is described in the appended preprint by Mitchel (1977).

- Alterman, Z., H. Jarosch and C. L. Pekeris (1959). Oscillations of the Earth, Proc. Roy. Soc., A 252, 80-95.
- Alterman, Z. and D. Loewenthal (1972). Computer generated seismograms, in Methods in Computational Physics, volume 12 (edited by B. A. Bolt), Academic Press, New York, 25-164.
- Arkangel'sakaya, V. M. (1960). Dispersion of surface waves and crustal structure, Bull. (Izv.) Acad. Sci. USSR, Geophys. Ser. No. 9, 904-927.
- Backus, G. and F. Gilbert (1968). The resolving power of gross Earth data, Geophys. J. Roy. astr. Soc., 16, 169-205.
- Backus, G. and F. Gilbert (1970). Uniqueness in the inversion of inaccurate gross Earth data, Phil. Trans. Roy. Soc. Lond., Ser. A, 266, 123-192.
- Ben-Menahem, A. and D. G. Harkrider (1964). Radiation patterns of seismic surface waves from buried dipolar point sources in a flat stratified earth, J. Geophys. Res., 69, 2605-2620.
- Ben-Menahem, A. and M. N. Toksöz (1963). Source mechanism from spectra of long-period seismic surface waves. 2. The Kamchatka earthquake of November 4, 1952, J. Geophys. Res., 68, 5207-5222.
- Biswas, N. N. and L. Knopoff (1970). Exact earth-flattening calculation for Love waves, Bull. Seismol. Soc. Amer., 60, 1123-1137.
- Biswas, N. N. and L. Knopoff (1974). Structure of the upper mantle under the United States from the dispersion of Rayleigh waves, Geophys. J. R. astr. Soc., 36, 515-539.

- Bolt, B. A. and J. Dorman (1961). Phase and group velocities of Rayleigh waves in a spherical, gravitating Earth, J. Geophys. Res. 66, 2965-2981.
- Brune, J. and J. Dorman (1964). Seismic waves and earth structure in the Canadian shield, Bull. Seis. Soc. Am., 53, 167-210.
- Brune, J., J. Nafe and J. Oliver (1960). A simplified method for the analysis and synthesis of dispersed wave trains. J. Geophys. Res., 65, 287-305.
- Burridge, R. and L. Knopoff (1964). Body force equivalents for seismic dislocations, Bull. Seismol. Soc. Amer., 54, 1875-1888.
- Calcagnile, G., G. F. Panza, F. Schwab and E. G. Kausel (1976). On the computation of theoretical seismograms for multi-mode surface waves, Geophys. J. R. astr. Soc. 47, 73-81.
- Chun, Kin-Kip and Toshikatsu Yoshii (1977). Crustal structure of the Tibetan plateau: A surface wave study by a Moving Window. Bull. Seis. Soc. Amer., 67, 735-750.
- Dorman, J. and M. Ewing (1962). Numerical inversion of surface wave dispersion data and the crust-mantle structure in the New York-Pennsylvania area, J. Geophys. Res., 67, 5227-5241.
- Frez, J. and F. Schwab (1976). Structural dependence of the apparent initial phase of Rayleigh waves, Geophys. J. R. astr. Soc., 44, 311-331.
- Gilbert, F. and A. M. Dziewonski (1975). An application of normal mode theory to the retrieval of structure parameters and source mechanisms from seismic spectra, Phil. Trans. Roy. Soc. London, Ser. A, 278, 187-269.

- Harkrider, D. G. (1964). Surface waves in multilayered elastic media. Part I. Rayleigh and Love waves from buried sources in a multilayered elastic half-space, Bull. Seismol. Soc. Amer. 54, 627-679.
- Harkrider, D. G. (1970). Surface waves in multilayered elastic media. Part II. Higher mode spectra and spectral ratios from point sources in plane layered earth models, Bull. Seismol. Soc. Amer., 60, 1937-1987.
- Haskell, N. A. (1953). The dispersion of surface waves on multilayered media, Bull. Seismol. Soc. Amer., 43, 17-34.
- Hoskins, L. M. (1920). The strain of gravitating sphere of variable density and elasticity. Trans. Am. Math. Soc., 21, 1-43.
- Jackson, D. D. (1972). Interpretation of inaccurate, insufficient and inconsistent data, Geophys. J., 28, 97-109.
- James, D. E. and A. T. Linde (1971). A source of major error in the digital analysis of World Wide Standard Station seismograms, Bull. Seismol. Soc. Amer., 61, 723-728.
- Kausel, E. G., A. R. Leeds and L. Knopoff (1974). Variation of Rayleigh wave phase velocities across the Pacific Science, 186, 139-141.
- Kausel, E. and F. Schwab (1973). Contributions to Love wave transformation theory: Earth-flattening transformation for Love waves from a point source in a sphere, Bull. Seismol. Soc. Amer., 63, 983-993.

- Kausel, E. G., F. Schwab and E. Mantovani (1977). Oceanic Sa  
Geophys. J. R. astr. Soc., 50, 407-440.
- Keilis-Borok, V. I. and T. B. Yanovskaya (1967). Inverse seis-  
mic problems (structural review), Geophys. J., 13, 223-  
233.
- Khain, V. E. and M. V. Muratov (1969). Crustal movements and  
tectonic structure of continents, in The Earth's Crust  
and Upper Mantle, (edited by P. J. Hart), Geophysical  
Monograph 13, American Geophysical Union, Washington, DC.
- Knopoff, L. (1961). Green's function for eigenvalue problems  
and the inversion of Love wave dispersion data, Geophys. J.,  
4, 161-173.
- Knopoff, L. (1962). Higher order Born approximation for the  
inversion of Love wave dispersion, Geophys. J., 7, 149-157.
- Knopoff, L. (1964). A matrix method for elastic wave problems,  
Bull. Seismol. Soc. Amer., 54, 431-438.
- Knopoff, L. (1969). Phase and group slownesses in inhomogeneous  
media, J. Geophys. Res., 74, 1701.
- Knopoff, L. (1972). Observation and inversion of surface  
wave dispersion, Tectonophysics, 13, 497-519.
- Knopoff, L. and D. D. Jackson (1972). The analysis of undetermined  
and overdetermined systems, in The Dynamic Response of Structures  
G. Herrmann, ed., Pergamon Press, 289-305.

- Knopoff, L., S. Mueller, and W. L. Pilant (1966). Structure of the crust and upper mantle in the Alps from the phase velocity of Rayleigh waves, Bull Seismol. Soc. Amer. 56, 1009-1044.
- Knopoff, L. and J. W. Schlue (1972). Rayleigh wave phase velocities for the path Addis Abba-Nairobi, Tectonophysics, 15, 157-163.
- Knopoff, L. and F. Schwab (1968). Apparent initial phase of a source of Rayleigh waves, J. Geophys. Res., 73, 755-760.
- Knopoff, L., F. Schwab and E. Kausel (1973). Interpretation of Lg, Geophys. J. R. astr. Soc., 33, 389-404.
- Knopoff, L., F. Schwab, K. Nakanishi and F. Chang (1974). Evaluation of Lg as a discriminant among different continental crustal structures, Geophys. J. R. astr. Soc., 39, 41-70.
- Kosminskaya, I. P., N. A. Belyaevsky and I. S. Volvovsky (1969). Explosion seismology in the USSR, in The Earth's Crust and Upper Mantle, (edited by P. J. Hart), Geophysical Monograph 13, American Geophysical Union, Washington, DC.
- Leeds, A. R. (1973). Rayleigh wave dispersion in the Pacific Basin. Ph.D. thesis, University of California, Los Angeles.
- Leeds, A. R. (1975). Lithospheric thickness in the Western Pacific, Phys. Earth Planet. Int., 11, 61-64.
- Leeds, A. R., L. Knopoff and E. G. Kausel (1974). Variations of upper mantle structure under the Pacific Ocean, Science, 186, 141-143.

- Liao, H. M., F. Schwab and E. Mantovani (1977). Computation of complete theoretical seismograms for torsional waves (appended).
- Lubimova, E. A. and B. G. Polyak (1969). Heat flow map of Eurasia, in The Earth's Crust and Upper Mantle (edited by P. J. Hart), Geophysical Monograph 13, American Geophysical Union, Washington, DC.
- Mantovani, E., F. Schwab, H. Liao and L. Knopoff (1976). Generation of complete theoretical seismograms for SH. Part II, Geophys. J. R. astr. Soc., 48, 531-536.
- Mantovani, E., F. Schwab, L. Knopoff and H. Liao (1977). Teleseismic Sn: A guided wave in the mantle, Geophys. J. R. astr. Soc., 51, 709-726.
- Mantovani, E. (1977a). Generation of complete theoretical seismograms for SH. Part III, submitted to Geophys. J. R. astr. Soc. (appended).
- Mantovani, E. (1977b). Generation of complete theoretical seismograms for SH. Part IV, in preparation.
- Mitchel, R. G. (1977). Improved scheme of inversion of seismometer impulse response to obtain electromagnetic instruments constants (appended).
- Nakanishi, K., F. Schwab and E. G. Kausel (1976). Interpretation of  $S_a$  in a continental structure, Geophys. J. R. astr. Soc., 47, 211-223.
- Nakanishi, K., F. Schwab and L. Knopoff (1976). Generation of complete theoretical seismograms for SH. Part I, Geophys. J. R. astr. Soc., 48, 525-530.

- Parker, C. L. and D. E. Oldenburg (1973). Thermal model of ocean ridges, Nature Physical Science, 242, 137-139.
- Pekeris, C. L. and H. Jarosch (1958). The free oscillations of the Earth, in Contributions in Geophysics, Volume 1, Pergamon Press, London, 171-192.
- Popov, I. I. (1960). Dispersion of long-period Love waves in the continental and oceanic crust along the path Indonesia-Crimea, Bull. (Izv.) Acad. Sci. USSR, Geophys. Ser. No. 10, 970-973.
- Press, F. (1968). Earth models obtained by Monte Carlo inversion, J. Geophys. Res., 73, 5223-5233.
- Press, F. (1969). The sub-oceanic mantle, Science, 165, 174-176.
- Saito, M. (1967). Excitation of free oscillations and surface waves by a point source in a vertically heterogeneous earth, J. Geophys. Res., 72, 3689-3699.
- Satô, Y., T. Usami and M. Landisman (1968). Theoretical seismograms of torsional disturbances excited at a focus within a heterogeneous spherical earth -- Case of a Gutenberg-Bullen earth model, Bull. Seismol. Soc. Amer., 58, 133-170.
- Savarensky, E. F., G. N. Bozhko, T. I. Kukhtikova, A. B. Peshkov, I. I. Popov, B. N. Sheshkov, O. I. Yurkevich and L. M. Yudakova (1969). On the earth structure in some regions of the USSR from surface wave data, Pure and Applied Geophysics, 73, 99-119.

- Savarensky, E. F. and A. B. Peshkov (1968). On the use of surface wave velocities in choosing a model of crustal structure, Akad. Nauk SSR Izv., Fizika Zemli No. 10, 79-87.
- Savarensky, E. F. and Sh.S. Ragimov (1958). Determining the velocity of Rayleigh waves and direction to the epicenter by three nearby stations, Bull. (Izv.) Acad. Sci. USSR, Geophys. Ser. No. 12, 866-869.
- Savarensky, E. F. and Sh.S. Ragimov (1959). On the determination of the average thickness of the earth's crust from Rayleigh wave group velocity measurements, Bull. (Izv.) Acad. Sci. USSR, Geophys. Ser. No. 9, 969-971.
- Savarensky, E. F. and B. N. Schechkov (1961). The structure of the earth's crust in Siberia and in the Far East from Love and Rayleigh wave dispersion data, Bull. (Izv.) Acad. Sci. USSR, Geophys. Ser. No. 5, 454-456.
- Savarensky, E. F. and D. I. Sikharulidze (1959). Crustal thickness determinations from measured Love wave dispersion, Bull. (Izv.) Acad. Sci. USSR, Geophys. Ser. No. 6.
- Savarensky, E. F., O. N. Solov'eva and B. N. Shechkov (1959). Love wave recording at seismological station Moscow and crustal structure, Bull. (Izv.) Acad. Sci. USSR, Geophys. Ser. No. 5.
- Schwab, F. (1970). Surface wave dispersion computations: Knopoff's method, Bull. Seismol. Soc. Amer., 60, 1491-1520.
- Schwab, F. (1977). Surface-wave dispersion computations: Improved algorithm for Rayleigh waves on a spherical gravitating earth, in preparation.

- Schwab, F. and E. G. Kausel (1976). Long-period surface wave seismology: Love wave phase velocity and polar phase shift, Geophys. J. R. astr. Soc., 45, 407-435.
- Schwab, F. and L. Knopoff (1970). Surface wave dispersion computations, Bull. Seismol. Soc. Amer., 60, 321-344.
- Schwab, F. and L. Knopoff (1971). Surface waves on multi-layered anelastic media, Bull. Seismol. Soc. Amer., 61, 893-912.
- Schwab, F. and L. Knopoff (1972). Fast surface wave and free mode computations, Chapter 3, in Methods in Computational Physics, Volume 11 (edited by B. A. Bolt) Academic Press, New York, 87-180.
- Schwab, F. and L. Knopoff (1973). Love waves and the torsional free modes of a multilayered anelastic sphere, Bull. Seismol. Soc. Amer. 63, 1107-1117.
- Schwab, F., G. F. Panza, H. M. Liao, E. G. Kausel and J. Frez (1977). Surface-wave dispersion computation: Rayleigh waves on a spherical gravitating earth, submitted to Bull. Seism. Soc. Am. (appended)
- Shechkov, B. N. (1961). Structure of the earth's crust in Eurasia from the dispersion of surface waves, Bull. (Izv.) Acad. Sci. USSR, Geophys. Ser. No. 5, 450-453.
- Shechkov, B. N. (1964). Seismic surface wave dispersion and Eurasian crustal structure, Bull. (Izv.) Acad. Sci. USSR, Geophys. Ser. No. 3, 183-187.

- Shechkov, B. N. (1970). Surface wave group velocities on Eurasian paths, Akad. Nauk SSR Izv. Fizika Zemli No. 8, 80-87.
- Shechkov, B. N. and O. N. Solov'eva (1961). Group velocities of Rayleigh waves traveling along a mixed continental-oceanic path, Bull. (Izv.) Acad. Sci. USSR, Geophys. Ser. No. 8, 768-771
- Sikharulidze, D. I. and R. K. Makharadze (1968). The problem of using surface waves in seismic exploration, Akad. Nauk Gruzin. SSR Soobshch. 52, 335-360.
- Sollogub, V. B. (1969). Seismic crustal studies in South-eastern Europe, in The Earth's Crust and Upper Mantle, (edited by P. J. Hart), Geophysical Monograph 13, American Geophysical Union, Washington, DC.
- Sykes, L. R. (1967). Mechanism of earthquakes and nature of faulting on the mid-oceanic ridges, J. Geophys. Res. 72, 2131-2153.
- Takeuchi, H. and M. Saito (1972). Seismic surface waves, in Methods in Computational Physics, Volume 11 (edited by B. A. Bolt), Academic Press, New York, 217-295.
- Thomson, W. T. (1950). Transmission of elastic waves through a stratified solid medium, J. Appl. Phys., 21, 89-93.
- Wiggins, R. A. (1972). The general linear inverse problem: Implication of surface waves and free oscillations for earth structure, Revs. Geophys. and Space Phys., 10, 251-285.

Zakharova, A. I., L. M. Matasova and O. V. Soboleva (1971).

Mechanism of the focus of the main shock from instrumental data, in Tashkent Earthquake of 26 April 1966 (ed. G. A. Mavlyanov) F.A.N. Tashkent Publ. House, Tashkent, USSR, 53-58.

SURFACE-WAVE DISPERSION COMPUTATIONS:  
RAYLEIGH WAVES ON A SPHERICAL GRAVITATING EARTH

F. Schwab, G. F. Panza<sup>1</sup>, H. M. Liao, E. G. Kausel<sup>2</sup> and J. Frez

Publication No. 1700  
Institute of Geophysics and Planetary Physics  
University of California, Los Angeles

Publication No. 121  
Department of Geophysics  
University of Chile, Santiago

Sponsored by  
Advanced Research Projects Agency (DOD)  
ARPA Order No. 3291

Monitored by AFOSR Under Contract #F49620-76-C-0038

<sup>1</sup>Istituto di Geodesia e Geofisica, Università di Bari, Italia; and  
Dipartimento di Scienze della Terra, Università degli Studi  
della Calabria, 87030 Castiglioni Scalo--Cas. Post. 14, Cosenza,  
Italia.

<sup>2</sup>Departamento de Geofísica, Universidad de Chile, Casilla 2777,  
Santiago, Chile.

## ABSTRACT

Algorithmic and numerical analyses are carried out for Rayleigh-wave dispersion computations on a spherical, gravitating earth. Our work is based on the direct, Alterman-Jarosch-Pekeris formulation. For practical purposes, we fix period and determine the associated phase velocity (or polar order number). Neither this, nor integration downward from the free surface -- both "non-standard" procedures -- results in unexpected difficulties. The latter procedure yields a simplification of the computational algorithm, the clarity of which allows it to be extended to group-velocity evaluations. The AJP, direct-integration formulation is optimized and compared with the fastest -- Knopoff's method -- of the techniques based on the flat, homogeneous-layer approximation. The optimized form of the AJP method (spherical) is three times slower than Knopoff's (flat, non-gravitating) method when gravity is included in the AJP formulation; and is 1.36 times slower when gravity is not included. Additional programming would reduce the former estimate to a lower bound of 2.42 times slower, and the latter, to a lower bound of 1.30. In size and number, the treatment of integration "steps" in the direct-integration procedure, is equivalent to the treatment of "layers" in the homogeneous-layer approximation; thus the usual assumption that the former method does a better job of treating continuous parameter-depth distributions, appears to be invalid. Overflow problems in the AJP formulation can be controlled by

simple normalization. Loss-of-precision problems appear to be intrinsic to the AJP formulation. At a fixed period, this results in the attainable accuracy of the phase velocity decreasing as mode number increases; and, for fixed accuracy in the phase velocity, as period decreases the maximum mode number that can be treated successfully decreases.

## 1. INTRODUCTION

Dorman, Ewing and Oliver (1960) described the use of an electronic computer to calculate surface-wave dispersion for multilayered, perfectly-elastic half-spaces. Their computations were based on the technique devised by Thomson (1950) and Haskell (1953). Press, Harkrider and Seafeldt (1961) also used the Thomson-Haskell technique, and with a more advanced computer, greatly improved the speed of computation. Randall (1967) later applied Knopoff's (1964) method to this problem and reported a further improvement in speed for the Rayleigh-wave case.

In a later series of papers, Schwab (1970) and Schwab and Knopoff (1970, 1971, 1972, 1973) improved the optimization, for computer application, of both the Thomson-Haskell and Knopoff's methods for flat, multilayered media. These papers also provide complete details for obtaining full control over the accuracy of the computations, and for generalizing the algorithms to include computation of attenuation due to the intrinsic anelasticity of the earth.

For Love waves, the use of spherical-to-flat structure transformations (Biswas and Knopoff, 1970; Schwab and Knopoff, 1971; 1972; 1973; Kausel and Schwab, 1973) makes it possible to carry out all spherical dispersion, attenuation, and focal-response problems using the optimized algorithms for flat structures. Several attempts have been made to develop the same type of transformation for Rayleigh-wave computations (Alterman, Jarosch and Pekeris, 1961; Bolt and Dorman, 1961; Biswas, 1972; Schwab and

and Knopoff, 1972), but these have all yielded only empirical results which lack general applicability. Thus, at the present time at least, it appears that one cannot apply transformation theory to Rayleigh-wave dispersion computations on any arbitrary, spherical, gravitating earth. Bhattacharya's (1976) recent results -- although we will not pursue this approach in the present paper -- suggest the feasibility of an interesting new procedure for treating spherical, gravitating structures: Gravitation alone might be handled by transformation techniques, while Bhattacharya's approach could be used to optimize the treatment of sphericity.

The primary purposes of the present paper are: (1) to report on our study of the optimization of the direct computations (see Wiggins (1976) for a discussion of computations based on the variational technique), (2) to report the results of our study concerning accuracy considerations, and (3) to determine the efficiency of these direct computations relative to the analogous computations for non-gravitating structures. Also, a new computational technique is developed, for the calculation of group velocities, which does not depend on the numerical evaluation of "energy integrals." Our second purpose is to present -- we believe for the first time -- an explicit, quantitative comparison of the relative efficiencies of the two basic techniques for performing surface-wave dispersion computations: that in which an exact structural specification is employed with approximate mathematical methods, and that in which exact analytical techniques are applied to an approximate model of the structure, i.e., where the structure is replaced by a sequence of homogeneous layers.

## 2. ALTERMAN-JAROSCH-PEKERIS (AJP) FORMULATION

The basic formulation for our problem (Pekeris and Jarosch, 1958) involves the solution of three second-order, ordinary differential equations constrained by a set of boundary conditions. For purposes of numerical solution it is advisable to reduce this system to six, linear, first-order differential equations, as was done by Alterman, Jarosch and Pekeris (1959). Bolt and Dorman (1961) applied this formulation, to the evaluation of Rayleigh-wave dispersion, and reported on those numerical details which it was economically feasible to investigate with second-generation computing equipment. Detailed algorithmic testing of accuracy, precision, and efficiency characteristics really requires the present, third-generation machinery, which we have employed in the current study; the work we report here can be considered as the logical extension of the above series of papers.

To sketch the AJP formulation, if we let  $\bar{y}_i = dy_i/dr$ , where  $r$  is the distance from the center of the earth, then the sixth-order system is

$$\begin{bmatrix} \bar{y}_1 \\ \bar{y}_2 \\ \bar{y}_3 \\ \bar{y}_4 \\ \bar{y}_5 \\ \bar{y}_6 \end{bmatrix} = \begin{bmatrix} a_{11} & a_{12} & a_{13} & 0 & 0 & 0 \\ a_{21} & a_{22} & a_{23} & a_{24} & 0 & a_{26} \\ -a_{33} & 0 & a_{33} & a_{34} & 0 & 0 \\ a_{41} & a_{42} & a_{43} & a_{44} & a_{45} & 0 \\ a_{51} & 0 & 0 & 0 & 0 & 1 \\ 0 & 0 & a_{63} & 0 & a_{65} & a_{66} \end{bmatrix} \begin{bmatrix} y_1 \\ y_2 \\ y_3 \\ y_4 \\ y_5 \\ y_6 \end{bmatrix} \quad (2.01)$$

with  $\underline{y}_1$  and  $\underline{y}_3$  related to the components of displace-

ment  $u_r(r, \theta, \phi)$ ,  $u_\theta(r, \theta, \phi)$ , and  $u_\phi(r, \theta, \phi)$  by

$$\begin{aligned} u_r &= y_1(r) \chi_\ell^m(\theta) e^{im\phi} e^{i\omega t} \\ u_\theta &= y_3(r) \frac{d}{d\theta} \chi_\ell^m(\theta) e^{im\phi} e^{i\omega t} \\ u_\phi &= \frac{im}{\sin\theta} y_3(r) \chi_\ell^m(\theta) e^{im\phi} e^{i\omega t} . \end{aligned} \quad (2.02)$$

For propagating surface waves diverging from the epicenter,

$$\chi_\ell^m = \frac{1}{2} (P_\ell^m + i \frac{2}{\pi} Q_\ell^m), \quad (2.03)$$

for waves converging toward the epicenter,

$$\chi_\ell^m = \frac{1}{2} (P_\ell^m - i \frac{2}{\pi} Q_\ell^m). \quad (2.04)$$

For a treatment of the situations which require the use of (2.03), (2.04), or their sum, see Schwab and Kausel (1976). In this same reference, the justification is given for our major departure from previously reported computations of Rayleigh wave dispersion on a sphere. Strictly speaking, Rayleigh waves only exist on a sphere at the discrete set of frequencies corresponding to integral values of the polar order number  $\underline{\ell}$ . However, fixing  $\underline{\ell}$  and evaluating the corresponding angular frequency  $\underline{\omega}$  does not yield the dispersion data at equal frequency intervals, which we desire to use in the usual numerical technique for obtaining time series by inverse Fourier transformation. Schwab and Kausel (1976) have shown that, for most practical applications of propagating surface waves, non-integral  $\underline{\ell}$  at equally-spaced frequencies

can be used without introducing significant errors; therefore, we adopt the procedure of fixing  $\underline{\omega}$  and computing  $\underline{\ell}$ , or

$$\bar{c} = a\omega/(\ell+1/2), \quad (2.05)$$

where  $\underline{a}$  is the radius of the earth. The relation between  $\bar{c}$  and the true spherical phase velocity is also treated by Schwab and Kausel (1976). In equation (2.01),  $\underline{y}_2$  and  $\underline{y}_4$  are, respectively, the radial dependences of the  $\underline{r}_r$ , and the  $\underline{r}_\theta$  and  $\underline{r}_\phi$  components of stress;  $\underline{y}_5$  and  $\underline{y}_6$  arise from the presence of the gravitational field.

Since, in any numerical integration procedure, it is important to initiate the integration with accurate values, we have chosen to proceed from the free surface downward. This allows us to specify the initial vector exactly. The integration is then carried down to a depth sufficient to make it immaterial--to  $\underline{n}$  significant figures in  $\underline{\ell}$  or  $\bar{c}$ --just how we terminate the integration: with an approximation of a free surface or rigid surface, for example. The fact that such a termination process is valid has been checked by extensive numerical tests in the course of this work. These tests follow the lines of the layer-reduction experiments described by Schwab and Knopoff (1970; 1972), and will be described in some detail below. In Section 7 we discuss the termination of the structure at depth by either a solid or liquid, homogeneous, gravitating sphere.

Here, we should point out that the warning given by Takeuchi and Saito (page 241, 1972) against proceeding downward from the free surface when integrating the system of differential equations, or when forming the layer-matrix product if applying the Thomson-Haskell technique or Knopoff's method, does not appear to be justified by our experience. In the work upon which we report herein, downward integration did not give rise to any unexpected difficulties; in previous, extensive work with matrix methods applied to Rayleigh-wave dispersion computations (Schwab, 1970; Schwab and Knopoff, 1970; 1972), the formation of matrix products upward toward the free surface (Thomson-Haskell formulation) was not found to have any advantage over formation of the product in the downward direction (Knopoff's formulation).

Continental structure. In this case,  $y_2$  and  $y_4$  vanish, and  $y_6 = -y_5(l+1)/a$  at  $r=a$ . Thus we can write the starting vector as

$$\begin{aligned}
 Y_S(a) = \begin{bmatrix} y_1(a) \\ y_2(a) \\ y_3(a) \\ y_4(a) \\ y_5(a) \\ y_6(a) \end{bmatrix} &= \begin{bmatrix} y_1(a) \\ 0 \\ y_3(a) \\ 0 \\ y_5(a) \\ -y_5(a)(\ell+1)/a \end{bmatrix} = y_1(a) \begin{bmatrix} 1 \\ 0 \\ 0 \\ 0 \\ 0 \\ 0 \end{bmatrix} + y_3(a) \begin{bmatrix} 0 \\ 0 \\ 1 \\ 0 \\ 0 \\ 0 \end{bmatrix} + y_5(a) \begin{bmatrix} 0 \\ 0 \\ 0 \\ 0 \\ 1 \\ -(\ell+1)/a \end{bmatrix} \quad (2.06)
 \end{aligned}$$

or

$$Y_S(a) = y_1(a)X_1(a) + y_3(a)X_2(a) + y_5(a)X_3(a), \quad (2.07)$$

and for  $r < a$

$$Y_S(r) = y_1(a)X_1(r) + y_3(a)X_2(r) + y_5(a)X_3(r) \quad (2.08)$$

The three quantities which are unknown --  $y_1(a)$ ,  $y_3(a)$ , and  $y_5(a)$  -- can be carried implicitly in the computations, while we integrate the vectors whose starting values are known exactly:  $X_1$ ,  $X_2$ , and  $X_3$ . That is, we integrate to obtain  $X_1$  at depth; this is repeated, in turn, with  $X_2$  and  $X_3$ . Thus we actually use equation(2.01) in the form

$\underline{X}_i = A \underline{X}_i$  to integrate from the surface  $\underline{r} = \underline{a}$  to the depth at which the boundary conditions are to be applied:  $\underline{r} = \underline{r}_0$ , where we can again express  $\underline{Y}_S$  in terms of the undetermined coefficients by using equation (2.08).

If we define a rigid boundary at depth by

$$y_1(r_0) = y_3(r_0) = y_5(r_0) = 0, \quad (2.09)$$

we then obtain three linear, homogeneous equations in three unknowns--the undetermined coefficients--and the determinant of the coefficient matrix must vanish if we are to have a non-trivial solution. Thus the dispersion function,  $\underline{F}_A$ , takes the form

$$F_A(\bar{c}, \omega) = \begin{vmatrix} [X_1(r_0)]_1 & [X_2(r_0)]_1 & [X_3(r_0)]_1 \\ [X_1(r_0)]_3 & [X_2(r_0)]_3 & [X_3(r_0)]_3 \\ [X_1(r_0)]_5 & [X_2(r_0)]_5 & [X_3(r_0)]_5 \end{vmatrix}, \quad (2.10)$$

zeros of which define valid  $(\bar{c}, \omega)$  dispersion pairs. For the two approximations to free boundaries at depth, we have used the definitions

$$y_2(r_0) = y_4(r_0) = 0 \quad (2.11)$$

and either

$$y_6(r_0) = -y_5(r_0)(\ell+1)/r_0 \quad (2.12)$$

or

$$y_6(r_0) = -y_5(r_0)(\ell+1)/a, \quad (2.13)$$

which yield, respectively, dispersion functions

$$F_B(\bar{c}, \omega) = \begin{vmatrix} [X_1(r_0)]_2 & [X_2(r_0)]_2 & [X_3(r_0)]_2 \\ [X_1(r_0)]_4 & [X_2(r_0)]_4 & [X_3(r_0)]_4 \\ [X_1(r_0)]_6 + \frac{\ell+1}{r_0} [X_1(r_0)]_5 & [X_2(r_0)]_6 + \frac{\ell+1}{r_0} [X_2(r_0)]_5 & [X_3(r_0)]_6 + \frac{\ell+1}{r_0} [X_3(r_0)]_5 \end{vmatrix} \quad (2.14)$$

and

$$F_C(\bar{c}, \omega) = \begin{vmatrix} [X_1(r_0)]_2 & [X_2(r_0)]_2 & [X_3(r_0)]_2 \\ [X_1(r_0)]_4 & [X_2(r_0)]_4 & [X_3(r_0)]_4 \\ [X_1(r_0)]_6 + \frac{\ell+1}{a} [X_1(r_0)]_5 & [X_2(r_0)]_6 + \frac{\ell+1}{a} [X_2(r_0)]_5 & [X_3(r_0)]_6 + \frac{\ell+1}{a} [X_3(r_0)]_5 \end{vmatrix} \quad (2.15)$$

Oceanic Structure. In this case, the analog of equation (2.01) is, for the homogeneous oceanic (liquid) layer,

$$\begin{bmatrix} \bar{y}_1 \\ \bar{y}_2 \\ \bar{y}_5 \\ \bar{y}_6 \end{bmatrix} = \begin{bmatrix} b_{11} & b_{12} & b_{15} & 0 \\ b_{21} & b_{22} & b_{25} & -\rho \\ 4\pi G\rho & 0 & 0 & 1 \\ b_{61} & b_{62} & b_{65} & b_{66} \end{bmatrix} \begin{bmatrix} y_1 \\ y_2 \\ y_5 \\ y_6 \end{bmatrix} \quad (2.16)$$

At  $\underline{r} = \underline{a}$ ,  $\underline{y}_2$  vanishes and  $\underline{y}_6 = -y_5(\ell+1)/a$ , and we can write the starting vector as

$$Y_L(a) = \begin{bmatrix} y_1(a) \\ y_2(a) \\ y_5(a) \\ y_6(a) \end{bmatrix} = \begin{bmatrix} y_1(a) \\ 0 \\ y_5(a) \\ -y_5(a)(\ell+1)/a \end{bmatrix} = y_1(a) \begin{bmatrix} 1 \\ 0 \\ 0 \\ 0 \end{bmatrix} + y_5(a) \begin{bmatrix} 0 \\ 0 \\ 1 \\ -(\ell+1)/a \end{bmatrix} \quad (2.17)$$

or

$$Y_L(a) = y_1(a) Z_1(a) + y_5(a) Z_2(a), \quad (2.18)$$

and for  $r < a$

$$Y_L(r) = y_1(a) Z_1(r) + y_5(a) Z_2(r). \quad (2.19)$$

Again, we carry the unknown quantities --  $y_1(a)$  and  $y_5(a)$  -- implicitly, and integrate the vectors whose starting values we know exactly:  $Z_1$  and  $Z_2$ , using equation (2.16) in the form  $\bar{Z}_i = B Z_i$ .

On the oceanic side of the liquid-solid boundary at the bottom of the ocean,  $r = r_1$ , we then have

$$Y_L(r_1) = y_1(a) \begin{bmatrix} [Z_1(r_1)]_1 \\ [Z_1(r_1)]_2 \\ [Z_1(r_1)]_5 \\ [Z_1(r_1)]_6 \end{bmatrix} + y_5(a) \begin{bmatrix} [Z_2(r_1)]_1 \\ [Z_2(r_1)]_2 \\ [Z_2(r_1)]_5 \\ [Z_2(r_1)]_6 \end{bmatrix} \quad (2.20)$$

At this boundary,  $y_1$ ,  $y_2$ ,  $y_5$ , and  $y_6$  are continuous,  $y_4$  must vanish, and  $y_3$  is undetermined. Thus on the solid side of this interface, we have

$$y_S(r_1) = y_1(a) \begin{bmatrix} |z_1(r_1)|_1 \\ |z_1(r_1)|_2 \\ 0 \\ 0 \\ |z_1(r_1)|_5 \\ |z_1(r_1)|_6 \end{bmatrix} + y_3(r_1) \begin{bmatrix} 0 \\ 0 \\ 1 \\ 0 \\ 0 \\ 0 \end{bmatrix} + y_5(a) \begin{bmatrix} |z_2(r_1)|_1 \\ |z_2(r_1)|_2 \\ 0 \\ 0 \\ |z_2(r_1)|_5 \\ |z_2(r_1)|_6 \end{bmatrix} \quad (2.21)$$

or

$$y_S(r_1) = y_1(a)X_1(r_1) + y_3(r_1)X_2(r_1) + y_5(a)X_3(r_1), \quad (2.22)$$

and the integration proceeds and terminates, from  $r_1$  to  $r_0$ , exactly as in the continental case.

**Best  
Available  
Copy**

### 3. ALGORITHM FOR GROUP VELOCITY DETERMINATION

When treating Rayleigh waves on a spherical, gravitating earth, the variational technique is usually employed to compute group velocities (Takeuchi and Saito, 1972, Section III). This involves the evaluation, by numerical approximation, of integrals having the form

$$\int_0^a f(r) y_i(r) y_j(r) dr . \quad (3.01)$$

Since the functions  $y_k(r)$  become highly oscillatory for large (radial) mode numbers, this numerical evaluation can become inaccurate (Knopoff et al., 1974, Appendix). Further,  $|y_k(r)|$  become spuriously large at depths much below those at which there is significant energy in the mode, at the period being treated. Although, somewhat surprisingly, these spurious magnitudes do not seem to affect the location of a root of the dispersion function, they can cause large errors in the evaluation of integrals such as (3.01). Thus one must specify  $r_2$ , the value of  $r$  below which the spurious magnitudes occur, prior to seeking the group velocity, and then evaluate

$$\int_{r_2}^a f(r) y_i(r) y_j(r) dr \quad (3.02)$$

in place of (3.01). However, without prior knowledge of the group velocity,  $r_2$  can be quite difficult to determine in period ranges such as those in which the energy shifts back and forth repeatedly between the crustal wave guide and the low-velocity channel in the upper mantle (Panza, Schwab and Knopoff, 1972; Frantsuzova, Levshin and Shkadinskaya, 1972; Schwab and Knopoff, 1971; 1972). Since the integrals must eventually be evaluated to obtain excitation

functions for earthquake sources, and since group velocity can be used to specify whether the energy is in the crust or low-velocity channel, it is desirable to develop an algorithm for obtaining these velocities, which is not dependent upon prior knowledge of  $r_2$ .

Since we have a dispersion function,  $F(\bar{c}, \omega)$ , which vanishes when the point  $(\bar{c}, \omega)$  falls on a dispersion curve, we can use implicit-function theory to define the group velocity  $\bar{u}$ :

$$\bar{u} = \bar{c} / (1 - \frac{\omega}{\bar{c}} \frac{d\bar{c}}{d\omega}) \quad (3.03)$$

with

$$\frac{d\bar{c}}{d\omega} = - \frac{\left(\frac{\partial}{\partial \omega}\right)_{\bar{c}} F}{\left(\frac{\partial}{\partial \bar{c}}\right)_{\omega} F}, \quad (3.04)$$

where the partial derivatives are evaluated at a point on a dispersion curve. If we agree to use the rigid boundary at depth, then

$$F' = \left(\frac{\partial F}{\partial \omega}\right)_{\bar{c}} = \begin{vmatrix} [X_1'(r_0)]_1 & [X_2'(r_0)]_1 & [X_3'(r_0)]_1 \\ [X_1(r_0)]_3 & [X_2(r_0)]_3 & [X_3(r_0)]_3 \\ [X_1(r_0)]_5 & [X_2(r_0)]_5 & [X_3(r_0)]_5 \end{vmatrix} + \begin{vmatrix} [X_1(r_0)]_1 & [X_2(r_0)]_1 & [X_3(r_0)]_1 \\ [X_1'(r_0)]_3 & [X_2'(r_0)]_3 & [X_3'(r_0)]_3 \\ [X_1(r_0)]_5 & [X_2(r_0)]_5 & [X_3(r_0)]_5 \end{vmatrix} \\ + \begin{vmatrix} [X_1(r_0)]_1 & [X_2(r_0)]_1 & [X_3(r_0)]_1 \\ [X_1(r_0)]_3 & [X_2(r_0)]_3 & [X_3(r_0)]_3 \\ [X_1'(r_0)]_5 & [X_2'(r_0)]_5 & [X_3'(r_0)]_5 \end{vmatrix} \quad (3.05)$$

and

$$\dot{\bar{F}} = \left( \frac{\partial F}{\partial \bar{c}} \right)_{\omega} \quad (3.06)$$

is given by the same type of expression as (3.05), with dots replacing the primes. The elements  $\underline{|X_i(r_0)|}_j$  in (3.05) and (3.06) are obtained exactly as described in Section 2. The evaluation of  $\underline{|X'_i(r_0)|}_j$  and  $\underline{|\dot{X}_i(r_0)|}_j$  requires a simple extension of the algorithm.

Continental Structure. In this case we start with the sixth-order system

$$\bar{Y} = AY, \quad (3.07)$$

and form

$$\bar{Y}' = A'Y + AY' \quad (3.08)$$

$$\bar{\dot{Y}} = \dot{A}Y + A\dot{Y}. \quad (3.09)$$

Here again, we use these equations of motion in terms of the vectors,  $\underline{X_i}$ ,  $\underline{X'_i}$ ,  $\underline{\dot{X}_i}$ , that we know exactly at the surface:

$$\bar{X'}_i = A' X_i + AX'_i \quad (3.10)$$

$$\bar{\dot{X}}_i = \dot{A} X_i + A\dot{X}_i \quad (3.11)$$

Since  $\underline{X_i}$  can be determined independently, we can treat  $\underline{A'X_i}$  and  $\underline{\dot{A} X_i}$  as known vectors at each depth, and we have

$$\overline{X}_i' = AX_i' + C_i \quad (3.12)$$

$$\overline{X}_i = A\dot{X}_i + D_i, \quad (3.13)$$

where

$$C_i(r) = A'(r)X_i(r) = -2\rho(r)\omega \quad (3.14)$$

$$\begin{bmatrix} 0 \\ [X_i(r)]_1 \\ 0 \\ [X_i(r)]_3 \\ 0 \\ 0 \end{bmatrix}$$

$$D_i(r) = \dot{A}(r)X_i(r) = -\frac{a\omega}{c^2 r} (2\ell+1)$$

$$\begin{bmatrix} [\lambda/(\lambda+2\mu)] [X_i(r)]_3 \\ [\rho g - 2\mu(3\lambda+2\mu)/(\lambda+2\mu)r] [X_i(r)]_3 + [X_i(r)]_4 \\ 0 \\ [4\mu(\lambda+\mu)/(\lambda+2\mu)r] [X_i(r)]_3 \\ 0 \\ [-4\pi G\rho] [X_i(r)]_3 + [1/r] [X_i(r)]_5 \end{bmatrix} \quad (3.15)$$

Oceanic structure. Here we begin with the fourth-order system (2.16), and form

$$\begin{bmatrix} \overline{y_1} \\ \overline{y_2} \\ \overline{y_5} \\ \overline{y_6} \end{bmatrix} = B' \begin{bmatrix} y_1 \\ y_2 \\ y_5 \\ y_6 \end{bmatrix} + B \begin{bmatrix} y'_1 \\ y'_2 \\ y'_5 \\ y'_6 \end{bmatrix} \quad (3.16)$$

$$\begin{bmatrix} \dot{\overline{y_1}} \\ \dot{\overline{y_2}} \\ \dot{\overline{y_5}} \\ \dot{\overline{y_6}} \end{bmatrix} = \dot{B} \begin{bmatrix} y_1 \\ y_2 \\ y_5 \\ y_6 \end{bmatrix} + B \begin{bmatrix} \dot{y_1} \\ \dot{y_2} \\ \dot{y_5} \\ \dot{y_6} \end{bmatrix} \quad (3.17)$$

These equations are then used with the vectors for which we have solutions at the surface,  $\underline{Z_i}$ :

$$\overline{Z'_i} = B' Z_i + B Z'_i \quad (3.18)$$

$$\dot{\overline{Z}}_i = \dot{B} Z_i + B \dot{Z}_i, \quad (3.19)$$

which can be written in terms of known vectors,  $\underline{B'Z_i}$  and  $\underline{\dot{B}Z_i}$ , at each depth:

$$\underline{Z'_i} = \underline{BZ'_i} + \underline{E_i} \quad (3.20)$$

$$\underline{\dot{Z}_i} = \underline{B\dot{Z}_i} + \underline{G_i}, \quad (3.21)$$

where

$$\underline{E_i}(r) = \underline{B'(r)Z_i}(r) = [2\ell(\ell+1)/r^2\omega^3] \begin{bmatrix} -H_i(r) \\ I_i(r) \\ 0 \\ [4\pi G\rho(r)] H_i(r) \end{bmatrix} \quad (3.22)$$

$$\underline{G_i}(r) = \underline{\dot{B}(r)Z_i}(r) = [-a(2\ell+1)/\bar{c}^2 r^2 \omega] \begin{bmatrix} H_i(r) \\ [g(r)\rho(r)]H_i(r) \\ 0 \\ J_i(r) \end{bmatrix} \quad (3.23)$$

and

$$H_i(r) = g(r)[Z_i(r)]_1 - [1/\rho(r)][Z_i(r)]_2 - [Z_i(r)]_5 \quad (3.24)$$

$$I_i(r) = -\rho(r) [\omega^4 r^2 / \ell(\ell+1) + g^2(r)] [Z_i(r)]_1 + g(r) \{ [Z_i(r)]_2 + \rho(r) [Z_i(r)]_5 \} \quad (3.25)$$

$$J_i(r) = 4\pi G \{ -\rho(r)g(r) [Z_i(r)]_1 + [Z_i(r)]_2 + [\rho(r) + \omega^2 / 4\pi G] [Z_i(r)]_5 \} \quad (3.26)$$

Application of (3.20) and (3.21) will allow us to carry the integration to the bottom of the oceanic layer at  $r=r_1$ , where we can apply the boundary conditions of continuity of  $y_1, y'_1, \dot{y}_1, y_2, y'_2, \dot{y}_2, y_5, y'_5, \dot{y}_5, y_6, y'_6, \dot{y}_6$ , and the vanishing of  $y_4, y'_4, \dot{y}_4$ , to obtain the necessary starting values to apply in (3.12) and (3.13):

$$X'_1(r_1) = \begin{bmatrix} [Z'_1(r_1)]_1 \\ [Z'_1(r_1)]_2 \\ 0 \\ 0 \\ [Z'_1(r_1)]_5 \\ [Z'_1(r_1)]_6 \end{bmatrix}, X'_2(r_1)=0, X'_3(r_1) = \begin{bmatrix} [Z'_2(r)]_1 \\ [Z'_2(r)]_2 \\ 0 \\ 0 \\ [Z'_2(r)]_5 \\ [Z'_2(r)]_6 \end{bmatrix} \quad (3.27)$$

and a like set of starting values with primes replaced by dots.

Although precise computation-time estimates are given in Section 5, a few general observations will be appropriate here. At any given frequency, the phase velocity is evaluated by repeated determination of the dispersion function until a root is bracketed; this root is then refined until the desired accuracy in  $\bar{c}$  is obtained. Each determination of  $\underline{F}$  involves the integration of the three vectors  $\underline{X}_i$ . If we assume that  $\underline{X}_i(r)$  have been saved from the last set of integrations to obtain a value of  $\bar{c}$ , then to obtain the group velocity at this same frequency requires the integration of six

vectors, i.e. approximately twice the amount of time it takes to compute a single value of the dispersion function while iterating for  $\bar{c}$ . The number of iterations required in the computation of  $\bar{c}$  is variable, but for the present purpose, ten iterations may be taken as a representative value. Thus 30 integrations would be required to obtain  $\bar{c}$ , and only 6 to obtain  $\bar{u}$ . To the accuracy of this estimate then,  $\bar{u}$  can be obtained in only 20 percent of the time the evaluation of  $\bar{c}$  requires.

4. NUMERICAL TECHNIQUE FOR INTEGRATING THE SYSTEM OF DIFFERENTIAL EQUATIONS

To optimize the computations, it is useful to constrain the structural specification somewhat. For this purpose:

1. The liquid, oceanic layer is limited to a single, homogeneous layer. A special fourth-order Runge-Kutta technique (see below) is used for the first three steps of the integration-- step size of about 1 km-- and a fourth-order predictor-corrector method (see below) is employed, if necessary, to continue the integration to the bottom of the oceanic layer with the same step size.
2. The sedimentary layers are limited to a sequence of homogeneous layers, each of which does not exceed 1 km in thickness. These layers are treated with one fourth-order Runge-Kutta step.
3. The subsedimentary crustal layers must also be homogeneous, and each is treated as the oceanic layer; the step size fixed at about 1 km.
4. The sub-Moho mantle requires continuous velocity-depth and density-depth distributions, although discontinuities

can be approximated as closely as desired by specifying large gradients. As with the oceanic layer, three Runge-Kutta steps are followed by a fourth-order predictor-corrector method. The initial step size is 1.5625 km, with which we execute three Runge-Kutta, and seven predictor-corrector steps. The step size is then doubled and five predictor-corrector steps are performed; this procedure is repeated until the step size reaches 12.5 km, and the predictor-corrector method is then applied with this fixed step size. The results of our numerical testing have shown that this dependence of step size on depth is sufficient to yield 4-significant-figure accuracy in the computed values of  $\bar{c}$ . Concerning this point, one should review the treatment given by Schwab and Knopoff (1972), in which piecewise-continuous velocity- and density-depth distributions are treated with the homogeneous-layer approximation. Comparison will show that the thickness of the layers as a function of depth, in that approximation, is roughly the same as the integration step size in the present analysis. That is, to the degree of accuracy which two such dissimilar methods can be compared, if the step sizes above are used as layer thicknesses in the homogeneous layer approximation, that technique will yield 4 significant figures in the computed values of  $\bar{c}$ .

Runge-Kutta technique. To start the predictor-corrector method we have used a Runge-Kutta technique designed specifically for this purpose. Here one is only interested in being able to minimize the bounds on the truncation error. Ralston (1962) has treated this problem, and gives the following algorithm for obtaining the first four points for starting a predictor-corrector method.

In terms of a single, first-order differential equation:

$$\bar{y} = f(r, y), \quad y(r_0) = y_0, \quad (4.1)$$

at  $r_1, r_2, \dots$ , the Runge-Kutta method is given by

$$y_{n+1} - y_n = \sum_{i=1}^4 w_i K_i. \quad (4.2)$$

Here,  $y_n = y(r_n)$ , the  $w_i$  are constants, and

$$K_i = h_n f(r_n + \alpha_i h_n, y_n + \sum_{j=1}^{i-1} \beta_{ij} K_j) \quad (4.3)$$

with  $h_n = r_{n+1} - r_n$ , and

$$\alpha_1 = 0$$

$$\alpha_2 = 2/5$$

$$\alpha_3 = (14 - 3\sqrt{5})/16$$

$$\alpha_4 = 1$$

(4.4)

$$\begin{aligned}
\beta_{21} &= \alpha_2 \\
\beta_{31} &= \alpha_3 - \beta_{32} \\
\beta_{32} &= [\alpha_3(\alpha_3 - \alpha_2)] / [2\alpha_2(1 - 2\alpha_2)] \\
\beta_{41} &= \alpha_4 - \beta_{42} - \beta_{43} \\
\beta_{42} &= \frac{(1 - \alpha_2)[\alpha_2 + \alpha_3 - 1 - (2\alpha_3 - 1)^2]}{2\alpha_2(\alpha_3 - \alpha_2)[6\alpha_2\alpha_3 - 4(\alpha_2 + \alpha_3) + 3]} \\
&\quad (1 - 2\alpha_2)(1 - \alpha_2)(1 - \alpha_3) \\
\beta_{43} &= \frac{(1 - 2\alpha_2)(1 - \alpha_2)(1 - \alpha_3)}{\alpha_3(\alpha_3 - \alpha_2)[6\alpha_2\alpha_3 - 4(\alpha_2 + \alpha_3) + 3]}
\end{aligned} \tag{4.5}$$

$$\begin{aligned}
w_1 &= \frac{1}{2} + [1 - 2(\alpha_2 + \alpha_3)] / [12\alpha_2\alpha_3] \\
w_2 &= (2\alpha_3 - 1) / [12\alpha_2(\alpha_3 - \alpha_2)(1 - \alpha_2)] \\
w_3 &= (1 - 2\alpha_2) / [12\alpha_3(\alpha_3 - \alpha_2)(1 - \alpha_3)] \\
w_4 &= \frac{1}{2} + [2(\alpha_2 + \alpha_3) - 3] / [12(1 - \alpha_2)(1 - \alpha_3)]
\end{aligned} \tag{4.6}$$

Predictor-corrector method. The fourth-order method we have used (Hamming, 1959) is fully described, along with the details concerning doubling of step size, by Ralston (1960). Highly practical details concerning the combination of the Runge-Kutta and predictor-corrector routines, which we have employed, will be found in Anon. (1970). One should be warned, however, that the use of the subroutines therein described is highly inadvisable for our present purposes. The use of these general purpose subroutines can increase computation expense by a factor of 10 to 100 over that of the optimized algorithm.

## 5. OPTIMIZATION OF THE ALTERMAN-JAROSCH-PEKERIS FORMULATION

The key to optimizing the integration is to apply our knowledge about this specific problem to specify all the depths,  $r_k$ , at which  $a_{ij}(r)$  are to be evaluated. The evaluation of these elements can then be removed from the innermost, integration loops of the program. The details concerning these depths are contained in the preceding section. In Figure 1, the optimized scheme for the evaluation of  $a_{ij}(r_k)$ -- for the solid sedimentary layers, subsedimentary crustal layers, and mantle--is indicated in outline form. This figure shows that most of the procedure for evaluating  $a_{ij}(r_k)$  can even be removed from within the  $\omega$  and  $\bar{c}$  loops: within the  $\bar{c}$  loop, each new  $\bar{c}$  value requires only  $6N+1$  assignments,  $6N+1$  multiplications, and  $N+1$  additions; within the  $\omega$  loop, each new  $\omega$  value requires only  $3N+1$  assignments,  $N+1$  additions, and  $2N$  subtractions, where  $N$  is the number of depths at which  $a_{ij}(r_k)$  must be evaluated. All other portions of the element determinations are performed external to these loops. In Figure 2 the same information is given for the elements,  $b_{ij}(r)$  of the matrix describing the integration through the liquid, oceanic layer. Again, all elements can be evaluated external to the integration routine.

In the integration procedures themselves, it is very important to form matrix products, such as those in (2.01) and (2.16), in an explicit manner. This permits full use to be made of the many zero elements, and those that are independent of  $r$ , or are equal to another matrix element. For example, the basic

AJP matrix multiplication for solid layers is illustrated in Figure 3.

In reports on our earlier work with Love-wave dispersion and dispersion-attenuation computations, for both flat and spherical structures, it was possible to give the short, key, FORTRAN program segments (Figure 2, Schwab and Knopoff, 1972; Figures 4 and 5, Schwab and Knopoff, 1973). These together with descriptions of the root-bracketing and root-refining procedures, completely specify the optimization when the multi-,homogeneous-layer approximation is employed. When this approximation is used with Rayleigh waves on flat structures, the optimization can be specified in the same manner (Figures 11, 12 and 13, Schwab and Knopoff, 1972). When employing the method of direct integration of the equations of motion, it is not possible to exhibit the complete program optimization in this compact, simple manner for Rayleigh-wave dispersion on a spherical, radially heterogeneous, gravitating earth. However, it is possible to present the most important part of the algorithm as a relatively compact program segment. This is given in Figure 4a, which illustrates the predictor-corrector method we have applied to the integration from below the Moho to the selected value of  $r_0$ ; the automatic doubling of integration step size is included in the segment. Most of the computation time is spent in this program segment, which is entered with:

```
COEFF1 = (4/3) H
COEFF2 = 3H
COEFF6 = (121/36) H
H = -25/16;
```

the indices for the successive integration step-size regions are given in Table 1; for the details concerning  $B(I,J)$ , see the description of subroutine DHPCL (Anon., 1970). In this type of programming there are important, machine-dependent considerations:

the manner in which the 6x6 matrix elements are stored in memory, and the manner in which indices are handled in the program segment given in Figure 4a. In fact, the indices ITP1, ITP3, ITP8, ITP9, ITP10 which are used for compactness in Figure 4, actually slow computation speed on the IBM 360/91; these subscripts are best used in explicit form IT+1, IT+3, IT+8, IT+9, IT+10. The key program segment is given in the form shown in Figure 4a for two reasons: (1) to illustrate the logic as clearly and simply as possible, and (2) to provide an illustrative example of the importance of handling subscripting and storage in the manner most appropriate for a given machine. The time required to execute DO-loop 170 once, specifies the necessary time to execute one integration step for each of the three vectors  $\underline{X}_i$ ; thus, to perform one integration step in forming the dispersion function, DO-loop 170 must be executed three times. The time for one integration step in forming  $\underline{F}$  is termed the characteristic time  $\underline{\tau}$ , which we use to illustrate the importance of correct subscripting and storage. The characteristic time for the segment in Figure 4a is 489  $\mu$ sec/step/iteration. By simply reversing the order of the subscripts of B(I,J), this time is improved by 92  $\mu$ sec/step/iteration; if ITP1, etc. are used explicitly as IT+1, etc.,  $\underline{\tau}$  is decreased still further by an amount of 67  $\mu$ sec/step/iteration; and if  $\underline{a}_{ij}$  are stored more efficiently, still another 44  $\mu$ sec/step/iteration can be saved, bringing  $\underline{\tau}$  down to 286  $\mu$ sec/step/iteration. DO-loop 170, in a form incorporating the above improvements, is shown in Figure 4b.

It should be understood that 286  $\mu\text{sec}/\text{step}/\text{iteration}$  is a lower bound; the corresponding effective characteristic time -- given in (5.02) -- must reflect time spent in other parts of the program than DO-loop 170, e.g., time spent in starting the predictor-corrector scheme with the Runge-Kutta procedure.

Our computations have been performed on IBM 360 and 370 installations: a 360/91 in Los Angeles, a 360/65 in Bari, and a 370/145 in Santiago and in Cosenza. The first installation was also used in the final optimization of the flat-structure Rayleigh-wave work (Schwab and Knopoff, 1972), which allows us to make an accurate evaluation of the relative characteristic times (Schwab and Knopoff, 1972) for computations with flat, non-gravitating structures and with spherical, gravitating models. In the former case, this time is

$$\text{FLAT } \tau_{\text{RAYLEIGH}} = 110 \mu\text{sec}/\text{layer}/\text{iteration} \quad (5.01)$$

(which corresponds to Knopoff's method applied to a sequence of homogeneous layers), and in the latter case,

$$\text{SPHERICAL } \tau_{\text{RAYLEIGH}} = 336 \mu\text{sec}/\text{step}/\text{iteration} \quad (5.02)$$

(which corresponds to the optimization of the AJP formulation herein described). Again, these characteristic times were measured on the IBM 360/91 at UCLA. As we have noted above,

an integration "step" can be considered nearly equivalent to a "layer" in computations based on the homogeneous-layer approximation. Also, to the accuracy possible in this type of comparison, the "iterations" required in the two cases (see Schwab and Knopoff (1972) for details concerning iteration procedures) can be considered equivalent. Thus, the relative efficiencies of the two types of Rayleigh-wave dispersion computation can be evaluated by simple comparison of their characteristic times, and we find that the inclusion of sphericity and gravitation triples actual computation time. Thus, the time required to integrate each of the three vectors over depth in the spherical, gravitating case, is the same as that required to carry out the analogous operation -- the formation of the matrix product -- for the flat, non-gravitating case.

To obtain a valid comparison of the direct-integration method, with the homogeneous-layer technique, clearly we should not include gravity in the former method. The removal of gravity reduces the vectors  $\underline{X}_1$ , that must be integrated, from three to two, and the number of elementary operations (multiplications and additions) in (2.01) from 34 to 23. Thus, the ratio of computation times for non-gravitating and gravitating spheres, when treated with the direct-integration method, is approximately  $(2 \times 23) / (3 \times 34)$ ; or, for the non-gravitating case,

$$\text{SPHERICAL } \tau_{\text{RAYLEIGH}} = 151 \text{ } \mu\text{sec/step/iteration.} \quad (5.03)$$

Thus the direct integration method, for a non-gravitating sphere, is only 36 percent slower than the optimized computations for a flat, non-gravitating structure, where the latter is treated with the homogeneous-layer approximation.

From this result we are led to conclude that attempts to devise Rayleigh-wave transformation techniques -- which have hitherto been concentrated on curvature corrections to permit spherical, gravitating structures to be treated with algorithms for flat, non-gravitating models -- might also be directed toward gravity corrections that would allow one to use programs for spherical, non-gravitating structures to handle the spherical, gravitating case.

A final improvement in the lower bounds of the AJP characteristic times is possible. The limiting bound for the gravitating case was obtained by including the integration of all three  $X_i$ , simultaneously, within DO-loop 170; the result was 266  $\mu\text{sec}/\text{step}/\text{iteration}$ . If the two vectors of the non-gravitating case are handled simultaneously within the loop (see Figure 4c), the lower bound of  $\underline{t}$  becomes 143  $\mu\text{sec}/\text{step}/\text{iteration}$ .

It is obviously of interest, to those involved in surface-wave computations, to have some idea of the relative speeds of such computations for the various computers currently in use at the larger installations. In Table 2 we present the results of a first effort to summarize this information for the computers that are available to us for testing. The test routine we

have employed is that given by Schwab and Knopoff (Figure 2, 1972). A 100-layer structure was used; the program segment was enclosed within a DO-loop that was executed either 100 or 1000 times; case 1 involved tests with  $\bar{c} < \beta_m$ , and case 2, tests with  $\bar{c} > \beta_m$ . Results from a more extensive set of relative computer-time tests, for both Love- and Rayleigh-wave dispersion computations are given by Porter et al. (1977).

## 6. EXISTENCE OF SOLUTIONS AS A FUNCTION OF NUMERICAL AND ALGORITHMIC PROCEDURES

On IBM 360 equipment, large-scale numerical work is routinely carried out in double precision: about 16 decimal digits. Except where indicated otherwise, this precision was used to investigate the existence criteria for solutions from our optimization of the basic AJP formulation.

Our testing procedure followed the lines of the layer-reduction experiments described by Schwab and Knopoff (1972): At each of a set of periods,  $\bar{c}$  is computed for a complete range of terminating values,  $r_0$ , for the integration. At each, fixed period, by comparing the values of  $\bar{c}$  as a function of  $r_0$ , the range of  $r_0$ , over which  $\bar{c}$  is stable to 4 significant figures is immediately evident. In terms of  $r_0$  and period, our results for an oceanic, and a continental shield structure (Figure 5) are given in Figure 6; the fundamental and first seven higher modes are treated in each case.

The results are similar to those previously obtained for Rayleigh waves when the homogeneous-layer approximation is employed (Figures 14, 15, 17, Schwab and Knopoff, 1972): At each period, a certain minimum amount of structure (maximum  $r_0$ ) must be retained to ensure 4 significant figures in  $\bar{c}$ . This maximum value of  $r_0$  is a physical limitation. For the mode and period of interest, there is significant energy content down to a depth of  $a-r_0$ , and the structure above this point thus affects all 4 figures of  $\bar{c}$ .

In the initial program testing, it is useful if one can integrate to any depth, irregardless of whether this results in loss of accuracy in the computed phase velocity, or in the expenditure of more computer time than if the integration were terminated at the minimum acceptable depth for the desired accuracy in the phase velocity. The use of a very large value of  $r_0$ , or more precisely, a large number of wavelengths of structure, will result in overflow; thus a simple, temporary solution to this problem is useful. Such a solution is the simple extension of the normalization technique described by Schwab and Knopoff (1970; 1972). The application of normalization to the direct-integration procedure is quite simple; it is not necessary to begin normalization until the application of the predictor-corrector method has begun in the mantle. To normalize, all one need do is determine the maximum of the absolute values of  $y_i$  at the end of each integration step; one then divides all  $y_i(r_j)$  and  $\bar{y}_i(r_j)$  by this value, where  $r_j$  are the seven positions at which  $y_i$  and  $\bar{y}_i$  must be specified so as to permit the next step of the fourth-order predictor-corrector method. Seven, rather than four  $r_j$  are required to allow the automatic doubling of step size when certain depths are reached.

For ease of reference, a normalization scheme which is appropriate for the program segment in Figure 4a, is given in Figure 7. Two warnings: (1) If only sparing use of normalization is planned, or it is to be invoked from an IF statement, the segment in Figure 7 will be satisfactory; how-

ever, if large-scale use is envisioned, efficiency requires the inclusion of normalization directly within the coding in Figure 4a.

(2) Unless absolutely necessary, normalization should not be included in these computations; it can result in a very significant increase in computation time.

Our numerical tests of the overflow problem were performed with the average (oceanic) earth structure given by Wiggins (1968). The results are given in Table 3. For IBM 360 equipment, when using double-precision computation, overflow occurs when  $|F| \approx 10^{70}$  to  $10^{80}$ .

Returning to Figure 6, for routine use of the AJP formulation, it is important to integrate only down to slightly below the position the  $r_0$  lines in the figure, and to thereby minimize computation time and expense. For this purpose we have devised empirical "laws" for determining the maximum depth

$$H = a - r_0$$

to which the integration must be performed if the resulting phase velocity is to be valid to 4 significant figures. The data for these determinations are collected in Figure 8. The "laws" specifying the number of wavelengths of structure to be retained, if 4 significant figures are desired in the computed phase velocities, are

$$H/\lambda = 7 - \bar{c} \quad \text{for mode 0} \quad (6.01)$$

$$H/\lambda = 9.5 - \bar{c} \quad \text{for mode 1} \quad (6.02)$$

$$H/\lambda = \left[ 11 + \frac{4}{10}(M-2) \right] - \bar{c} \quad \text{for modes 2-7} \quad (6.03)$$

where  $\lambda$  is the wavelength, and  $M$  is the mode number.

From the results shown in Figures 6 and 8 we also have the maximum periods and values of  $\bar{c}$  which can be determined without taking the structure of the core into consideration (other than to determine the values of  $g(r)$ ). These results are shown in Figure 9, along with the corresponding values of the minimum order number  $\underline{\ell}$ .

Relative to the computation of theoretical seismograms, the combination of the results in Figure 9 and those given by Schwab and Kausel (Section 5, 1976), indicate a potentially useful conclusion: (1) When  $\underline{\ell} > \underline{\ell}_{\min}$ , only the crust-mantle system need be used in the computations;  $\bar{c}$  can be computed at specified, equally-spaced frequencies and inverse Fourier transformation can be used to calculate the theoretical seismogram for this range of periods; and the first term of the asymptotic expansions for  $P_{\underline{\ell}}^m$  and  $Q_{\underline{\ell}}^m$  can be used (possibly corrected by automatic numerical interpolation from the data in Figures 2 and 3 of Kausel and Schwab (1976)). (2) When  $\underline{\ell} < \underline{\ell}_{\min}$ , the core must be included in the computations;  $\omega$  should be computed at integral values of  $\underline{\ell}$ , and summation over  $\underline{\ell}$  should replace Fourier synthesis; and the exact, integral- $\underline{\ell}$  expressions should be used to evaluate the associated Legendre functions.

A point of considerable interest to those involved in the actual computation of surface wave dispersion, is whether or not a difficulty analogous to the Thomson-Haskell "loss-of-precision" problem (Schwab and Knopoff, 1970; Schwab, 1970) is intrinsic to the AJP formulation. In computations based on the homogeneous-layer approximation, when the original version (Haskell, 1953) of the Thomson-Haskell formulation for Rayleigh waves is used, this problem can cause serious difficulties if the computer is employed in a low-precision mode. To test for an analog to this "loss-of-precision" problem, in our optimization of the AJP formulation, we simulated single-precision (about 6 decimal digits) computation by replacing DO-loop 160 (Figure 4a) in our double-precision program, with the program segment shown in Figure 10. The function SNGL accepts a double-precision argument, and returns the single-precision equivalent.

The results of our single-precision tests are similar to those from the original Thomson-Haskell formulation (Figure 2, Schwab and Knopoff, 1970), and are illustrated in Figure 11. In the  $\underline{r}$ - $\underline{\sigma}$  range shown, our results indicate that there is no problem with modes 0-4 in double-precision computations; but when computations are reduced to single precision, the loss-of-precision problem is clearly illustrated. In the latter case, there is seen to exist a minimum value of  $\underline{r}_0$ , below which we cannot go and still retain a given accuracy in the computed phase

velocities. Thus the AJP formulation does indeed exhibit the analog to the Thomson-Haskell loss-of-precision problem.

Since practical work with dispersion computations on IBM 360 equipment is routinely carried out in double precision, it is important to estimate the numerical limitations imposed by the loss-of-precision problem in this computational mode. The results of our tests at 50 and 25 seconds are shown in Figures 12 and 13. Less extensive tests were also carried out at a period of 65 seconds. At a given period, the right-most point of each of the smoothed curves was used to determine the maximum accuracy possible for each mode. This information was then collected in the Figures 14 and 15. Although the data is necessarily sparse, due to the expense of this type of experiment, the results are strikingly clear: For a fixed period, as we go to higher and higher mode numbers, the attainable accuracy in  $\bar{c}$  becomes less and less; for a fixed accuracy in  $\bar{c}$ , as we go to shorter and shorter periods, the maximum mode number that can be successfully treated becomes smaller and smaller.

In the near future we intend to present the details of our numerical analysis of the various possible methods for dealing with the loss-of-precision problem. See, for example, Wiggins (1968), Nolet (Appendix A, 1976), Neigauz and Skadinskaya (1972), Gilbert and Backus (1966), and Takeuchi and Saito (Section II.D.4, 1972).

## 7. TERMINATING BOUNDARY CONDITIONS

In our present programming efforts we are concentrating on the computation of phase velocities at arbitrarily specified (equally-spaced) frequencies. To keep our algorithms as simple as possible, and to avoid the difficulties involved in the evaluation of spherical Bessel functions of non-integral order, we have chosen to terminate our integrations at depth with free, or rigid, terminating boundary conditions. For completeness, we also include the technique for: (1) terminating the integration within the mantle by applying terminating boundary conditions for a gravitating, homogeneous, solid sphere below  $\underline{r_c}$  and, (2) terminating at the mantle-core boundary by applying the conditions for a homogeneous liquid sphere below  $\underline{r_0}$ .

In the former case, just above  $\underline{r_0}$  we have

$$Y_+(r_0) = y_1(a)X_1(r_0) + y_3(b)X_2(r_0) + y_5(a)X_3(r_0) \quad (7.01)$$

where

$$b = \begin{cases} a & \text{for a continental structure} \\ r_1 & \text{for an oceanic structure} \end{cases} \quad (7.02)$$

For the homogeneous, gravitating, solid sphere below  $\underline{r_0}$ , there are three classes of solutions:  $\underline{Y_1(r), Y_2(r), Y_3(r)}$ ; thus just below  $\underline{r_0}$ ,

$$Y_-(r_0) = D Y_1(r_0) + E Y_2(r_0) + M Y_3(r_0), \quad (7.03)$$

where  $\underline{D}$ ,  $\underline{E}$ , and  $\underline{M}$  are undetermined constants. Applying the boundary conditions of continuity of  $\underline{y_i}$  at  $\underline{r_0}$ , we obtain

$$\begin{bmatrix} [X_1(r_0)]_1 & [X_2(r_0)]_1 & [X_3(r_0)]_1 & -[Y_1(r_0)]_1 & -[Y_2(r_0)]_1 & -[Y_3(r_0)]_1 \\ [X_1(r_0)]_2 & [X_2(r_0)]_2 & [X_3(r_0)]_2 & -[Y_1(r_0)]_2 & -[Y_2(r_0)]_2 & -[Y_3(r_0)]_2 \\ [X_1(r_0)]_3 & [X_2(r_0)]_3 & [X_3(r_0)]_3 & -[Y_1(r_0)]_3 & -[Y_2(r_0)]_3 & -[Y_3(r_0)]_3 \\ [X_1(r_0)]_4 & [X_2(r_0)]_4 & [X_3(r_0)]_4 & -[Y_1(r_0)]_4 & -[Y_2(r_0)]_4 & -[Y_3(r_0)]_4 \\ [X_1(r_0)]_5 & [X_2(r_0)]_5 & [X_3(r_0)]_5 & -[Y_1(r_0)]_5 & -[Y_2(r_0)]_5 & -[Y_3(r_0)]_5 \\ [X_1(r_0)]_6 & [X_2(r_0)]_6 & [X_3(r_0)]_6 & -[Y_1(r_0)]_6 & -[Y_2(r_0)]_6 & -[Y_3(r_0)]_6 \end{bmatrix} \begin{bmatrix} y_1(a) \\ y_3(b) \\ y_5(a) \\ D \\ E \\ M \end{bmatrix} = \begin{bmatrix} 0 \\ 0 \\ 0 \\ 0 \\ 0 \\ 0 \end{bmatrix} \quad (7.04)$$

or

$$NW = 0 \quad (7.05)$$

and the dispersion function has the form

$$F(\omega, \bar{c}) = \det(N) \quad (7.06)$$

The components of  $\underline{Y}_i(r)$  are given in convenient form by Takeuchi and Saito (1972):  $\underline{Y}_1(r)$  by their equations (98), with the negative sign in (99);  $\underline{Y}_2(r)$  by (98), with the positive sign in (99); and  $\underline{Y}_3(r)$  by their equations (100). Note that their definition of  $\underline{y}_6$  differs slightly from that used here.

When the structure used to form the dispersion function is terminated at the mantle-core boundary by the conditions for a homogeneous liquid sphere below  $\underline{r}_0$ , above  $\underline{r}_0$  we have (7.01); below,

$$\underline{Y}_i(r_0) = P \underline{Y}_1(r_0) + Q \underline{Y}_3(r_0) , \quad (7.07)$$

where  $\underline{P}$  and  $\underline{Q}$  are undetermined constants,

and  $\underline{Y}_i$  in (7.07) have the form

$$\underline{Y}_i(r_0) = \begin{bmatrix} y_1(r_0) \\ y_2(r_0) \\ y_5(r_0) \\ y_6(r_0) \end{bmatrix} \quad (7.08)$$

Again, Takeuchi and Saito (1972) give the form of these vector components for the gravitating, homogeneous, liquid sphere. From the conditions of continuity of  $\underline{y}_1, \underline{y}_2, \underline{y}_5, \underline{y}_6$  at  $\underline{r}_0$ , and the vanishing of  $\underline{y}_4(r_0)$ , we have

$$\begin{bmatrix}
 [X_1(r_0)]_1 & [X_2(r_0)]_1 & [X_3(r_0)]_1 & -[Y_1(r_0)]_1 & -[Y_3(r_0)]_1 \\
 [X_1(r_0)]_2 & [X_2(r_0)]_2 & [X_3(r_0)]_2 & -[Y_1(r_0)]_2 & -[Y_3(r_0)]_2 \\
 [X_1(r_0)]_4 & [X_2(r_0)]_4 & [X_3(r_0)]_4 & 0 & 0 \\
 [X_1(r_0)]_5 & [X_2(r_0)]_5 & [X_3(r_0)]_5 & -[Y_1(r_0)]_5 & -[Y_3(r_0)]_5 \\
 [X_1(r_0)]_6 & [X_2(r_0)]_6 & [X_3(r_0)]_6 & -[Y_1(r_0)]_6 & -[Y_3(r_0)]_5
 \end{bmatrix}
 \begin{bmatrix}
 y_1(a) \\
 y_3(b) \\
 y_5(a) \\
 P \\
 Q
 \end{bmatrix}
 =
 \begin{bmatrix}
 0 \\
 0 \\
 0 \\
 0 \\
 0
 \end{bmatrix}
 \quad (7.09)$$

or

$$R S = 0, \quad (7.10)$$

and the dispersion function takes the form

$$F(\omega, \bar{c}) = \det(R). \quad (7.11)$$

To obtain the group velocity we still employ (3.03) and (3.04). The forms of  $\underline{F}'$  and  $\dot{\underline{F}}$  which result from (7.06), or (7.11), can be obtained by analogy with the way in which (3.05) is obtained from (2.10). In the present case, however, the analog of (3.05) will comprise the sum of six, sixth-order determinants when (7.06) is used to form the dispersion function, and the sum of five, fifth-order determinants when (7.11) is used.

As would be expected, our numerical tests of a terminating solid sphere show that, to obtain a given accuracy in  $\bar{c}$ , less structure must be retained in this case than when using terminating rigid or free boundaries within the solid mantle. A complete set of tests, comparable to those in Figure 12, was

performed for a period of 50 seconds; the results showed that the increase in the maximum  $r_0$  values was surprisingly independent of mode number and  $\sigma$  :  $(300 \pm 25)$  km, or in most cases, about 24 fewer integration steps when terminating with a solid sphere. Thus the use of the "correct" terminating boundary condition appears to be important only for the lowest (radial) mode numbers. Our tests with mode 7 at 25 seconds, show the increase in  $r_0$  to be about  $(110 \pm 10)$  km. Thus, from our limited number of tests, it appears that  $\delta r_0 / r_0$  is roughly constant with about the value  $0.14 \pm 0.02$  ; where  $r_0$  is maximum value required by the structural limitation when the condition of a rigid terminating boundary is employed, and  $\delta r_0$  is the increase possible in  $r_0$  when one then employs the condition of a terminating solid sphere.

Tests of the loss-of-precision problem were also performed with the "correct" boundary condition at depth. Again, a complete set of tests was carried out at 50 seconds, and mode 7 was tested at a period of 25 seconds. The right-hand extremes of the analogs of the smooth curves in Figures 12 and 13, occurred at the same depths in these new tests; thus, as a result of the increased  $r_0$  values of the upper portions of the curves when solid-sphere termination is used, the maximum accuracy for any given mode is significantly improved by using this type of boundary at depth.

## 8. CONCLUSIONS

An analysis of direct, Rayleigh-wave dispersion computations on a spherical, gravitating earth has been performed using the Alterman-Jarosch-Pekeris (1959) formulation.

1. No difficulty was encountered when we reversed the usual procedure, for practical purposes, and computed phase velocities (or polar order numbers) at specified periods.

2. Integration from the free surface downward, again reversing the "standard" procedure, resulted in no unexpected difficulties. In fact, this procedure much simplified the specification of the algorithm for integrating the system of differential equations to obtain phase-velocity dispersion. This procedure makes the generalization from the algorithm for continental, to oceanic structures relatively trivial; also, it makes it possible to develop direct algorithms for obtaining group velocities for the two types of structures. The usual variational techniques are not required for this latter purpose.

3. Our optimization of the AJP formulation is based on removing all function evaluations from the innermost, integration (over  $r$ ) loops of the program. In fact, most of the evaluation procedure for  $a_{ij}(r_k)$  can even be removed from the phase velocity and frequency loops. This optimization of the AJP formulation yields a characteristic time of 336  $\mu$ seconds/integration step/iteration for spherical, gravitating structures, and a time of 151  $\mu$ seconds/integration step/iteration for spherical,

non-gravitating structures. These characteristic times, for the AJP direct-integration procedure, provide a basis of comparison with the homogeneous-layer approximation for a non-gravitating flat structure, which has a characteristic time of 110  $\mu\text{sec}/\text{layer}/\text{iteration}$  (Knopoff's method, Schwab and Knopoff, 1972). The lower bounds of the characteristic times, for our final optimizations of the AJP formulation, are 266  $\mu\text{sec}/\text{step}/\text{iteration}$  for the gravitating case and 143  $\mu\text{sec}/\text{step}/\text{iteration}$  when gravity is not included. All of the above times apply to the IBM 360/91 computer at UCLA.

4. Our results here, combined with those of Schwab and Knopoff (1972), indicate that an integration "step" (in the AJP procedure) can be considered nearly equivalent to a "layer" in computations based on the homogeneous-layer approximation. Also, to the accuracy possible in this type of comparison, the "iterations" required in the two techniques (see Schwab and Knopoff (1972) for details) can be considered equivalent. Thus the relative efficiencies of the two types of Rayleigh-wave dispersion computations can be evaluated by simple comparison of the above characteristic times. The fact that approximately the same number and sizes of "steps" must be used in the direct-integration procedure, as number and sizes of "layers" in the homogeneous-layer approximation, means that the usual assumption that the former method does a better job of treating continuous parameter-depth distributions, appears to be invalid.

5. The overflow problem in the AJP formulation can be controlled by simple normalization. Program segments are given which describe the procedure explicitly.

6. A loss-of-precision problem appears to be intrinsic to the AJP formulation. Results of this problem: For a fixed period, as mode number increases, the attainable accuracy in the phase velocity decreases; for a fixed accuracy in the phase velocity, as period decreases the maximum mode number that can be treated successfully decreases.

ACKNOWLEDGEMENTS

This research was partly supported by the Advanced Research Projects Agency of the Department of Defense and was monitored by the Air Force Office of Scientific Research under Contract No. F49620-76-C-0038, and partly supported by the Earth Sciences Section, National Science Foundation, NSF Grant DES75-04376. Part of the work was carried out while F. Schwab and H. M. Liao were Visiting Scientists at the University of Chile (Santiago), supported by the Multinational Project on Earth Sciences (Regional Scientific and Technological Development Program) of the Organization of American States. The original program development and testing, and much of the later algorithmic tests, were carried out at the Campus Computing Network at UCLA; we wish to express our gratitude for that portion of these computations which was supported by intramural, University computing funds. A large part of the numerical testing herein reported was performed at the Dipartimento di Scienze della Terra, Università della Calabria and at the Istituto di Geodesia e Geofisica, Università di Bari; we are grateful to these institutions for supporting our computations. We also wish to express our gratitude to the Centro de Computación, Universidad de Chile (Santiago) for supporting the remainder -- and not insignificant portion -- of our numerical analyses.

We are grateful to Dr. J. K. Gardner for advice concerning optimum usage of IBM 360 hardware, and to Dr. L. D. Porter for tests of a key program segment for dispersion

computations (Figure 2, Schwab and Knopoff (1972)), that have provided computation speeds for CDC and UNIVAC computers, relative to the IBM 360/91 at UCLA.

# REFERENCES

- Alterman, Z., Jarosch, H. and C.L. Pekeris (1959). Oscillations of the Earth, Proc. Roy. Soc., A 252, 80-95.
- Alterman, Z., H. Jarosch and C.L. Pekeris (1961). Propagation of Rayleigh waves in the Earth, Geophys. J.R. Astr. Soc. 4, 219-241.
- Anon. (1970). System/360 Scientific Subroutine Package, Version III Programmer's Manual (Program Number 360A-CM-03X), IBM Corp., White Plains, New York, 343-350.
- Bhattacharya, S. N. (1976). Extension of the Thomson-Haskell method to non-homogeneous spherical layers, Geophys. J. R. astr. Soc. 47, 411-443.
- Biswas, N.N. and L. Knopoff (1970). Exact earth-flattening calculation for Love waves, Bull. Seism. Soc. Am. 60, 1123-1137.
- Biswas, N.N. (1972). Earth-flattening procedure for the propagation of Rayleigh wave, Pure and Applied Geophys. 96, 61-74.
- Bolt, B.A. and J. Dorman (1961). Phase and group velocities of Rayleigh waves in a spherical, gravitating Earth, J. Geophys. Res. 66, 2965-2981.
- Dorman, J., M. Ewing and J. Oliver (1960). Study of shear-velocity distribution in the upper mantle by mantle Rayleigh waves, Bull. Seism. Soc. Am. 50, 87-115.
- Frantsuzova, V.I., A.L. Levshin and G.V. Shkadinskaya (1972). Higher modes of Rayleigh waves and upper mantle structure, in Computational Seismology, ed. V.I. Keilis-Borok, Consultants Bureau, New York, 93-100.
- Gaulon, R., N. Jobert, G. Poupinet and G. Roullet (1970). Application de la méthode de Haskell au calcul de la dispersion des ondes de Rayleigh sur un modèle sphérique, Annales de Géophys. 26, 1-8.
- Gilbert, F. and G. E. Backus (1966). Propagator matrices in elastic wave and vibrational problems, Geophysics 31, 326-332.

- Hamming, R.W. (1959). Stable predictor corrector methods for ordinary differential equations, J.Assoc.Comp.Mach. 6, 37-47.
- Haskell, N.A. (1953). The dispersion of surface waves on multilayered media, Bull. Seism. Soc. Am. 43, 17-34.
- Kausel, E. and F. Schwab (1973). Contributions to Love-wave transformation theory; Earth-flattening transformation for Love waves from a point source in a sphere, Bull. Seism. Soc. Am. 63, 983-993.
- Knopoff, L. (1964). A matrix method for elastic wave problems, Bull. Seism. Soc. Am. 54, 431-438.
- Knopoff, L., F. Schwab, K. Nakanishi and F. Chang (1974). Evaluation of Lg as a discriminant among different continental crustal structures, Geophys. J. R. Astr. Soc. 39, 41-70.
- Neigauz, M. G. and G. V. Skadinskaya (1972). Method for calculating surface Rayleigh waves in a vertically inhomogeneous half-space, in Computational Seismology, ed. V. I. Keilis-Borok, Consultants Bureau, New York.
- Nolet, A. M. H. (1976). Higher modes and the determination of upper mantle structure, Doctoral thesis, University of Utrecht.
- Panza, G.F., F. Schwab and L. Knopoff (1972). Channel and crustal Rayleigh waves, Geophys. J.R. Astr. Soc. 30, 273-280.
- Pekeris, C.L. and H. Jarosch (1958). The free oscillations of the Earth, in Contributions in Geophysics, Volume 1, Pergamon Press, London, 171-192.
- Porter, L. D., F. Schwab, I. F. Weeks, H. M. Liao, K. K. Nakanishi, G. F. Panza, E. G. Kausel, E. Mantovani, J. Landoni, N. N. Biswas and F.-S. Chang (1977). Relative computer speeds for surface-wave dispersion computations in preparation.

- Press, F., D. Harkrider and C.A. Seafeldt (1961). A fast, convenient program for computation of surface-wave dispersion curves in multilayered media, Bull. Seism. Soc. Am. 51, 495-502.
- Ralston, A. (1960). Numerical integration methods for the solution of ordinary differential equations, in Mathematical Methods for Digital Computers, Volume 1, ed. A. Ralston and H.S. Wilf, John Wiley and Sons, New York, 95-109.
- Ralston, A. (1962). Runge-Kutta methods with minimum error bounds, Math. Comp. 16, 431-437.
- Randall, M. J. (1967). Fast programs for layered half-space problems, Bull. Seism. Soc. Am. 57, 1299-1316.
- Schwab, F. (1970). Surface-wave dispersion computations: Knopoff's method, Bull. Seism. Soc. Am. 60, 1491-1520.
- Schwab, F. and E.G. Kausel (1976). Long-period surface wave seismology: Love wave phase velocity and polar phase shift, Geophys. J.R. Astr. Soc. 45, 407-435.
- Schwab, F. and L. Knopoff (1970). Surface-wave dispersion computations, Bull. Seism. Soc. Am. 60, 321-344.
- Schwab, F. and L. Knopoff (1971). Surface waves on multilayered anelastic media, Bull. Seism. Soc. Am. 61, 893-912.
- Schwab, F. and L. Knopoff (1972). Fast surface wave and free mode computations, in Methods in Computational Physics, Volume 11, ed. B.A. Bolt, Academic Press, New York, 87-180.
- Schwab, F. and L. Knopoff (1973). Love waves and the torsional free modes of a multilayered anelastic sphere, Bull. Seism. Soc. Am. 63, 1107-1117.
- Takeuchi, H. and M. Saito (1972). Seismic surface waves, in Methods in Computational Physics, Volume 11, ed. B.A. Bolt, Academic Press, New York, 217-295.

- Thomson, W.T. (1950). Transmission of elastic waves through a stratified solid medium, J. Appl. Phys. 21, 89-93.
- Wiggins, R.A. (1968). Terrestrial variational tables for the periods and attenuation of the free oscillations, Phys. Earth Planet. Interiors 1, 201-266.
- Wiggins, R. A. (1976). A fast, new computational algorithm for oscillations and surface waves, Geophys. J.R. Astr. Soc. 47, 135-150.

Table 1. Constants for integration through successive step-size regions illustrated in program segment given in Figure 4. Constants correspond to 4 significant figures in computed phase velocity.

I	N1(I)	N2(I)	Integration step size (km)
1	5	11	-1.5625
2	12	16	-3.1250
3	17	21	-6.2500
4	22	*	-12.5000

\* N2(4) is specified so as to allow integration to proceed to the deepest point within the solid mantle, while maintaining a step size of -12.5 km. NEND is determined, at each period, by the input value of r<sub>0</sub>; it must satisfy  $NEND \leq N2(4)$ .

able 2. Relative speeds, for surface-wave dispersion computations, for several computers.

Test cases are described in the text. Actual execution times are obtained by multiplying relative times by  $47.1 \times 10^{-6}$  seconds.

Computer	Location	Compiler	Precision	Relative Characteristic Times	Relative Characteristic Times		
					Case 1	Case 2	Average
BM 360/91	Central Facility Campus Computing Network UCLA Los Angeles, California	FORTAN H, OPT=2 FORTAN G	double (64 bits) "		1.00 1.20	1.37 1.45	1.19 1.33
BM 360/75	Previously installed at UCLA	FORTAN	"		5.5	7.0	6.3
BM 360/65	Università di Bari Bari, Italy	FORTAN	"		8.64	10.4	9.5
BM 370/145	Università degli Studi della Calabria Cosenza, Italy	FORTAN	"		40	52	46
BM 370/145	Centro de Computacion Universidad de Chile (Santiago), Santiago Chile	FORTAN	"		40	52	46
DC 7600	Lawrence Berkeley Laboratory University of California Berkeley, California	RUN76 MNF FTN, OPT=2	single (60 bits) " "		0.38 0.37 0.30	0.46 0.45 0.42	0.42 0.41 0.36
DC 6600	Lawrence Berkeley Laboratory University of California Berkeley, California	RUN76 MNF FTN	" " "		1.97 1.81 1.64	2.25 1.97 2.10	2.11 1.89 1.87
DC 6400	Lawrence Berkeley Laboratory University of California Berkeley, California	RUN76 MNF FTN	" " "		7.23 7.08 7.11	9.82 9.72 10.1	8.53 8.40 8.61
NIVAC 1108	Jet Propulsion Laboratory	FORTAN	double (72 bits)		8.1	11	9.5

Table 3. Results of numerical tests of the overflow problem when normalization is not included in our optimization of the basic AJP formulation. An average (oceanic) earth structure (Wiggins, 1968), and a period of 50 seconds, were used in the tests. The value of  $r_0$  is the maximum at which overflow occurs;  $H/\lambda$  is the corresponding number of wavelengths of structure, from the surface of the earth down to  $r=r_0$ . These, and larger values of  $H/\lambda$ , yield overflow.

Mode Number	$r_0$ (km)	$H/\lambda$
0	4600	8.7
1	4300	8.3
2	4000	8.2
3	3800	7.9

## FIGURE CAPTIONS

Figure 1. Schematic representation of optimized scheme for evaluating the matrix elements  $a_{ij}(r_k)$  in the treatment of the solid sedimentary layers, the subsedimentary crustal layers, and the mantle. The quantities  $\lambda$  and  $\mu$  are Lamé's constants,  $G$  is the gravitational constant, and  $N$  is the number of depths at which  $a_{ij}(r_k)$  must be evaluated.

Figure 2. Schematic representation of optimized scheme for evaluating the matrix elements  $b_{ij}(r_k)$  in the treatment of the homogeneous oceanic (liquid) layer. The quantity  $\alpha$  is the compressional-wave velocity,  $\rho$  is the density,  $g(r)$  is acceleration due to gravity, and  $M$  is the number of depths at which  $b_{ij}(r_k)$  must be evaluated.

Figure 3. (a) FORTRAN IV program segment for the basic matrix multiplication for our optimization of the AJP formulation for solid layers; (b) symbolic representation of (a), which is used in Figure 4; and (c) definition of one-dimensional array used in (a) to represent 6x6 matrix in (2.01). The integer IPT is the index specifying the value of  $r$ , and A1 through A36 are dimensioned to 300.

Figure 4a. FORTRAN IV program segment in which the predictor-corrector portion of the integration from below the Moho to  $r_0$  is handled; most of the computation time is spent in this segment. The boxed segments refer to the basic AJP matrix multiplication illustrated in Figure 3

Figure 4b. FORTRAN IV program segment demonstrating subscripting and storage improvements, relative to the segment in Figure 4a, that are required to optimize computation time on an IBM 360 computer.

Figure 4c. FORTRAN IV program segment illustrating our final optimization for the non-gravitating case.

- Figure 5. Oceanic and continental (shield) models used in program testing.
- Figure 6. Values of  $r_0$ , the depth at which integration is terminated, which yield 4-significant-figure accuracy in the computed values of  $\bar{c}$  with the optimized version of the basic AJP formulation. At each period, 4-figure accuracy is attained only if  $r_0$  is specified to be smaller than the indicated curve.
- Figure 7. Normalization scheme appropriate to program segment in Figure 4a. The procedure should be included between statement numbers 160 and 170 in Figure 4a. See text for warnings concerning loss of efficiency when normalization is employed.
- Figure 8. Results of tests for determining general, multimode "laws" for specifying the required values of  $r_0$  to use when computing phase-velocity dispersion for mantle Rayleigh waves, if  $\bar{c}$  is desired to 4-figure accuracy.
- Figure 9. Maximum periods, maximum phase velocities, and minimum order numbers,  $\ell$ , that can be used if  $\bar{c}$  is desired to 4-figure accuracy, when the integration is limited to the mantle and the core is excluded from the computations (other than for use in the determination of  $g(r)$ ).

Figure 10. FORTRAN IV Program segment used to simulate single-precision computations when using our double-precision optimization on the basic AJP formulation. This program segment is used to replace DO-loop 160 in Figure 4a.

Figure 11. Test of the effect of reducing IBM 360 computations from double (about 16 decimal digits) to single precision (about 6 decimal digits), while keeping period fixed at 50 seconds. For a given mode, in order to obtain  $\underline{g}$  significant figures in the computed phase velocity,  $\underline{r_0}$  must not exceed the value given by the upper portion of the dashed line (structural limitation) nor fall below the lower portion (loss-of-precision limitation).

Figure 12. IBM 360 double-precision tests of loss-of-precision problem at a period of 50 seconds. At left, raw results of structure reduction experiments; at right, smoothed curves for each mode. Latter curves are drawn such that all data points, for a given mode, fall to the right of corresponding curve.

Figure 13. IBM 360 double-precision tests of loss-of-precision problem at a period of 25 seconds.

Figure 14. Maximum possible mode number,  $n_{\max}$ , for which  $\sigma$  significant figures can be obtained with our optimization of the AJP formulation. This limitation is due to the loss-of-precision problem.

Figure 15. Relationship between maximum possible mode number,  $n_{\max}$ , and minimum period, for several values of  $\sigma$ . This limitation of our optimization of the AJP formulation is due to the loss-of-precision problem.

Elements to be evaluated external to both  $\omega$  and  $\bar{c}$  loops:

$a_{11}$	$a_{12}$	$a_{33}$	$a_{45}$
$a_{41}$	$a_{22}$	$a_{34}$	$a_{26}$
$a_{51}$	$a_{42}$	$a_{44}$	$a_{66}$

Auxiliary quantities to be evaluated external to both  $\omega$  and  $\bar{c}$  loops:

$$d_{21} = 4\mu(3\lambda + 2\mu)a_{12}/r^2$$

$$d_{43} = -2\mu/r^2$$

$$d_{13} = \lambda a_{12}/r$$

$$d_{63} = -4\pi G\rho$$

$$d_{65} = 1/r^2$$

$$e_{43} = 4\mu(\lambda + \mu)a_{12}/r^2$$

$\omega$  loop

$$\text{OMEGSQ} = \omega^2$$

DO 10 I=1,N

$$\text{TEMP} = -a_{26}(I) \times \text{OMEGSQ}$$

$$a_{21}(I) = d_{21}(I) - \text{TEMP}$$

$$10 \quad f_{43}(I) = d_{43}(I) - \text{TEMP}$$

$\bar{c}$  loop

$$\text{ORDER} = \ell(\ell + 1)$$

DO 20 I=1,N

$$a_{13}(I) = d_{13}(I) \times \text{ORDER}$$

$$a_{23}(I) = a_{41}(I) \times \text{ORDER}$$

$$a_{63}(I) = d_{63}(I) \times \text{ORDER}$$

$$a_{24}(I) = a_{33}(I) \times \text{ORDER}$$

$$a_{65}(I) = d_{65}(I) \times \text{ORDER}$$

$$20 \quad a_{43}(I) = f_{43}(I) + e_{43}(I) \times \text{ORDER}$$

Evaluate  $b_{66}$  external to both  $\omega$  and  $\bar{c}$  loops. Auxiliary quantities to be evaluated external to both  $\omega$  and  $\bar{c}$  loops:

$$\begin{aligned} \text{XLAINV} &= 1/\alpha^2 \rho & p_{65} &= p_{62} \rho & p_{21} &= -p_{25} g(r) \\ p_{12} &= -1/\rho r^2 & p_{61} &= -p_{65} g(r) & s_{21} &= -4\pi g(r)/r \\ p_{62} &= 4\pi G/r^2 & p_{22} &= -g(r)/r^2 \\ p_{15} &= -1/r^2 & p_{25} &= p_{22} \rho \end{aligned}$$

$\omega$  loop

```

      RHMQSQ = -\rho \omega^2
      OMSQIN = 1/\omega^2

      DO 10 I=1,M
        h21(I) = p21(I) * OMSQIN
        q21(I) = s21(I) + RHMQSQ
        h61(I) = p61(I) * OMSQIN
        h12(I) = p12(I) * OMSQIN
        h22(I) = p22(I) * OMSQIN
        h62(I) = p62(I) * OMSQIN
        h15(I) = p15(I) * OMSQIN
        h25(I) = p25(I) * OMSQIN
      10 h65(I) = p65(I) * OMSQIN

```

$\bar{c}$  loop

```

      ORDER = l(l+1)

      DO 20 I=1,M
        b22(I) = h22(I) * ORDER
        b11(I) = b66(I) - b22(I)
        b21(I) = h21(I) * ORDER + q21(I)
        b61(I) = h61(I) * ORDER
        b12(I) = h12(I) * ORDER + XLAINV
        b62(I) = h62(I) * ORDER
        b15(I) = h15(I) * ORDER
        b25(I) = h25(I) * ORDER

```

(a)

$$\begin{aligned}
 YBAR(1) &= A1(IPT) * Y(1) + A7(IPT) * Y(2) + A13(IPT) * Y(3) \\
 YBAR(2) &= A2(IPT) * Y(1) + A8(IPT) * Y(2) + A14(IPT) * Y(3) + \\
 &1 \quad A20(IPT) * Y(4) + A32(IPT) * Y(6) \\
 YBAR(3) &= A15(IPT) * (Y(3) - Y(1)) + A21(IPT) * Y(4) \\
 YBAR(4) &= A4(IPT) * Y(1) + A10(IPT) * Y(2) + A16(IPT) * Y(3) + \\
 &1 \quad A22(IPT) * Y(4) + A28(IPT) * Y(5) \\
 YBAR(5) &= A5(IPT) * Y(1) + Y(6) \\
 YBAR(6) &= A18(IPT) * Y(3) + A30(IPT) * Y(5) + A36(IPT) * Y(6)
 \end{aligned}$$

(b)

YBAR, IPT
-----------

(c)

$[a_{ij}] =$

A1	A7	A13	0	0	0
A2	A8	A14	A20	0	A32
-A15	0	A15	A21	0	0
A4	A10	A16	A22	A28	0
A5	0	0	0	0	1
0	0	A18	0	A30	A36

```

C BEGIN APPLICATION OF PREDICTOR-CORRECTOR METHOD.
      DO 110 I=1,6
110   PMNUSC(I)=0.0D+00
      HH=0.5D+00*1.5625D+00
C LOOP OVER REGIONS WITH DIFFERENT STEP SIZES.
      DO 180 IREG=1,NUMREG
      HH=HH+HH
      NSTART=N1(IREG)
      NSTOP=N2(IREG)
      NTEMP=5
      IT=0
C LOOP OVER DEPTH IN CURRENT STEP-SIZE REGION.
      DO 170 N=NSTART,NSTOP
      IF(IT.EQ.4) GO TO 115
      IT=NTEMP-4
      ITP1=IT+1
      ITP3=IT+3
      ITP8=IT+8
      ITP9=IT+9
      ITP10=IT+10
115   DO 120 I=1,6
C SET PREDICTOR P(I).
      P(I)=B(IT,I)+COEFF1*(2.0D+00*(B(ITP10,I)+B(ITP8,I))
          -B(ITP9,I))
C SET MODIFIED PREDICTOR XM(I).
120   XM(I)=P(I)-.9256198347107438D+00*PMNUSC(I)
      IPT=IPT+1
      [XMBAR, IPT]
      DO 130 I=1,6
C SET CORRECTOR C(I)
      C(I)=.125D+00*(9.0D+00*B(ITP3,I)-B(ITP1,I)
          +COEFF2*(XMBAR(I)+2.0D+00*B(ITP10,I)
          -B(ITP9,I)))
      PMNUSC(I)=P(I)-C(I)
C SET SOLUTION VECTOR AT NTH DEPTH.
130   Y(I)=C(I)+.07438016528925620D+00
          *PMNUSC(I)
      IF(N.EQ.NEND) RETURN
C SET DERIVATIVE OF SOLUTION VECTOR AT NTH DEPTH.
      [YBAR, IPT]
      IF(NTEMP.GT.7) GO TO 150
      NTMPP7=NTEMP+7
      DO 140 I=1,6
      B(NTEMP,I)=Y(I)
140   B(NTMPP7,I)=YBAR(I)
      NTEMP=NTEMP+1
      GO TO 170
150   DO 160 I=1,6
      B(1,I)=B(2,I)
      B(2,I)=B(3,I)
      B(3,I)=B(4,I)
      B(4,I)=B(5,I)

```

```

      B(5,I)=B(6,I)
      B(6,I)=B(7,I)
      B(7,I)=Y(I)
      B(8,I)=B(9,I)
      B(9,I)=B(10,I)
      B(10,I)=B(11,I)
      B(11,I)=B(12,I)
      B(12,I)=B(13,I)
      B(13,I)=B(14,I)
160   B(14,I)=YBAR(I)
170   CONTINUE
C  RESET STORED VALUES OF COEFFICIENTS IN PREPARATION FOR
C  DOUBLED STEP SIZE.
      COEFF1=COEFF1+COEFF1
      COEFF2=COEFF2+COEFF2
      COEFF6=COEFF6+COEFF6
C  RESET STORED VALUES OF Y(I),YBAR(I),and PMNUSC(I) IN
C  PREPARATION FOR DOUBLED STEP SIZE.
      DO 180 I=1,6
      PMNUSC(I)=8.962962962962963D+00*(Y(I)
        -B(1,I))-COEFF6*(YBAR(I)+B(8,I)
        +3.0D+00*(B(12,I)+B(10,I)))
      B(2,I)=B(3,I)
      B(3,I)=B(5,I)
      B(4,I)=B(7,I)
      B(9,I)=B(10,I)
      B(10,I)=B(12,I)
180   B(11,I)=B(14,I)

```

```

        DIMENSION B(6,14),Y(6),YBAR(6),XM(6),XMBAR(6),P(6),C(6),PMNUSC(6),
1          A(2090)
        EQUIVALENCE (Y(1),Y1)
        EQUIVALENCE (XM(1),XM1)
        EQUIVALENCE (XMBAR(1),XMBAR1)
        IPT=-18

        .
        .
        .

C LOOP OVER DEPTH IN CURRENT STEP-SIZE REGION.
        DO 170 N=NSTART,NSTOP
        IF(IT.EQ.4) GO TO 115
        IT=NTEMP-4
115 DO 120 I=1,6
C SET PREDICTOR P(I) .
        P(I)=B(I,IT)+COEFF1*(2.0D+00*(B(I,IT+10)+B(I,IT+8))-B(I,IT+9))
C SET MODIFIED PREDICTOR XM(I).
120 XM(I)=P(I)-.9256198347107438D+00*PMNUSC(I)
        IPT=IPT+19
        XMBAR(1)=A(IPT)*XM(1)+A(IPT+1)*XM(2)+A(IPT+2)*XM(3)
        XMBAR(2)=A(IPT+3)*XM(1)+A(IPT+4)*XM(2)+A(IPT+5)*XM(3)
1          +A(IPT+6)*XM(4)+A(IPT+7)*XM(6)
        XMBAR(3)=A(IPT+8)*(XM(3)-XM(1))+A(IPT+9)*XM(4)
        XMBAR(4)=A(IPT+10)*XM(1)+A(IPT+11)*XM(2)+A(IPT+12)*XM(3)
1          +A(IPT+13)*XM(4)+A(IPT+14)*XM(5)
        XMBAR(5)=A(IPT+15)*XM(1)+XM(6)
        XMBAR(6)=A(IPT+16)*XM(3)+A(IPT+17)*XM(5)+A(IPT+18)*XM(6)
        DO 130 I=1,6
C SET CORRECTOR C(I) .
        C(I)=.125D+00*(9.0D+00*B(I,IT+3)-B(I,IT+1)+COEFF2*(XMBAR(I)+2.0D+0
1          *B(I,IT+10)-B(I,IT+9)))
        PMNUSC(I)=P(I)-C(I)
C SET SOLUTION VECTOR AT NTH DEPTH.
130 Y(I)=C(I)+.07438016528925620D+00*PMNUSC(I)
        IF(N.EQ.NEND) RETURN
C SET DERIVATIVE OF SOLUTION VECTOR AT NTH DEPTH.
        YBAR(1)=A(IPT)*Y(1)+A(IPT+1)*Y(2)+A(IPT+2)*Y(3)
        YBAR(2)=A(IPT+3)*Y(1)+A(IPT+4)*Y(2)+A(IPT+5)*Y(3)
1          +A(IPT+6)*Y(4)+A(IPT+7)*Y(6)
        YBAR(3)=A(IPT+8)*(Y(3)-Y(1))+A(IPT+9)*Y(4)
        YBAR(4)=A(IPT+10)*Y(1)+A(IPT+11)*Y(2)+A(IPT+12)*Y(3)
1          +A(IPT+13)*Y(4)+A(IPT+14)*Y(5)
        YBAR(5)=A(IPT+15)*Y(1)+Y(6)
        YBAR(6)=A(IPT+16)*Y(3)+A(IPT+17)*Y(5)+A(IPT+18)*Y(6)
        IF(NTEMP.GT.7) GO TO 150
        DO 140 I=1,6
        B(I,NTEMP)=Y(I)
140 B(I,NTEMP+7)=YBAR(I)
        NTEMP=NTEMP+1
        GO TO 170

```

C RESET STORED VALUES OF Y AND YBAR IN PREPARATION FOR NEXT INTEGRATION  
C STEP.

```
150 DO 160 I=1,6
    B(I,1)=B(I,2)
    B(I,2)=B(I,3)
    B(I,3)=B(I,4)
    B(I,4)=B(I,5)
    B(I,5)=B(I,6)
    B(I,6)=B(I,7)
    B(I,7)=Y(I)
    B(I,8)=B(I,9)
    B(I,9)=B(I,10)
    B(I,10)=B(I,11)
    B(I,11)=B(I,12)
    B(I,12)=B(I,13)
    B(I,13)=B(I,14)
160 B(I,14)=YBAR(I)
170 CONTINUE
```

```

      DIMENSION B(4,14),D(4,14),X(4),Y(4),XBAR(4),YBAR(4),XM(4),YM(4),
1      XMBAR(4),YMBAR(4),P(4),Q(4),C(4),F(4),PMNUSC(4),
2      QMNUSF(4),A(1430)
      EQUIVALENCE (X(1),X1)
      EQUIVALENCE (Y(1),Y1)
      EQUIVALENCE (XM(1),XM1)
      EQUIVALENCE (YM(1),YM1)
      EQUIVALENCE (XMBAR(1),XMBAR1)
      EQUIVALENCE (YMBAR(1),YMBAR1)
      IPT=-12

```

```

      .
      .
      .

```

C LOOP OVER DEPTH IN CURRENT-STEP-SIZE REGION.

```

      DO 170 N=NSTART,NSTOP
      IF(IT.EQ.4) GO TO 115
      IT=NTEMP-4
115 DO 120 I=1,4
C SET PREDICTORS P(I) , Q(I) .
      P(I)=B(I,IT)+COEFF1*(2.0D+00*(B(I,IT+10)+B(I,IT+8))-B(I,IT+9))
      Q(I)=D(I,IT)+COEFF1*(2.0D+00*(D(I,IT+10)+D(I,IT+8))-D(I,IT+9))
C SET MODIFIED PREDICTORS XM(I) , YM(I) .
      XM(I)=P(I)-.9256198347107438D+00*PMNUSC(I)
120 YM(I)=Q(I)-.9256198347107438D+00*QMNUSF(I)
      IPT=IPT+13
      XMBAR(1)=A(IPT)*XM(1)+A(IPT+1)*XM(2)+A(IPT+2)*XM(3)
      YMBAR(1)=A(IPT)*YM(1)+A(IPT+1)*YM(2)+A(IPT+2)*YM(3)
      XMBAR(2)=A(IPT+3)*XM(1)+A(IPT+4)*XM(2)+A(IPT+5)*XM(3)
1      +A(IPT+6)*XM(4)
      YMBAR(2)=A(IPT+3)*YM(1)+A(IPT+4)*YM(2)+A(IPT+5)*YM(3)
1      +A(IPT+6)*YM(4)
      XMBAR(3)=A(IPT+7)*(XM(3)-XM(1))+A(IPT+8)*XM(4)
      YMBAR(3)=A(IPT+7)*(YM(3)-YM(1))+A(IPT+8)*YM(4)
      XMBAR(4)=A(IPT+9)*XM(1)+A(IPT+10)*XM(2)+A(IPT+11)*XM(3)
1      +A(IPT+12)*XM(4)
      YMBAR(4)=A(IPT+9)*YM(1)+A(IPT+10)*YM(2)+A(IPT+11)*YM(3)
1      +A(IPT+12)*YM(4)
      DO 130 I=1,4
C SET CORRECTORS C(I) , F(I) .
      C(I)=.125D+00*(9.0D+00*B(I,IT+3)-B(I,IT+1)+COEFF2*(XMBAR(I)+2.0D+0
1      *B(I,IT+10)-B(I,IT+9)))
      F(I)=.125D+00*(9.0D+00*D(I,IT+3)-D(I,IT+1)+COEFF2*(YMBAR(I)+2.0D+0
1      *D(I,IT+10)-D(I,IT+9)))
      PMNUSC(I)=P(I)-C(I)
      QMNUSF(I)=Q(I)-F(I)
C SET SOLUTION VECTORS AT NTH DEPTH.
      X(I)=C(I)+.07438016528925620D+00*PMNUSC(I)
130 Y(I)=F(I)+.07438016528925620D+00*QMNUSF(I)
      IF(N.EQ.NEND) RETURN

```

C SET DERIVATIVES OF SOLUTION VECTORS AT NTH DEPTH.

XBAR(1)=A(IPT)\*X(1)+A(IPT+1)\*X(2)+A(IPT+2)\*X(3)

YBAR(1)=A(IPT)\*Y(1)+A(IPT+1)\*Y(2)+A(IPT+2)\*Y(3)

XBAR(2)=A(IPT+3)\*X(1)+A(IPT+4)\*X(2)+A(IPT+5)\*X(3)

1 +A(IPT+6)\*X(4)

YBAR(2)=A(IPT+3)\*Y(1)+A(IPT+4)\*Y(2)+A(IPT+5)\*Y(3)

1 +A(IPT+6)\*Y(4)

XBAR(3)=A(IPT+7)\*(X(3)-X(1))+A(IPT+8)\*X(4)

YBAR(3)=A(IPT+7)\*(Y(3)-Y(1))+A(IPT+8)\*Y(4)

XBAR(4)=A(IPT+9)\*X(1)+A(IPT+10)\*X(2)+A(IPT+11)\*X(3)

1 +A(IPT+12)\*X(4)

YBAR(4)=A(IPT+9)\*Y(1)+A(IPT+10)\*Y(2)+A(IPT+11)\*Y(3)

1 +A(IPT+12)\*Y(4)

IF(NTEMP.GT.7) GO TO 150

DO 140 I=1,4

B(I,NTEMP)=X(I)

D(I,NTEMP)=Y(I)

B(I,NTEMP+7)=XBAR(I)

140 D(I,NTEMP+7)=YBAR(I)

NTEMP=NTEMP+1

GO TO 170

C RESET STORED VALUES OF X , Y AND XBAR , YBAR IN PREPARATION FOR NEXT

C INTEGRATION STEP.

150 DO 160 I=1,4

B(I,1)=B(I,2)

B(I,2)=B(I,3)

B(I,3)=B(I,4)

B(I,4)=B(I,5)

B(I,5)=B(I,6)

B(I,6)=B(I,7)

B(I,7)=X(I)

B(I,8)=B(I,9)

B(I,9)=B(I,10)

B(I,10)=B(I,11)

B(I,11)=B(I,12)

B(I,12)=B(I,13)

B(I,13)=B(I,14)

B(I,14)=XBAR(I)

D(I,1)=D(I,2)

D(I,2)=D(I,3)

D(I,3)=D(I,4)

D(I,4)=D(I,5)

D(I,5)=D(I,6)

D(I,6)=D(I,7)

D(I,7)=Y(I)

D(I,8)=D(I,9)

D(I,9)=D(I,10)

D(I,10)=D(I,11)

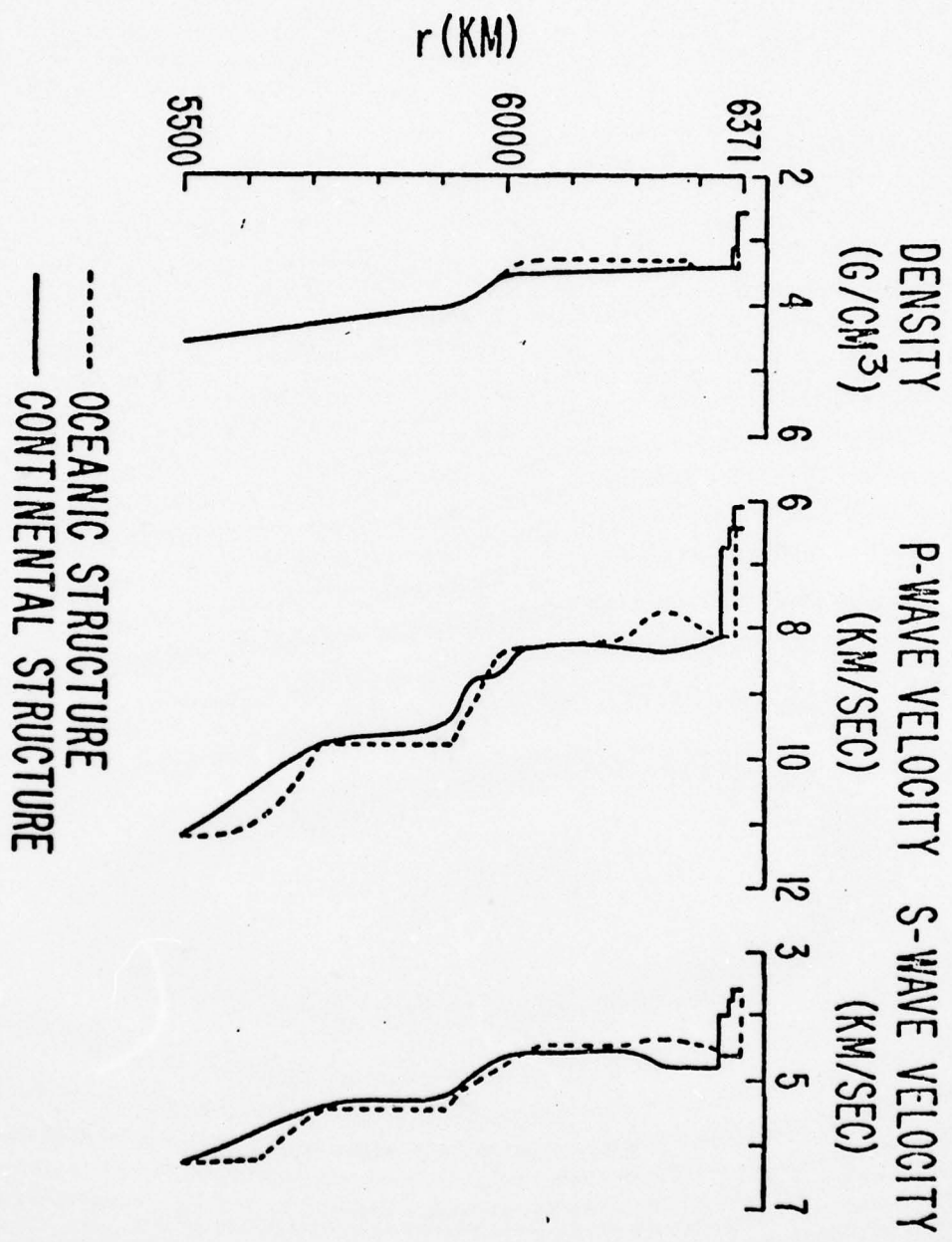
D(I,11)=D(I,12)

D(I,12)=D(I,13)

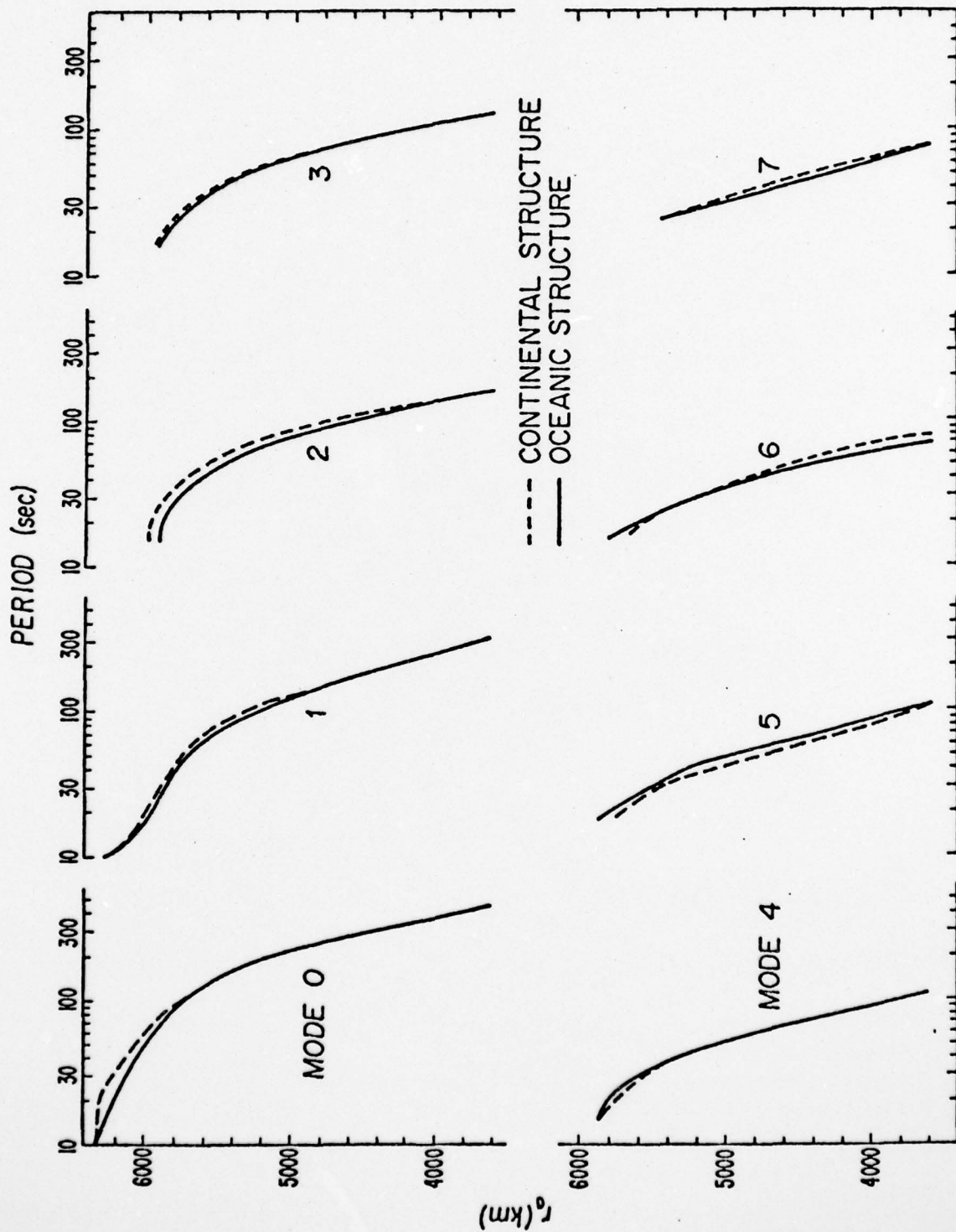
D(I,13)=D(I,14)

160 D(I,14)=YBAR(I)

170 CONTINUE







C NORMALIZATION.

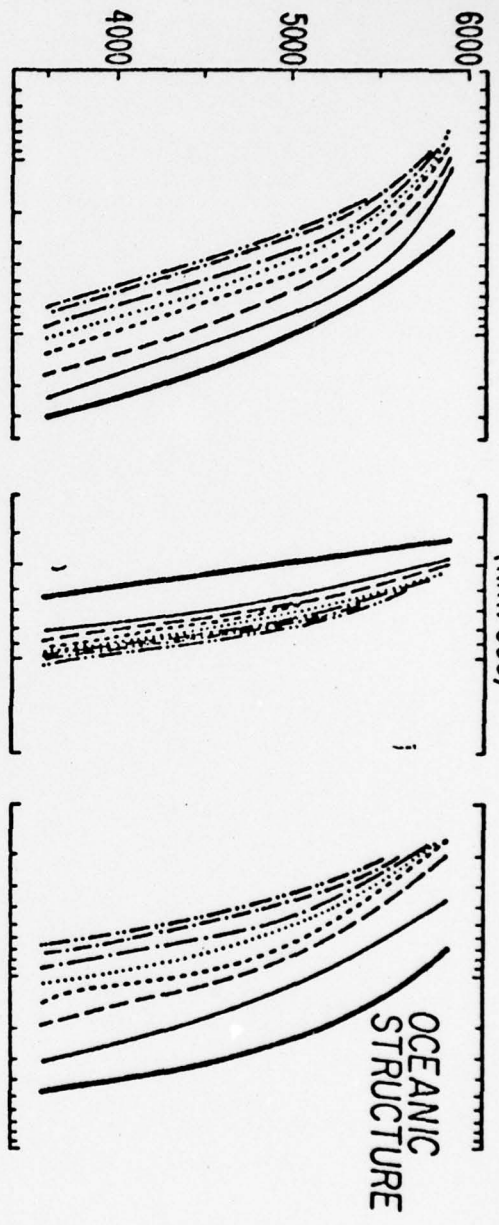
```
      AMXINV=1.0D+00/DMAX1(DABS(B(7,1)),DABS(B(7,2)),  
1      DABS(B(7,3)),DABS(B(7,4)),  
2      DABS(B(7,5)),DABS(B(7,6)))  
      DO 165 I=1,6  
      PMNUSC(I)=PMNUSC(I)*AMXINV  
      Y(I)=Y(I)*AMXINV  
      YBAR(I)=YBAR(I)*AMXINV  
      DO 165 J=1,14  
165  B(J,I)=B(J,I)*AMXINV
```

WAVELENGTH (km)

PHASE VELOCITY  
(km/sec)

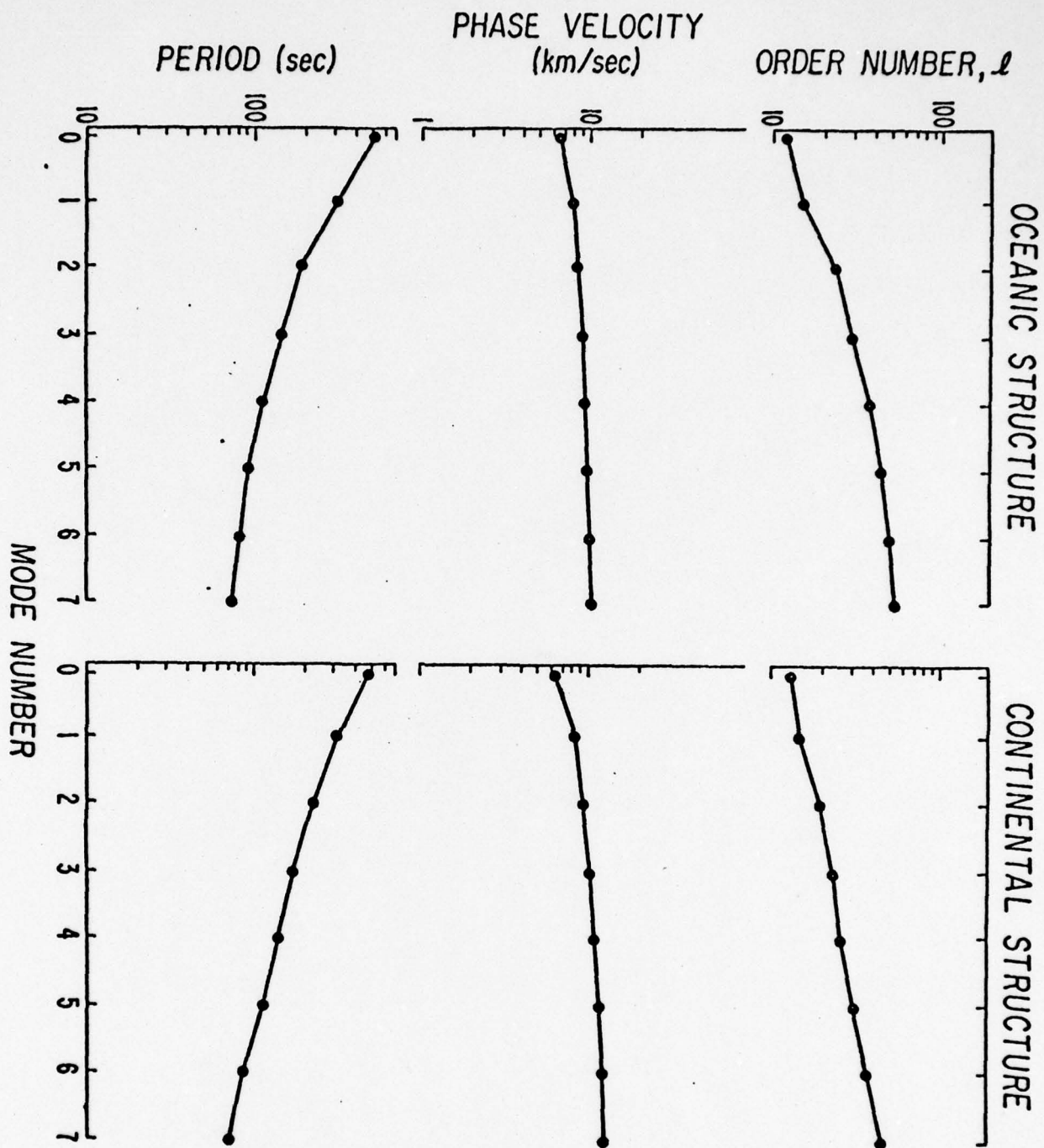
PERIOD (sec)

$r_0$  (km)



MODE 0  
1  
2  
3

MODE 4  
5  
6  
7



150 DO 160 I=1,6

B(1,I)=SNGL(B(2,I))

B(2,I)=SNGL(B(3,I))

B(3,I)=SNGL(B(4,I))

B(4,I)=SNGL(B(5,I))

B(5,I)=SNGL(B(6,I))

B(6,I)=SNGL(B(7,I))

B(7,I)=SNGL(Y(I))

B(8,I)=SNGL(B(9,I))

B(9,I)=SNGL(B(10,I))

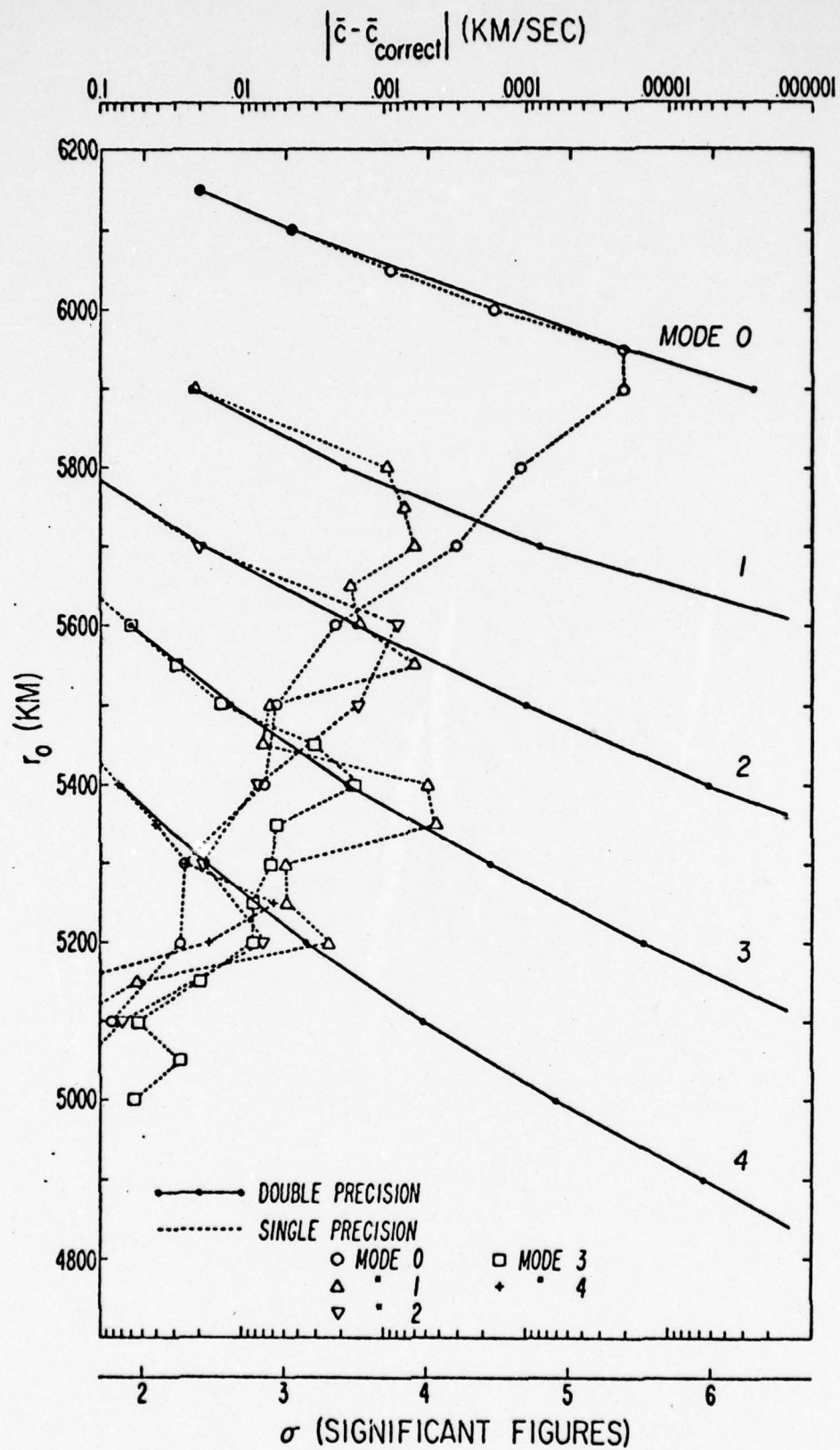
B(10,I)=SNGL(B(11,I))

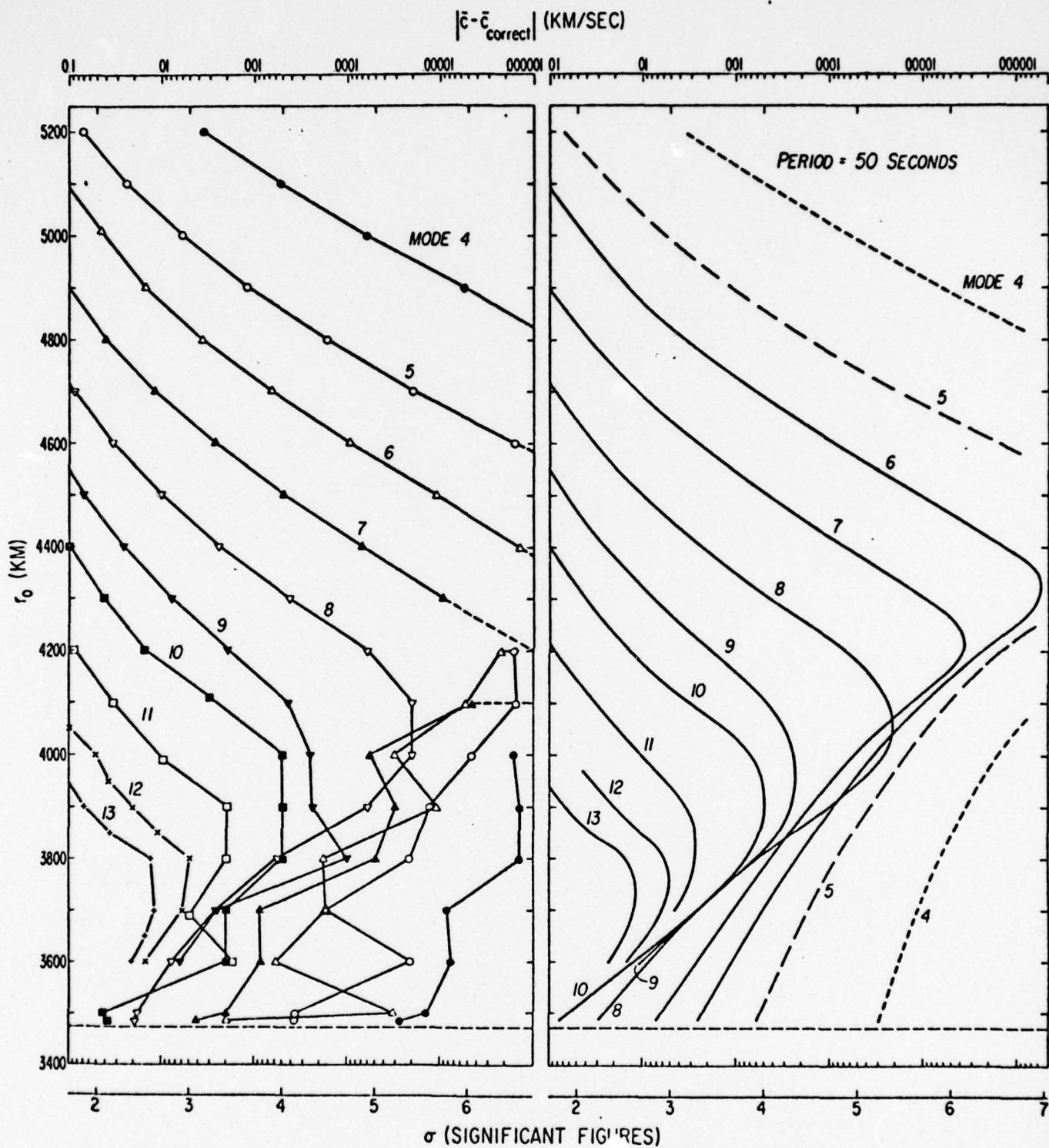
B(11,I)=SNGL(B(12,I))

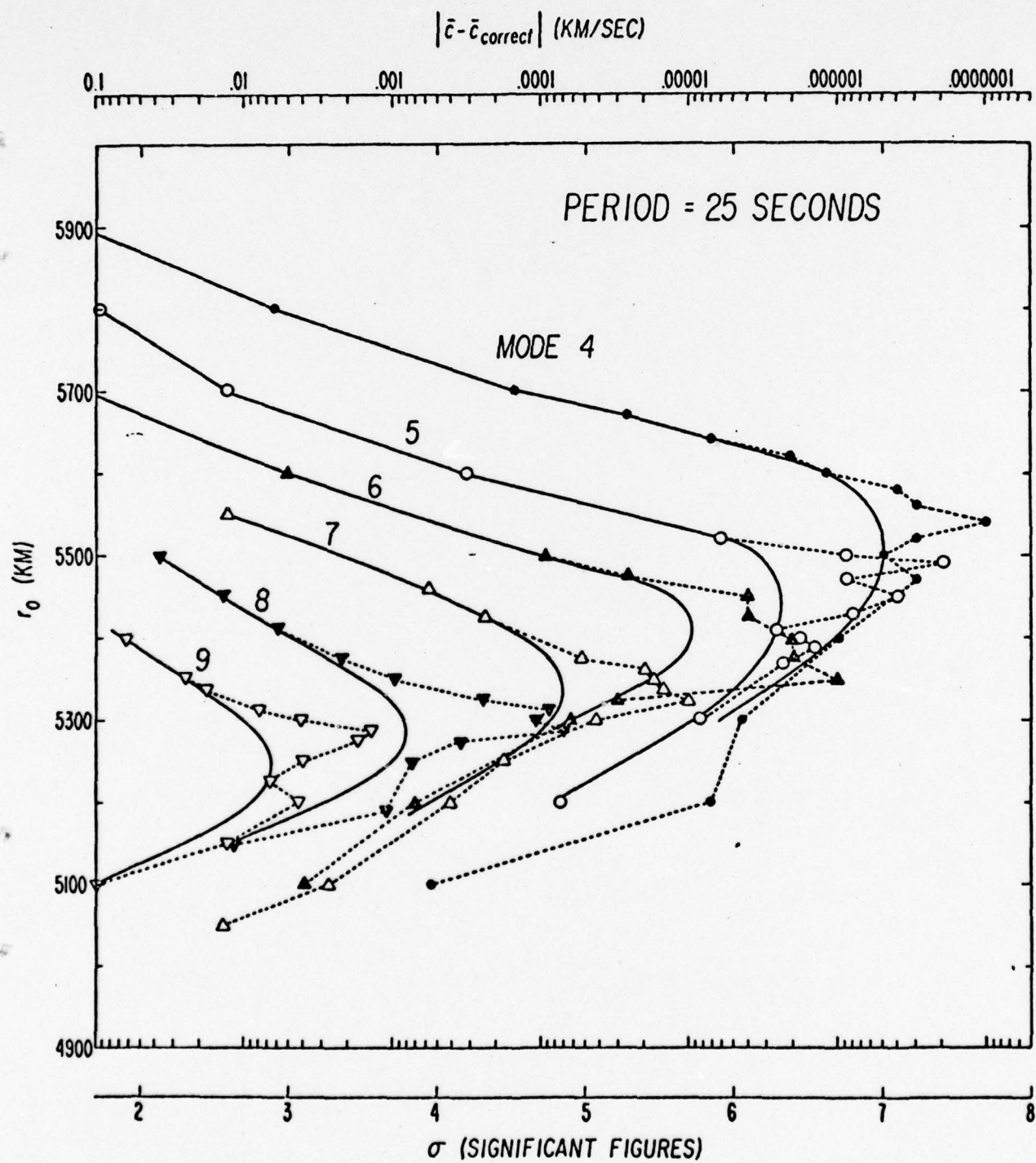
B(12,I)=SNGL(B(13,I))

B(13,I)=SNGL(B(14,I))

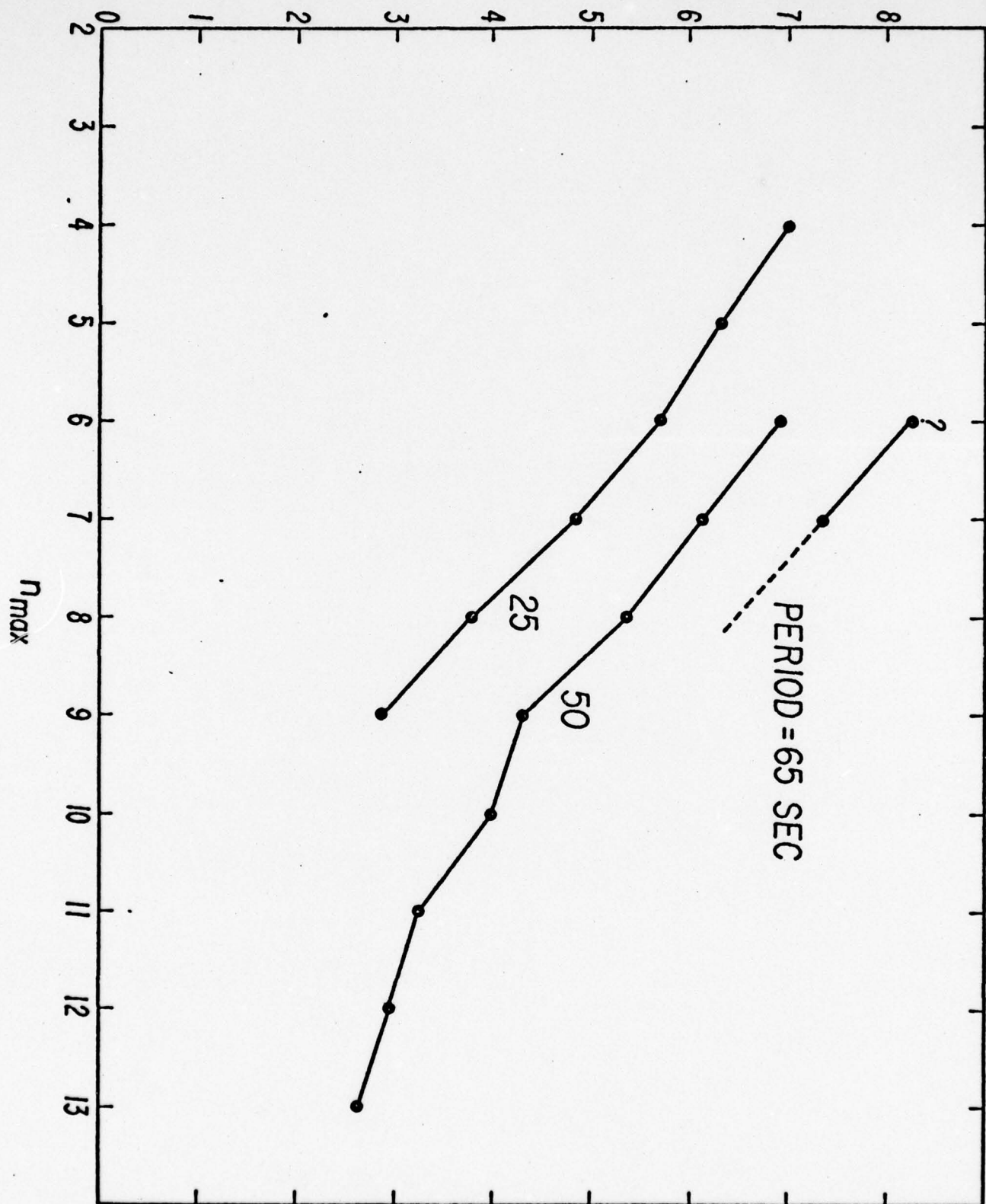
160 B(14,I)=SNGL(YBAR(I))

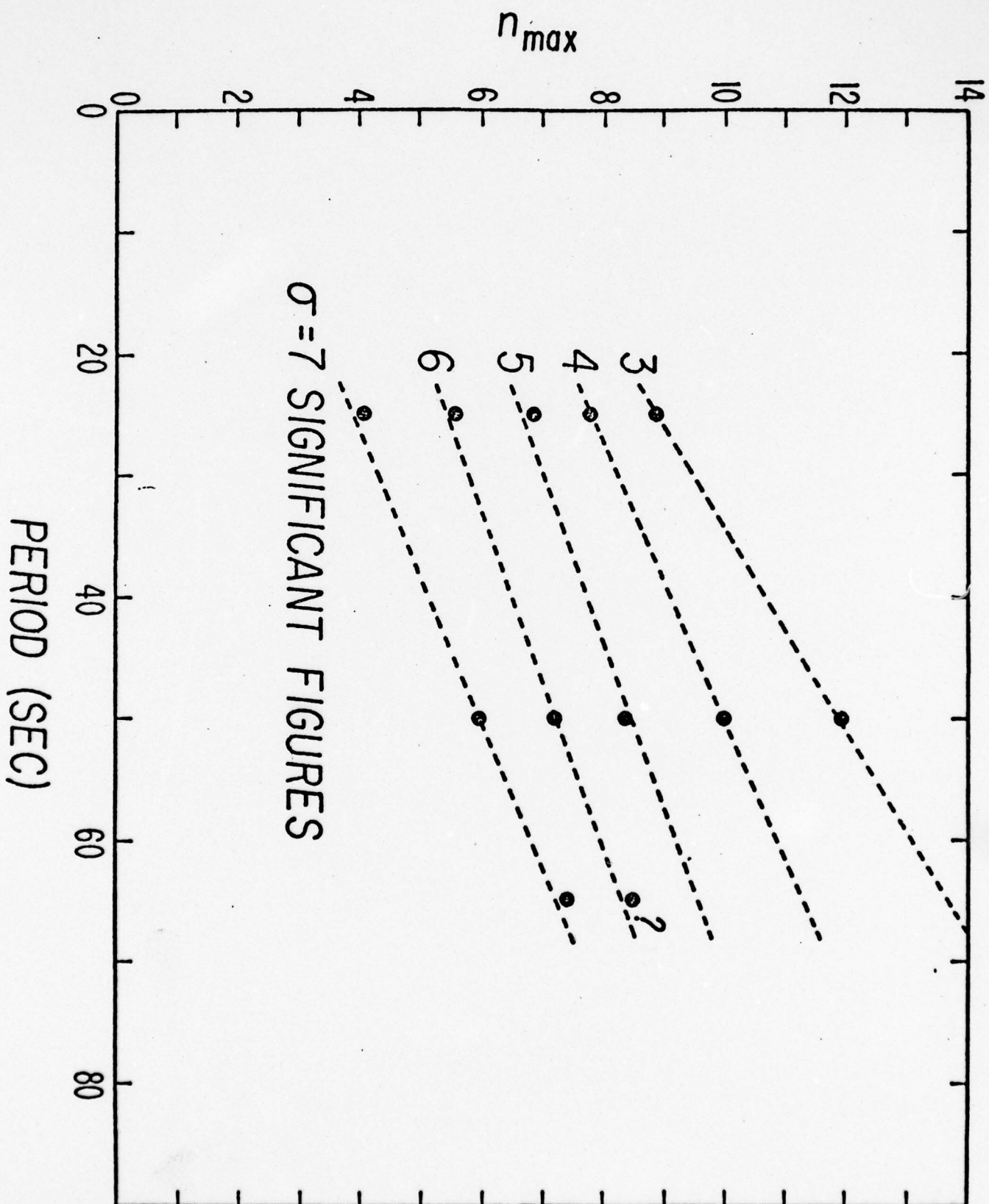






$\sigma$  (SIGNIFICANT FIGURES)





GENERATION OF COMPLETE THEORETICAL SEISMOGRAMS FOR

SH III

Enzo Mantovani\*

Publication No. 1718

Institute of Geophysics and Planetary Physics

University of California, Los Angeles

Publication No. 000, authorized by the  
Director of the Geodynamics Project (CNR), Italy

Sponsored by

Advanced Research Projects Agency (DOD)

ARPA Order No. 3291

Monitored by AFOSR Under Contract #F49620-67-C-0038

\*Osservatorio Geofisico, Università di Siena, Italy

RESEARCH NOTE  
GENERATION OF COMPLETE THEORETICAL SEISMOGRAMS  
FOR SH III  
Enzo Mantovani

Summary

Earlier efforts to generate the entire theoretical seismograms, including both body and surface waves for realistic sources buried in a radially heterogeneous anelastic, spherical Earth, are extended to include the summation of sixteen modes. The comparison between a real seismogram and theoretical time series, relative to different attenuation models in the upper mantle, yields information concerning the anelasticity under the Pacific Ocean.

## Introduction

Complete seismograms which include both body and surface waves for a spherical, anelastic, radially heterogeneous Earth have been generated by simple inverse Fourier transformation of the propagating fundamental and higher-mode surface waves (Nakanishi et al., 1977, Mantovani et al., 1977). Efficient computational algorithms permit us to deal with highly realistic models of the Earth, whose radial heterogeneity is approximated by 200 layers, and to employ 2000 frequency points per radial mode.

## Theoretical seismograms

The tests we report here were carried out on a CIT-11 oceanic structure (Anderson and Toksoz, 1963). The first sixteen Love wave, or torsional modes were used, and for each, the dispersion, attenuation and excitation are computed down to a minimum period of 1 second. The source model we have adopted is a dip-slip displacement dislocation on a vertical fault at a depth of 180 km.

In Fig. 1 we illustrate the improvement in the details of the theoretical seismograms as the number of radial modes used in the synthesis increases. From top to bottom, as the number of modes increases, the amplitude, clarity and short period content are seen to increase for each arrival in a manner corresponding to the depth of penetration of the modes and the depth at which the arrival is produced: the first six modes appear sufficient to reproduce, almost completely, the  $S_a$  surface waves train, that is, the late-arriving, dominant energy whose penetration is limited to approximately 400 km of depth (Kausel et al., 1977); in the second trace, synthesized from the first eleven modes, also the shallow body wave phase  $SS$ , having a group velocity of about 5.7 km/sec, appears to be almost completely formed; in the last trace, synthesized from 16 modes, the deeper body wave phases  $S$  and  $SS$ , i.e., the first bursts on the time series begin to appear as two resolvable pulses, but are still developing in amplitude and short-period content.

The core reflections ScS and sScS, whose penetration is much greater than that of the first 16 modes, at the predominant periods comprising these pulses, are still unrecognizable in the seismograms.

In Fig. 2 we show a range of results out to an epicentral distance of 8000 km; the direct waves and those reflected by the surface of the Earth are recognizable in almost every case; the waves reflected by the core however are represented only by their long period components (see traces for distances of 3000 and 4000 km.). Relative to the corresponding figure in Part II (Mantovani et al., 1977), it is possible to note a general improvement in the impulsive shape and resolution of individual body waves and is particularly clear at short distance in those traces for the 15-100 WWSSN instrument.

The comparison between experimental and theoretical seismograms for 30-100 WWSSN instruments is given in Fig. 3.

Details concerning the event and a preliminary comparison between theoretical and experimental time series using surface waves is reported by Kausel et al. (1977). Our purpose here is to continue the discussion, begun in Part II, on the qualitative aspects of the theoretical - experimental comparison as more and more higher modes are included in the synthesis of the theoretical traces. We also report on some tests of the sensitivity of the amplitudes and arrival times of the pulse bursts to the model of the Earth's intrinsic attenuation and to the source parameters.

In Part II the variation of relative amplitudes of body and surface waves caused by changes in crustal and upper-mantle attenuation was noted, and it was suggested that this effect might be a useful tool in the investigation of the Earth's intrinsic anelasticity. We have used two models of attenuation. Model I is based on model MM8 of Anderson et al. (1965). This model was obtained from measurements of the decay of Rayleigh and Love waves traveling globe circling paths; thus it cannot be expected to be an accurate representation of the anelasticity in a specific oceanic region.

Model II is based on that given by Mitchell (1976) derived from inversion of Rayleigh-wave attenuation measurements in the "older portions of the Pacific crust and upper mantle". Models I and II are shown in Fig.4.

Since the average anelasticity in the first 400 km is very similar for model I (  $Q = 0.00825$  ) and model II (  $Q = 0.00774$  ) the  $S_a$  waves have about the same attenuation. The ratio of amplitudes of  $S_a/S$  is about the same for both models since amplitudes of  $S$  are only slightly affected by variations of anelasticity in a small portion of their path. Since  $S_a$  waves sample the uppermost 400 km of the structure almost uniformly, they are more sensitive to the average attenuation in this region than to its detailed depth distribution.

A comparison of traces A and B (Fig.3), with the help of TABLE 1, indicates that, for a source at 180 km, the relative amplitudes of  $S$  and  $S_a$  are not so different for model I and II. The striking feature of trace B, relative to A, is the remarkable increase in the amplitudes of SS arrivals. It is reasonable to suppose that this effect is connected with the lower attenuation of model II between about 250 and 700 km, that is in that part of the structure in which the SS rays have a significant portion of their path.

A comparison of the well pronounced SS phase in trace B, with even the largest amplitudes around the same arrival in the experimental series, leads us to suspect that model II has a drop in attenuation which is too large between 250 and 700 km of depth (Fig.4).

On the basis of the results shown in Fig.1, we infer that the above observations are little affected by the finite number of radial modes used in this study since the phase SS appears to be converging both to a definitive wavelet form and amplitude.

A final note in this series, which will describe theoretical seismograms generated by even more radial modes, will give more information on this point.

To investigate further the effect produced by changes in the average anelasticity of the crust and upper mantle, we generated time series (Fig.3, trace C) corresponding to an anelasticity distribution derived from model I, but with the phase attenuation  $B_2$ , reduced to 0.000700 sec/km from the top of the low-velocity channel down to the 400 km discontinuity. Comparison of traces C and A shows an appreciable decrease in the amplitude ratio  $S/S_a$ , and a significant increase of the energy in the tail of the  $S_a$  wave train.

As a limiting case for the anelasticity tests we have also exhibited the time series (Fig. 3, trace D) for a perfectly elastic Earth. In this case, for reasons reported in Part II, the surface waves completely dominate those body waves that penetrate deeply.

The phases SS show a less drastic decrease in amplitude because they are relatively strongly affected by the high attenuation in the upper mantle.

To give a representation of the effect, on the time series, produced by variations in source depth, we present theoretical seismograms (Fig. 3, trace E) for a source at 10 km depth.

res as traces A,B,C,D but with a focal depth of 140 km. We see that variation of the source depth has an effect on the arrival times and the amplitudes of body waves; the feature of the time series, which is most sensitive to the source depth, at least for the focal and structural parameters we used, is the amplitude of the SS phase.

Aknowledgments

I am very greateful to Prof. Leon Knopoff and to Fred Schwab for critically reading the manuscript and for the useful suggestions.

This work was supported by the Italian Research Council(CNR) Geodynamics Project under Contract n. 7600.902.89 . The research was also partly supported by the advanced research Projects Agency Department of Defense and was monitored by the Air Force Office of Scientific Research under Contract n. F49 620-76-C-0038, and was partly supported by the Earth Sciences Section, National Science Fundation, NSF Grant EAR 75-04376.

### FIGURE CAPTIONS

- Fig. 1 Representation of the effect of adding more higher (radial) modes in the synthesis of theoretical seismograms recorded at the surface of the Earth. Source mechanism is a dip slip displacement dislocation on a vertical fault at a depth of 180 km. Epicenter-station separation is 6788 km. The model we have used for the intrinsic anelasticity of the Earth is an adaptation (Fig.4) of model MM8 (Anderson, Ben Menahem & Archambeau, 1965) to our oceanic structure.
- Fig. 2 Torsional-wave response, at the surface of the Earth, to a dip-slip displacement dislocation on a vertical fault, at a depth of 180 km. The expected body-wave arrival times are indicated for S( $\bullet$ ), SS( $\blacktriangle$ ), ScS( $\blacktriangledown$ ), SS( $\blacksquare$ ), sScS( $\blacklozenge$ ). See caption of Fig.1 for anelasticity model.
- Fig. 3 Comparison of theoretical and experimental seismograms for 30-100 WWSSN instruments, 6788 km from the epicenter; short traces are copies of the long-period experimental record (SH) measured at Honiara (HNR) for the event occurring at the foot of the Kamchatka peninsula at 14:30:30.3 GCT on 1964 December 26 (See Kausel et al., 1977 for full details on this event, our theoretical treatment of the source mechanism, and the analysis of the S<sub>a</sub> portion of the time series). Traces denoted by capital letters are theoretical seismograms: trace A represents the anelasticity Model I (Fig. 4); trace B, anelasticity Model II (Fig. 4); trace C, Model I with the phase attenuation  $B_2$  reduced to 0.000700 sec/km from the top of the low velocity channel down to the "400-km" discontinuity; trace D does not include attenuation in the Earth model. Traces

E, F, G, and H represent the same models respectively as A, B, C and D but with the source depth reduced from 180 to 140 km.

Fig. 4 S-wave velocity structure, transverse-wave phase attenuation  $B_2$ , and intrinsic attenuation  $Q^{-1}$ , obtained from the adaptation, to our velocity structure, of two anelasticity models reported in the literature: (I) world-wide average model (Anderson, Ben Menahem, Archambeau, 1965), (II) Oceanic model (Mitchell, 1976). Model I is given by solid lines, Model II by dotted lines .

TABLE 1

Amplitude-ratios  $S/S_a$  and  $SS/S_a$  measured, peak to peak, on the traces A, B, C, E, F and G in Fig. 3.

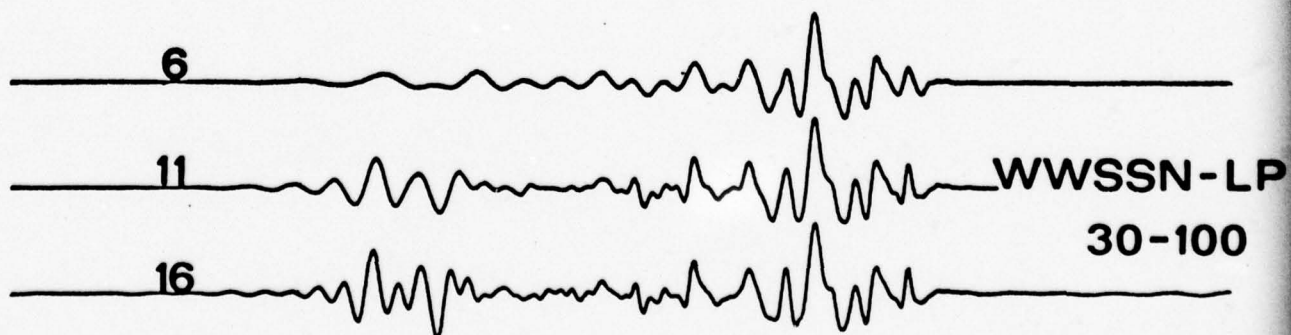
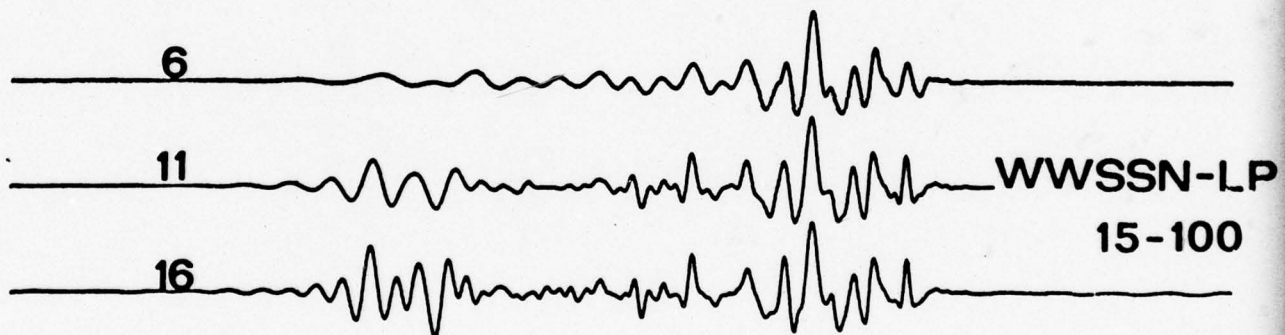
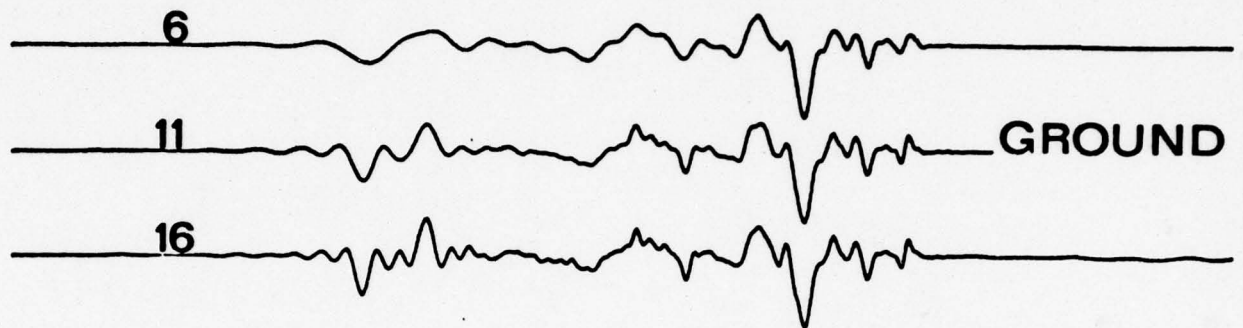
	180 km			140 km		
	A	B	C	E	F	G
$S/S_a$	0.66	0.62	0.54	0.59	0.50	0.43
$SS/S_a$	0.27	0.39	0.25	0.48	0.58	0.41

# REFERENCES

- Anderson D., L., Ben-Menahem A. & Archambeau C.B., 1965- Attenuation of seismic energy in the upper mantle. J. geophys. Res., 70 , 1441-1448.
- Anderson D.D. & Toksoz M.N., 1963- Surface waves on a spherical earth. 1. Upper Mantle structure from Love waves. J. Geophys. Res. 68, 3483-3500.
- Kausel E., Schwab F., Mantovani E., 1977 - Oceanic Sa. Geophys. J.R. Astron. Soc. in press.
- Mantovani E., Schwab F., Liao H., Knopoff L. 1977- Generation of complete theoretical seismograms for SH.II. Geophys. J.R. Astr. Soc. 48, 531-536.
- Mitchell B.J., 1976 - Anelasticity of the Crust and Upper Mantle beneath the Pacific Ocean from the Inversion of Observed Surface wave attenuation. Geophys. J. R. Astr. Soc. 46, 521-533.
- Nakanishi K. , Schwab F. & Knopoff L., 1977 - Generation of complete theoretical seismograms for SH I. Geophys. J. R. Astr. Soc. 48, 525-530.
- Schwab F. & Kausel E.G., 1976 - Long period surface wave seismology: Love wave phase velocity and polar phase shift. Geophys. J.R. Astr. Soc. 45, 407-435.

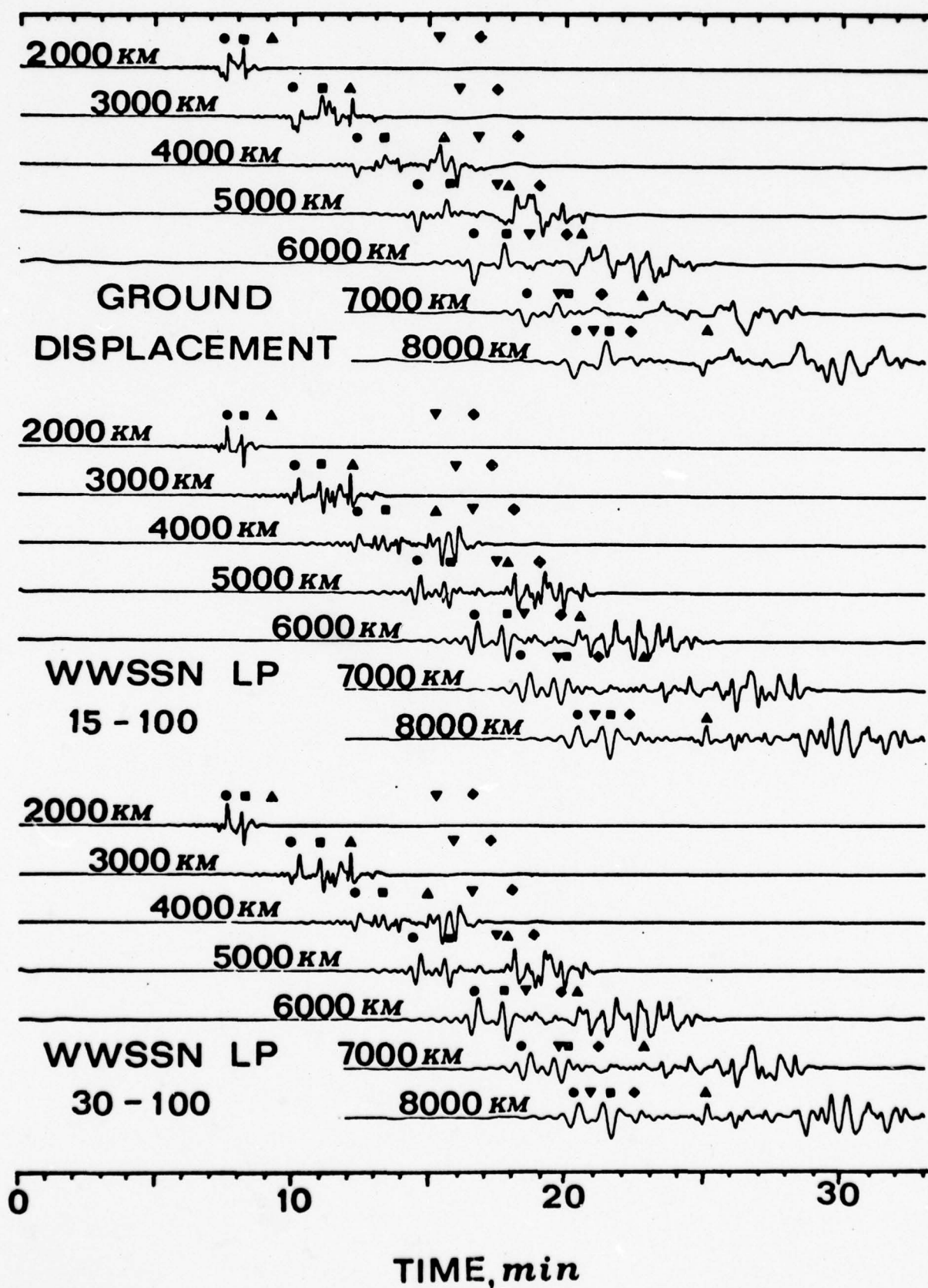
GROUP VELOCITY (KM/SEC)

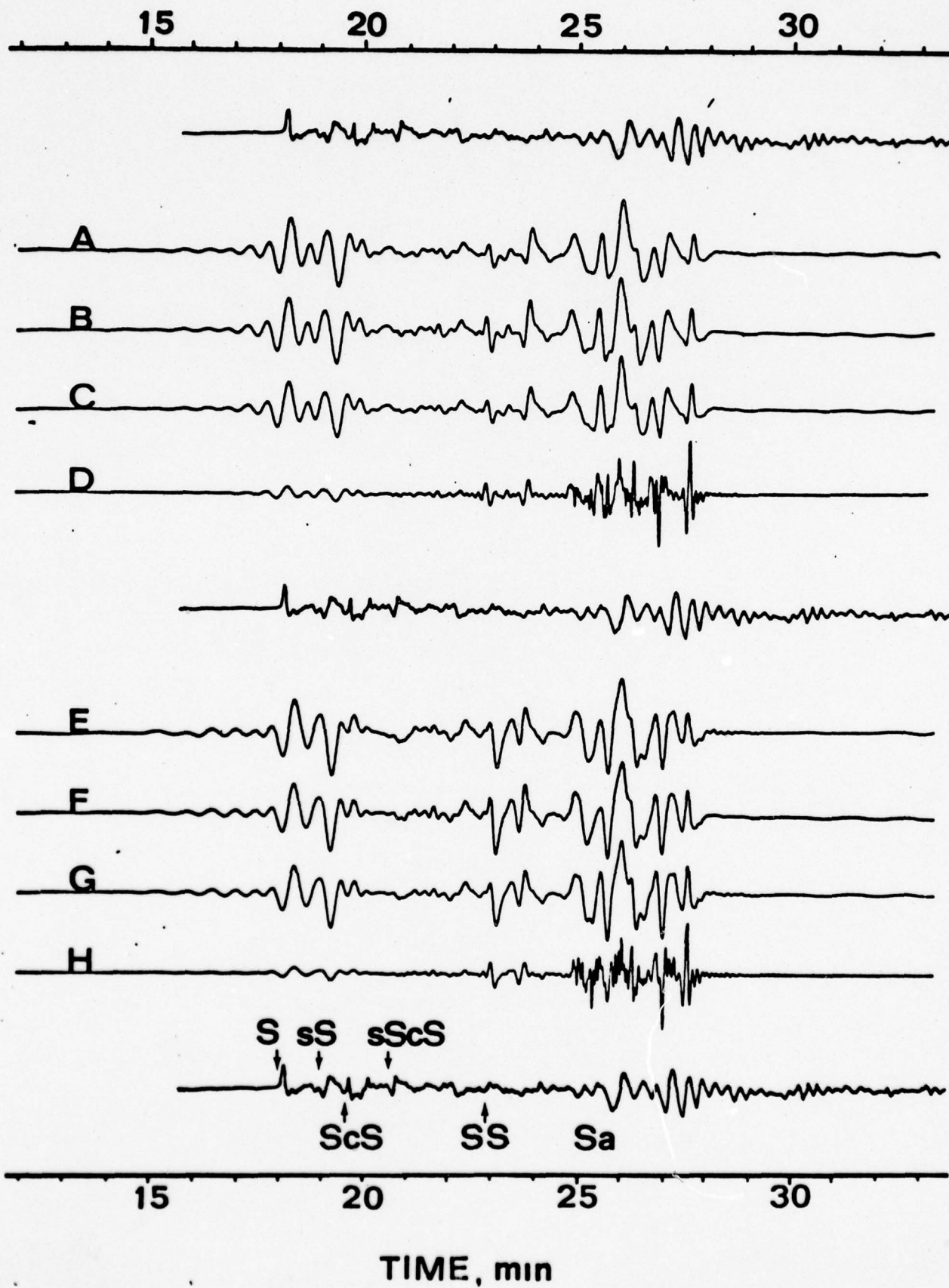
8 7 6 5 4

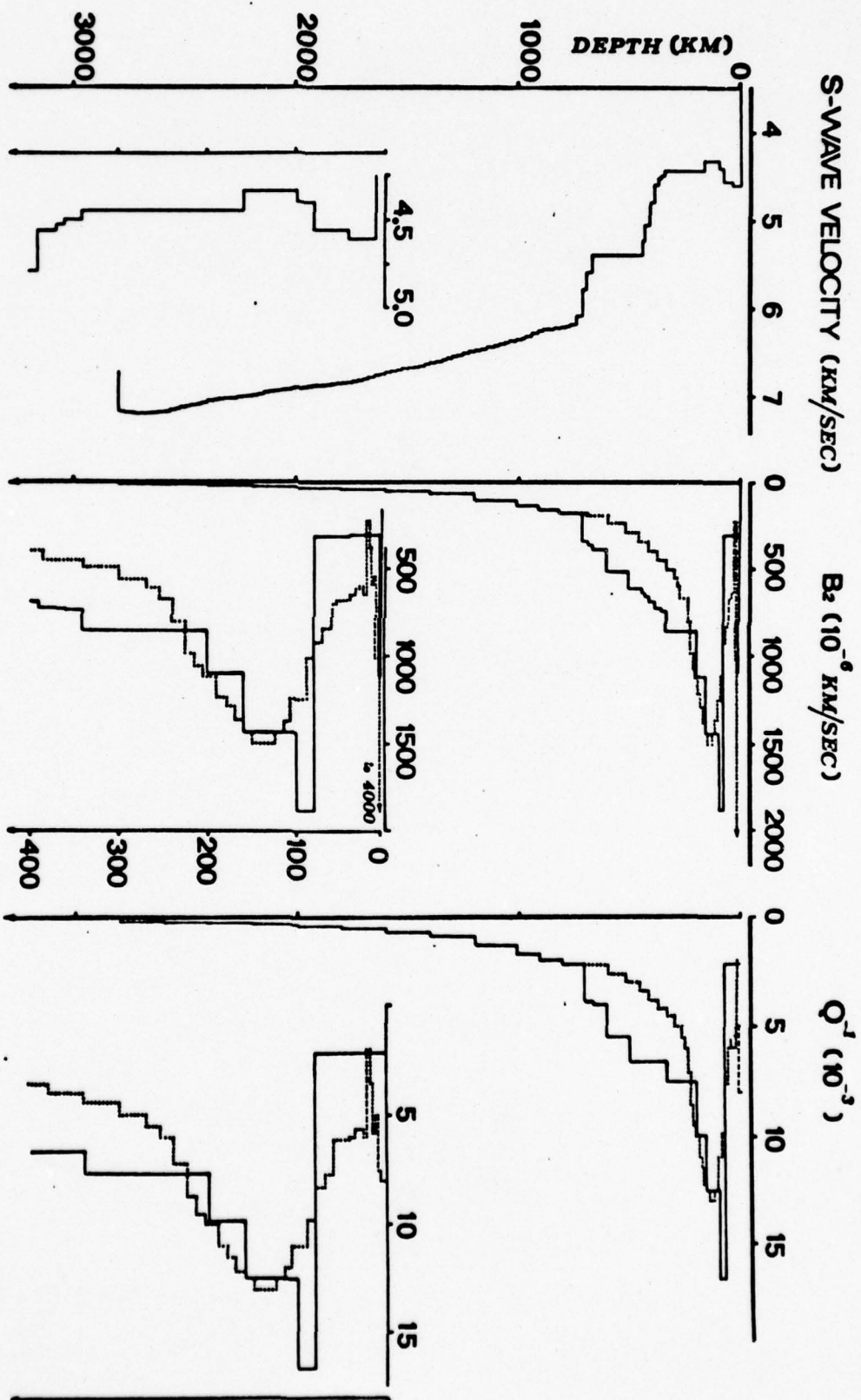


15 20 25 30

TIME, min







DETERMINATION OF SEISMOMETER INSTRUMENTAL PARAMETERS  
BY GENERAL LINEAR INVERSION

Robert Mitchel\*

Sponsored by  
Advanced Research Projects Agency (DOD)  
ARPA Order No. 3291  
Monitored by AFOSR Under Contract F49620-67-C-0038

\*Gulf Research and Development, P.O. Drawer 2038,  
Pittsburgh, Pennsylvania 15230

# DEFINITIONS OF QUANTITIES USED IN THIS PAPER

- $\theta$  Angular deflection of seismometer boom in radians  
 $\phi$  Angular deflection of galvanometer mirror in radians  
 $\omega_1$  Angular frequency of seismometer free period,  $= 2\pi/T_1$ , (radians/sec)  
 $\omega_2$  Angular frequency of galvanometer free period,  $= 2\pi/T_2$ , (radians/sec)  
 $\epsilon_1$  Seismometer damping parameter,  $= h_1 \cdot \omega_1$   
 $\epsilon_2$  Galvanometer damping parameter,  $= h_2 \cdot \omega_2$   
 $h_1$  Seismometer damping constant (1.0 = critical damping)  
 $h_2$  Galvanometer damping constant (1.0 = critical damping)  
 $\sigma_1$  Seismometer coupling constant  
 $\sigma_2$  Galvanometer coupling constant  
 $\sigma^2 = \sigma_1 \cdot \sigma_2$ , coupling constant between seismometer and galvanometer  
 (1.0 = direct coupled)  
 $M_1$  Seismometer boom mass (kilograms)  
 $H$  Distance between center of gravity of mass and rotation point  
 of seismometer boom (meters)  
 $K$  Moment of inertia of seismometer boom ( $\text{kg-m}^2$ )  
 $x$  Displacement of the ground (meters)  
 $K = G i_p / M_1$ , magnitude of the force impressed on the boom by  
 the calibration current (Newtons)  
 $i_p$  Calibration current (milliamperes)  
 $G$  Motor constant of the calibration coil (Newtons/Ampere)  
 $X_{ip}$  Height of the impulse response as measured on the record (milli-  
 meters)  
 $H(t)$  Heaviside step function of time  
 $\delta(t)$  Dirac delta function of time  
 $T_1', T_2', h_1', h_2'$  Pseudoparameter forms of the seismometer and galvanome-  
 ter free periods and dampings

- T The time at which the calibration current was switched on
- A An apparent amplitude factor that is determined in the inversion
- C A constant term to be subtracted from the digitized data to give best agreement with theoretical impulse responses
- L A linear trend to be subtracted from the digitized data to give best agreement with theoretical impulse responses
- $\theta$  A rotation to be applied to the impulse response to correct for incorrect digitizing of the impulse

## IMPULSE RESPONSE INVERSION

Quantitative time series analysis using the World-Wide seismic network records (WWSSN) requires that corrections be made for the response of the seismograph. In the usual method of calculation of instrumental corrections the seismograph is considered as a black box. From Fourier analysis of the response to a known transient impulse (usually a step function in acceleration applied to the seismometer mass) corrections can be obtained. In general, at frequencies in the neighborhood of the peak instrumental response this is an accurate method of correction. However, periods shorter than the seismometer free period are not strongly excited in the impulse response and significant errors in the computation of ground motion may occur.

Studies involving short period crustal and higher mode surface waves have obliged us to seek an alternative method of determining these corrections, in order to reduce errors caused by instrumental uncertainties. The parameters of the seismometer system have been determined directly using a linear inversion method. Mitchell and Landisman's (1969) analytical expressions can then be used to derive the phase and amplitude corrections at all periods. This method uses a stabilized least-squares technique which allows more parameters to be used while maintaining convergence in the inversion process. Arbitrary values of the coupling constant and the seismometer period can be used in this form of the calculation. Also, the scale factor determined in the inversion can be used to obtain an expression for seismograph magnification that is independent of the rated value.

The procedure for inversion (Jackson, 1972) involves solving a system of linear equations for the corrections  $\Delta x_j$  to the model parameters. In our case these parameters are the seismograph instrumental constants. The equations are set equal to the data residuals  $\Delta y_i$  which are the residuals between the data and the predictions from the model. The linear equations take the form

$$\Delta y_i = A_{ij} \Delta x_j + \epsilon_i$$

where the matrix  $A_{ij} = \partial y_i / \partial x_j$ , the partial derivatives of the data residuals with respect to the model parameters. The least-squares solution results from the straightforward minimization of the error residuals (Mitchell and Landisman, 1969). They noted that the inclusion of too many parameters tended to cause instabilities in the inversion. Thus certain parameters, such as the scale factor and impulse 'on' time, had to be empirically adjusted in the inversion. In our experience with digitizing actual impulse responses there is error introduced due to baseline choice, and so a constant, linear trend, and rotation parameters were introduced. Although all the partial derivatives have linearly independent components, in the presence of noise not all of them can be resolved, and an unstable inversion resulted using least-squares method with the nine parameters listed in figure 1. The inversion was stabilized by decreasing the degrees of freedom in the inversion (Wiggins, 1972). The  $A_{ij}$  matrix of partial derivatives is first normalized with respect to the data standard deviations and a priori uncertainties assigned to the model parameters. The matrix, now in normal form (Jackson, 1972), is factored according to the Lanczos factorization (Lanczos 1961) into eigenvalue and eigenvector matrices. In this form eigenvalues less than 1.0 correspond in some sense to parameter combinations that cannot be

resolved from the data, and so these eigenvalues are set to zero, removing these degrees of freedom from the inversion. In general the number of independent degrees of freedom in the inversion when this was done was six or seven. All the parameters necessary to obtain phase and magnification information were obtainable, but careful digitization was necessary to insure good results.

### COMPUTATIONS

The actual computation of the partial derivatives was done using an analytical formula for the impulse response as a function of the parameters. Mitchell and Landisman(1969) used the inverse Fourier transform of the frequency domain representation of the impulse response to calculate the partial derivatives. While this has certain advantages, I felt that the number of Fourier transforms needed per inversion would be a significant cost factor even with FFT, and so a method was followed as illustrated in figure 2. Starting with the representation of the seismometer and galvanometer as coupled damped harmonic oscillators, the equation of motion of the rotation of the galvanometer is solved by inverse Laplace transform. The magnitude of the impulse given to the mass,  $K$ , is just  $G_0/M$ . Jarosch and Curtis (1973) noted that the denominator cannot be factored unless the term containing  $\sigma^2$  is set to zero. When this is done the pseudo-parameter equation can be solved uniquely to obtain new values of  $\omega_1, \omega_2, \xi_1, \xi_2$ , and we call the new values of  $T_1, T_2, h_1, h_2$  the 'pseudoparameters'. As can be seen from the figure, the effect of this conversion is small for  $\sigma^2$  small, but may be significant for larger  $\sigma^2$ .

Furthermore, the pseudoparameters become complex for larger

We can obtain finally an analytic expression for the impulse response:

$$\phi(t) = \frac{K}{\left\{ \left[ (\xi_1' - \xi_2')^2 + K_1^2 - K_2^2 \right]^2 + 4K_2^2 (\xi_1' - \xi_2')^2 \right\} \left\{ \left[ 2(\xi_1' - \xi_2') \cos K_1 t + \left[ (\xi_1' - \xi_2')^2 + K_2^2 - K_1^2 \right] \frac{\sin K_1 t}{K} \right] e^{-\xi_1' t} + \left[ 2(\xi_1' - \xi_2') \cos K_2 t + \left[ (\xi_1' - \xi_2')^2 + K_1^2 - K_2^2 \right] \frac{\sin K_2 t}{K_2} \right] e^{-\xi_2' t} \right\}}$$

where  $K_1 = \sqrt{\omega_1'^2 - \xi_1'^2}$ ,  $K_2 = \sqrt{\omega_2'^2 - \xi_2'^2}$

This will be in general complex-valued for complex parameters;

the real part corresponds to the impulse response function.

If the seismometer or galvanometer becomes critically damped,

we must remember that  $K_1 = 0$  or  $K_2 = 0$ , and so

$$\frac{\sin K_1 t}{K_1} = t, \quad \frac{\sin K_2 t}{K_2} = t; \quad \cos K_1 t = 1, \quad \cos K_2 t = 1.$$

For the case when the seismometer or galvanometer is overdamped,

$K_1$  or  $K_2$  becomes complex, and so the appropriate sin and cos are replaced by sinh and cosh. In figure 3 are some impulse responses calculated using the above formula. The reference impulse response corresponds in some way to a standard WSSN instrument.

Some notion of what the partial derivatives look like can be gained from this figure. The effect of changing the seismometer free period can be seen to be very similar to the effect of changing the gain, or amplitude factor of the impulse response. This effect can be seen in the Lookout Mountain calibration tests, in which two different impulse responses from the instrument were inverted independently. The seismometer free period values show somewhat larger discrepancies than the other parameters. The theoretical values for the parameters compare very well with those determined experimentally using the usual tests for damping and

free period. In the case of the galvanometer constants, there is a very good argument for determining the constants through inversion rather than by other methods, since this seems to be at least as accurate and does not disturb the instrument in any way.

The seismometer constants, especially the free period, are probably better determined by other experimental methods, and constrained in the inversion. Once the instrumental constants are determined, the instrumental effects on amplitude and phase can be determined theoretically. Following Mitchell and Landisman (1969) the phase can be written as:

$$\phi(\omega) = \tan^{-1} \left[ \frac{\omega^4 - [\omega_1^2 + \omega_2^2 + 4\varepsilon_1\varepsilon_2(1-\sigma^2)]\omega^2 + \omega_1^2\omega_2^2}{2(\varepsilon_1 + \varepsilon_2)\omega^3 - 2(\varepsilon_1\omega_2^2 + \varepsilon_2\omega_1^2)\omega} \right]$$

The convention here is that  $d\phi/d\omega$  is positive, which corresponds to positive instrumental group delay time. The magnification of the instrument can similarly be expressed in terms of the parameters of the instrument:

$$M(\omega) = \frac{AM\omega^3/(Gi_p)}{\left\{ [\omega^4 - (\omega_1^2 + \omega_2^2 + 4\varepsilon_1\varepsilon_2(1-\sigma^2))\omega^2 + \omega_1^2\omega_2^2]^2 + [-2(\varepsilon_1 + \varepsilon_2)\omega^3 + 2(\varepsilon_1\omega_2^2 + \varepsilon_2\omega_1^2)\omega]^2 \right\}^{1/2}}$$

$A$  is the inversion gain constant,  $i_p$  is the calibration coil current, and  $G$  is the motor constant of the coil. For WSSN stations there is an empirical formula for the gain at the seismometer free period:

$$M = \frac{0.449 \chi_{ip}}{Gi_p} \quad \text{for } T_1 = 15 \text{ seconds;}$$

$$M = \frac{0.135 \chi_{ip}}{Gi_p} \quad \text{for } T_2 = 30 \text{ seconds}$$

$\chi_{ip}$  is the height of the impulse response in millimeters. This formula was checked against the analytical formula for gain and agreement to a few percent or better was found. However, the

empirical formula assumes all the constants are at the rated values and so a badly tuned instrument would give erroneous gains.

A long period WSSN station, NDI-LPZ, was used in inversion to get instrumental parameters. The amplitudes in the impulse response must be multiplied by  $\omega^3$ , to get the ground magnification. This means that the gains at the long period end are well determined, where the original impulse had a strong signal. However, below 30 seconds period the amplitudes become relatively worthless and it is advisable to use the theoretical values. The same considerations hold for the phases. An additional source of error in the phase of the impulse is introduced because the 'on' time of the impulse is not known a priori, but must be estimated from the record. An error of one second or more is common here. This leads to a systematic bias in the phases determined as can be seen in figure 5, where the empirically determined 'on' time is wrong by one second. No bias is evident in the phases derived using the 'on' time from inversion.

A note concerning baseline determination is relevant here. Although it was not possible in the inversion to use the rotation as an independent parameter, the rotation is quite important, especially for very large, steep impulses, and a wrong baseline will distort the constants obtained and resultant phases quite badly. However, drawing the correct baseline is not just a matter of connecting the ends of the trace and making sure the impulse does not occur in a disturbed part of the record. Figure 7 shows an impulse on our instrument. The minute marks line up, which makes it easy to notice the offset of the minute mark near the top of the pulse. This is probably due to a lens misalignment. This effect may be

common among WSSN instruments, as noted by James and Linde (1971). What I did for this was to rotate the impulse on the digitizer until the minute marks on the pulse fell at equal intervals on the digitizer scale. This meant that the digitizer scale was then aligned parallel to the direction of motion of the galvanometer light beam. Digitizing the impulse in this manner gave satisfactory results even for large impulse responses.

Some conclusions I have reached in this work are that the application of a generalized inversion scheme to instrument impulse responses allows inclusion of more parameters without sacrificing the stability and validity of the inversion. In particular, the use of the amplitude factor allows an independent measure of the magnification to be made. The inclusion of the 'on' time means that this source of phase error can be practically eliminated. The constant and linear trend terms are important because of digitizing considerations in which a baseline must be assumed and later corrected for. Careful digitizing is necessary to assure that the correct baseline is used.

Noise on the record during the impulse response did not seem to be a significant factor in the inversion. In general I chose only impulses that occurred during clear, quiet times and without visible noise except for microseisms. Examining the residuals that remain after inversion, I found that much of the error seemed to be associated with digitizing errors on the steep parts of the impulse. This is unavoidable because of the steepness of the pulse and the uncertainty in the digitizer scale. The largest magnitude of these errors appeared to be of the order of 1% of the impulse height

for good impulses that had successful inversions. These errors did not appear to cause much error in the parameters determined as shown by the good agreement between independent impulse inversions from the same instrument.

#### ERROR ANALYSIS AND CONCLUSIONS

Errors in the determination of parameter values are of several different types. One type of error arises because of the finite line thickness and other digitizing errors, and because of microseisms and other types of noise present on the record. These effects can all be included as noise in the impulse response signal. Figure 8 shows the results of inversion of theoretical and actual impulse responses. Random noise (white noise) was added to one theoretical impulse and inversion was done. Convergence of error to the noise level was quite rapid, and after that essentially no change took place. Similar results were obtained for two actual impulses, LM0-2 and NDI-LPZ. The digitizing noise level was obtained by an estimation of the random error to be about .14 mm on the record on the average. However, in the steep parts of the impulse the errors became greater, and residuals of amplitude equal to about 1% of the impulse response amplitude (about 1 mm) were occasionally seen. Since the steep regions of the impulse response are most critical in determination of the instrumental parameters, this upper bound was taken as the representative noise level in the analysis of propagation of errors. The effect of

random errors in the data on the parameters was estimated by computing the covariances of the model parameters by the method of Jackson (1972):

$$\text{var}(\hat{x}_k) = \sum_{i=1}^n H_{ki}^2 \text{var}(y_i)$$

The matrix  $H$  is  $= V K' U^{-1}$ , the general inverse of the matrix of partial derivatives. The results obtained using 1 mm as the random error are shown in table 1. The instrumental parameters for LMO-1 and LMO-2 appear to agree within the uncertainties given for the parameters, although the errors in the data may not actually be random as assumed. The errors on the seismometer and galvanometer free periods are about equal for the severely underdamped case, LMO-1 and LMO-2, but change for the overdamped case, LMO-NEW. The impulse response was activated by an automatic relay at exactly 12-hour intervals. There appears to be some difference between the 'on' times of the impulses LMO-1 and LMO-2 on the seismogram, as judged by measurements relative to the minute marks. This may account for the difference between the  $T_0$  times of LMO-1 and LMO-2 impulse responses.  $\theta$ , the rotation, was constrained to equal zero throughout the inversions.

Another type of error is not random, and results because the seismometer free period and the amplitude scale parameter  $A$  cannot be resolved from the data. Because of this trade-off effect, errors due to lack of resolution will have little effect on the calculated magnifications or phases. It could be corrected by

constraining  $T_1$  in the inversion, since this parameter can be accurately measured. Table 2 shows the result of constraining  $T_1$  by adding in the parameter eigenvector to the solution.  $T_1$  and  $A$  have both been made consistent by this procedure.

Some conclusions that can be drawn from this work are that application of generalized linear inversion to seismograph impulse responses to derive the instrument constants yields useful and consistent results, and makes possible more accurate estimates of gain and phase shift at short periods. An independent means of deriving the gain as a function of period is possible using the inversion amplitude parameter. Errors in phase due to uncertainty in impulse 'on' time are reduced. There is a trade-off of  $T_1$ , the seismometer free period and  $A$ , the gain constant, but these can be resolved by constraining  $T_1$ , which is in general well-known. Noise caused by digitizing errors or microseisms does not appear to be a problem in this work. The residuals were usually of amplitude less than 1% of the original impulse amplitude. It was necessary to take great care in choosing the correct baseline for digitizing. Application of the inversion technique to actual impulse responses yielded consistent results and enabled amplitude and phase shifts to be calculated at all periods.

## BIBLIOGRAPHY

Burdick, L. and G. Mellman, The response of the WWSSN short period seismometer (in press).

Espinosa, A.F., G.H. Sutton and H.J. Miller, S.J., A transient technique for seismograph calibration - manual and standard set of theoretical transient responses, VESIAC special report No. 4410-106X.

Hagiwara, T. (1958), A note on the theory of the electromagnetic seismograph, Bull. Earthquake Res. Inst. 36, 139-164.

Jackson, D.D. (1972), Interpretation of inaccurate, insufficient and inconsistent data, Geophys. J.R. astr. Soc. 28, 97-110.

James, D.E., and A.T. Linde (1971), A source of major error in the digital analysis of World-Wide Standard Station seismograms, Bull. Seis. Soc. Am. 61, 723-728.

Jarosch, H. and A.R. Curtis (1973), A note on the calibration of the electromagnetic seismograph, Bull. Seis. Soc. Amer. 63, 1145-1155.

Lanczos, C. (1961), Linear differential operators, D. Van Nostrand Co., London.

Mitchell, B.J. and M. Landisman (1969), Electromagnetic seismograph constants by least-squares inversion, Bull. Seis. Soc. Am. 59, 1335-1348.

Operation and maintenance manual World-Wide Seismograph System, model 10700, The Geotechnical Corporation, 3401 Shiloh Road, Garland, Texas.

Wiggins, R.A. (1972), The general linear inverse problem: implication of surface waves and free oscillations for Earth structure, Rev. Geophys. Space Phys. 10, 251-285.

# APPENDIX A

## ANALYTICAL METHOD FOR OBTAINING PSEUDOPARAMETERS

From figure 2 we have the equality involving original and pseudoparameters that must be satisfied:

$$(s^2 + 2\epsilon_1 s + \omega_1^2)(s^2 + 2\epsilon_2 s + \omega_2^2) - 4\epsilon_1 \epsilon_2 \sigma^2 s^2 = (s^2 + 2\epsilon_1' s + \omega_1'^2)(s^2 + 2\epsilon_2' s + \omega_2'^2) - 4\epsilon_1' \epsilon_2' \sigma^2 s^2$$

Following Jarosch and Curtis (1971), we equate powers of  $s$

$$(1) \quad \epsilon_1' + \epsilon_2' = \epsilon_1 + \epsilon_2$$

$$(2) \quad \omega_1'^2 + \omega_2'^2 + 4\epsilon_1' \epsilon_2' = \omega_1^2 + \omega_2^2 + 4\epsilon_1 \epsilon_2 - 4\epsilon_1 \epsilon_2 \sigma^2$$

$$(3) \quad \omega_1'^2 \epsilon_2' + \omega_2'^2 \epsilon_1' = \omega_1^2 \epsilon_2 + \omega_2^2 \epsilon_1$$

$$(4) \quad \omega_1'^2 \omega_2'^2 = \omega_1^2 \omega_2^2$$

To simplify, let

$$(5) \quad \omega_1^2 = a$$

$$(6) \quad \omega_1'^2 \omega_2'^2 = p$$

$$(7) \quad \epsilon_1' + \epsilon_2' = q$$

$$(8) \quad \omega_1'^2 + \omega_2'^2 + 4\epsilon_1' \epsilon_2' + 4\epsilon_1 \epsilon_2 \sigma^2 = r$$

$$(9) \quad \omega_1'^2 \epsilon_1' + \omega_2'^2 \epsilon_2' = t$$

We can then derive the characteristic equation in  $a$

$$(10) \quad a^6 - r a^5 + (4qt - p) a^4 + (2pr - 4p\epsilon_1^2 - 4t^2) a^3 + (4pqt - p^2) a^2 - p^2 r a + p^3 = 0$$

Rather than solve this equation numerically as Jarosch and Curtis did, I needed the complex solutions to the equation. The equation can be factored as

$$(11) \quad (a^2 + \alpha a + p)(a^2 + \gamma a + p)(a^2 + \epsilon a + p) = 0$$

We must solve for  $x, y, z$ . Since there is symmetry between  $x, y$  and  $z$  they may be interchanged:

$$(12) \quad x, y, z = A+B, \quad \frac{-(A+B)}{2} + \frac{(A-B)\sqrt{-3}}{2}, \quad \frac{-(A+B)}{2} - \frac{(A-B)\sqrt{-3}}{2}$$

where

$$(13) \quad A = \left( -b/2 + \sqrt{b^2/4 + g^3/27} \right)^{1/3}$$

$$(14) \quad B = \left( -b/2 - \sqrt{b^2/4 + g^3/27} \right)^{1/3}$$

and

$$(15) \quad g = \beta - r^3/3$$

$$(16) \quad b = 2r^3/27 - \beta r/3 - \alpha$$

$$(17) \quad \alpha = 4rp - 4t^2 - 4p^2$$

$$(18) \quad \beta = 4qt - 4p$$

The solution for  $\omega_1^2$  is

$$(19) \quad \begin{aligned} \omega_1^2 &= (-x \pm \sqrt{x^2 - 4p})/2 \\ &= (-y \pm \sqrt{y^2 - 4p})/2 \\ &= (-z \pm \sqrt{z^2 - 4p})/2 \end{aligned}$$

I always used the positive sign in the root. If one root was  $\omega_1^2$  the other two corresponded to  $\omega_2^2$  and  $\omega_3^2$ . It was always possible to distinguish which was which.

## FIGURE CAPTIONS

Figure 1: Schematic model of the impulse response inversion program. The periods and dampings are in pseudoparameter form as used in the inversion. Up to five iterations were used in convergence to the stabilized least-squares solution.

Figure 2: Equations for the seismometer and galvanometer motions, following Jarosch and Curtis (1973). The effect of the pseudoparameter conversion is small for small, but significant for larger .

Figure 3: Effect of various parameters on the impulse response function. The solid line is the for all figures. Changing the seismometer free period has a large effect on the impulse amplitude.

Figure 4: Results of inversion on our long period vertical instrument. The parameters were measured in situ using overshoot ratio tests and timing the free periods by stopwatch.

Figure 5: Phase determination of NDI-LPZ impulse response, using direct Fourier transform method and the inversion method. The Fourier method is degraded at periods below 30 seconds. The 'on' time had been picked by eye at 4 seconds after the minute mark; the inversion showed it actually occurred at 3 seconds after the minute. The large black dots correspond to the best estimate of the phase.

Figure 6: Amplitude determination of NDI-LPZ using the Fourier method and inversion method. The curve on the left corresponds to impulse amplitudes. These become very small below 30 seconds, which accounts for the degradation of the phases and amplitudes. To obtain ground displacement magnification, this curve is multiplied by .

Figure 7: Impulse response on the Lookout Mountain (LMO) LPZ record. There is a slight misalignment of the light beam relative to the drum as shown by the offset of the minute mark on the impulse. This minute mark was used to help align the impulse for correct digitization.

Figure 8: Convergence of the linear inversion method for theoretical and actual impulse responses. For all successful solutions the method converged within 5 iterations.

# LINEARIZED INVERSION METHOD

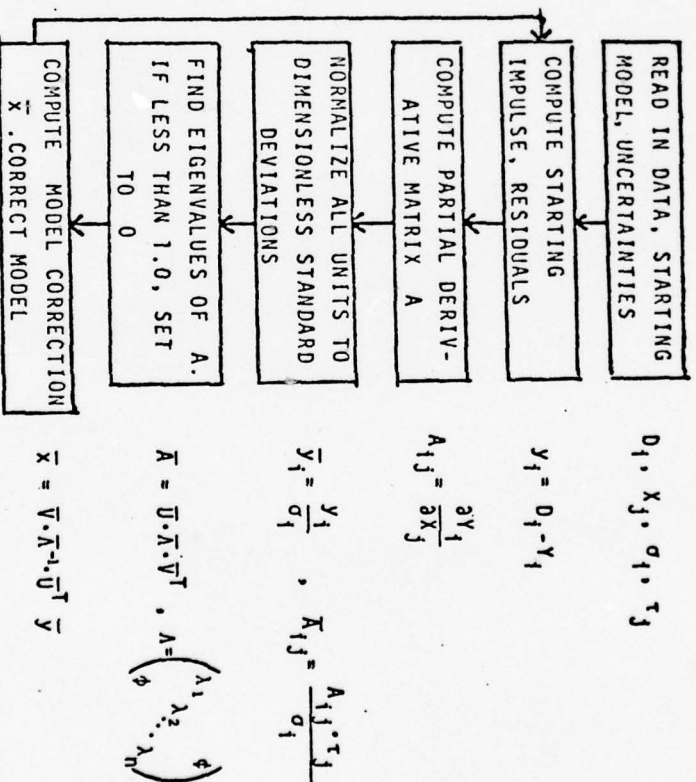
## MODEL PARAMETERS $X_j$

- $T_1$  Seismometer Free Period
- $T_2$  Galvanometer Free Period
- $h_1$  Seismometer Damping
- $h_2$  Galvanometer Damping
- $T_0$  Impulse "on" time
- $A$  Amplitude Factor
- $C$  Constant
- $L$  Linear trend
- $\theta$  Rotation

## DATA VECTOR $D_1$

Digitized points at  
2-second intervals

$$\text{INVERSION: } Y_1 = A_{1j} X_j + \epsilon_1$$



$$D_1, X_j, \sigma_1, \tau_j$$

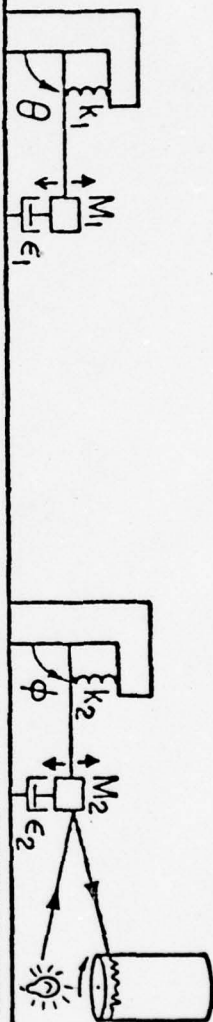
$$Y_1 = D_1 - Y_1$$

$$A_{1j} = \frac{\partial Y_1}{\partial X_j}$$

$$\bar{Y}_1 = \frac{Y_1}{\sigma_1}, \quad \bar{A}_{1j} = \frac{A_{1j} \cdot \tau_j}{\sigma_1}$$

$$\bar{A} = \bar{U} \cdot \bar{A} \cdot \bar{V}^T, \quad \bar{A} = \begin{pmatrix} \lambda_1 & & \\ & \lambda_2 & \\ & & \ddots \\ \phi & & & \lambda_n \end{pmatrix}$$

$$\bar{X} = \bar{V} \cdot \bar{A}^{-1} \cdot \bar{U}^T \bar{Y}$$



### SEISMOMETER

$$\frac{d^2\theta}{dt^2} + 2c_1\frac{d\theta}{dt} + \omega_1^2\theta = -\frac{M_1H}{K}\frac{d^2X}{dt^2} + 2c_1\epsilon_1\frac{d\phi}{dt}$$

$$\frac{d^2X}{dt^2} = K \cdot H(t)$$

### GALVANOMETER RECORDING DRUM

$$\frac{d^2\phi}{dt^2} + 2c_2\frac{d\phi}{dt} + \omega_2^2\phi = 2c_2\epsilon_2\frac{d\theta}{dt}$$

$$\begin{aligned} \frac{d^4\phi}{dt^4} + [2c_1 + 2c_2]\frac{d^3\phi}{dt^3} + [\omega_1^2 + 4c_1c_2\epsilon_1 + \omega_2^2 - 4c_1\epsilon_2\sigma_1\sigma_2]\frac{d^2\phi}{dt^2} \\ + [2c_1\omega_2^2 + 2c_2\omega_1^2]\frac{d\phi}{dt} + \omega_1^2\omega_2^2\phi = 2c_2\epsilon_2K\delta(t) \end{aligned}$$

$$\phi(t) = \frac{1}{2\pi i} \int_{\Gamma} \frac{2c_2\epsilon_2 K e^{st} ds}{(s^2 + 2c_1s + \omega_1^2)(s^2 + 2c_2s + \omega_2^2) - 4c_1\epsilon_2\sigma_1^2s^2}$$

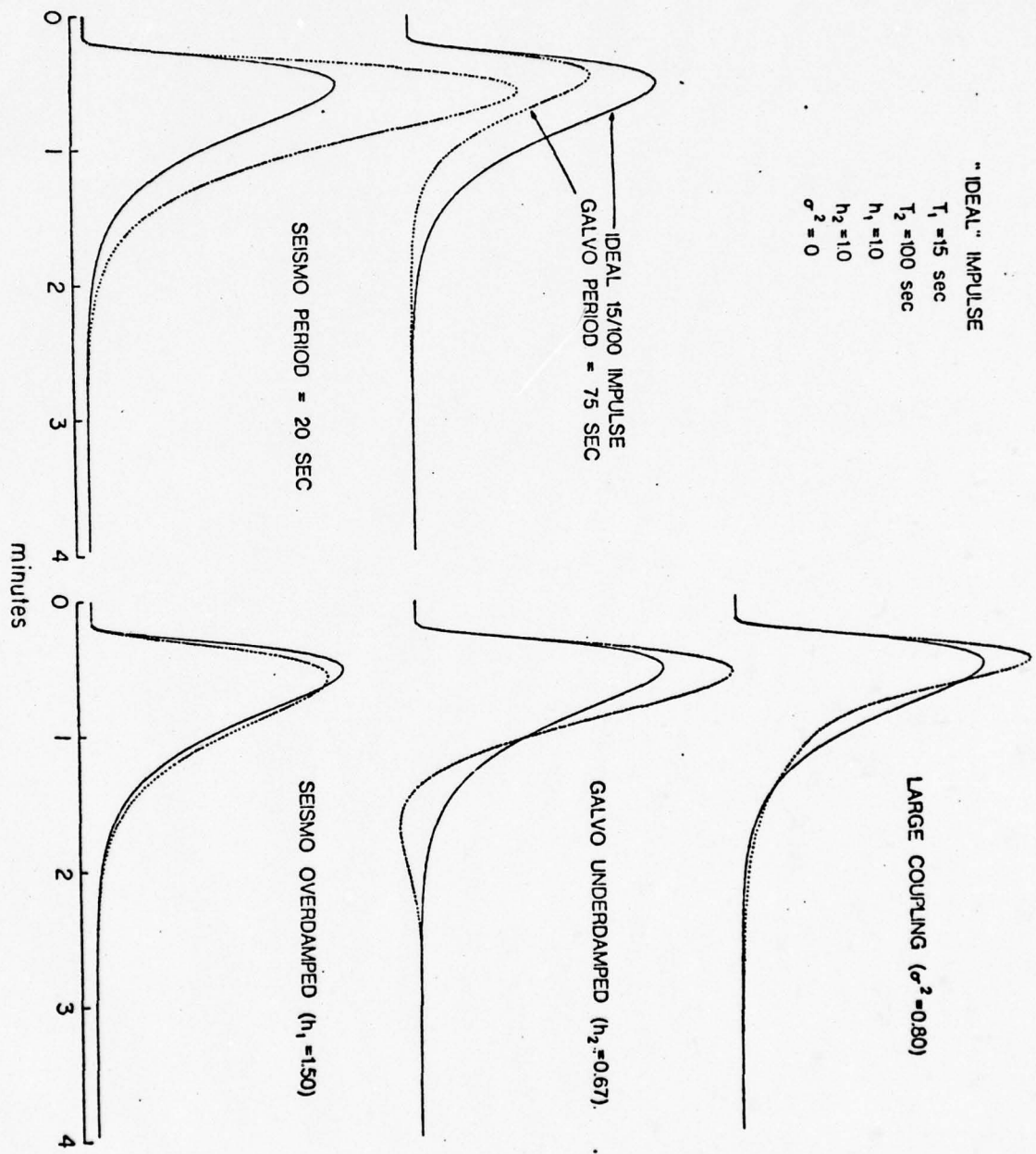
### PSEUDO-PARAMETER CONVERSION

$$(s^2 + 2c_1s + \omega_1^2)(s^2 + 2c_2s + \omega_2^2) - 4c_1\epsilon_2\sigma_1^2s^2 = (s^2 + 2c_1's + \omega_1'^2)(s^2 + 2c_2's + \omega_2'^2)$$

PARAMETER	ORIGINAL	PSEUDO	ORIGINAL	PSEUDO
$T_1$	15.0 sec	15.46 sec	30.0 sec	29.98 + 11.45i sec
$T_2$	100.0 sec	97.03 sec	100.0 sec	87.33 - 33.37i sec
$h_1$	1.0	1.022	1.0	1.071 + .20i
$h_2$	1.0	1.022	1.0	1.071 + .20i
$\sigma^2$	0.05	0.0	.195	0.0

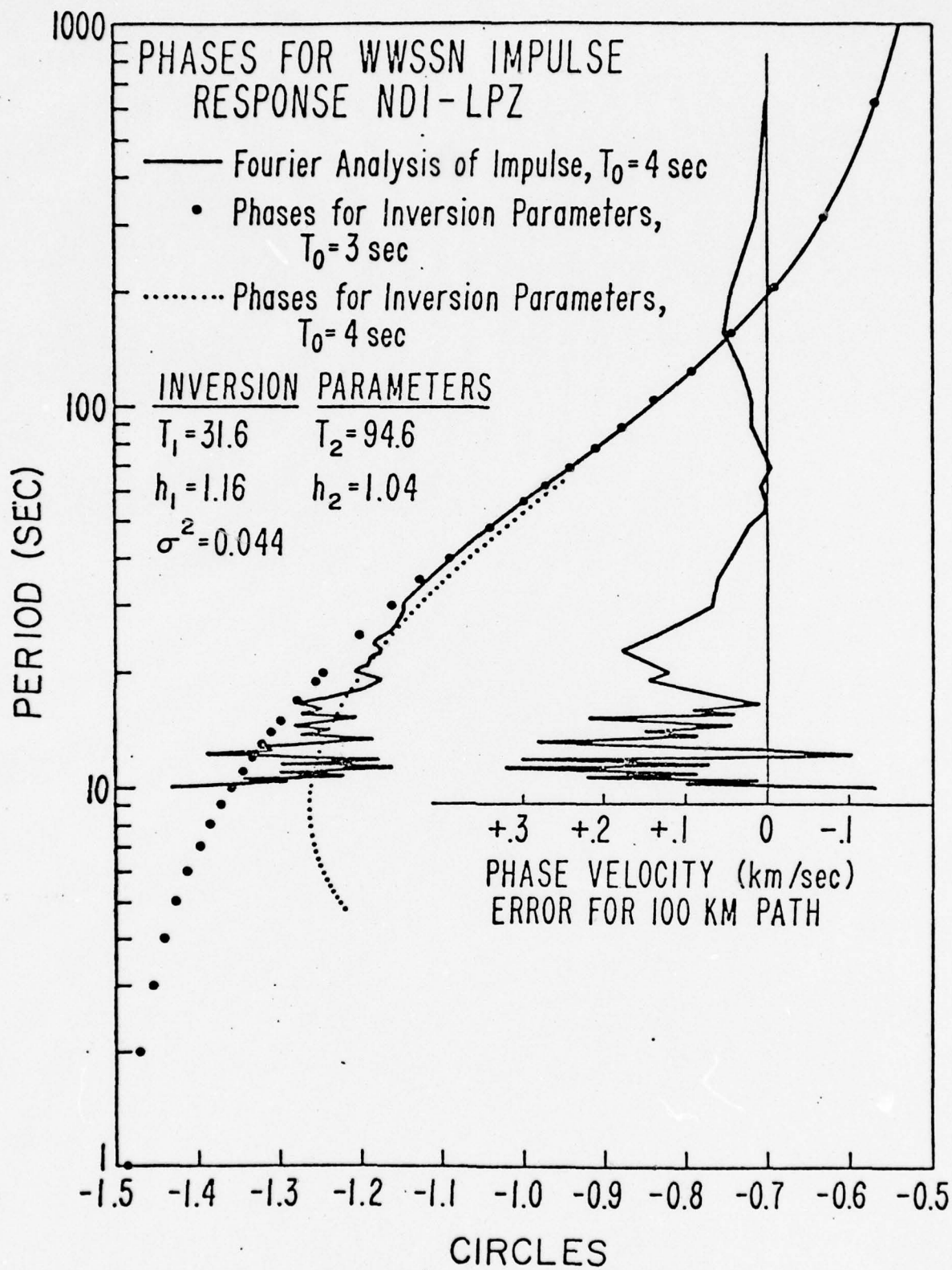
# "IDEAL" IMPULSE

$T_1 = 15 \text{ sec}$   
 $T_2 = 100 \text{ sec}$   
 $h_1 = 10$   
 $h_2 = 10$   
 $\sigma^2 = 0$

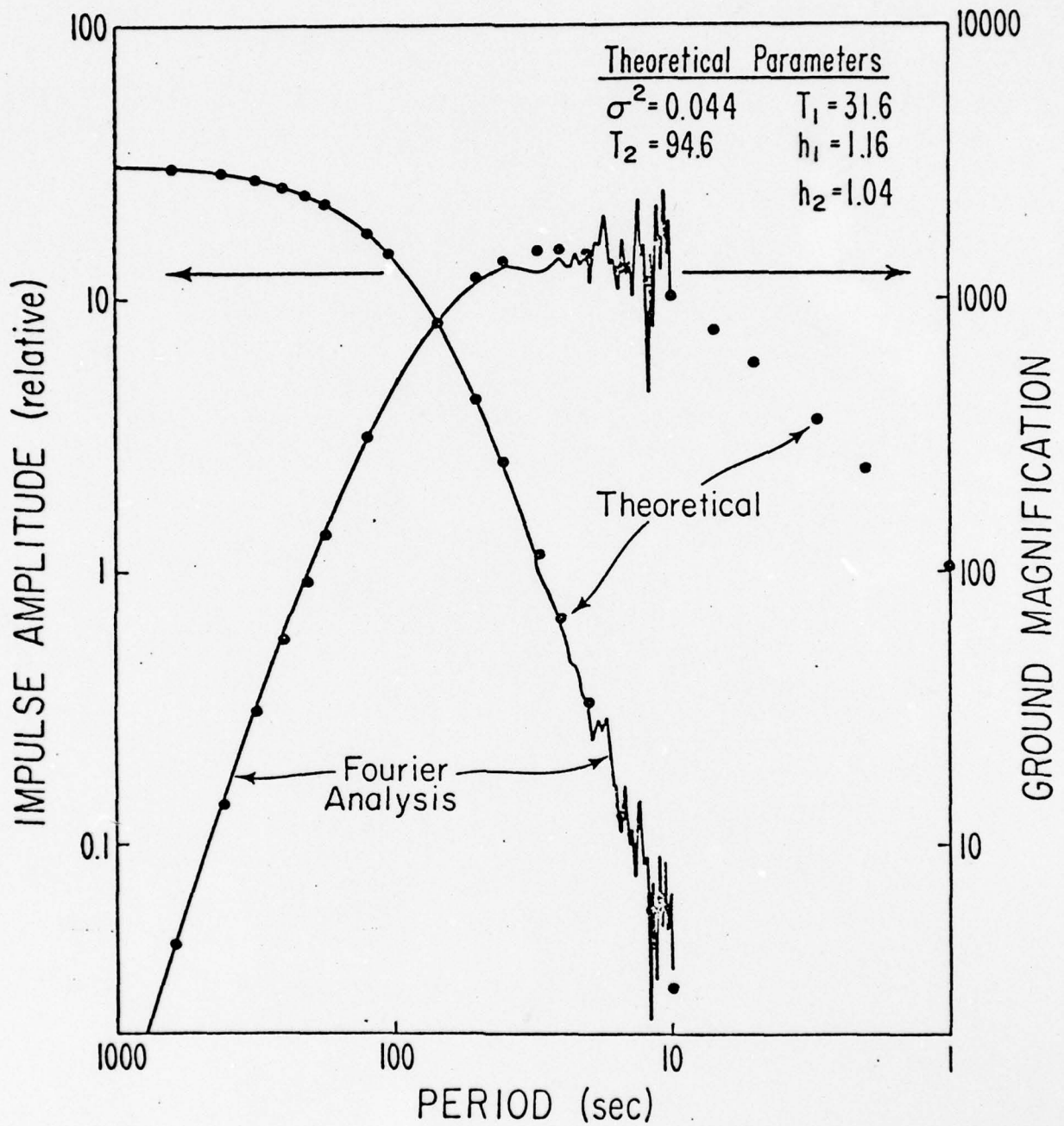


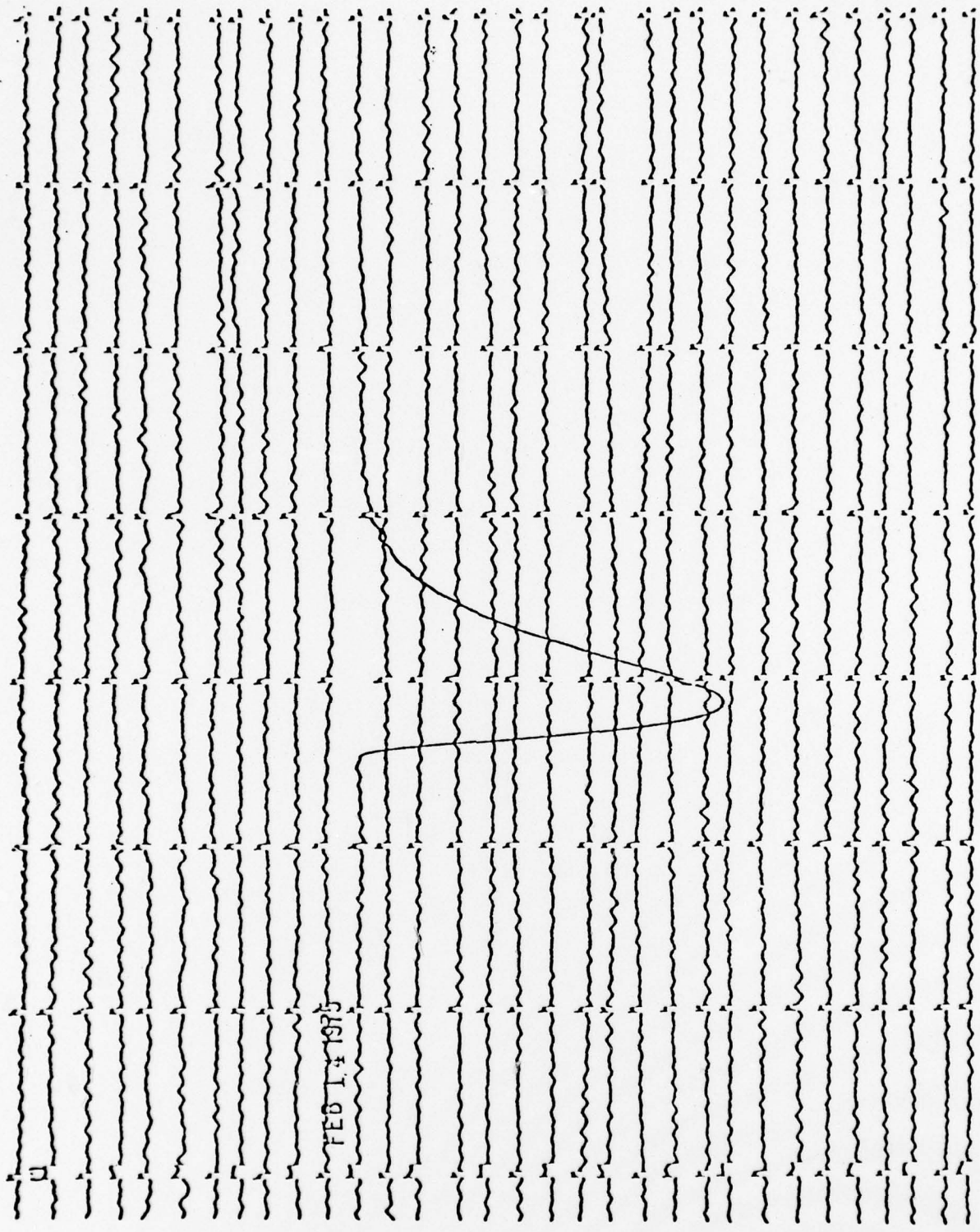
# LOOKOUT MOUNTAIN STATION CALIBRATION RESULTS

	<u>T<sub>1</sub></u>	<u>T<sub>2</sub></u>	<u>h<sub>1</sub></u>	<u>h<sub>2</sub></u>
<u>Underdamped</u>				
Measured <i>in situ</i>	15.2±.1	94.0±1	.43±.01	.75±.02
Inversion I	15.0	91.0	.46	.76
Inversion II	16.0	93.0	.43	.74
<u>Overdamped</u>				
Measured <i>in situ</i>	15.2±.1	94.0±1	1.01±.01	1.19±.02
Inversion I	15.4	94.4	1.00	1.19



# AMPLITUDE FOR WWSSN IMPULSE RESPONSE NDI-LPZ





FEB 14 1975

Table 1

Inversion Results

	LMO-1	$\sigma_{xx}$	LMO-2	$\sigma_{xx}$	LMO-NEW	$\sigma_{xx}$
$T_1$	15.0 sec.	0.8 sec.	16.0 sec.	0.7 sec.	15.4 sec.	0.2 sec.
$T_2$	91.0 sec.	0.8 sec.	92.9 sec.	0.8 sec.	94.4 sec.	2.9 sec.
$h_1$	0.46	0.03	0.435	0.02	0.995	0.07
$h_2$	0.76	0.01	0.745	0.01	1.19	0.03
$T_0$	33.6 sec.	0.2 sec.	33.1 sec.	0.2 sec.	33.7 sec.	0.07 sec.
$A$	4.21	0.5	3.55	0.34	6.69	0.245
$C$	-0.41	0.2	-0.032	0.2	-0.219	0.28
$L$	-0.005	.006	-0.009	0.006	-0.0045	0.006
$\theta$	0.0	0.0	0.0	0.0	0.0	0.0
$\sigma^2$	0.012	--	0.012	--	0.029	--

Table 2

DELETED EIGENVECTOR USED TO CORRECT INSTRUMENTAL PARAMETERS FOR IMPULSES LMO-1 and LMO-2

Parameter	LMO-1 Inversion Results	LMO-1 Deleted Eigenvector	Parameter Uncertainties	LMO-1 Parameter Eigenvector	LMO-1 Corrected Parameters	LMO-2 Inversion Results	LMO-2 Corrected Parameters
$T_1$ (sec)	15.0	-.33	1.0	-.33	15.2	16.0	15.2
$T_2$ (sec)	91.0	-.034	5.0	-.17	91.1	92.9	92.5
$h_1$	0.46	.094	0.2	.02	0.45	0.435	0.48
$h_2$	0.76	.0052	0.2	.001	0.76	0.745	0.747
$T_0$ (sec)	33.6	.186	0.25	.05	33.6	33.1	33.2
A	4.21	.919	0.25	.23	4.07	3.55	4.10
C	-0.41	-.012	0.1	-.0012	-0.41	-.032	-.035
L	-0.005	-.006	0.012	-.00006	-0.005	-.009	-.009
$\theta$	0.0	0.0	0.0	0.0	0.0	0.0	0.0

COMPUTATION OF COMPLETE THEORETICAL SEISMOGRAMS  
FOR TORSIONAL WAVES

A. H. Liao,<sup>1</sup> F. Schwab,<sup>2</sup> and E. Mantovani<sup>3</sup>

Publication No. 1756

Institute of Geophysics and Planetary Physics  
University of California, Los Angeles

Publication No. 00, authorized by the  
Director of the Geodynamics Project (CNR) Italy

Sponsored by  
Advanced Research Projects Agency (DOD)

ARPA Order No. 3291

Monitored by AFOSR Under Contract #F49620-67-C-0038

<sup>1</sup>Institute of Geophysics and Planetary Physics, University of  
California, Los Angeles, California 90024

<sup>2</sup>P. O. Box 131, 308 Westwood Plaza, Los Angeles, California 90024

<sup>3</sup>Osservatorio Geofisico, Università di Siena, Italy

## COMPUTATION OF COMPLETE THEORETICAL SEISMOGRAMS FOR TORSIONAL WAVES

BY A. H. LIAO, F. SCHWAB, AND E. MANTOVANI

### INTRODUCTION

In the study of earth structure, and earthquake source mechanism, the handiest and probably most important information is that provided by the seismic waves recorded on seismograms. Therefore, the direct comparison between theoretical and experimental seismograms is a very appealing subject for most seismologists.

The computation of theoretical seismograms has been studied by various authors. Some tried to obtain long-period seismograms by combining a few normal modes; some tried to obtain a few body-wave phases. The results of the investigations that led to the present letter are reported by Schwab (1970); Schwab and Knopoff (1970, 1971, 1972, 1973); Kausel and Schwab (1973); Schwab and Kausel (1976); Knopoff *et al.* (1973); Knopoff *et al.* (1974); Schwab *et al.* (1974); Nakanishi *et al.* (1976); Kausel *et al.* (1977); Nakanishi *et al.* (1976); Mantovani *et al.* (1976); Mantovani (1977a); and Mantovani *†* in preparation). The results of our most recent work now allow us to generate *complete* theoretical seismograms for torsional-wave motion. By saying complete, we mean that *all* modes that exist for periods above 10 sec are included in our seismograms, i.e., that all amplitude and phase information down to a period of 10 sec is included. This means that the body-wave phases, as well as surface-wave arrivals, are obtained with this method.

The computational technique is somewhat involved; however, anyone who is interested in the details can obtain program copies from the authors. Briefly, we compute all of the required frequency-domain information such as phase and group velocity dispersion, attenuation, amplitude excitation, apparent initial phase, depth of penetration (and if desired, partial derivatives with respect to structural parameters) from the longest existing period for each mode, down to 10 sec. This requires between 90 and 100 radial modes, and is accomplished in a single, relatively short computer run. This computation corresponds to about 50,000 free oscillating modes. Theoretical seismograms in the time domain are then obtained by inverse Fourier transformation as described by Kausel and Schwab (1973) and Schwab and Kausel (1976). The cost of computing the volume of frequency-domain information, which is required to construct the synthetic seismograms down to a period as short as 10 sec, has been prohibitively high up to the present time; but, with our current optimization we have succeeded in reducing the computation time to about 6 min on our IBM 360/91 computer (an expenditure of about \$50) for a given earth structure. The corresponding time on a CDC 7600 computer is about 2 min. [For corresponding times on other computers see Schwab *et al.* (1977) and Porter *et al.* (in preparation).] These time estimates should be considered only as upper bounds; relatively simple improvements—which a little practical experience will be needed to justify—are expected to cut these times at least in half.

The purposes of the present letter are (1) to report that the capability now exists for computing realistic, torsional-wave seismograms that contain *all* of the seismic energy and arrivals down to a period of 10 sec; (2) to announce the availability, for general distribution, of the associated program; and (3) to exhibit the results of our

ssa-april 18403

we  
appis.

a. h. Liao, J. Schwab & E. Mantovani

318

LETTERS TO THE EDITOR

initial tests of direct comparison of these complete theoretical seismograms with an experimental record from a standard, long-period instrument of the WWSSN.

#### EXAMPLES

For our comparison of theoretical and experimental seismograms, we have chosen an event with its epicenter near the foot of the Kamchatka peninsula [see Kausel *et al.* (1977) for a discussion of this event]. Analysis of this earthquake indicates that the source is approximated by purely dip-slip motion on a vertical fault plane. We used the station at HNR, which provides a N-S path, so that the recording on the E-W instrument can be considered to contain only the azimuthal component of displacement. The focal depth is in the intermediate range. The initial earth model that we used in our calculations was a somewhat smoothed version of the average oceanic structure described in Kausel *et al.* (1977), which is essentially the CIT-11 structure (Figure 10, Toksöz and Anderson, 1966). About 200 layers were used to model the vertical heterogeneity of the crust-mantle system; an adaptation of model MM8 (Anderson *et al.* 1965) was used to approximate the dependence of the intrinsic attenuation on depth.

To prepare the experimental and theoretical seismograms for comparison, the usual ramp function was removed from the experimental time series (James and Linde, 1971). The result of this is the upper trace in Figure 1. Since the theoretical seismograms do not contain periods below 10 sec, we ran a low-pass frequency (boxcar) filter, with cutoff at 10 sec, over the experimental data (second trace in Figure 1). A Gaussian roll-off filter with peak at 15 sec and a 90 per cent decay at 10 sec, was then applied to suppress the time-domain oscillations introduced by the abrupt cutoff of the boxcar filter. The result of these operations on the experimental seismogram is shown in the third trace of Figure 1. The same Gaussian roll-off filter is applied to the theoretical seismograms, so that both the theoretical and experimental time series are processed in the same way. Thus, we can compare these time series directly.

In our sample computations, we have varied the source parameters over the possible range of variation from our point-source solution. The first figure shows the dip angle dependence. With the theoretical seismograms available for comparison, we can easily identify several of the arrivals on the experimental record. The most striking of these are the body-wave phases S, sS, ScS, sScS, and the later, surface-wave arrivals. (The various arrivals are identified in Figure 5.) For this particular event, the surface waves are composed of multimode, oceanic Sa (Kausel *et al.*, 1977). In Figure 1 we have varied the dip angle from that of a vertical (90°) fault plane, to 70°; the results show that as dip angle decreases, the normalized S and ScS phases remain unchanged, but sS and sScS diminish. Thus, the dip angle appears to have its main effect on body waves when they leave the focus above the equator of the focal sphere. Both the long- and short-period energy increase, in the surface-wave portion of the seismogram, when the dip angle decreases from vertical. Figure 2 illustrates the dependence of the seismogram on source depth. Here we have varied this depth from 220 to 140 km; the consequent separation of body-wave arrivals, and development of the Sa wave train in the lower set of theoretical traces, clearly exhibit the power of complete theoretical seismograms as interpretive tools. As Figure 3 illustrates, the theoretical seismograms from this class of sources are less sensitive to changes in slip angle than to changes in fault dip or source depth.

The azimuthal-component seismogram is composed, in principle, of two contri-

Should be  
"attenuation"

5  
8

# computation of complete theoretical seismographs, for torsional waves

LETTERS TO THE EDITOR

319

butions: that from the torsional-mode excitation, and that from the spheroidal modes. The general depressions for the polar ( $\theta$ ) and azimuthal ( $\phi$ ) components of displacement are given below for the torsional (T) and spheroidal (S) excitations

DIP ANGLE  
DEPENDENCE

1 MIN

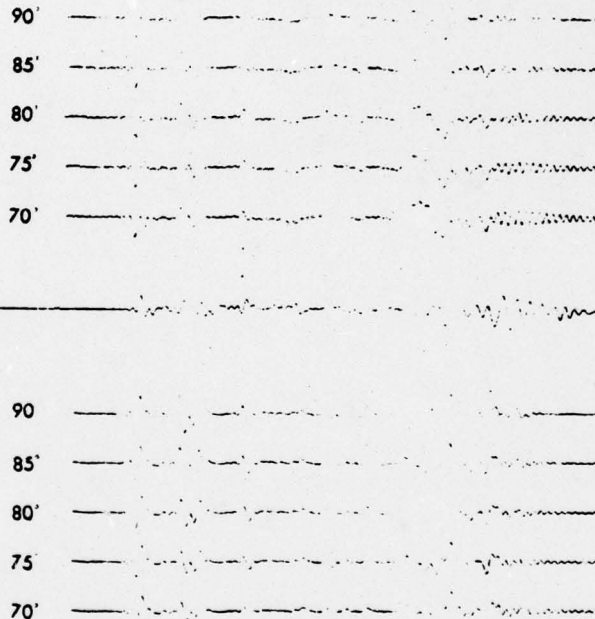


FIG. 1. Dependence of computed seismograms on dip angle at the source. For contrast, the experimental traces extend further to the left and right, and the dominant eastward lobe of the first arrival—S—is upward; on the shorter, theoretical seismograms, eastward is down. Each trace is normalized relative to its maximum displacement from zero. From the top down, the experimental traces show the E-W long-period seismogram at HNR with the ramp function removed, then with a low-pass frequency filter applied (cutoff at 0.1 Hz) after ramp removal, and the lower two also have a Gaussian roll-off filter applied. In Figures 1 to 3 we show the effects of varying source parameters from an initial focal mechanism: dip angle of the fault plane below the horizontal,  $\delta$ , of 90°; azimuthal angle between strike line and epicenter-to-station line,  $\phi$ , of 40°; source depth,  $h$ , is initially set at 180 km (Kausel *et al.* 1977, give the reason for this initial choice of source depth); slip angle of the hanging wall relative to the foot wall,  $\lambda$ , of 90°; and, a step-function displacement dislocation is assumed at the focus, where a point source is assumed, as well as a component of stress, normal to the fault plane, which is continuous during the dislocation. [See Figure 2, Kausel *et al.* (1977) for fault plane geometry.] In the above figure, the associated dip angle is given at the left of each theoretical trace; the upper group of these time series represents actual ground displacement, and the lower set includes instrumental response [the 30 to 100 instrument described by Knopoff *et al.* (1973)] and Gaussian roll-off filter.

This must be set  
as "30-100"  
a special  
displacement and  
does not mean  
30 to 100.

## Torsional Oscillations

$$(u_\theta)_T = im \frac{Pr^m(\cos\theta)}{\sin\theta} (V_T(r)e^{im\phi}e^{i\omega t})$$

$$(u_\phi)_T = \frac{dPr^m(\cos\theta)}{d\theta} (-V_T(r)e^{im\phi}e^{i\omega t})$$

## Spheroidal Oscillations

$$(u_\theta)_S = \frac{dPr^m(\cos\theta)}{d\theta} (V_S(r)e^{im\phi}e^{i\omega t})$$

$$(u_\phi)_S = im \frac{Pr^m(\cos\theta)}{\sin\theta} (V_S(r)e^{im\phi}e^{i\omega t})$$

trace also has

Cap "p"

SSA 18403

A. H. Liao, J. Schmalz &amp; E. Miniswani

320

LETTERS TO THE EDITOR

with  $m \leq 2$ . Since  $(u_\phi)_T$  and  $(u_\theta)_S$  are of the same order of magnitude, so must  $V_T$  and  $V_S$ . Thus, in terms of an order-of-magnitude estimate, the relative sizes of the two contributors to azimuthal-component seismograms,  $(u_\phi)_T$  and  $(u_\phi)_S$ , are governed by the relative  $\theta$  dependences of these contributions. Since these dependences for  $(u_\phi)_S$  and  $(u_\theta)_T$  are the same, the order-of-magnitude comparison of the two contributors to the azimuthal displacement is the same as the comparison of the

SOURCE DEPTH  
DEPENDENCE

1 MIN

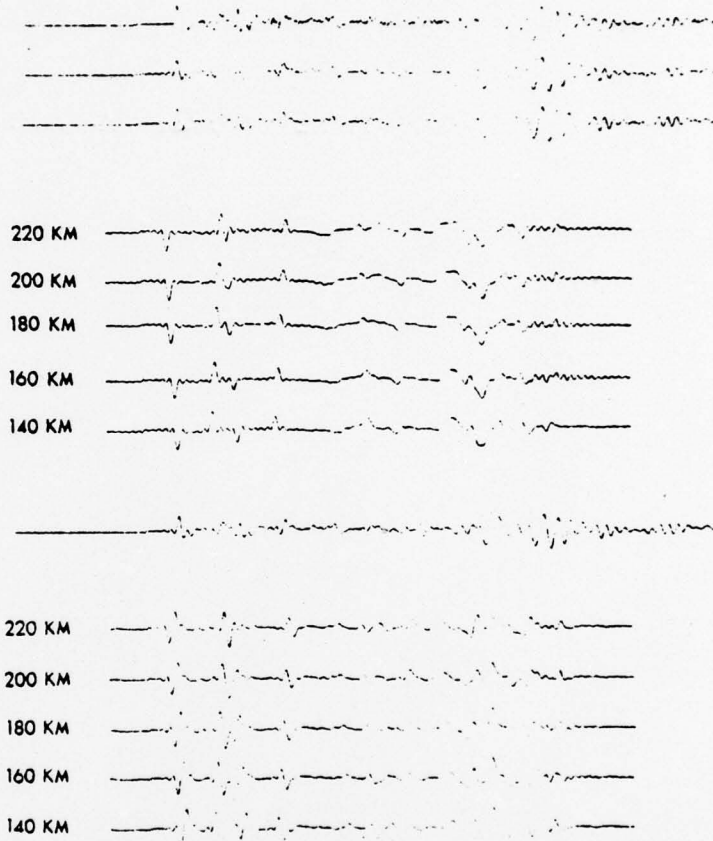


FIG. 2. Dependence of computed seismograms on source depth, which is given at the left of each theoretical seismogram. See caption of Figure 1 for further details.

polar and azimuthal displacements from torsional excitation, i.e.

$$\left| \frac{(u_\phi)_S}{(u_\phi)_T} \right| \approx \left| \frac{(u_\theta)_T}{(u_\phi)_T} \right|.$$

The results of our direct computation of  $(u_\theta)_T$  and  $(u_\phi)_T$  are shown in Figure 4, where we see that relative to the azimuthal displacements, the polar seismogram is a straight line. In fact, the numerical results show that the ratio of maximum displacements in the two cases is about 100 to 1. We therefore conclude that for normal WWSSN seismograms which contain all of the generated energy down to a

# computation of complete theoretical seismograms for torsional waves

SSA 18403

LETTERS TO THE EDITOR

321

SLIP ANGLE  
DEPENDENCE

1 MIN

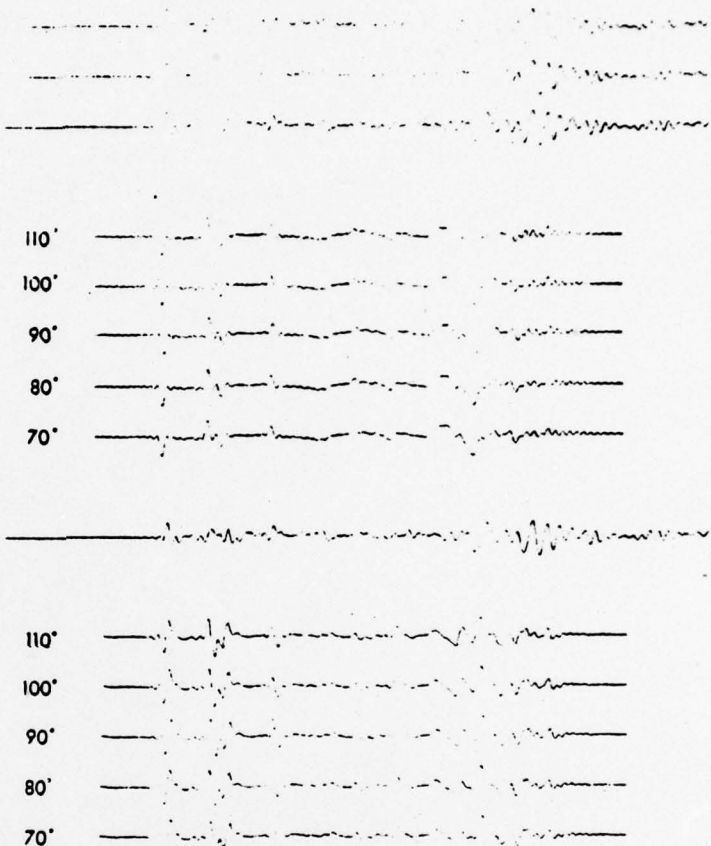


FIG. 3. Dependence of computed seismograms on slip angle, which is given at the left of each theoretical seismogram. See caption of Figure 1 for further details.

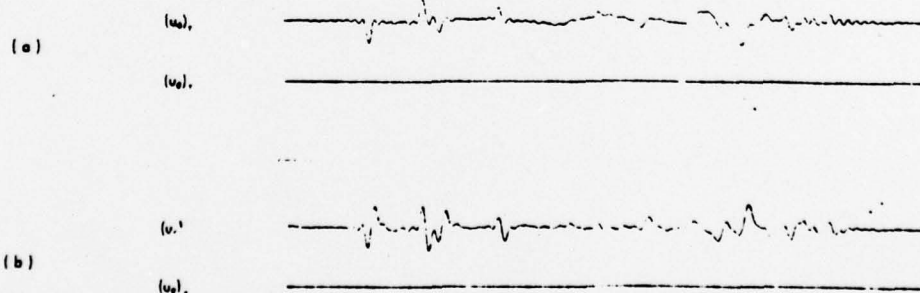


FIG. 4. Comparison of azimuthal (a) and polar (b) components of displacement from torsional wave excitation. Traces (a) illustrate actual ground displacement, and traces (b) include the 30 to 100 instrument described in the caption of Figure 1, and the Gaussian roll off filter. Computational parameters place the epicenter at the foot of Kamcharka peninsula, the station at HNR,  $\delta = 90^\circ$ ,  $\phi = 40^\circ$ ,  $A = 180$  km,  $\lambda = 90^\circ$ , and a step-function time dependence at the focus.

period of 10 sec, the total azimuthal component of displacement can be computed by considering only the torsional-wave contribution.

Before going into a specific, direct comparison of theoretical and experimental seismograms, it should be emphasized that we have not made any special attempt

This must  
be set at  
30-100  
since I  
a special  
diagram  
not mean  
to be 10

(a. z. liao, f. schwab & e. mentovani)

ssa-april 18403

322

~~LETTERS TO THE EDITOR~~

to fit the experimental data yet. We have just picked the best fit to the experimental record from among the theoretical traces shown in Figures 1 to 3. Even so, the feature-by-feature agreement is striking over much of the record. This is shown in Figure 5. The first point to note is the success of the theoretical work in generating the phases ScS and sScS that are reflected from the core-mantle boundary. This means that we can expect this kind of analysis to be useful over the entire mantle down to the core. The second point is the phase-by-phase agreement in the body waves identified in the figure, and the decrease in the quality of the agreement beyond them. According to the recent paper by Kausel *et al.* (1977), the properties of Sa are determined by the structure from the vicinity of the "650-km" discontinuity upward. Therefore, the good agreement in initial body waves, and the relatively

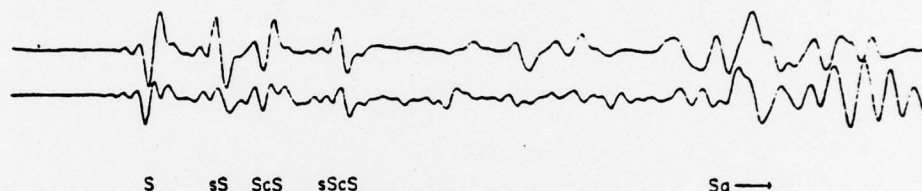


FIG. 5. Best fit to experimental seismogram (lower trace) from theoretical traces shown in Figures 1 to 3, i.e., that with  $\delta = 90^\circ$ ,  $\phi = 40^\circ$ ,  $h = 140$  km,  $\theta = 90^\circ$ . East is downward.

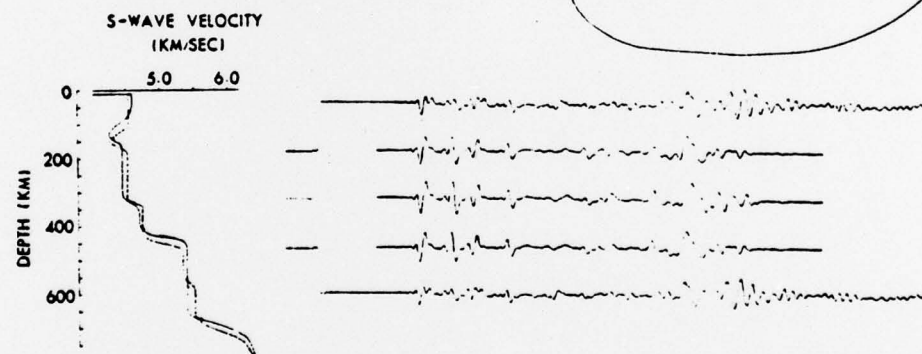


FIG. 6. Test of relative effects on initial body-wave phases and on later, shallower sampling arrivals composing the theoretical seismogram, when the structure above a depth of 700 km is varied. Upper and lower traces reproduce the experimental record; shorter traces are theoretical seismograms from indicated structure. These velocity structures are variations from CIT-11 (Ringwood, 1975); all use the attenuation model for the Pacific that is given by Mitchel (1976).

poorer agreement in surface waves implies that we have essentially the right structure below 700 km, but that we need some modification in our earth model above that. As mentioned above, the structure we used is an average oceanic model; however, the Kamchatka-KNR path is along the "old" edge of the Pacific plate. Recent seismic studies (e.g., Leeds, *et al.* 1974; Leeds, 1975) indicate that the thickness of the lid grows with increasing distance from the ridges. Therefore, along the path, the lid should be thicker than average. This may be one source of the discrepancies between the theoretical and experimental traces in Figure 5. Another may be oceanic crustal thicknesses, for perhaps 1000 km north of HNR, that may exceed 30 km (Furumoto *et al.*, 1973).

To give some indication of whether modifications in the structure above 700 km can be expected to improve the comparison in Figure 5, we have repeated the computations with three modified structures. The structures and results are shown in Figure 6, which indicates that quite a bit can be done with the single-structure

Should be  
c.c. limit  
"x"

Should be  
"x"

interpretation before making the obvious generalization of the technique to include lateral heterogeneity. Consideration of the experimental coda is beyond the scope of this letter.

report.

### CONCLUSIONS

It is now feasible to make direct comparisons of theoretical and experimental seismograms, for torsional-wave records obtained from the long-period instruments of the WWSSN. With our present technique, all of the generated energy—at periods above 10 sec—is exhibited on the calculated time series, body waves as well as surface waves. Application of this result might be expected to provide the highest source and structural resolution that has yet been achieved.

Our latest work (Schwab *et al.*, 1977) with spheroidal waves on spherical, gravitating models of the earth, shows that even when we employ highly optimized versions of the current algorithms, these calculations are six times slower than the comparable torsional-wave computations. We conclude from this that new algorithms are required before the efficiency of spheroidal-wave computations (including gravity) will approach a level justifying computation of the associated theoretical seismograms, down to a period as low as 10 sec.

### ACKNOWLEDGMENTS

This research was partly supported by the Advanced Research Projects Agency of the Department of Defense and was monitored by the Air Force Office of Scientific Research under Contract F49620-76-C-0038, and partly supported by the Earth Sciences Section, National Science Foundation, NSF Grant EAR75-04376.

### REFERENCES

- Anderson, D. L., A. Ben-Menahem, and C. B. Archambeau (1965). Attenuation of seismic energy in the upper mantle, *J. Geophys. Res.* 70, 1441-1447.
- Furumoto, A. S., W. A. Wiebenga, J. P. Webb, and G. H. Sutton (1973). Crustal structure of the Hawaiian Archipelago, Northern Melanesia, and the Central Pacific Basin by seismic refraction methods, *Tectonophysics* 20, 153-164.
- James, D. E. and A. T. Linde (1971). A source of major error in the digital analysis of World Wide Standard Station seismograms, *Bull. Seism. Soc. Am.* 61, 723-728.
- Kausel, E. and F. Schwab (1973). Contributions to Love-wave transformation theory: Earth-flattening transformation for Love waves from a point source in a sphere, *Bull. Seism. Soc. Am.* 63, 983-993.
- Kausel, E. G., F. Schwab, and E. Mantovani (1977). Oceanic *Sa*, *Geophys. J.* 50, 407-440.
- Knopoff, L., F. Schwab, and E. Kausel (1973). Interpretation of *Lg*, *Geophys. J.* 33, 387-402.
- Knopoff, L., F. Schwab, K. K. Nakanishi, and F. Chang (1974). Evaluation of *Lg* as a discriminant among different continental crustal structures, *Geophys. J.* 39, 41-70.
- Leeds, A. R. (1975). Lithospheric thickness in the Western Pacific, *Phys. Earth Planet Interiors* 11, 61-64.
- Leeds, A. R., L. Knopoff, and E. G. Kausel (1974). Variations of upper mantle structure under the Pacific Ocean, *Science* 186, 141-143.
- Mantovani, E. (1977a). Generation of complete theoretical seismograms for SH. III, submitted for publication.
- Mantovani, E., F. Schwab, H. M. Liao, and L. Knopoff (1976). Generation of complete theoretical seismograms for SH. II, *Geophys. J.* 48, 531-536.
- Mitchell, B. J. (1976). Anelasticity of the crust and upper mantle beneath the Pacific Ocean from the inversion of observed surface wave attenuation, *Geophys. J.* 48, 521-533.
- Nakanishi, K. K., F. Schwab, and E. Kausel (1975). Interpretation of *Sa* on a continental structure, *Geophys. J.* 47, 211-223.
- Nakanishi, K. K., F. Schwab, and L. Knopoff (1976). Generation of complete theoretical seismograms for SH. I, *Geophys. J.* 48, 525-530.
- Ringwood, A. E. (1975). *Composition and Petrology of the Earth's Mantle*. McGraw-Hill, New York. Chapters 9 and 14.
- Schwab, F. (1970). Surface wave dispersion computations: Knopoff's method, *Bull. Seism. Soc. Am.* 60, 1201-1206.

done at the  
"atmosphere"

3  
3

cap

ssa-april 18403

## LETTERS TO THE EDITOR

- INSTITUTE OF GEOPHYSICS AND PLANETARY PHYSICS  
UNIVERSITY OF CALIFORNIA, LOS ANGELES  
LOS ANGELES, CALIFORNIA 90024  
PUBLICATION No. 1756

□ Manuscript received October 3, 1977

UNCLASSIFIED

SECURITY CLASSIFICATION OF THIS PAGE (When Data Entered)

REPORT DOCUMENTATION PAGE		READ INSTRUCTIONS BEFORE COMPLETING FORM
1. REPORT NUMBER <b>AFOSR-TR- 78-1011</b> ✓	2. GOVT ACCESSION NO.	3. RECIPIENT'S CATALOG NUMBER
4. TITLE (and Subtitle) REGIONALIZATION OF THE <b>ARCTIC</b> REGION, SIBERIA AND EURASIAN CONTINENTAL AREA		5. TYPE OF REPORT & PERIOD COVERED Final ✓
		6. PERFORMING ORG. REPORT NUMBER
7. AUTHOR(s) Leon Knopoff		8. CONTRACT OR GRANT NUMBER(s) F49620-76-C-OC38 <i>New</i>
9. PERFORMING ORGANIZATION NAME AND ADDRESS Institute of Geophysics and Planetary Physics ✓ University of California Los Angeles, California 90024		10. PROGRAM ELEMENT, PROJECT, TASK AREA & WORK UNIT NUMBERS AO 1827 62701E 6F10
11. CONTROLLING OFFICE NAME AND ADDRESS ARPA/NMR 1400 Wilson Boulevard Arlington, Va 22209		12. REPORT DATE <b>10 OCTOBER 1977</b> ✓
14. MONITORING AGENCY NAME & ADDRESS (if different from Controlling Office) AFOSR/NP Bolling AFB, Bldg. #410 Wash., D.C. 20332		13. NUMBER OF PAGES 198
		15. SECURITY CLASS. (of this report) Unclassified
		15a. DECLASSIFICATION/DOWNGRADING SCHEDULE
16. DISTRIBUTION STATEMENT (of this Report)  Approved for public release: distribution unlimited.		
17. DISTRIBUTION STATEMENT (of the abstract entered in Block 20, if different from Report)		
18. SUPPLEMENTARY NOTES		
19. KEY WORDS (Continue on reverse side if necessary and identify by block number)		
20. ABSTRACT (Continue on reverse side if necessary and identify by block number) One purpose of this investigation has been to regionalize the upper several hundred kilometers of the mantle under the Arctic region, Siberia and the Eurasian continental area using seismic surface waves. A second purpose has been to develop and test efficient computer techniques for the computation of accurate theoretical seismograms for hypothetical sources located within Eurasia and which make use of the results of the regionalization part of this study. These theoretical seismograms are complete in the sense that they contain both body		

DD FORM 1 JAN 73 1473

EDITION OF 1 NOV 65 IS OBSOLETE

UNCLASSIFIED

SECURITY CLASSIFICATION OF THIS PAGE (When Data Entered)

UNCLASSIFIED

SECURITY CLASSIFICATION OF THIS PAGE(When Data Entered)

and surface waves; they can be applied directly in a discrimination program by comparing the theoretical seismograms, computed for both earthquakes and underground explosions, with the actual recorded seismogram.

SECURITY CLASSIFICATION OF THIS PAGE(When Data Entered)